STUDIES OF INTERACTIONS BETWEEN ROD-LIKE CELLULOSE NANOCRYSTALS AND XYLAN AND PULLULAN DERIVATIVES: A LIGHT SCATTERING STUDY

Jae Hyun Sim

A dissertation submitted to the faculty of the
Virginia Polytechnic Institute and State University
in partial fulfillment of the requirements for the degree of

Doctor of Philosophy
in
Chemistry

Alan R. Esker, Chair

Harry W. Gibson

Diego Troya

Louis A. Madsen

November 28, 2012
Blacksburg, Virginia

Keywords: Light Scattering, Cellulose Nanocrystal, Pullulan, Xylan

STUDIES OF INTERACTIONS BETWEEN ROD-LIKE CELLULOSE NANOCRYSTALS AND XYLAN AND PULLULAN DERIVATIVES: A LIGHT SCATTERING STUDY

Jae Hyun Sim

ABSTRACT

Interactions between polysaccharide derivatives and rod-like cellulose nanocrystals were studied by light scattering. Two replicates of cellulose nanocrystals (DOE-2-12A and DOE-2-12B) were probed with polarized and depolarized dynamic light scattering. X-ray photoelectron spectroscopy experiments showed sulfate groups on cellulose nanocrystals. Decay rates from polarized dynamic light scattering experiments exhibited a significantly smaller angular dependence for both samples. However, DOE-2-12B showed a smaller angular dependence than DOE-2-12A. Lengths and diameters of DOE-2-12A and DOE-2-12B obtained by Broersma's formula were 229 ± 19 and 19 ± 7 nm and 240 ± 18 and 22 ± 6 nm, respectively. The resultant length and diameter of DOE-2-12B were comparable to those for cellulose whiskers obtained from cotton.

Adsorption of pullulan 4-chlorocinnamate (P4CC03) onto cellulose nanocrystals (DOE-2-12B) was also studied by UV-Vis spectroscopy, zeta-potential measurements, and polarized and depolarized dynamic light scattering. UV-Vis spectroscopy of the P4CC03/water binary system and *in situ* light scattering showed UV crosslinking of pullulan 4-chlorocinnamate occurred in binary and ternary systems but led to different aggregation behavior in the two ternary systems: PreX where P4CC03 crosslinking occurred prior to the addition of cellulose nanocrystals and Rxn where cellulose nanocrystals were present during UV exposure. These studies showed P4CC03 adsorbed onto cellulose nanocrystals and UV induced crosslinking occurred at the surface of the cellulose nanocrystals. Zeta-potential measurements also showed that P4CC03 adsorbed onto cellulose nanocrystals.

Finally, adsorption of 2-hydroxypropyltrimethylammonium xylans (HPMAXs) of degree of molar substitution MS = 0.34 onto rod-like cellulose nanocrystals (DOE-2-12Bs) were probed with zeta-potential measurements and polarized and depolarized dynamic light scattering. Zeta-potential changes of HPMAX/water, HPMAX/DOE-2-12B/water, and DOE-2-12B/water systems showed HPMAX adsorption onto DOE-2-12Bs. Intensity autocorrelation functions from Hv and Vv mode exhibited partial heterodyning. Decay time distributions of the binary and ternary systems showed that aggregates existed in the binary system but disappeared in the ternary system. These observations revealed that HPMAX adsorbed onto a fraction of the cellulose nanocrystals in the ternary system at low concentrations of HPMAX. Decreasing translational and rotational diffusion coefficients with increasing HPMAX concentration indicated HPMAX adsorption onto cellulose nanocrystals. A significant HPMAX concentration dependence of the ratio of rotational diffusion coefficient to translational diffusion coefficient showed strong adsorptive interactions between HPMAX and DOE-2-12B.

These studies showed there were interactions between polysaccharides and cellulose nanocrystals even in very dilute solutions. Also, it was shown that probe diffusion studies with rod-like cellulose nanocrystals is a promising strategy for probing complicated polymer solutions.

ACKNOWLEDGEMENTS

I need to thank many people during my Ph. D. study in Virginia Tech. First of all, I would like to appreciate my Ph. D. advisor, Alan R. Esker, for his guidance. He is strict but humane and always encouraging. Beyond my surprise about his enthusiastic hard-working attitude and scientific talent, the most astonishing thing is his generosity and consideration over the last four years. Without his help, this work would not have been possible.

Also, I would like to thank my committee members: Prof. Harry W. Gibson, Prof. Diego Troya, Prof. Sungsool Wi, and Prof. Louis A. Madsen. I appreciate their acceptance of this task and helpful comments and suggestions with respect to my courses and project. These conversations gave me deeper insights into chemistry. I also appreciate Prof. Paul Deck for his help to arrange my Ph. D. program as the Director of Graduate Studies in the Chemistry Department. In particular, I appreciate Prof. Richey M. Davis and Prof. Maren Roman for valuable discussion and comments on my Ph. D. work.

Next, I also grateful my former and present group members and other colleagues: Jianjun Deng, Woojin Lee, Suolong Ni, Rituparna Paul, Bingbing Li, Abdulaziz Kaya, Ufuk Karabiyik, Wen Yin, Qiongdan Xie, Joshua Kittle, Zelin Lin, Yang Liu, Xiaosong Du, Chuanzi OuYang, Shuping Dong and Dr. Chunying Shu. In particular, I would like to thank Woojin Lee for his great help and brotherly affection during my studies. I would also like to thank my friends from my time in Blacksburg: Youngki Kwon, Sungyong Park, Minjae Lee, and Joohong Lee.

I wish to express my sincere appreciation and gratitude to Prof. Daewon Sohn at Hangyang University who always encouraged me to finish my Ph. D. pursuing. Without his help, my career as scientist would not have been possible. As always, I appreciate my family for their unconditional love and support over the years. Last but not the least, I would like to thank all my friends not listed in here for all the great times. Although I did not list you individually here, you know who you are.

TABLE OF CONTENTS

List of Figures

Chapter 2

Chapter 3

Chapter 4

Chapter 5

Chapter 6

Chapter 7

Chapter 8

List of Tables

Chapter 2

Chapter 4

Chapter 5

Chapter 6

Chapter 7

Chapter8

CHAPTER 1

Overview

Understanding the interactions between polysaccharides in solution is important for the preparation of biocomposites that overcome chemical incompatibility with aqueous processing. The polysaccharide/colloidal particle/solvent ternary system is one of those systems not yet fully examined. One aim of this study was to provide fundamental guidelines for probing interactions in complicated polysaccharide solutions. Another aim was to use anisotropic cellulose nanocrystals as probes in diffusion studies of polysaccharide solutions.

This dissertation consists of eight chapters. Chapter 2 delivers an overall introduction and literature review related to this study. The main three chemical components of wood (cellulose, hemicellulose, and lignin) are discussed at the start of the chapter. The subsequent discussion includes introductory remarks for polymer physical chemistry. Next, the discussion addresses representative topics of polymer physical chemistry that provide the fundamental theoretical basis for the reminder of the dissertation. This discussion is followed by exemplary remarks about polymer physical chemistry of polysaccharides.

In Chapter 3, various light scattering techniques are reviewed. Static light scattering (SLS) has the longest history and provides theoretical concepts for other scattering techniques. Hence, the fundamental theories, measurement techniques, and analysis methods of static light scattering are discussed first. Next, dynamic light scattering (DLS) is discussed with theoretical background and experimental techniques. The dissertation then moves to the discussion of depolarized dynamic light scattering (DDLS) by focusing on data fitting and analysis.

Brief introductions to the preparation of materials and sample systems for this study are described in Chapter 4. The preparation of sample systems is the principle focus. Cellulose nanocrystals, pullulan 4-chlorocinnamates (P4CC03s), and 2-hydroxypropyltrimethylammonium xylans (HPMAXs) are introduced at the start of each section. The introduction of materials will be followed by details about the preparation of binary or ternary systems. A detailed description of materials and experimental methods will not be repeated in subsequent chapters.

Chapter 5 describes light scattering studies of rod-like cellulose nanocrystals. Two replicates of cellulose nanocrystals prepared from the hydrolysis of milled black spruce pulp in H_2SO_4 (DOE-2-12A and DOE-2-12B) were probed with atomic force microscopy (AFM), X-ray photoelectron spectroscopy (XPS), and polarized and depolarized dynamic light scattering. The angular dependence of intensity autocorrelation functions and size distributions are discussed. Decay rates from six different scattering angles were obtained. Resultant translational and rotational diffusion coefficients are summarized. We demonstrate that cellulose nanocrystals are potential rigid anisotropic probes to investigate polysaccharide/probe/solvent ternary systems.

In Chapter 6, light scattering studies of the interaction between pullulan cinnamates and rod-like cellulose nanocrystals are presented. Characterization of pullulan derivative adsorption onto cellulose nanocrystals is the focus of this chapter. UV-Vis spectroscopy and light scattering studies of various model binary and ternary systems with pullulan cinnamates and cellulose nanocrystals were performed. Also, a light scattering study of pullulan cinnamate exposed to UV light with and without cellulose nanocrystals is described. Zeta-potentials were measured to investigate the adsorption. This study yielded information about pullulan derivative adsorption onto anisotropic cellulose nanocrystals.

Chapter 7 contains light scattering studies of the interaction between xylan derivatives and rod-like cellulose nanocrystals. Polysaccharide adsorption onto cellulose nanocrystals was characterized with zeta-potential measurements. Intensity autocorrelation functions and decay time distributions are used to discuss the ergodicity of ternary systems containing different concentrations of xylan derivatives. This discussion is followed by a presentation of translational and rotational diffusion coefficients from a fitting analysis of decay rate - squared scattering vector profiles. Differences in xylan derivative adsorption onto cellulose nanocrystals with various concentrations of xylan derivative are the key result.

The overall conclusions of the dissertation and suggestions for further studies are provided in Chapter 8. In particular some possible directions to explore interactions of polysaccharides in colloidal solutions through probe diffusion studies are presented.

CHAPTER 2

Introduction and Literature Review

2.1. Introduction to Wood

Wood is a fascinating biological composite material (i.e. a complex tissue composed of different types of cells) possessing excellent mechanical properties. These interesting properties can be thoroughly understood by understanding the structure of the cell wall. Wood consists of numerous cells arranged into more complex structures that form interior parts of major stems, branches, and roots. As a porous heterogeneous material, these cells are responsible for the mechanical properties of wood. Trees consist of dead cells, lacking cytoplasm, and food storing cells, that are alive. Both dead cells and living cells are derived from the outer layer of the tree known as the vascular cambium.[1,2]

There are two kinds of cells in the vascular cambium: spindle-shaped cells (fusiform initials) and axially elongated cells (ray initials). The cells of the vascular cambium do not directly form new elements of wood, whereas they divide into daughter cells, some of which are deposited as the primary wall. At the very first stage, vascular cambium cells between xylem and phloem form the protective barriers around living cells. Then, xylem cells are developed through four stages: cell division, the growth of the daughter cells into mature cells, development of the secondary cell wall, and lignification. During the second step, active growth of daughter cells accompanies the formation of the cellulose microfibrils. As the cells consisting of the primary wall extended longitudinally as well as radially and reach maturity, a secondary wall, which is much stiffer than the primary wall, starts to deposit onto the internal side of the primary wall.[3,4]

2.1.1 Chemical Composition of the Cell Wall

About 96% of the cell wall is made up of three chief materials: cellulose, hemicellulose, and lignin. Cellulose and hemicellulose are relatively simple in structure, whereas lignins are complex phenylpropane polymers that are strongly intermeshed and chemically bonded by non-covalent forces and by covalent crosslinks to hemicelluloses.[1,2] The rest of the cell wall is developed with some polymeric constituents such as starch, pectin, and ash. Also, chemical composition varies between two different categories of wood: hardwood and softwood. The cellulose and hemicellulose contents are quite similar for both woods. However, softwood contains more lignin (ca. 30% by mass) than hardwood (ca. 20% by mass). Lignin provides not only structural stiffness but also structural cavities called pores or vessels. These vessels are found in xylem and show considerable variation of size, shape, and structure.[5-7]

2.1.1.1 Cellulose

In 1838, Anselme Payen suggested that the cell walls of a variety of plants were constructed of a substance, to which he gave the name cellulose.[8,9] Cellulose molecules are arranged into microfibrils containing crystalline and amorphous regions that are linked by hydrogen bonds, endowing a strong association that provides highly ordered alignment of the cellulose chain.[10] This polysaccharide derivative is chemically composed of anhydro-D-glucopyranose units linked by β-(1-4) glucosidic bonds as shown in Figure 2.1. Zehmeister, Toth[11] and Friudenberg[12] showed that those pyranose rings have chair conformations in which hydroxyl groups are in equatorial positions.

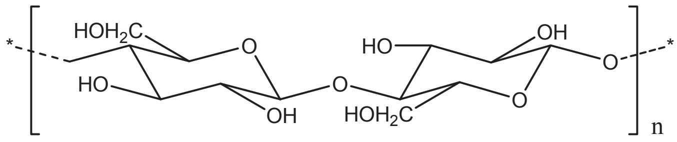

Figure 2.1 Repeating unit of cellulose.

Figure 2.1 shows the disaccharide cellobiose - the actual repeating unit of cellulose. Anhydroglucose units (AGUs) that are not a part of linear bridges of acetal-oxygen bonds (all 2nd AGUs) rotate 180º in the plane relative to the previous AGU in the chain to maintain appropriate bond angles.[13] Also, AGUs determine the degree of polymerization (DP or n) of cellulose. The DP of cellulose varies from ca. 300 to 10000 according to different chemical treatments used in its isolation.

Initially, cellulose molecules exist as microfibrils and form a porous membrane with hemicellulose. The pores are later occupied by lignin. Cellulose structures show various polymorphism that is well defined by X-ray crystallography.[14,15] The native form is denoted as cellulose I and several other polymorphs (mostly II, III, and IV) can be obtained through chemical treatments (Figure 2.2).

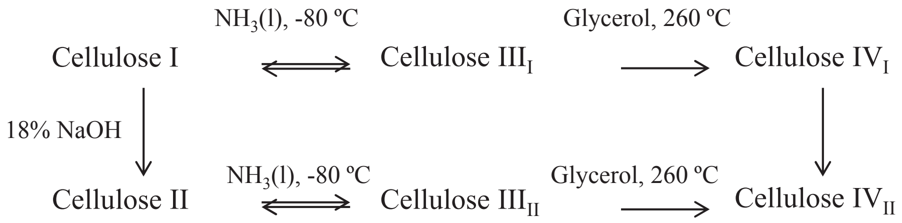

Figure 2.2 Illustration of the conversion scheme between cellulose polymorphs.

Cellulose II is obtained from cellulose I by applying concentrated aqueous alkali solution (e.g. 18% sodium hydroxide). This reaction is irreversible because cellulose I is the natural material obtained from biosynthesis. Regenerating cellulose produces cellulose II, not cellulose I. Cellulose III is obtained from cellulose I as well as cellulose II by applying and evaporating liquid ammonium at low temperature (ca. -80ºC).[16] Two cellulose polymorphs named cellulose III_I and cellulose III_{II} from cellulose I and cellulose II, respectively, have different infrared spectra and X-ray diffraction patterns.[17,18] As shown in Figure 2.2, each reaction producing cellulose III_I and III_{II} is reversible and they are the only reversible reactions in the scheme. Cellulose IV polymorphs are obtained by applying glycerol at high temperature (ca. 260 ºC) to cellulose III polymorphs.[19]

An X-ray crystallography study by Marchessault *et al.*[20] and Gardner *et al.*[21] proposed a structure for cellulose I by modeling with one molecular parameter and three packing parameters: (1) self-molecular motion - the stagger of the central chain along the helical axis with respect to the origin, (2) intramolecular motion - the coupled rotation of the chains with respect to the helical axis, and (3) intermolecular motion - the rotation of the second chain with respect to the first chain. Resultant structures had two intramolecular hydrogen bonds along the chain: OH-3’···O-5 and OH-2···OH-6’ as well as one intermolecular hydrogen bond along the chain axis: OH-6···OH-3. This result showed that cellulose I had a parallel structure.

With similar methods, the structure of cellulose II was investigated. The conformation of main chain is very similar to that of cellulose I: OH-3’···O-5 and OH-2···OH-6’. However, Kolpak *et al.*[22] showed that cellulose II had two more hydroxymethyl oxygens at the end of chain and one more in the center of chain relative to cellulose I. Additionally, the three groups combined to yield an anti-parallel structure with extensive 3-dimensional hydrogen bonding. As a result, cellulose II had a lower crystallinity than cellulose I.

Cellulose III_I and III_{II} have x-ray diffraction patterns that are similar but have different chain polarity which leads to different infrared spectra.[23] Also, cellulose III derivatives show relatively weak rotation of hydroxymethyl groups due to strict chain symmetry. As is the case with cellulose III polymorphs, cellulose IV_I and IV_{II} show very similar x-ray diffraction patterns. Upon heterogeneous acetylation, cellulose IV_I produces cellulose triacetate I (parallel chain structure) and cellulose IV_{II} produces cellulose triacetate II (antiparallel chain structure).[24,25]

2.1.1.2 Lignin

Lignin is a high molecular weight solid compound present in wood at 25% to 30% by mass. Lignin is formed biosynthetically through reactions between subunits of *p*-phenyl-propanoic acids.[26,27] Extensive crosslinking makes lignin a three-dimensional polymer containing aliphatic and aromatic units that make it difficult to decompose the structure into lower molecular weight species without inducing structural changes.[27,28] Within wood, lignin is present in the cell wall, conferring structural support and impermeability against microbial attack and oxidative stress.[29]

Lignins can be broadly sorted into three groups: softwood lignin, hardwood lignin, and grass lignin. Softwood lignin is mostly composed of guaiacyl units from the predominant precursor, *trans*-coniferyl alcohol. Hardwood lignin is composed of guaiacyl and syringyl units from trans-coniferyl and trans-sinapyl alcohol, respectively. Grass lignin is derived from the two previously mentioned units with along p-hydroxyphenyl units from p-coumaryl alcohol. Figure 2.3 shows the chemical structures of the three main repeating units of lignin and more or less all plants consist of all three units: guaiacyl, syringyl, and p-hydroxyphenyl moieties.

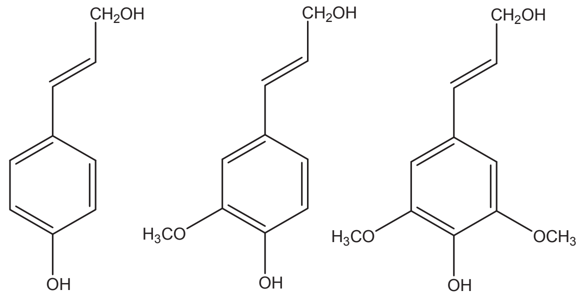

1 2 3

Figure 2.3 Chemical structures of lignin repeating units: (1) p-coumaryl alcohol, (2) conniferyl alcohol, and (3) sinapyl alcohol.

Lignin is one of the most complex polymers in nature with random 3-dimensional linkages that include extensive carbon-to-carbon bonds that make it difficult to degrade. Furthermore, it is extremely difficult to isolate all components of lignin completely or to dissolve lignins. Thus, the molar mass cannot be determined. Genuine lignin from wood is insoluble in all known simple solvents but isolated lignin shows limited solubility in solvents like dioxane, acetone, THF, and DMSO.[30]

Numerous studies aimed at the elucidation of the structure of lignin have taken place over several decades and this is still an active area of research. Investigations of lignin result in classification by structural elements: (1) formula of milled wood lignin,[31] (2) end groups with unlinked side chains,[32,33] (3) carbonyl groups,[34] (4) phenolic and aliphatic hydroxyl groups,[35] (5) condensed units,[36-38] (6) β-5 linked units,[39] (7) benzyl alcohols and benzyl ethers,[40,41] (8) β-O-4 linked units,[42] (9) biphenyl units,[43] (10) 4-O-5 linked units,[44] (11) β-β linked units,[45] (12) β-6 and β-2 linked units,[45] and (13) other linkage units.[44]

2.1.1.3 Hemicellulose

Hemicelluloses are the second most abundant renewable organic material next to cellulose. These hemicelluloses are non-crystalline heteropolysaccharides composed of several different sugar units and are generally of lower molar mass than cellulose. It can be converted to primary chemicals such as xylose, xylitol, furfural, etc. Also, hemicelluloses are branched polymers consisting of D-glucose, D-galactose, D-xylose, D-mannose, L-arabinose, 4-O-methylglucuronic, D-galacturonic and D-glucuronic acids. [2] Figure 2.4 shows some structural units for these sugars. The name is actually a misnomer, hemicelluloses are not forms of cellulose but may hydrogen bond to cellulose fibrils.[46] The main structural difference between cellulose and hemicelluloses is short lateral chain branches consisting of different sugars. The short chain branching enhances the solubility of hemicelluloses and also enhances their susceptibility to hydrolysis.[2,47,48] Hemicelluloses comprise a group of polysaccharides that can remain associated with cellulose after lignin has been removed.

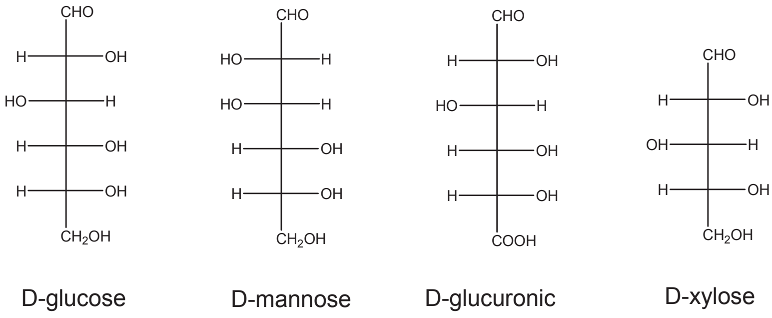

Figure 2.4 Fisher projections of four common sugar units in hemicelluloses.

The hemicelluloses from hardwood and softwood are different. The dominant hemicelluloses in hardwood are O-acetyl-(4-O-methylglucurono)-xylan and a small portion of glucomannan (ca. 4%).[49] The structure of O-acetyl-(4-O-methylglucurono)-xylan is well defined (Fig. 2.5). It consists of a backbone of ca. 200 (1→4)-linked β-D-xylopyranose residues. On average, C-2 in every 10th xylose residue is substituted by a 4-O-methylglucuronic acid residue. The ratio of glucose and mannose in the purified glucomannan is 1:1 or 1:2. Also, the isolation of softwood shows arabino-(4-O-methylglucurono)xylan, galactoglucomannan and glucomannan derivatives, and arabinogalactan. Figure 2.6 shows some partial chemical structures of isolated softwood hemicelluloses.[50,51]

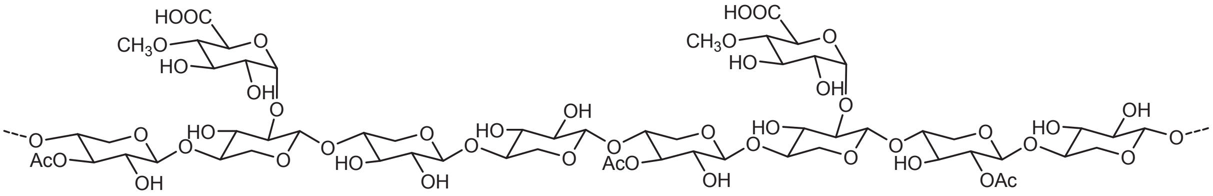

Figure 2.5 Schematic chemical structure of O-acetyl-(4-O-methylglucurono)-xylan from hardwood.

(1)

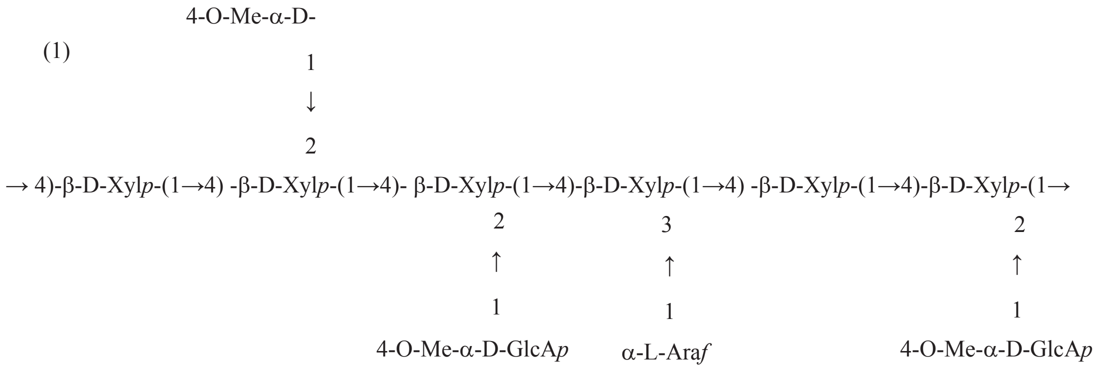

$$\rightarrow 4)\text{-}\beta\text{-D-Xyl}p\text{-}(1\rightarrow 4)\text{-}\overset{\substack{\text{4-O-Me-}\alpha\text{-D-}\\ 1\\ \downarrow\\ 2}}{\beta\text{-D-Xyl}p}\text{-}(1\rightarrow 4)\text{-}\underset{\substack{2\\ \uparrow\\ 1\\ \text{4-O-Me-}\alpha\text{-D-GlcA}p}}{\beta\text{-D-Xyl}p}\text{-}(1\rightarrow 4)\text{-}\underset{\substack{3\\ \uparrow\\ 1\\ \alpha\text{-L-Ara}f}}{\beta\text{-D-Xyl}p}\text{-}(1\rightarrow 4)\text{-}\beta\text{-D-Xyl}p\text{-}(1\rightarrow 4)\text{-}\underset{\substack{2\\ \uparrow\\ 1\\ \text{4-O-Me-}\alpha\text{-D-GlcA}p}}{\beta\text{-D-Xyl}p}\text{-}(1\rightarrow$$

(2)

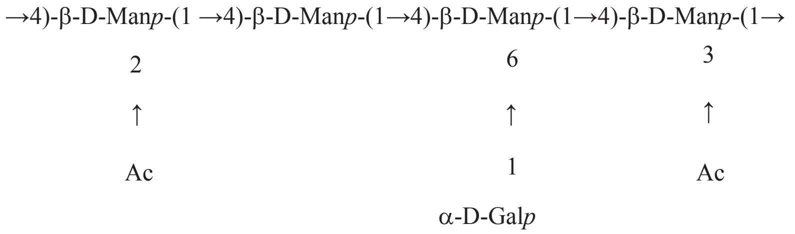

$$\rightarrow 4)\text{-}\underset{\substack{2\\ \uparrow\\ \text{Ac}}}{\beta\text{-D-Man}p}\text{-}(1\rightarrow 4)\text{-}\beta\text{-D-Man}p\text{-}(1\rightarrow 4)\text{-}\underset{\substack{6\\ \uparrow\\ 1\\ \alpha\text{-D-Gal}p}}{\beta\text{-D-Man}p}\text{-}(1\rightarrow 4)\text{-}\underset{\substack{3\\ \uparrow\\ \text{Ac}}}{\beta\text{-D-Man}p}\text{-}(1\rightarrow$$

(3)

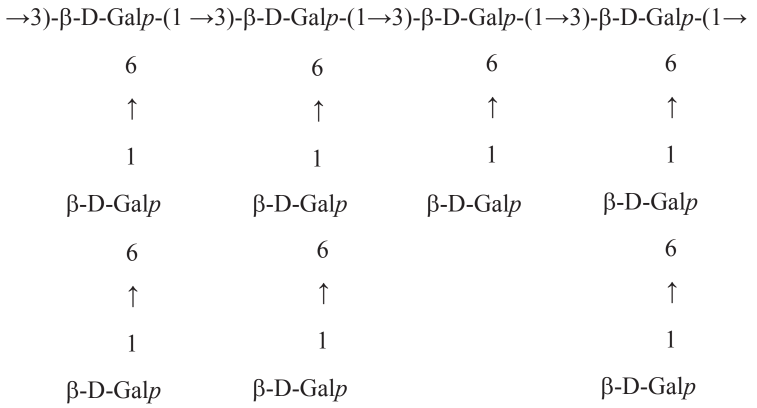

$$\rightarrow 3)\text{-}\underset{\substack{6\\ \uparrow\\ 1\\ \beta\text{-D-Gal}p\\ 6\\ \uparrow\\ 1\\ \beta\text{-D-Gal}p}}{\beta\text{-D-Gal}p}\text{-}(1\rightarrow 3)\text{-}\underset{\substack{6\\ \uparrow\\ 1\\ \beta\text{-D-Gal}p\\ 6\\ \uparrow\\ 1\\ \beta\text{-D-Gal}p}}{\beta\text{-D-Gal}p}\text{-}(1\rightarrow 3)\text{-}\underset{\substack{6\\ \uparrow\\ 1\\ \beta\text{-D-Gal}p}}{\beta\text{-D-Gal}p}\text{-}(1\rightarrow 3)\text{-}\underset{\substack{6\\ \uparrow\\ 1\\ \beta\text{-D-Gal}p\\ 6\\ \uparrow\\ 1\\ \beta\text{-D-Gal}p}}{\beta\text{-D-Gal}p}\text{-}(1\rightarrow$$

Figure 2.6 Partial structures of (1) arabino-(4-O-methylglucurono) xylan, (2) O-acetyl-galactoglucomannan, and (3) arabinogalactan.[50,51] (GlcA = glucuronic acid, Xyl = xylose, Ara = arabinose, Man = mannose, Gal = galactose, Ac = acetyl group, *p* = pyranosyl ring, and *f* = fyranosyl ring)

2.2 Polymer Physical Chemistry with Polysaccharides

2.2.1 Introduction to Polymer Physical Chemistry

In the early 19th century, Henri Braconnot and Christian F. Schönbein introduced the first artificial cellulose (a synthetic derivative of natural cellulose, i.e. cellulose acetate) having high molar mass.[52] This macromolecule would later be known as a polymer.[53,54] About a century later, Baekeland introduced the first commercial synthetic polymer, Bakelite (polyoxy-benzylmethylenglycolanhydride) in 1910.[55-58] As early polymers were recognized as low cost and artificial, interest in those materials grew as people recognized a wide range of potential applications. Now, polymer science is a widely studied research area.

Polymer science is inherently multidisciplinary including the synthesis and characterization of polymers that has evolved into various subfields: polymer chemistry, polymer physics, polymer engineering, etc. With the advance of synthetic macromolecules, two of the topics have attracted scientific attention: (1) synthesis and (2) properties. We will briefly review the second area.

2.2.2 Representative Topics of Polymer Physical Chemistry

First of all, we will briefly review some topics of polymers in solution. In polymer physics and polymer chemistry, the properties of polymers have largely been studied on the basis of two categories: static and dynamic (rheological) properties. For static properties, size and shape were the principal focus.[59] Molar mass, length scales (statistical radii like an end-to-end distance), and theories based on structure factor models with various scattering methods are closely related with size and shape. For dynamic properties, diffusion and viscosity depend on the relative movement between polymers in solution.[60] Also, polymer motion strongly depends upon the state of matter. In this literature review, physicochemical properties of *polymer solutions* are the focus.

2.2.2.1 Molar Mass

Most polymer samples contain molecules having various *degrees of polymerization* and numerous statistical concepts have been developed to describe the molar mass distributions.[61] A polymer sample having chains of different lengths is said to be *polydisperse*. Due to the differences in the degrees of polymerization, molar masses are average values. Here we consider two methods to select one polymer chain from a sample. The first method is related with the number of *i*-mers, a polymer chain having a degree of polymerization of *i*, in the sample and the second method is related with the weight of *i*-mers in a sample. For the first method, *a* sample containing *n* *i*-mers where n_i is an *i*-mer of specific length can be expressed as a number fraction, x_i:

$$x_i = \frac{n_i}{\sum_i n_i} \tag{2.1}$$

and the molar mass from the number fraction is called the number average molar mass, M_n:

$$M_n = \sum_i x_i M_i = \frac{\sum_i n_i M_i}{\sum_i n_i} = M_0 \frac{\sum_i i n_i}{\sum_i n_i} \tag{2.2}$$

where M_0 is the molar mass of the repeating unit.

For the second method, a weight of *i*-mer provides the weight fraction, w_i:

$$w_i = \frac{i n_i}{\sum_i i n_i} \quad \text{or} \quad w_i = \frac{x_i M_i}{\sum_i x_i M_i} \tag{2.3}$$

and the weight average molar mass, M_w, is obtained from a weight fraction.

$$M_w = \sum_i w_i M_i = \frac{\sum_i i n_i M_i}{\sum_i i n_i} = M_0 \frac{\sum_i i^2 n_i}{\sum_i i n_i} = \frac{\sum_i n_i M_i^2}{\sum_i n_i M_i} \tag{2.4}$$

Both molar masses can be expressed in terms of the molar mass of the repeating unit (M_0) as seen in Eqn. 2.2 and 2.4 and fractions that define the *k*-th moment of the number fraction distribution (m_k):[61,62]

$$m_k = \sum_i x_i M_i^k \tag{2.5}$$

The zeroth ($k = 0$) moment is one because the distribution is normalized:

$$m_0 = \sum_i x_i = 1 \tag{2.6}$$

Then, M_w and M_n are defined with moments of the number fraction distribution:

$$M_w \equiv \frac{m_2}{m_1} = \frac{\sum_i x_i M_i^2}{\sum_i x_i M_i} = \frac{\sum_i x_i M_i^2}{M_n} = \sum_i w_i M_i \tag{2.7}$$

and

$$M_n \equiv \frac{m_1}{m_0} = \frac{\sum_i x_i M_i}{\sum_i n_i} = \sum_i x_i M_i \tag{2.8}$$

We used the weight fraction to obtain weight average molar masses and the weight fraction is related with mass concentration: the mass of molecules with degrees of polymerization, *i*, per unit volume (c_i).

$$w_i = \frac{c_i}{c} \tag{2.9}$$

where *c* is the total mass concentration. Eqns. 2.3 and 2.8 provide:

$$w_i = \frac{M_i}{M_n} x_i = \frac{i}{i_n} x_i \tag{2.10}$$

where i_n is the number average degree of polymerization ($i_n \equiv M_n / M_0$). The total number density of chains is obtained from the sum of the number density of all chains:

$$\frac{cN_{Av}}{M_n} = \sum_i \frac{c_i N_{Av}}{M_i} \tag{2.11}$$

where N_{Av} is Avogadro's number. Also, Eqn. 2.9 provides an alternative definition of the number average molar mass:

$$M_n = \frac{c}{\sum_i c_i / M_i} = \frac{1}{\sum_i w_i / M_i} \tag{2.12}$$

and similarly the weight average molar mass is defined as:

$$M_w = \sum_i w_i M_i = \sum_i \frac{c_i}{c} M_i \,. \tag{2.13}$$

So far, the weight average molar mass and the number average molar mass are defined from the weight fraction, the number fraction, k-th order of moment of the number fraction distribution, and the mass concentration. From previous concepts, the k-th moment provides higher order molar masses. In Eqns. 2.7 and 2.8, each molar mass is expressed with the ratio between (k+1)-th moment and k-th moment and more ratios provide:

$$M_z \equiv \frac{m_3}{m_2} = \frac{\sum_i x_i M_i^3}{\sum_i x_i M_i^2} = \frac{\sum_i w_i M_i^2}{\sum_i w_i M_i} = \frac{\sum_i c_i M_i^2}{\sum_i c_i M_i} \tag{2.14}$$

$$M_{z+1} \equiv \frac{m_4}{m_3} = \frac{\sum_i x_i M_i^4}{\sum_i x_i M_i^3} = \frac{\sum_i w_i M_i^3}{\sum_i w_i M_i^2} = \frac{\sum_i c_i M_i^3}{\sum_i c_i M_i^2} \tag{2.15}$$

It is possible to obtain higher order molar masses; however, as the order increases, the molar mass is more strongly influenced by the chains with large molar masses (high molar mass tail of the molar mass distribution) than the chains of lower molar mass.

To this point, average molar masses were reviewed. However, a single average molar mass cannot define a polymer sample without knowledge of how chain lengths (molar mass of each chain) of a polymer sample are distributed. Thus the ratio of two molar masses provides a very useful method for addressing this question for standard molar mass distributions. The ratio is called *the polydispersity index* (PDI):

$$PDI = \frac{M_w}{M_n} \tag{2.16}$$

We know that molar mass of higher order is larger than that of lower order and consequently PDI is always greater than unity.

When average values are obtained, standard deviations need to be discussed. The mean of a distribution of variable, i, is defined as:

$$\langle i \rangle \equiv \frac{\sum_i i n_i}{\sum_i n_i} = \sum_i i x_i \approx \int_0^\infty i P(i) \mathrm{d}i \tag{2.17}$$

where a bracket means the average defined with discrete (x_i) and continuous probability distributions ($P(i)$). $\langle i \rangle$ is the number average degree of polymerization because the degree of polymerization was used to define the molar mass at the very first stage of this chapter. The standard deviation, σ, is defined with Eqn. 2.17:

$$\sigma \equiv \left(\frac{\sum_i n_i (i - \langle i \rangle)^2}{\sum_i n_i} \right)^{1/2} = \left(\sum_i x_i (i - \langle i \rangle)^2 \right)^{1/2} \tag{2.18}$$

Then, the variance from Eqn. 2.18 is obtained:

$$\sigma^2 = \frac{\sum_i n_i i^2}{\sum_i n_i} - 2\langle i \rangle \frac{\sum_i n_i i}{\sum_i n_i} + \langle i \rangle^2 \tag{2.19}$$

and from the definition of average we obtain:

$$\sigma^2 = \left\langle i^2 \right\rangle - 2\left\langle i \right\rangle^2 + \left\langle i \right\rangle^2 = \left\langle i^2 \right\rangle - \left\langle i \right\rangle^2 \tag{2.20}$$

We already know that $\left\langle i^2 \right\rangle$ is larger than $\left\langle i \right\rangle^2$ and Eqn. 2.20 provides another expression of the standard deviation:

$$\sigma = \left(\left\langle i^2 \right\rangle - \left\langle i \right\rangle^2 \right)^{1/2} \tag{2.21}$$

In Eqn. 2.18 the number average degree of polymerization was used to define the standard deviation. In the same way, the number average molar mass and associated molar masses of individual chains, $M_i = iM_0$, provide the standard deviation:

$$\sigma = \left[\sum_i x_i \left(M_i - M_n \right)^2 \right]^{1/2} \tag{2.22}$$

Here, the standard deviation of Eqn. 2.21 is unitless but that in Eqn. 2.22 has the unit of molar mass. A simple calculation shows:

$$\sigma = \left[\left(\sum_i x_i M_i^2 \right) - M_n^{\,2} \right]^{1/2} \tag{2.23}$$

and

$$\sigma = M_n \left[\frac{\sum_i x_i M_i^{\,2}}{\left(\sum_i x_i M_i \right)^2} - 1 \right]^{1/2} \tag{2.24}$$

Eqn. 2.4 is invoked to obtain:

$$\sigma = M_n \left[\frac{M_w}{M_n} - 1 \right]^{1/2} \tag{2.25}$$

Eqn. 2.25 shows PDI is always larger than unity and the standard deviation is closely related to the number average molar mass.[60-64]

2.2.2.2. Conformations and Length Scales of Polymers

Many properties of polymers depend on their size and shape. Size is defined with a length scale that can be changed relative to the environment of the polymer. If a polymer is in a solvent, interactions between polymer chains and solvent molecules affect the size. We start with the first length scale for size: root-mean-square (rms) end-to-end distance, $\langle h^2 \rangle^{1/2}$, for a hypothetical polymer chain having n rigid links and each link has a length of l. Squared values are used because a fully random walk for an ensemble of polymer chains has an average value of zero. When the arbitrary chain is selected, the link has one end as a starting point and the other end is a literal end point. The start point and end point define the direction of the link and each link is defined with a vector: $\mathbf{l}_i$ with $i = 1, 2, 3, \ldots$, n. Thus the end-to-end vector of one chain is the sum of all link vectors. The instantaneous end-to-end vector, $\mathbf{h}$, is just a sum of all link vectors (Appendix A):

$$\mathbf{h} = \sum_{i=1}^{n} \mathbf{l}_i \tag{2.26}$$

In solution, a polymer chain shows thermal motion and the end-to-end vector of the chain is able to point in any direction with equal probability. Consequently, the average of $\mathbf{h}$ with an isotropic chain is zero. Although the average end-to-end vector is zero, the root-mean-square (rms) end-to-end distance:

$$\langle \mathbf{h}^2 \rangle^{1/2} = \langle \mathbf{h} \bullet \mathbf{h} \rangle^{1/2} = \left\langle \sum_{i=1}^{n} \mathbf{l}_i \bullet \sum_{j=1}^{n} \mathbf{l}_j \right\rangle^{1/2} \tag{2.27}$$

is not zero. Also, the length of each vector is defined as l:

$$l = |\mathbf{l}_i| \tag{2.28}$$

and the scalar product of the given vector is:

$$\mathbf{l}_i \bullet \mathbf{l}_j = l^2 \cos\theta_{ij} \tag{2.29}$$

Thus, Eqns. 2.27 and 2.29 provide:

$$\left\langle h^2 \right\rangle \approx \left\langle \mathbf{h}^2 \right\rangle = \sum_{i=1}^{n}\sum_{j=1}^{n} \left\langle \mathbf{l}_i \bullet \mathbf{l}_j \right\rangle = l^2 \sum_{i=1}^{n}\sum_{j=1}^{n} \left\langle \cos\theta_{ij} \right\rangle \tag{2.30}$$

So far, we assumed that the polymer sample was an ideal chain and there was no correlation between bond vectors. The model depicts the ideal chain as a *freely jointed chain*. When bond vectors wiggle independently (i.e. no correlation), the cosine term in Eqn. 2.29 has two values:

$$\left\langle \cos\theta_{ij} \right\rangle = 0, \text{ when } i \neq j \tag{2.31}$$

$$\left\langle \cos\theta_{ij} \right\rangle = 1, \text{ when } i = j \tag{2.32}$$

Eqns. 2.30 ~ 2.32 provide the rms end-to-end distance of the freely jointed chain model:

$$\left\langle h^2 \right\rangle = nl^2 \tag{2.33}$$

Next, we assume that adjacent bonds are correlated and show free rotation but the angle is confined as θ. Average cosine shown in Eqn. 2.31 is no longer zero because the angle is restricted. Let $\alpha = \cos\theta$ for a simpler notation in subsequent equations. Now the average cosine provides:

$$\left\langle \mathbf{l}_i \bullet \mathbf{l}_j \right\rangle = l^2 \alpha \tag{2.34}$$

for adjacent bonds ($|i - j| = 1$). Furthermore, bonds that are not directly connected to each other ($|i - j| = 2$ or more) also have to be considered. Next, assume that the axis vector of rotation parallel to the bond vector $\mathbf{l}_{i-1}$ as $\boldsymbol{\beta}$. When the bond $\mathbf{l}_{i-1}$ recognizes the bond $\mathbf{l}_i$, there are two lengths: one is perpendicular to $\boldsymbol{\beta}$ and the other is parallel to $\boldsymbol{\beta}$. The former is $l\sin\theta$ and the latter is $l\cos\theta$. Angle is fixed in the model but rotation is not fixed (free rotation) and consequently the average of the component perpendicular to $\boldsymbol{\beta}$ is zero. Thus, the length of the component parallel to $\boldsymbol{\beta}$ is $l\alpha$. In case of $|i-j|=2$, the average of the scalar product between the bond $\mathbf{l}_{i-2}$ and the bond $\mathbf{l}_i$ provides:

$$\langle l_{i-2} \bullet l_i \rangle = l^2\alpha^2 \tag{2.35}$$

$\mathbf{l}_{i-2}$ still has the component of l but $\mathbf{l}_{i-2}$ recognize that $\mathbf{l}_i$ has the component of $l\alpha$ with angle θ and, consequently, the average of the scalar product is $l^2\alpha^2$ as shown in Eqn. 2.35. A similar argument can be extended to other bonds. For example, the average of the scalar product between $\mathbf{l}_{i-3}$ and $\mathbf{l}_i$ provides:

$$\langle \mathbf{l}_{i-3} \bullet \mathbf{l}_i \rangle = l^2\alpha^3 \tag{2.36}$$

Each component of $\mathbf{l}_{i-a}$ (a = 0, 1, 2, 3, …) in the calculations is always l, but $\mathbf{l}_i$ is changed by a factor of α $(=\cos\theta)$ when the bond $\mathbf{l}_{i-a}$ recognizes $\mathbf{l}_i$. Consequently, the average of the scalar product with $|i-j|=k$ is obtained:

$$\langle \mathbf{l}_i \bullet \mathbf{l}_j \rangle = l^2\alpha^k \tag{2.37}$$

Then, the rms end-to-end distance of the freely rotating chain is defined as:

$$\sum_{i}^{n}\sum_{i\neq j}^{n}\langle \mathbf{l}_i \bullet \mathbf{l}_j \rangle = \sum_{i}^{n}\sum_{i\neq j}^{n} l^2\alpha^k \tag{2.38}$$

From Eqns. 2.27, 2.29, and 2.30, we obtain:

$$\begin{aligned}\left\langle h^2\right\rangle &= \sum_{i=1}^{n}\sum_{j=1}^{n}\left\langle \mathbf{h}_i \bullet \mathbf{h}_j\right\rangle = \sum_{i=1}^{n}\left(\sum_{j=1}^{i-1}\left\langle \mathbf{h}_i \bullet \mathbf{h}_j\right\rangle + \left\langle \mathbf{h}_i^2\right\rangle + \sum_{j=i+1}^{n}\left\langle \mathbf{h}_i \bullet \mathbf{h}_j\right\rangle\right) \\ &= \sum_{i=1}^{n}\left\langle \mathbf{h}_i^2\right\rangle + l^2\sum_{i=1}^{n}\left(\sum_{j=1}^{i-1}\alpha^{i-j} + \sum_{j=i+1}^{n}\alpha^{j-i}\right)\end{aligned} \tag{2.39}$$

In Eqn. 2.39 the first summation is comprised of “self-terms” whose vector is dotted into itself and the second summation is “cross-terms” whose vector is dotted into n-1 other vectors. It is possible to expend the self-terms in Eqn. 2.39:

$$\left\langle h^2\right\rangle = nl^2 + l^2\sum_{i=1}^{n}\left(\sum_{j=1}^{i-1}\alpha^{i-j} + \sum_{j=i+1}^{n}\alpha^{j-i}\right) \tag{2.40}$$

To obtain the cross-terms in the Eqn. 2.40, a mathematical trick can be used:

$$(\cos\theta)^{|j-i|} = \exp\left[|j-i|\ln(\alpha)\right] = \exp\left[-\frac{|j-i|}{\kappa}\right] \tag{2.41}$$

where κ is a scaling parameter that is related to how fast correlations between bond vectors decay:

$$\kappa = -\frac{1}{\ln(\alpha)} \tag{2.42}$$

If the decay is very fast, there is little difference between results of a finite sum (with i, j, and n) and an infinite series (with m and ∞) and the second summation in Eqn. 2.39 reduces to:

$$\begin{aligned}l^2\sum_{i=1}^{n}\left(\sum_{j=1}^{i-1}\alpha^{i-j} + \sum_{j=i+1}^{n}\alpha^{j-i}\right) &= l^2\sum_{i=1}^{n}\left(\sum_{m=1}^{i-1}\alpha^{m} + \sum_{m=1}^{n-1}\alpha^{m}\right) \\ &\cong 2\sum_{i=1}^{n}\sum_{m=1}^{\infty}\alpha^{m} \\ &= 2n\sum_{m=1}^{\infty}\alpha^{m} \\ &= 2n\left(\frac{\alpha}{1-\alpha}\right)\end{aligned} \tag{2.43}$$

Hence, Eqn. 2.40 becomes:

$$\begin{aligned}\left\langle h^2\right\rangle &= nl^2 + 2nl^2\left(\frac{\alpha}{1-\alpha}\right)\\ &= nl^2\left(\frac{1+\cos\theta}{1-\cos\theta}\right)\end{aligned}\tag{2.44}$$

Eqn. 2.45 exhibits some interesting features. $\left\langle h^2\right\rangle$ is still proportional to nl^2 and larger than that of the freely jointed chain model because assumptions were made that the angle is less than 90º ($\cos\theta > 0$) and *n* is large.

Length scales that have been discussed thus far are based upon the assumptions related to an ideal chain. In a real polymer chain, each rotation is not free. Steric hindrance confines rotation of bonds and a backbone of a polymer chain has some specific arrangements: *gauche* and *trans*. Thus, two angles are introduced (θ and ϕ) from these conformations having dihedral angles.[66,67]

For the large *n*, we have:

$$\left\langle h^2\right\rangle = nl^2\left(\frac{1+\cos\theta}{1-\cos\theta}\right)\left(\frac{1+\left\langle\cos\phi\right\rangle}{1-\left\langle\cos\phi\right\rangle}\right)\tag{2.45}$$

where $\left\langle\cos\phi\right\rangle$ is the average of $\cos\phi$ from an appropriate potential energy curve and it is assumed that only the global minimum and local minima affect the overall stability of the chain conformation (Appendix A ~ E). End-to-end distances (rms) from both cases still depend on nl^2. Thus, a numerical constant, *C*, is applied:

$$\left\langle h^2\right\rangle = Cnl^2\tag{2.46}$$

C in Eqn. 2.46 does not depend on *n*. Consider the case of one chain having *n* links. The first link and the last link do not show any correlation but we can still make one big link connecting the first atom and the last atom. From the freely jointed chain assumption, the former and the latter have the same $\langle h^2 \rangle$. In unperturbed dimension:

$$C_n \equiv \frac{\langle h^2 \rangle_0}{nl^2} \tag{2.47}$$

where C_n is called the *characteristic ratio* and the numerator on the right-hand side of Eqn. 2.47 is the actual mean-square end-to-end distance. C_n depends on n but as n increases it converges to a specific constant. Thus, we can rewrite Eqn. 2.47 with a new length scale:

$$\langle h^2 \rangle_0 = C_\infty nl^2 = nl_{eff}^2 = Nb^2 \tag{2.48}$$

where $l_{eff} = l\sqrt{C_\infty}$, l_{eff} is the *effective length* and the proportionality constant between the real chain with local constraints and freely jointed chains having the same n, i.e. the same number of bonds but a different length scale. n is the number of bonds and can be substituted with the number of monomer or repeating unit, N. C_∞ is the characteristic ratio with large n. b in Eqn. 2.48 is the proportionality constant between n and N and called the *statistical segment length*.[61,62] As shown in Eqn. 2.48, b is *statistical* and does not have any physical correlation with a real chain length. Otherwise, $\langle h^2 \rangle_0$ directly depends on the molar mass but C_∞ and b do not.

While unperturbed states with freely jointed and freely rotating chain models have been discussed, the reality is that bonds affect each other and tend to be directional. This consideration leads to a *semiflexible* chain and there is a certain length over which the chain direction is correlated. This length is called the *persistence length*, l_p. If we make a unit vector in a certain direction, $\mathbf{l}_1/l$, a projection of end-to-end vector over the direction of the first vector provides:

$$
\begin{aligned}
l_p &\equiv \left\langle \frac{\mathbf{l}_1}{l} \bullet \mathbf{h} \right\rangle = \left\langle \frac{\mathbf{l}_1}{l} \bullet \sum_{i=1}^{n} \mathbf{l}_i \right\rangle \\
&= \frac{1}{l} \left\{ \left\langle \mathbf{l}_1 \bullet \mathbf{l}_1 \right\rangle + \left\langle \mathbf{l}_1 \bullet \mathbf{l}_2 \right\rangle + \left\langle \mathbf{l}_1 \bullet \mathbf{l}_3 \right\rangle + \cdots + \left\langle \mathbf{l}_1 \bullet \mathbf{l}_n \right\rangle \right\}
\end{aligned}
\tag{2.49}
$$

For rod-like chains, all bonds point in the same direction and the persistence length is infinite and we make a length, L:

$$\mathbf{l}_p > L \tag{2.50}$$

where L is the *contour length* and the maximum length that the chain can have (Appendix F):

$$L = nl \tag{2.51}$$

Eqn. 2.49 can be rewritten as:

$$
\begin{aligned}
l_p &= \frac{1}{l} \sum_{j=1}^{n} \left\langle \mathbf{l}_1 \bullet \mathbf{l}_j \right\rangle \\
&= \frac{1}{l} \sum_{j=x}^{n} \left\langle \mathbf{l}_x \bullet \mathbf{l}_j \right\rangle
\end{aligned}
\tag{2.52}
$$

With flexible chains, only a small number of bonds proceed in the same direction and we select one arbitrary bond, x, to set a short memory of the direction:

$$2l_p = \frac{1}{l} \sum_{j=1}^{n} \left\langle \mathbf{l}_x \bullet \mathbf{l}_j \right\rangle + l \tag{2.53}$$

In Eqn. 2.53, a double summation from the opposite direction related to bond x provides $2l_p$, not l_p , which means each set of two bonds gives a double summation too:

$$|x - j| = |j - x| \tag{2.54}$$

However, there is the only one summation when i is equal to j. Making sure that x is an arbitrarily selected bond, the summation should be performed over all possible x. Here, we make two assumptions to obtain the most probable result: (1) each selection of x will give different results but we assume that the summation over all possible x gives the same result, and (2) n is infinitely large to minimize the effect from chain ends and the short chain correlation among the bonds. These two assumptions lead to:

$$l_p = \frac{1}{2l}\sum_{j=1}^{n}\sum_{x=1}^{n}\left\langle \mathbf{l}_x \bullet \mathbf{l}_j \right\rangle + \frac{l}{2} \tag{2.55}$$

In Eqn. 2.55, we added *n* identical terms in the summation based on the assumption of the same result for all possible *x*. Thus, we need to divide the summation in Eqn. 2.55 by *n* to remove overcounted terms:

$$l_p = \frac{1}{2nl}\sum_{j=1}^{n}\sum_{x=1}^{n}\left\langle \mathbf{l}_x \bullet \mathbf{l}_j \right\rangle + \frac{l}{2} \tag{2.56}$$

From the Eqn. 2.27, we obtain:

$$\begin{aligned} l_p &= \frac{1}{2nl}\left\langle h^2 \right\rangle + \frac{l}{2} \\ &= \frac{1}{2nl} C_\infty n l^2 + \frac{l}{2} \\ &= \left(C_\infty + 1\right)\frac{l}{2} \end{aligned} \tag{2.57}$$

The assumption that *i* is infinitely large means that *l* is relatively small, $l \to 0$, as *n* increases. Thus, the *l*/2 term vanishes:

$$\begin{aligned} l_p &= \frac{1}{2nl}\left\langle h^2 \right\rangle \\ &= \frac{1}{2nl} C_\infty n l^2 \\ &= C_\infty \frac{l}{2} \end{aligned} \tag{2.58}$$

Eqns. 2.57 and 2.58 show different values for l_p but for most chains, C_∞ is much larger than unity and a difference, *l*/2, does not affect l_p significantly. Thus,

$$C_\infty l = 2l_p \equiv l_k \tag{2.59}$$

where l_k is the *Kuhn length* (effective bond length) which is twice the persistence length.[13] Finally we obtain:

$$\left\langle h^2 \right\rangle_0 = C_\infty n l^2 = N b^2 = L l_k \tag{2.61}$$

where the contour length, $L=nl$. In Eqn. 2.49, higher terms in the series vanish with decreasing correlation or memory, which means that the persistence length is the maximum length that one can follow along a skeletal bond to the point where the chain bends over 90º: $\cos\theta$ is surely zero. Also, the Kuhn length is twice the persistence length, which means the length along the skeletal bond to the point the chain bends by 180º.

Eqn. 3.49 is rewritten with previous assumptions ($n \to \infty, l \to 0$):

$$\begin{aligned} l_p &= \frac{1}{l}\left\{\left\langle \mathbf{l}_1 \bullet \mathbf{l}_1 \right\rangle + \left\langle \mathbf{l}_1 \bullet \mathbf{l}_2 \right\rangle + \left\langle \mathbf{l}_1 \bullet \mathbf{l}_3 \right\rangle + \cdots + \left\langle \mathbf{l}_1 \bullet \mathbf{l}_n \right\rangle\right\} \\ &= \frac{1}{l}\left\{l^2 + l^2\alpha + l^2\alpha^2 + \cdots + l^2\alpha^{n-1}\right\} \\ &= l\left\{1 + \alpha + \alpha^2 + \cdots + \alpha^{n-1}\right\} \\ &= l\left(\frac{1-\alpha^n}{1-\alpha}\right) \\ &= \frac{l}{1-\alpha}, n \to \infty \end{aligned} \tag{2.62}$$

and we obtain:

$$\alpha = 1 - \frac{l}{l_p} \approx \exp\left(-\frac{l}{l_p}\right), l \to 0 \tag{2.63}$$

From the freely rotating chain model we can retain α^n:

$$\begin{aligned}\left\langle h^2\right\rangle &= nl^2\frac{1+\alpha}{1-\alpha}-2l^2\alpha\frac{\left(1-\alpha^n\right)}{\left(1-\alpha\right)^2}\\ &= nl^2\left(\frac{2-l/l_p}{l/l_p}\right)-2l^2\left(1-\frac{l}{l_p}\right)\left[\frac{1-\exp\left(-L/l^p\right)}{\left(l/l_p\right)^2}\right]\\ &= Ll_p\left(2-\frac{l}{l_p}\right)-2l_p^2\left(1-\frac{l}{l_p}\right)\left(1-\exp\left(-L/l_p\right)\right)\end{aligned}\tag{2.64}$$

and we still have the assumption, $l \to 0$. Thus Eqn 2.64 is rewritten (Appendix G) as:

$$\left\langle h^2\right\rangle = 2l_pL-2l_p^2\left[1-\exp\left(-L/l_p\right)\right]\tag{2.65}$$

and we can see two limiting situations:

$$\begin{aligned}\left\langle h^2\right\rangle &= L^2, \qquad L \ll l_p(\text{rod})\\ \left\langle h^2\right\rangle &= 2Ll_p, \qquad L \gg l_p(\text{coil})\end{aligned}\tag{2.66}$$

Eqn. 2.65 expresses the worm-like chain model as one specific case derived by Kratky and Porod when the freely rotating chain has a small angle (Appendix G).[68] L/l_p is the number of persistence lengths in the chain or the effective degree of polymerization. Thus, L/l_p would be small in rod-like chains and large in coil-like chain.

So far, several length scales have been discussed based on the end-to-end distance but they have fundamental limitations: (1) it is difficult to measure the end-to-end distance experimentally and (2) the definition can be ambiguous for some polymer architectures, e.g. rings, dendrimers, and combs. Also, only two monomers in the chain, the first and the last, were picked to define the end-to-end distance, which means all other monomers cannot have significant meaning in the end-to-end distance. Thus, we make a vector from the center of gravity to monomer, *i*, as $\boldsymbol{s}_i$. At any particular time, the average of the vector $\boldsymbol{s}_i$ is:

$$\sum_{i=1}^{n}\mathbf{s}_i = 0\tag{2.67}$$

and the radius of gyration is defined as:

$$\begin{aligned} R_g &= \left\langle s^2 \right\rangle^{1/2} \\ &= \left\{ \frac{1}{N} \sum_{i=1}^{N} \left\langle s_i^2 \right\rangle \right\}^{1/2} \end{aligned} \tag{2.68}$$

where N is the number of monomers and not a number of bonds. Various radii of gyration of the freely jointed model and freely rotating model are defined in Appendices C and D. As a starting point, consider the very first dot product of two vectors, s_i and s_j:

$$\begin{aligned} s_i \bullet s_j &= \left| s_i \right| \left| s_j \right| \cos\theta \\ &= \frac{1}{2}\left(s_i^2 + s_j^2 - r_{ij}^2 \right) \end{aligned} \tag{2.69}$$

where r_{ij}^2 is the square of the distance between monomers i and j. Eqns. 2.68 and 2.69 provide:

$$\sum_{i=1}^{N}\sum_{j=1}^{N} \left\langle \mathbf{s}_i \bullet \mathbf{s}_j \right\rangle = \frac{1}{2}\sum_{i=1}^{N}\sum_{j=1}^{N} \left\langle s_i^2 \right\rangle + \frac{1}{2}\sum_{i=1}^{N}\sum_{j=1}^{N} \left\langle s_j^2 \right\rangle - \frac{1}{2}\sum_{i=1}^{N}\sum_{j=1}^{N} \left\langle r_{ij}^2 \right\rangle \tag{2.70}$$

where $\left\langle r_{ij}^2 \right\rangle$ is the mean-square end-to-end distance between bonds i and j and is different from the mean-square end-to-end distance, $\left\langle h^2 \right\rangle$. The former is the distance between arbitrary monomers i and j and the latter is the distance between the first and the last bond vectors.

$$\begin{aligned} \sum_{i=1}^{N}\sum_{j=1}^{N} \left\langle \mathbf{s}_i \bullet \mathbf{s}_j \right\rangle &= \left\langle \sum_{i=1}^{N} s_i \bullet \sum_{j=1}^{N} s_j \right\rangle \\ &= \left\langle 0 \bullet 0 \right\rangle \\ &= 0 \end{aligned} \tag{2.71}$$

In Eqn. 2.70,

$$\frac{1}{2}\sum_{i=1}^{N}\sum_{j=1}^{N} \left\langle s_i^2 \right\rangle = \frac{1}{2}\sum_{i=1}^{N}\sum_{j=1}^{N} \left\langle s_j^2 \right\rangle = \frac{N^2}{2} R_g^2 \tag{2.72}$$

and the Eqns. 2.70 to 2.72 are combined to give:

$$R_g^2 = \frac{1}{2N^2}\sum_{i=1}^{N}\sum_{j=1}^{N}\left\langle r_{ij}^2 \right\rangle \tag{2.73}$$

Thus, $\left\langle r_{ij}^2 \right\rangle$ is related with the effective length scale, b:

$$\left\langle r_{ij}^2 \right\rangle = |i-j|b^2 \tag{2.74}$$

Upon rearrangement, Eqn. 2.73 becomes:

$$\begin{aligned} R_g^2 &= \frac{b^2}{2N^2}\sum_{i=1}^{N}\sum_{j=1}^{N}|i-j| \\ &= \frac{b^2}{2N^2}\sum_{k=1}^{N-1}2(N-k) \end{aligned} \tag{2.75}$$

and:

$$\begin{aligned} R_g^2 &= \frac{b^2}{N^2}\left[N\sum_{k=1}^{N-1}k - \sum_{k=1}^{N-1}k^2\right] \\ &= \frac{b^2}{N^2}\left[\frac{N^2(N-1)}{2} - \frac{N^2(N-1)(2N-1)}{6}\right] \\ &= \frac{Nb^2}{6} - \frac{b^2}{6N} \\ &\approx \frac{Nb^2}{6} \end{aligned} \tag{2.76}$$

The last approximation is satisfied when N is very large and with Eqns. 2.59 and 2.61 yields:

$$R_g^2 = \frac{\left\langle h^2 \right\rangle_0}{6} = \frac{C_\infty n l^2}{6} = \frac{Nb^2}{6} = \frac{2l_p L}{6} \tag{2.77}$$

Then, the radius of gyration of a worm-like chain can be defined as:

$$\left\langle R_g^2 \right\rangle = \frac{1}{3}l_p L - l_p^2 + \frac{2l_p^3}{L} - \frac{2l_p^4}{L^2}\left[1 - \exp\left(-\frac{L}{l_p}\right)\right] \tag{2.78}$$

as shown in Appendix H.

2.2.2.3 Diffusion

In general dynamics, *diffusion* is a time-dependent physical process constituted by the random motion of a given entity and leads to a statistical distribution in space of the probable position of a particle at some later time.[61] The question how fast a group of entities distribute in a given environment is controlled by the *diffusion coefficient*, *D*. In polymer chemistry it is defined as the proportionality constant between the three dimensional mean-square displacement of the colloidal particle and the time taken by the system to show a resultant displacement. Diffusion constants themselves can be classified into two distinct properties: the *tracer diffusion coefficient,* D_t and the *mutual diffusion coefficient,* D_m. In general, a diffusion coefficient, *D*, is:

$$\left\langle [\mathbf{r}(t) - \mathbf{r}(0)]^2 \right\rangle = 6Dt \tag{2.79}$$

$$\left\langle [\mathbf{r}(t) - \mathbf{r}(0)]^2 \right\rangle^{1/2} = (6Dt)^{1/2} \tag{2.80}$$

where **r** is a vector that depends on the time dependent displacement.[61,62] Motion satisfying Eqn. 2.79 is *diffusive motion*. For a given entity and liquid, the proportionality constant between velocity, **v**, and force, **f**, is the *friction coefficient*, ς :

$$\mathbf{f} = \varsigma\,\mathbf{v} \tag{2.81}$$

Eqns. 2.79 and 2.80 are related to the statistical length reviewed in the polymer conformation section (Section 2.2.2.2):

$$\lim_{t\to\infty} \frac{\left\langle r^2 \right\rangle}{t} = \frac{Nb^2}{t} \equiv 6D \tag{2.82}$$

where $\left\langle r^2 \right\rangle$ is the mean-square displacement. The prefactor of 6 is a historical convention and we will see it is reasonable in Eqns. 2.87 and 2.88. The tracer diffusion coefficient is a property of an individual particle undergoing *Brownian motion* and is affected by the size of particle and friction against the surrounding medium.[69] Einstein showed:[61]

$$D_t = \frac{kT}{\varsigma} \tag{2.83}$$

However, an actual particle undergoes viscous dissipation as well as Brownian motion, which leads to the time scale, τ, that is a function of the radius of the particle, R:

$$\tau \approx \frac{R^2}{D_t} \approx \frac{R^2 \varsigma}{kT} \tag{2.84}$$

and this time scale depends on the friction coefficient. For solids, the stress depends on the total deformation but the stress of a liquid (solution) only depends on the rate of deformation.[62] In Newtonian liquids the proportionality between the stress, σ, and the shear rate, $\dot{\gamma}$, provides the viscosity:

$$\sigma = \eta \dot{\gamma} \tag{2.85}$$

where η is the viscosity which will be discussed in the next section (Section 2.2.2.4). If we assume that we have a sphere with radius of R, then the friction coefficient depends on R and η:

$$\varsigma(\eta, R) \quad \text{or} \quad \varsigma \approx \eta R \tag{2.86}$$

Stokes obtained the actual relationship for a Newtonian liquid:

$$\varsigma = 6\pi\eta R \tag{2.87}$$

and Stokes law and the Einstein relationship provided the Stokes-Einstein relationship:

$$D_t = \frac{kT}{6\pi\eta R} \tag{2.88}$$

where R is very close to the *hydrodynamic radius*, R_h, for a tracer diffusion coefficient.[62]

For the case of mutual diffusion, the mutual diffusion coefficient (D_m) is a collective property that arises from movement of all the particles in the system and Fick invoked Fourier's law of heat conduction (Appendix I) to obtain Fick's first law:

$$J = -D_m \frac{\mathrm{d}c}{\mathrm{d}x} \tag{2.89}$$

Further discussion, including Fick's second law, can be found in Appendix I. So far, we discussed two diffusion coefficients, D_t and D_m. On the basis of the fact that diffusion itself acts to remove the gradients in the chemical potential, μ_2, rather than gradients in the concentration, D_t and D_m are related to each other, with a thermodynamic *driving force,* F_{diff}, for diffusion defined as:

$$F_{diff} = -\frac{1}{N_{av}} \frac{\mu_2}{\mathrm{d}x} \tag{2.90}$$

and further discussion (Appendix I) leads to:

$$\begin{aligned} D_m &= \frac{kT}{\varsigma}\left(1 + c\frac{\mathrm{d}\ln\gamma_2}{\mathrm{d}c}\right) \\ &= D_{t,0}\left(1 + c\frac{\mathrm{d}\ln\gamma_2}{\mathrm{d}c}\right) \end{aligned} \tag{2.91}$$

where γ_2 is the activity coefficient and we see $D_m \to D_{t,0}$ when $c \to 0$. The subscript "0" means *infinite dilution*. However the relationship in Eqn. 2.91 cannot be satisfied for *finite concentrations* where ς depends on concentration:

$$\varsigma(c) = \varsigma_0(1 + k_f c + \cdots) \tag{2.92}$$

Hence, Eqn. 2.91 is rewritten as:

$$\begin{aligned} D_m &= \frac{kT}{\varsigma_0(1+k_f\,c)}\left(1+c\frac{\mathrm{d}\ln\gamma_2}{\mathrm{d}c}\right) \\ &= D_{t,0}\left[1+c\left(\frac{\mathrm{d}\ln\gamma_2}{\mathrm{d}c}-k_f\right)\right] \end{aligned} \tag{2.93}$$

where the higher order terms in Eqn. 2.92 are truncated. A similar case for the solution of finite concentrations can be found in Appendix J. Recently, more sophisticated models have been reported and they can be found elsewhere.[70]

The first successive molecular model of polymer dynamics was obtained by *Rouse* who discussed a *bead and spring model* for an unentangled polymer system under *free-draining* conditions.[71] The total friction coefficient, ς_R, for N beads:

$$\varsigma_R = N\varsigma \tag{2.94}$$

where N is the number of beads. Diffusion coefficients of Rouse's model from the Einstein relationship are defined as:

$$D_R = \frac{kT}{\varsigma_R} = \frac{kT}{N\varsigma} \tag{2.95}$$

and we can invoke Eqn. 2.84 to obtain the *Rouse time*:

$$\tau_R \approx \frac{R^2}{D_R} \approx \frac{R^2}{kT/(N\varsigma)} = \frac{\varsigma}{kT}NR^2 \tag{2.96}$$

which is a product of the *Kuhn monomer relaxation time*, τ_0, for the motion of each bead:

$$\tau_0 \approx \frac{\varsigma b^2}{kT} \tag{2.97}$$

At times shorter than τ_R, a polymer shows *viscoelastic motion* and at times longer than τ_R, a polymers show diffusive motion.[62] As the radius of gyration, R_g, depends on the length of spring and the number of beads:

$$R_g \approx bN^{\nu} \tag{2.98}$$

where ν is the reciprocal *fractal dimension*, *d*, in *scaling theory* (e.g. *d* for ideal linear chain is 2) and Eqns. 2.96 and 2.97 provide:

$$\tau_R \approx \frac{\varsigma}{kT} NR^2 = \frac{\varsigma b^2}{kT} N^{1+2\nu} \approx \tau_0 N^{1+2\nu} \tag{2.99}$$

with $\nu = 1/2$ for an ideal linear chain. Thus, the Rouse time is proportional to the square of the number of monomers, $N \approx N_{mon} \approx N_{bead}$. Rouse published a full description of his model in 1953:

$$\tau_R = \frac{\varsigma b^2}{6\pi^2 kT} N^2 \tag{2.100}$$

Actually any movement of polymer in solvent is accompanied by a viscous resistance and a polymer will drag solvent molecules as it moves in solution.[71] This behavior is a *hydrodynamic interaction* and Zimm published the model with hydrodynamic interactions in 1956. This model will be discussed in Chapter 3.[72,73]

The discussion thus far focused on the dynamics of an unentangled polymer chain following conventional polymer physics, thereby explaining properties of polymers in unentangled systems. However, polymer chains can be entangled in solutions at finite concentrations (even closer to the polymer melt system) and the classical models do not explain the corresponding solution phenomena of these systems. Edwards made an assumption that individual chains behave as if they are in a tube of diameter, *a*:

$$a \approx bN_e^{1/2} \tag{2.101}$$

where N_e is the number of monomers.[74,75] In a segment of *a*, N_e monomers are observed, which means the total number of segments is N/N_e:

$$R_g \approx a\sqrt{\frac{N}{N_e}} = b\sqrt{N} \tag{2.102}$$

The average contour length, $\langle L_p \rangle$, along the path having the minimum potential among all possible potentials in the tube (primitive path) is surely shorter than a conventional contour length, l_k:

$$\langle L \rangle \approx a\frac{N}{N_e} \approx \frac{b^2 N}{a} \approx \frac{bN}{\sqrt{N_e}} \tag{2.103}$$

Eqn. 2.103 also works for polymer melts. Further discussion about another model can be found elsewhere.[63]

2.2.2.4 Viscosity

We have discussed that an actual particle in solution undergoes viscous dissipation as well as Brownian motion. As seen in the previous Section 2.2.2.3, friction is an important property for understanding the relationship between diffusion and viscosity.[61,62] The friction coefficient, **f**, was defined in Eqn. 2.81 under the assumption that the system was a single hard sphere. This assumption will be kept for the discussion that follows.

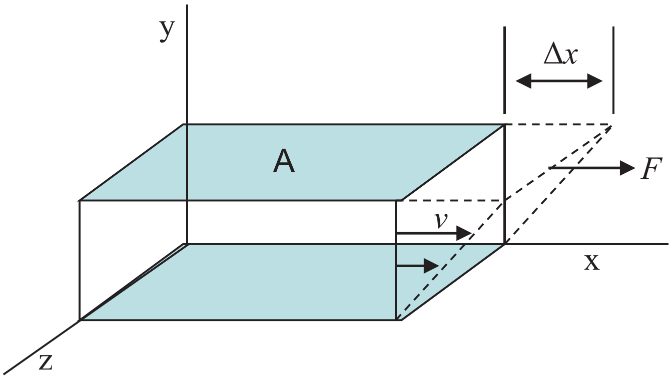

Figure 2.7 Schematic diagram for the relationship between the applied force, *F*, and the velocity, *v*.

Figure 2.7 depicts the change of displacement, Δx, in response to an applied force, *F*. The force per unit area is stress, and shear flow is given by the symbol, *q* (Appendix K). The shear stress, σ, is defined as:[62]

$$\sigma \equiv \frac{F}{A} \tag{2.104}$$

The velocity difference between two layers in Figure 2.7 is:

$$\Delta v = \frac{\Delta x}{\Delta t} \tag{2.105}$$

the velocity gradient is:

$$\frac{\Delta v}{\Delta y} = \frac{(\Delta x / \Delta y)}{\Delta t} \tag{2.106}$$

The *shear strain*, γ, and the *rate of shear*, $\dot{\gamma}$, are defined as:

$$\gamma \equiv \frac{\Delta x}{\Delta y} \quad \text{and} \quad \dot{\gamma} \equiv \frac{\Delta v}{\Delta y} = \frac{\Delta x / \Delta y}{\Delta t} = \frac{\gamma}{\Delta t} \tag{2.107}$$

Hence, the *shear viscosity* is defined as:[76]

$$\sigma \equiv \eta\dot{\gamma} \equiv \eta\frac{\Delta v}{\Delta y} = \frac{F}{A} \tag{2.108}$$

Eqn. 2.108 is Newton’s law of viscosity and a fluid that follows Eqn. 2.108 is called a *Newtonian* fluid. For a perfectly elastic material, the shear stress and the shear strain are proportional to each other and the proportionality constant is the *shear modulus*, *G*:

$$G \equiv \frac{\sigma}{\gamma} \tag{2.109}$$

Also, Eqn. 2.109 is known as Hooke’s law of elasticity. The stress relaxation modulus, *G*(*t*), is defined as:

$$G(t) \equiv \frac{\sigma(t)}{\gamma} \tag{2.110}$$

where $\sigma(t)$ is a *step strain* having a generic time dependence and Eqn. 2.110 is the time-dependent version of Hooke's law. Eqn. 2.109 reflects a linear response and can be satisfied as long as the strain of the material is small. The stress from any combination of small step strains is the linear combination of the stresses from each individual step (*Boltzmann superposition principle*):

$$\sigma(t)=\sum_i G(t-t_i)\,\delta\gamma_i \tag{2.111}$$

Eqn. 2.107 and 2.111 provide:

$$\sigma(t)=\sum_i G(t-t_i)\,\dot{\gamma}_i\delta\, t_i \tag{2.112}$$

A *smooth strain* leads to an integration rather than a summation for the stress:

$$\sigma(t)=\int_{-\infty}^{t} G(t-t')\dot{\gamma}(t')\,\mathrm{d}t' \tag{2.113}$$

In Eqn. 2.113, $-\infty$ is the low limit of the integration because the integration should be performed for all past times, not a starting point, $t=0$, which means the deformation of materials is influenced by past treatments of the system.[69]

In steady shear systems, the velocity of fluid is a constant and the shear rate, $\dot{\gamma}$, is independent of time. Thus, Eqn. 2.113 can be rewritten as:

$$\sigma(t)=\dot{\gamma}\int_{-\infty}^{t} G(t-t')\,\mathrm{d}t' \tag{2.114}$$

Integrating Eqn. 2.114 by the substitution, $s\equiv t-t'$, leads to:

$$\begin{aligned}\sigma(t)&=\dot{\gamma}\int_{-\infty}^{t} G(t-t')\,\mathrm{d}t'\\&=\dot{\gamma}\int_{0}^{\infty} G(s)\,\mathrm{d}s\end{aligned} \tag{2.115}$$

where the integration range is changed from $t' = -\infty, t' = t$ to $s = \infty, s = 0$, respectively. Eqn. 2.108 and 2.115 provide:

$$\eta = \int_0^\infty G(t)\, dt \tag{2.116}$$

At this point, the simple relaxation time, *t*, has been used to define the stress relaxation modulus. In Maxwell's model, the stress relaxation modulus also has an exponential decay and is generalized for longer relaxation times:

$$\begin{aligned} G(t) &\equiv \frac{\sigma(t)}{\gamma} = G_M \exp\left(\frac{-t}{\tau_M}\right), \\ G(t) &\equiv \frac{\sigma(t)}{\gamma} \approx G(\tau)\exp\left(\frac{-t}{\tau}\right) \qquad (t > \tau) \end{aligned} \tag{2.117}$$

where the relaxation time, τ, is a fundamental dynamic property of all viscoelastic fluids. Any polymer solution can have multiple relaxation modes with their relaxation times and relaxation moduli obtained from a combination of Maxwell elements (Appendix L).[77] Also, the Maxwell model can be related to a viscosity:

$$\begin{aligned} \eta &= G_M \int_0^\infty \exp\left(\frac{-t}{\tau_M}\right) \mathrm{d}t \\ &= G_M \tau_M \\ &= \eta_M \end{aligned} \tag{2.118}$$

For solids, the modulus never decays to zero, which means that the viscosity is infinite. The stress in fluids exponentially decays to zero for times that exceed the longest relaxation time ($t \gg \tau$) of the system:

$$\begin{aligned} \eta &\sim G(\tau)\int_0^\infty \exp\left(\frac{-t}{\tau}\right) \mathrm{d}t = G(\tau)\tau \int_0^\infty \exp(-s)\, \mathrm{d}s \\ &= G(\tau)\tau \end{aligned} \tag{2.119}$$

with the integration by substitution, $s \equiv t/\tau$. From the exponential relationship between a time ratio and a viscosity, Eqn. 2.116 can be rewritten as:

$$\eta = \int_{-\infty}^{\infty} tG(t)\,\mathrm{d}\ln t \tag{2.120}$$

where $\mathrm{d}t = t\mathrm{d}\ln t$ and $\ln t = -\infty$ when $t = 0$.

If the applied force is much stronger than the force required to make the system respond linearly (i.e. the shear rate is much larger), the measured apparent viscosity shows deviation from the expected zero shear rate viscosity, η. In most polymers, viscosity decreases or increases as the shear rate increases. The former is called *shear thinning* and the latter is called *shear thickening*. In general, the *viscosity* mentioned in this review is the *zero shear rate viscosity.*

To obtain the viscosity experimentally, the assumption from the first part of this chapter is normally made: we have spherical particles (roughly, polymer coil) and they are dispersed in the solution. Each particle contributes to the *solution viscosity*, η, and the solution viscosity is larger than the *solvent viscosity*, η_s. Einstein's equation of viscosity is:

$$\eta = \eta_s\left(1+\frac{1}{2}\phi\right)(1+\phi+\cdots)^2 = \eta_s\left(1+2.5\phi+4\phi^2+\cdots\right) \tag{2.121}$$

where ϕ is the volume fraction. Eqn. 2.121 provides:

$$\begin{aligned}
\eta_r &\equiv \frac{\eta}{\eta_s} \approx 1+2.5\phi \\
\eta_{sp} &\equiv \eta_r - 1 = \frac{\eta}{\eta_s} - 1 \approx 2.5\phi \\
\eta_{inh} &\equiv \frac{\ln\eta_r}{c} \\
\eta_{red} &\equiv \frac{\eta_{sp}}{c}
\end{aligned} \tag{2.122}$$

where η_r, η_{sp}, η_{inh}, and η_{red} are the relative viscosity, the specific viscosity, the inherent viscosity, and the reduced viscosity, respectively. c is concentration of solute (mass/volume). For an infinitely dilute solution, the intrinsic viscosity is defined as:

$$[\eta] \equiv \lim_{c \to 0} \left(\frac{\eta - \eta_s}{c \eta_s} \right) \tag{2.123}$$

In Eqns. 2.121 ~ 2.123, the polymer volume fraction, ϕ, and the polymer concentration, c, are used at the same time and this parallel can be found in the Flory-Huggins theory in thermodynamics of polymer solutions. Then the viscosity can be expressed as:

$$\eta = \eta_s \left(1 + 2.5 \frac{c}{M} N_{av} V_h + \cdots \right) \tag{2.124}$$

where M is molar mass. See Appendix M for more details. Eqns 2.123 and 2.124 lead to:

$$[\eta] = 2.5 \frac{N_{av} V_h}{M} \tag{2.125}$$

where the hydrodynamic volume, V_h, is the volume of a hard sphere in the solution:

$$V_h = \frac{4}{3} \pi r^3 \tag{2.126}$$

where r is the radius of sphere.

However, a polymer is not a hard sphere and hydrodynamic radii in Eqn. 2.126 do not represent the actual size of the polymer coil. Also, in a real solution, the motion of the polymer coil influences the solvent molecules as they are dragged by the polymer coil, which represents a long range interaction between molecules. This effect is called a *hydrodynamic interaction*. The Rouse model in Section 2.2.2.3 ignores this effect. By invoking the fractal nature of polymers, one obtains Eqn. 2.98.

Stokes law provides:

$$\varsigma_Z \approx \eta_s R \tag{2.127}$$

where ς_Z is the total friction coefficient of the whole Zimm chain. Eqn. 2.87 has the proportionality constant, 6π, based upon the assumption that the polymer chain is a hard sphere. However, the assumption cannot be applied to a real polymer system.[77] Then, the Einstein relation provides:

$$D_Z = \frac{kT}{\varsigma_Z} \approx \frac{kT}{\eta_s R} \approx \frac{kT}{\eta_s b N^{\nu}} \tag{2.128}$$

Eqn. 2.128 is the Stokes-Einstein relationship for a polymer in a dilute solution. Zimm published:[72]

$$D_Z = \frac{8}{3\sqrt{6\pi^3}} \frac{kT}{\eta_s R} \cong 0.196 \frac{kT}{\eta_s R} \tag{2.129}$$

With a similar approach, the Zimm time, τ_Z, is defined as:

$$\tau_Z \approx \frac{R^2}{D_Z} \approx \frac{\eta_s}{kT} R^3 \approx \frac{\eta_s \cdot b^3}{kT} N^{3\nu} \approx \tau_0 N^{3\nu} \tag{2.130}$$

where τ_0 is the monomer relaxation time. A full description of Eqn. 2.130 is:[72]

$$\tau_Z = \frac{1}{2\sqrt{3\pi}} \frac{\eta_s}{kT} R^3 \cong 0.163 \frac{\eta_s}{kT} R^3 \tag{2.131}$$

The Zimm time has a weaker dependence on chain length than the Rouse time in Eqn. 2.99 and the Zimm time is shorter than the Rouse time in a dilute solution. The relaxation modulus can be related to these two relaxation times:

$$G(\tau) \approx kT \frac{\phi}{Nb^3} \tag{2.132}$$

and

$$G(\tau)\tau \approx kT \frac{\phi}{Nb^3} \tau \approx \eta - \eta_s . \tag{2.133}$$

The intrinsic viscosity can be rewritten as:

$$[\eta] \approx \frac{kT\,N_{av}}{\eta_s M_0 N}\tau \tag{2.134}$$

as shown in Appendix M. The Rouse time and the Zimm time predict two different intrinsic viscosities:

$$\begin{aligned} [\eta] &\approx \frac{b^3 \cdot N_{av}}{M_0} N && \text{Rouse model} \\ [\eta] &\approx \frac{b^3 \cdot N_{av}}{M_0} N^{3\nu-1} && \text{Zimm model} \end{aligned} \tag{2.135}$$

Both models depend on the concentration of sample. In dilute solutions, the Rouse model poorly describes the dynamics, but does well for polymer solutions with little or no hydrodynamic interaction (melt-like) with short, unentangled chains.[61] In constrast, the Zimm model describes dilute solutions well, but fails for solutions at higher concentration.[61] In semidilute solution, the length scale (ξ_h) is called the hydrodynamic screening length and is different for the two models. When the end-to-end distance, h, of the polymer chain is smaller than the length scale ξ_h ($h < \xi_h$), the hydrodynamic interaction dominates and the Zimm model describes the dynamics of a solution well. When the end-to-end distance is lager than the length scale ξ_h ($h > \xi_h$), the hydrodynamic interactions are effectively screened by adjacent chains and the dynamics are well explained by the Rouse model.[78-80]

Also, Eqn. 2.135 implies that the intrinsic viscosity is proportional to the molar mass (M). Thus, the intrinsic viscosity can be rewritten as:

$$[\eta] = \Phi \frac{R^3}{M} \tag{2.136}$$

where Φ is $0.425N_{av}$ and is a universal constant for all polymer solutions. Also,

$$[\eta] \sim \frac{R^3}{M} \sim \frac{M^{3\nu}}{M} \sim M^{3\nu-1} \tag{2.137}$$

ν is 0.5 and 0.6 in theta and good solvents, respectively. A general expression of Eqns. 2.136 and 2.137 is called the Mark-Houwink equation:

$$[\eta] = kM^a \tag{2.138}$$

The constants k and a depend on the nature of polymer and solvent molecules as well as the temperature. In Eqn. 2.137, a is related to the fractal dimension, d:

$$a = 3\nu - 1 \tag{2.139}$$

and

$$a = \frac{3}{d} - 1. \tag{2.140}$$

Eqns. 2.124 and 2.125 provide:

$$\eta = \eta_s \left(1 + [\eta]c + k_H [\eta]c^2 + \cdots\right) \tag{2.141}$$

where k_H is the *Huggins coefficient* and the second virial coefficient of viscosity. Eqn. 2.141 can be expressed in two forms:

$$\frac{\eta - \eta_s}{\eta_s c} = [\eta] + k_H [\eta]c^2 + \cdots \tag{2.142}$$

and

$$\frac{\ln(\eta/\eta_s)}{c} = [\eta] + \left(k_H - \frac{1}{2}\right)[\eta]c^2 + \cdots \tag{2.143}$$

Eqns. 2.142 and 2.143 are called the *Huggins* and *Kraemer equation*, respectively. The two equations have the same intercept for the same solution and are satisfied in a dilute solution.

From Eqn. 2.141, the viscosity of a dilute solution can be expressed as:

$$\eta = \eta_s\left(1 + \sum_i c_i[\eta]_i + \cdots\right) \tag{2.144}$$

Subscript *i* means the polymer chains have different molar masses. Thus, Eqns. 2.123 and 2.140 provide:

$$\begin{aligned}[\eta] = \lim_{c\to 0}\left(\frac{\eta - \eta_s}{c\eta_s}\right) &\approx \lim_{c\to 0}\left(\frac{\sum c_i[\eta]_i}{\sum c_i}\right) \\ &= \frac{\sum (n_i M_i / V) k M_i^a}{\sum n_i M_i / V} \\ &= k\frac{\sum n_i M_i^{a+1}}{\sum n_i M_i}\end{aligned} \tag{2.145}$$

Experimentally, the intrinsic viscosity can be related to the molar mass and Eqn. 2.138 can be rewritten as:

$$[\eta] = kM_v^a \tag{2.146}$$

where M_v is the viscosity average molar mass. Eqn. 2.145 and 2.146 provide:

$$[\eta] \equiv \left(\frac{\sum_i n_i M_i^{a+1}}{\sum_i n_i M_i}\right)^{1/a} \tag{2.147}$$

Similar logic can be applied to the weight average molar mass obtained from light scattering and will be discussed in Chapter 3.

2.2.3 Studies of Polymer Physical Chemistry of Polysaccharides

For the past decade, several noteworthy reviews of physical chemistry in polysaccharides have been published with comprehensive knowledge of both the organic and the physical chemistry of polysaccharides.[81-84] However, questions about how morphological differences affect material properties and whether the morphology can be changed by physcochemical modification are left open for discussion.

With the development of theoretical physical chemistry of polymers and experimental methods of scattering, size exclusion chromatography, and viscometry, new parameters like root-mean-square end-to-end distance, molar mass distribution, fractal dimension, chain stiffness, and polymer-solvent interactions have been defined. The parameters have been successfully explained and applied to the properties of polysaccharides, however, most studies are still based on the rigorous molecular theory with assumptions of dilute solution or solid state. The theories provided information about local structure or local dynamics but could make few reliable predictions about the properties of macromolecules like polysaccharides.[85-89]

The primary objectives of polymer physical chemistry of polysaccharides are a reasonable description and prediction of properties of polysaccharides quantitatively as well as qualitatively. We can still start from the theories mentioned above and expand to studies of complex polysaccharide systems in semi-dilute solutions. Some representative parameters used to explain the properties are tabulated in Table 2.1.

Table 2.1 Representative solution parameters of physical chemistry in polysaccharides

Parameters	Experimental Method
Radius of gyration, R_g	Static light scattering (SLS)
Hydrodynamic radius, R_h	Dynamic light scattering (DLS)
The second virial coefficient, A_2	Static light scattering
Diffusion coefficient, D	Dynamic light scattering
Intrinsic viscosity, $[\eta]$	Viscometry

Characterization of polysaccharides in solution depends upon whether they are soluble. The preparation of polysaccharide solutions is still challenging because the macromolecular structure of polysaccharides provides complex interactions that affect their phase stability and solubility. Kishikawa *et al*. discussed thermodynamic translational movement of pullulan in water and DMSO determined by the Ludwig-Soret effect, mass transport induced by a temperature gradient.[90-92] Results imply that the thermal diffusion of polysaccharides depends upon the strength of hydrogen bonding and the capability of the solution to participate in hydrogen bonding. A more detailed review about the thermodynamics of polysaccharide solutions was published by Schmidt and Burchard.[93,94] The configurational entropy in Flory-Huggins theory was invoked to discuss the dissolution of biopolymers. The configurational entropy decreased as stiffness, concentration, and crosslinking increased, which meant entropy dominated dissolution at low concentrations of flexible biopolymers and consequently their dissolution is endothermic. For example, as the length of semi-flexible polysaccharides decreases closer to the Kuhn segment length, stiffness increased and the configurational entropy decreased, which meant the short semi-flexible polysaccharides were fairly insoluble in aqueous systems.[95] This effect could be explained by Flory-Huggins theory which was consistent with phase separation at low temperatures. However, if hydrophobic interactions between solvent molecules and polysaccharide chains are dominant in the system, ordering solvent molecules decreases their configurational entropy and the overall lower entropy leads to an exothermic process. Thus, polysaccharides with strong hydrophobic interactions phase separate upon heating.

Recently, various solvents for polysaccharides, especially cellulose and their derivatives, were experimentally probed by Saalwächter *et al*.[96,97] Cellulose has extensive hydrogen bonding capability, but does not readily dissolve in organic or aqueous solvents. This effect is normally attributed in intermolecular hydrogen bonding between cellulose chains. More recently, metal complexes from ionic liquids have been shown to coordinate with most anhydroglucose units (AGUs) in the chain and disrupt hydrogen bonding. Finally, cellulose can be dissolved in organometallic solvents. Without organometallic solvents, aggregation is inevitable. Schulz *et al.*[98] probed aggregation behavior of cellulose in aqueous solution with light scattering and small angle neutron scattering. The angular dependence of the scattered light and model studies by small angle neutron scattering experiments led to the fringed micelle model on the basis of two different structures present: a lager structure comparised of star-shaped macromolecules and the smaller structure consisting of worm-like chains. However, the fringed micelle model can explain association between polysaccharides in dilute solution.

In 1982, Silver *et al.* and Shogren *et al.* published the molar mass dependence of radii of gyration, hydrodynamic radii, and translational diffusion coefficients of hyaluronic acid and chick limb bud proteoglycan.[99,100] They also showed the ratio between the radius of gyration and hydrodynamic radius ($\rho \equiv R_g / R_h$) increased as the molar mass of the polysaccharide decreased, which was expected for branched polymers.[101] The molar mass dependence of R_g, R_h, and D_t can be explained with scaling concepts.[102] Geissler *et al*. and Förster *et al*. published reviews on the scaling theory of semi-dilute solution of hyaluronan as well as other polyelectrolyte systems and observed the diffusion coefficient was dominated by electrostatic screening.[103,104]

Coviello *et al.*[105] probed native and modified xantan and obtained the Kuhn length as well as chain stiffness. A dynamic structure factor was obtained and the results showed the xantan chain had a wormlike chain conformation. Esquenet *et al.*[106] also used xantan and hyaluronan and obtained the persistence length of 100 Å for hyaluronan and 1000 Å for xantan, which agreed well with the known results that hyaluronan is a semi-rigid polysaccharide and xantan is a rigid polysaccharide.[105,106] In dilute solutions with a good solvent both polysaccharides showed wormlike chain configurations with a single scattering mode. In semi-dilute solutions, bimodal scattering distributions were obtained. The short time relaxation (fast mode) showed a typical q^{-2} dependence, which meant the relaxation of concentration fluctuations was from cooperative diffusion. The long time relaxation (slow mode) was attributed to intraparticle relaxation (aggregation). Buhler *et al.*[107] studied the ionic strength dependence of a persistence length of semi-rigid polysaccharide, hyaluronan. In low ionic strength solution, SLS and DLS studies showed that scattering intensity crossed over from q^{-1} to q^{-4}, which meant that self-association increased. Otherwise, in high ionic strength solution, the intensity crossed over from q^{-1} to q^{-2}, which was in good agreement with results for conventional wormlike chains.

In 1988 Kojima *et al.*[108] probed the concentration effect on properties of polysaccharide solutions. Xantan in solutions with various concentrations was used as a model system and results from light scattering and rheological studies showed that the association started at low concentration with gelation occuring at higher concentration.[108] The ratio between the actual concentration (c) and the overlap concentration (c^*) was used to obtain a universal description of flexible polysaccharides in a good solvent by Burchard *et al.*:[109,110]

$$c^* = 1/\left(A_2 M_w\right) \tag{2.148}$$

$$X \equiv c/c^* = A_2 M_w c \tag{2.149}$$

where A_2 is the second virial coefficient that will be defined in Section 3.1.1. This reduced concentration (X) is the universal parameter that can be obtained from material quantities like M_w, R_g, and A_2. A modeling with other parameters like a reduced osmotic modulus and a reduced radius of gyration provides descriptions for polysaccharides at various concentrations.[111,112] Experiments based on the Benoit-Benmouma single contact approximation provided reliable results up to 8 times the overlap concentration.[113] Results showed good agreement with a model of weakly interpenetrating (high branching density) particles. Otherwise, a model of the deep interpenetration (low branching density) was better for explaining the low concentration data.

There are other ratios of other parameters that also provide information about the static and dynamic properties of polysaccharides as well as other macromolecules. In 1980, Burchard published the framework that provided answers about how to probe polysaccharides in solution with light scattering.[114] A ratio between the hydrodynamic radius and the radius of gyration was invoked and this ratio depended upon the architecture of the macromolecules. Some examples values relevant for polysaccharides can be found in Table 2.2.[114,115] As seen in Table 2.2, ρ values of the polysaccharides that have high segment density have ρ smaller than unity. In most configurations, polysaccharides have radii of gyration that are similar because they are only weakly affected by swelling from solvent penetration. In constrast, hydrodynamic radii of synthetic polymers are almost always affected by solvent penetration. Thus, R_h is larger than R_g and ρ is smaller than the unity for macromolecules having high segment density. Also, the higher the segment density a polysaccharide has, the smaller its hydrodynamic radius.

Table 2.2 Theoretical ρ values of different configurations of polysaccharides

Architecture of Macromolecules	ρ
Hard spheres	0.775
Hollow spheres	0.100
Linear chains	1.500
Microgels	0.600

Other parameter ratios from light scattering and viscometry data can also be derived, however, their validity is strongly affected by the fundamental difficulty of experiments. For most macromolecules in solution, aggregation is induced to reduce the surface energy of macromolecules, which leads to the need for a technique that breaks up aggregates so that intrinsic size differences can be probed. Thus, size exclusion chromatography (SEC) has been used with light scattering. Ioan *et al.*[116,117] published studies on glycogen from shellfish and dextran that combined light scattering with SEC. Experimental properties of glycogen in dilute solution such as M_n, M_w, and $[\eta]$ were in good agreement with predictions of the theories for hyperbranched macromolecules, but properties such as R_g, R_h, and X (Eqn. 149) of glycogen in semi-dilute solution were consistent with theories for large particles like latex particles and the scattered light intensity strongly depend upon angle. However, structure determination of polysaccharides in semi-dilute solution is generally regarded as impossible. Ioan *et al.*[118] published a genuine approach to determine the architecture of polysaccharides in semi-dilute solution. Parameters like molar mass and the diffusion coefficient at finite concentration were normalized by their values at zero concentration. The normalized parameters were used to prepare a master curve with respect to the ratio between the concentration at finite concentration, c, and overlap concentration, $c*$, from static light scattering and viscometry:

$$\frac{c}{c^*_{A_2}} \text{ and } \frac{c}{c^*_{[\eta]}} \tag{2.150}$$

where

$$c^*_{A_2} = \frac{1}{A_2 M_w} \sim \frac{M_w}{V_m} \tag{2.151}$$

$$c^*_{[\eta]} = \frac{1}{[\eta]} \sim \frac{M_w}{V_m} \tag{2.152}$$

Universal behavior was observed up to a specific concentration, $c / c^*_{A_2 \text{ or } [\eta]} < 4$, with deviation from the expected behavior at higher concentrations. Also, the concentration window of the universal behavior decreased as the molar mass of the polysaccharide increased. Self-association and branching between polysaccharide chains as well as solvent-polymer interactions (non-ideal solution behavior) complicated attempts to find universal behavior. Several normalized properties (V_r, g, and g') were examined:[119,120]

$$V_r \equiv \frac{A_2 M_w}{[\eta]} = \frac{4\pi^3 / 2N_A (R_g^3 / M)\Psi}{\Phi(R_g^3 / M)} = 4\pi^3 / 2N_A \frac{\Psi}{\Phi} \tag{2.153}$$

$$g = \frac{R_g,_{\ branch}}{R_g,_{\ linear}} \tag{2.154}$$

$$g' = \frac{[\eta],_{\ branch}}{[\eta],_{\ linear}} \tag{2.155}$$

where Ψ is the coil-coil interpenetration function and Φ is the solvent-coil penetration function or the draining factor. Eqn. 2.153 is fairly intuitive but acceptable because the ratio of Ψ / Φ depends upon the ratio between proportionality constants in Eqns. 2.151 and 2.152.

Experimental results were compared to previous studies but universal behavior was not observed.[116-122] While the combination of SEC, light scattering, and viscosity detectors have been applied for the determination of polysaccharide properties in solution, inherent limitations in the resolution obtained by gel columns, especially for water soluble polysaccharides, led to the more recent introduction of field flow fractionation with light scattering and viscosity detectors for more reliable results.[123-127]

CHAPTER 3

Light Scattering

3.1 Introduction to Light Scattering

If a small particle or molecule is placed in the path of a beam of light, the oscillating electric field makes the electrons of the obstacle oscillate with the same frequency as that of the incident light (i.e. oscillation of dipoles). Then, like any periodically moving charge, the oscillating electrons become a source of new electromagnetic radiation called scattered light and this phenomenon is designated as light scattering (LS). LS is the basic process that makes light deviate from a straight trajectory. All processes mentioned above can be observed when light travel through sparse medium like air. Otherwise, when light impinges onto an interface between the original medium and the second dense medium, scattered light travel back to the original medium or trespasses through the dense medium. The former is defined as reflection and the latter is defined as refraction.

Maxwell, Lord Rayleigh, and Mie provided fundamental theories for the characterization of matter with scattered light which have been utilized in many areas of science to determine particle size, molecular weight, shape, diffusion coefficients, and thermodynamic properties.[128] Light scattering, experimentally, can be classified into two principle techniques: static light scattering (SLS), which is sometimes called total intensity light scattering, that measures the average scattering intensity and contains information about the molecular weight and size of the scatterers; and dynamic light scattering (DLS) which measures the fluctuations in scattered intensity arising from particle diffusion.[129–131] Figure 3.1 shows the electric fields scattered from different particles, depending on the location of the scattering particle in space. Assuming that the dots in Figure 3.1 are elastic dipole scatterers, they will emit secondary electric fields with the same frequency, i.e. without any phase delay, when excited by an incident electric field with frequency ω. The observation angle, θ, and the scattered waves can be characterized by single wave vectors for the scattered wave, $\mathbf{k}_s$, of the incident wave, $\mathbf{k}_I$. As shown in Figure 3.1, the fields scattered from the particles (e.g. i and j) have traveled different distances, which results in a phase difference at the position of the observer. On the basis of Figure 3.1, the phase difference is given by:

$$\Delta\phi = \frac{2\pi}{\lambda}\left(\overline{AB} - \overline{CD}\right) \tag{3.1}$$

where λ is the wavelength of the incident light. These differences are related to the wave vectors of the incident and scattered fields by

$$\overline{AB} = (\mathbf{k}_s / k)\cdot \mathbf{P}_{ij} = \hat{\mathbf{k}}_s \cdot \mathbf{p}_{ij} \tag{3.2}$$

$$\overline{CD} = (\mathbf{k}_I / k)\cdot \mathbf{P}_{ij} = \hat{\mathbf{k}}_I \cdot \mathbf{p}_{ij} \tag{3.3}$$

where $\mathbf{p}_{ij}$ is the separation vector between the positions of two points, i and j, $\mathbf{p}_{ij} = \mathbf{r}_i - \mathbf{r}_j$, and $k = 2\pi/\lambda$. Then, the phase difference is defined as:

$$\Delta\phi \equiv \mathbf{r}_i(\mathbf{k}_S - \mathbf{k}_I)k - \mathbf{r}_j(\mathbf{k}_S - \mathbf{k}_I)k \tag{3.4}$$

Eqn. 3.3 allows one to assign a phase to any of the points considered

$$\phi_i = \mathbf{r}_i(\mathbf{k}_S - \mathbf{k}_I)k \tag{3.5}$$

$$\phi_j = \mathbf{r}_j(\mathbf{k}_S - \mathbf{k}_I)k \tag{3.6}$$

Generally speaking, a phase can be expressed with the position vector, $\mathbf{r}$, and the scattering vector, $\mathbf{q}$, ($\mathbf{q} \equiv (\hat{\mathbf{k}}_S - \hat{\mathbf{k}}_I)k = \mathbf{k}_S - \mathbf{k}_I$):[132]

$$\phi(\mathbf{r}) = \mathbf{r}\mathbf{q} \tag{3.7}$$

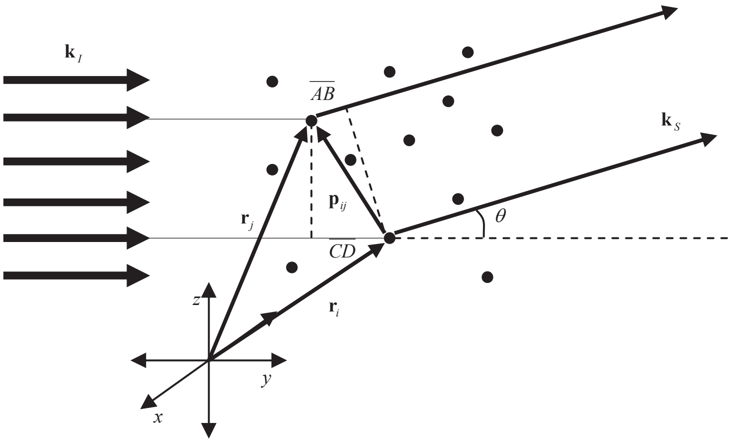

Figure 3.1 Schematic depiction of light scattering.

As the scattered field strength is proportional to the strength of the incident field, the scattered electric field from one volume element is given as:

$$\mathbf{E}_V(\mathbf{r},t) = f(\mathbf{r})\mathbf{E}_I \exp[i(\mathbf{qr} - rt)] \tag{3.8}$$

where $f(\mathbf{r})$ is the scattering strength per unit volume, which is proportional to the fraction of the incident field strength that is actually scattered and $\mathbf{E}_I$ is the strength of the incident field. The total electric field scattered from the entire scattering volume, $\mathbf{E}_S$, can be obtained by the sum of integrals over the volume of all individual particles in the scattering volume with the assumption that the scattered field of the volume elements outside particles is set to zero:

$$\mathbf{E}_S \propto \sum_{j=1}^{N} \mathbf{E}_I \int_{V_j} f(\mathbf{r}) \exp\{i\mathbf{qr}\} d\mathbf{r} \tag{3.9}$$

In Eqn. 3.9, V_j represents the volume of j th particle. Solvent effects can be excluded experimentally by subtracting the scattering intensity of the solvent from the scattering intensity of the solution.

In Eqn. 3.9, one has to integrate with respect to $\mathbf{r}$ for each particle whose limits of integration depend on their position. For convenience, $\mathbf{r}$ is replaced by two new position vectors ($\mathbf{r} = \mathbf{r}_j + \mathbf{r}'$) where $\mathbf{r}_j$ points to the center of the position of the j th particle and $\mathbf{r}'$ points from the center position to any arbitrary point within the particle (see Eqn. 3.9) to facilitate evaluation:

$$\mathbf{E}_S = \mathbf{E}_I \sum_{j=1}^{N} \exp\{i\mathbf{q}\mathbf{r}_j\} \cdot \int_{V_j^0} g(\mathbf{r}') \exp\{i\mathbf{q}\mathbf{r}'\} d\mathbf{r}' \tag{3.10}$$

where $g(\mathbf{r}') = f(\mathbf{r})$ with two simplifications: (1) the scattering power depends only on $\mathbf{r}'$ because the scattering strength outside the particles is zero, and (2) $d\mathbf{r}_j = 0$ because $\mathbf{r}_j$ was directed to a fixed point in space (the center of particle j). Therefore, the scattered intensity from a solution of identical particles can be written as

$$I(q) = \mathbf{E}_S{}^2 = \left| \int_{V_j^0} g(\mathbf{r}') \exp\{i\mathbf{q}\mathbf{r}'\} d\mathbf{r}' \right|^2 \cdot \left| \sum_{j=1}^{N} \exp\{i\mathbf{q}\mathbf{r}_j\} \right|^2 \tag{3.11}$$

In Eqn. 3.11, the second term only depends on the particle position, whereas the first term depends on the scattering power and positions within a particle. The former is called the structure factor of the solution:

$$S(q) \equiv \left\langle \left| \sum_{j=1}^{N} \exp\{i\mathbf{q}\mathbf{r}\mathbf{j}\} \right|^2 \right\rangle \tag{3.12}$$

while the latter is called the particle scattering factor or form factor:

$$P(q) \equiv \left\langle \left| \frac{\int_{V_j^0} g(\mathbf{r}') \exp\{i\mathbf{q}\mathbf{r}'\} d\mathbf{r}'}{\int_{V_j^0} g(\mathbf{r}') d\mathbf{r}'} \right|^2 \right\rangle \tag{3.13}$$

Hence,

$$I(q,N) \propto P(q)S(q) \tag{3.14}$$

where q is the magnitude of scattering vector which is defined as

$$|\mathbf{q}|^2 \equiv q = \frac{4\pi n_0}{\lambda_0}\sin\frac{\theta}{2} \tag{3.15}$$

where n_0 is refractive index of solvent, θ is the scattering angle defined in Figure 3.1, and λ_0 is the laser wavelength in a vacuum. Eqn. 3.14 leads to two major limiting cases:

$$\lim_{N\to 0} I(q,N) \propto P(q) \tag{3.16}$$

$$\lim_{q\to 0} I(q,N) \propto S(q=0) \tag{3.17}$$

3.1.1 Static Light Scattering (SLS)

3.1.1.1 Theoretical Background

Static light scatting represents the time averaged value of the scattering intensity measured as a function of the scattering angle. The data yields the weight average molecular weight (M_w), the z-average of the squared radius of gyration, $\langle R_g^2 \rangle_z$, and the second virial coefficient of the osmotic pressure of isotropic scatterers without reference to standards, A_2, along with other information about configurations of macromolecules.

Rayleigh found the relationship between the intensity of scattered light and the scattering angle under the assumption of randomly distributed molecules in space by applying Maxwell's theory of electrodynamics.[133] The relationship is called the Rayleigh ratio of scattered light, $R(\theta)$, and is given by

$$R(\theta) = \frac{Ir^2}{I_0} = \frac{8\pi^2}{\lambda_0^{\ 4}}\sum_{k=1}^{\infty} N_k \alpha_k^{\ 2}(1+\cos^2\theta) \tag{3.18}$$

where θ is the scattering angle, I is the scattered light intensity, I_0 is the primary beam intensity, r is the distance between the detector and the scattering volume, λ_0 is the wavelength of the laser, α_k is the polarizability of the scattering center k, and N_k is the number of scattering centers.

The measured scattering intensity has relative units; thus, the absolute scattering intensities of several pure liquids have been measured. These painstaking studies were carried out by early physicists for toluene and benzene, and now serve as calibration standards. The Rayleigh ratios for any other solutions, can be obtained from the relationship

$$R(\theta) = \left(\frac{I_{\text{solution}} - I_{\text{solvent}}}{I_{\text{standard}}} \right) R_{\text{standard}} \tag{3.19}$$

where R_{standard} is the absolute scattering intensity of the standard.

Subsequent to Rayleigh's work, Einstein and Smoluchowski developed a theory accounting for fluctuations of the polarizability, $\boldsymbol{\alpha}$, in a liquid, which arises from density and concentration fluctuations because of thermal motion.[134,135] In this sense, scattering occurs if there are refractive index differences within the scattering volume. Under these conditions, $R(\theta)$ is defined as:

$$R(\theta) \equiv \frac{4\pi^2}{\lambda_0{}^4 N_A} \left\{ \rho \cdot n_0{}^2 \left(\frac{dn}{d\rho} \right)^2 RT\beta + \left(n_0 \frac{dn}{dc} \right)^2 RT \frac{M_0}{\rho_0} \frac{c}{\left(\frac{-d\Delta\mu}{dc} \right)} \right\} \tag{3.20}$$

where N_A is Avogadro's number, ρ and ρ_0 are the density of the solution and solvent, respectively, n and n_0 are the refractive index of the solution and solvent, respectively, R is the gas constant, T is the absolute temperature, β is the isothermal compressibility, M_0 is the molar mass of the solvent, c is the solute concentration (mass/volume), $\Delta\mu$ is the chemical potential between solution and solvent, (dn/dc) is the refractive index increment due to concentration changes, and $(dn/d\rho)$ is the refractive index increment due to density changes.

In Eqn. 3.20, the first term describes the contribution of density fluctuations and the second term is the contribution of concentration fluctuations in the solution. For the case of dilute solutions, we can assume that the contribution of the density fluctuations for the solution and the pure solvent are the same. Therefore,

$$R(\theta) = R(\theta)_{solution} - R(\theta)_{solvent} = \frac{4\pi^2 n_0{}^2}{\lambda_0{}^4 N_A}\left(\frac{dn}{dc}\right)^2 \frac{RTM_0 c}{\rho_0\left(\frac{-d\Delta\mu}{dc}\right)} \tag{3.21}$$

The change of the chemical potential with the concentration is directly related to the change of the osmotic pressure with concentration:

$$-\left(\frac{d\Delta\mu}{dc}\right) = \frac{M_0}{\rho_0}\left(\frac{d\Pi}{dc}\right) \tag{3.22}$$

where Π is osmotic pressure which can be expressed in terms of a virial expansion in terms of concentration:

$$\left(\frac{d\Pi}{dc}\right) = RT\left(\frac{1}{M} + 2A_2 c + 3A_3 c^2 + \cdots\right) \tag{3.23}$$

where M is the number average molar mass of the solute and the A_i are virial coefficents.

With Eqns. 3.21, 3.22, and 3.23:

$$\frac{Kc}{R(\theta)} = \left(\frac{1}{M} + 2A_2 c + 3A_3 c^2 + \cdots\right) \tag{3.24}$$

where K is an optical constant:

$$K = \frac{4\pi^2 n_0{}^2}{\lambda_0{}^4 N_A}\left(\frac{dn}{dc}\right)^2 \tag{3.25}$$

In the limit of small angles and concentrations (truncation of c^2 and higher order terms), Eqn. 3.24 yields

$$\frac{Kc}{R(\theta)} = \frac{1}{M} + 2A_2 c \tag{3.26}$$

Thus far Eqn. 3.26 which is based on the zero angle approximation ($q \to 0$) from Eqn. 3.17 and only considers the interparticle interference; however, the intraparticle interference from Eqn. 3.26 can also affect the scattering intensity. Hence, Zimm suggested a correction to Eqn. 3.16 of:[136]

$$\frac{Kc}{R(\theta)} = \frac{1}{P(\theta)M} + 2A_2c \tag{3.27}$$

where $P(\theta)$ is the particle scattering factor defined by Debye and shows an angular dependence of scattered light.[137] $P(\theta)$ is given by

$$P(\theta) \equiv \frac{1}{N^2}\sum_i^N\sum_j^N \frac{\sin qr_{ij}}{qr_{ij}} \tag{3.28}$$

where N is the number of scattering centers within a particle. Eqn. 3.28 can be expanded as a Taylor series and terms of order greater than or equal to r_{ij}^3 can be truncated to yield:

$$P(\theta) = 1 - \frac{q^2}{3!N^2}\sum_i^N\sum_j^N \left\langle r_{ij}^2 \right\rangle \tag{3.29}$$

Here, the mean squared radius of gyration is defined as

$$\left\langle R_g^2 \right\rangle \equiv \frac{1}{2N^2}\sum_i^N\sum_j^N \left\langle r_{ij}^2 \right\rangle \tag{3.30}$$

Since the polydispersity influences both the form factor and the mean squared radius of gyration, a mean squared average radius of gyration is the z-average mean squared average radius of gyration ($\left\langle R_g^2 \right\rangle_z$) and the molar mass is the weight average molar mass (M_w). With Eqn. 3.27, 3.29, and 3.30, the most widely used formalism to evaluate static light scattering data, the Zimm equation is given and simplified:

$$\frac{Kc}{R(\theta)} = \frac{1}{M_w}\left(1 + \frac{q^2\left\langle R_g^2 \right\rangle_z}{3}\right) + 2A_2c \tag{3.31}$$

Eqn. 3.31 includes the Rayleigh-Gans-Debye (RGD) assumption: (1) a particle is not too large, $qR_g < 1$, (2) the refractive index of solution is not very different from the solvent, and (3) there is no multiple scattering.[138-141] Experimentally, different data analysis methods have been developed by Zimm and Berry, etc. and will be discussed in Section 3.1.1.2.[142-146]

3.1.1.2 Measurement and Analysis

In static light scattering experiments, time averaged scattering intensity containing information about the size and configuration of the scatterers is directly analyzed with various models. The only standard materials used are toluene or benzene to obtain $R_{standard}$. Also, samples are analyzed at the molecular level in dilute solution light scattering experiments. Thus, the critical issue in light scattering is preparing samples without scattering from impurities in a solution of refractive index matched solvent. There is no regularized guidance to prepare solutions and one needs to develop their own strategy.

All sample preparation processes should be done in an extremely clean environment like a cleanroom. Impurities in air can dissolve in the solution even when all impurities originally in the sample and solvent are removed. Then, everything including chemicals, instruments, and sample cells need to be purified and cleaned. Recrystallization is the most frequently adapted method to refine macromolecules. However, it can cause aggregation which provides deviation from theoretical models. Ultrasonication is well known technique but it can degrade macromolecules. Adding salts requires more studies of ionic strength and viscosity changes. Numerous studies related to aggregation, degradation, and stabilization of macromolecules have been performed.[147-152]

Filtration and centrifugation are relatively convenient and nondestructive methods to remove dust in solution as well as solvent. Most macromolecules do not precipitate during centrifugation and 0.02 ~ 0.1 μm membrane filters are widely selected. However, macromolecules and aggregates are small enough not to be filtered. Membranes in most commercial filters are made of hydrophilic or hydrophobic chemicals like cellulose acetate, PTFE, or nylon. Solvent properties should be checked before a solution is filtered. Otherwise, macromolecules are filtered with impurities and the final concentration of the sample will be different. Also, mechanical force is applied during filtration and macromolecules can be degraded, which reduces the molar mass.

Sample cells can have various shapes and be made of various materials. Generally tube-shaped glass or quartz cells have been adapted. Alcoholic KOH baths or acetone percolators are appropriate tools for cleaning sample cells. All cleaned cells are capped tightly and can be stored for several weeks but should be examined again before sampling. The cell surface is handled with optical lens cleaning paper to prevent any scratches. The position of the sample cell is fixed for measurements and scratches in a specific position provide unexpected damping in time averaged scattering intensity, especially for static light acattering.

In static light scattering experiments, several samples are prepared with different concentrations and are measured at several scattering angles. Then, the collected data is plotted according to the Zimm, Debye, or Berry methods mentioned in Section 3.1.1.1:

$$\frac{Kc}{R(\theta)} = \frac{1}{M_w}\left(1 + \frac{q^2\left\langle R_g^2 \right\rangle_z}{3}\right) + 2A_2c \qquad \text{(Zimm method)} \qquad (3.31)$$

$$\sqrt{\frac{Kc}{R(\theta)}} = \sqrt{\frac{1}{M_w}}\left(1 + \frac{q^2\left\langle R_g^2 \right\rangle_z}{6}\right) + A_2c\sqrt{\frac{1}{M_w}} \qquad \text{(Berry method)} \qquad (3.32)$$

$$\frac{R(\theta)}{Kc} = M_w\left(1 - \frac{q^2\left\langle R_g^2 \right\rangle_z}{3}\right) \qquad \text{(Debye method)} \qquad (3.33)$$

The Debye method is relatively straightforward and adapted to easily obtain molar mass. The Zimm method is frequently selected to analyze static light scattering data. Two extrapolations are performed with respect to concentration and scattering angle:

$$\lim_{c\to 0}\frac{Kc}{R(\theta)}=\frac{1}{M_w}+\frac{\left\langle R_g^2\right\rangle_z q^2}{3} \tag{3.34}$$

$$\lim_{\theta\to 0}\frac{Kc}{R(\theta)}=\frac{1}{M_w}+2A_2c \tag{3.35}$$

and each slope and intercept provide weight average molar mass, radius of gyration, and the second virial coefficient. Here, the second virial coefficient is defined as:[65,153]

$$A_2\equiv\frac{1}{\rho_p^2\overline{V}_1}\left(\frac{1}{2}-\chi_{12}\right)=\frac{\psi}{\rho_p^2\overline{V}_1}\left(1-\frac{\theta}{T}\right) \tag{3.36}$$

where ρ_p, χ_{12}, ψ, and $\overline{V}_1$ are the density of the polymer, interaction parameter between the solvent and polymer, entropy parameter, and molar volume of the solvent, respectively. Solvent quality, temperature, and molar mass can affect the second virial coefficient. Experimentally, A_2 is larger than zero for a good solvent and smaller than zero for a poor solvent.

Radius of gyration and weight-average molar mass are also obtained from the analysis methods in Eqns. 3.31, 3.32, and 3.33, however, they exhibit some differences. Anderson *et al.* rigorously examined applicability of each method.[145,154] Standard materials were probed with percentage errors of radius of gyration and weight-average molar mass. For examples, percentage errors of molar masses and radii of gyration from the Zimm and Berry methods are:

$$E(M)_{Zimm,\%}=\left(\frac{I}{I_m-1}\right)\times 100 \tag{3.37}$$

$$E\left(\left\langle R_g^2\right\rangle^{1/2}\right)_{Zimm,\%}=\frac{\sqrt{S_m\left(\left(E_M+100\right)/100\right)}-\sqrt{S}}{\sqrt{S}} \tag{3.38}$$

$$E(M)_{Berry,\%} = \left(\frac{I^2}{I_m^2 - 1}\right) \times 100 \tag{3.39}$$

$$E\left(\left\langle R_g^2 \right\rangle^{1/2}\right)_{Berry,\%} = \frac{\sqrt{S_m\left((E_M + 100)/100\right)^{1/2}} - \sqrt{S}}{\sqrt{S}} \tag{3.40}$$

where I, I_m, S, S_m, and E_M are the true intercept, measured intercept, true slope, measured slope, and error of molar mass, respectively. Results show that small scatterers at low scattering angles are appropriate objects for all static light scattering experiments and that the Debye method is superior to other methods in probing small spherical particles. Zimm plots are appropriate for the first approach as a visual inspection for linearity of data when no a priori knowledge of the macromolecules is known. Initial data points at low scattering angles or even at high scattering angles, in the resultant graph, occasionally show deviations from linearity. These deviations occur when the molar mass of the polymer is large or the polymer chain is semi-flexible or stiff.[155] A Berry plot is suitable for large random coil macromolecules but also is the most general procedure to probe a wide variety of polymers.

The configuration of macromolecules has been probed with the particle scattering factors in Eqns. 3.27 and 3.28. The particle scattering factor is simplified:

$$\frac{Kc}{R(\theta)} = \frac{1}{M_w P(\theta)} \tag{3.41}$$

and representative plots using $P(\theta)$ are Kratky-Porod plots and Holtzer-Casassa plots.[156,157] Experimentally, $P(\theta)$ is multiplied by u^2 when u is:

$$u = q\left\langle R_g^2 \right\rangle_z \tag{3.42}$$

and then, the data is plotted against u. Various configurations have been studied:[158-160]

$$P(\theta) = \frac{2}{u^2}\left[1 - u^2 + \exp\left(1 - \frac{1}{3}u^2\right)\right] \qquad \text{(for random coil polymers)} \tag{3.43}$$

$$P(\theta)=\frac{1+(1/3)u^2}{\left[1+(1/3)u^2\right]^2} \qquad \text{(for rod-like polymers)} \qquad (3.44)$$

$P(\theta)$ is also multiplied by q and data is plotted against u in a Holtzer-Casassa plot, examples of which can be found elsewhere.[154,155,161,162] Similar approaches are applicable to probe the configuration of block copolymers like coil-coil or rod-coil structures and Borsali *et al.*[163] reported microphase separation of block copolymers with static and dynamic light scattering. Also, a form factor provides the information about the persistence length (l_p) and contour length (L) of macromolecules found in Section 2.2.2.2. des Cloizeaux[164] and Sharp *et al.*[165] derived form factors for infinite and finite polymer chains:

$$P(\theta)=\frac{\pi}{qL}+\frac{2}{3q^2l_pL} \qquad [ql_p \geq 4 \text{ (infinite chain)}] \qquad (3.45)$$

$$P(\theta)=\left(\frac{2}{x^2}\right)\left(e^{-x}-1+x\right)+\frac{2}{15X}\left[4+\frac{7}{x}-\left(11+\frac{7}{x}\right)e^{-x}\right] \qquad [ql_p \leq 2 \text{ (finite chain)}] \qquad (3.46)$$

where $X = L/l_p$ and $x = q^2Ll_p/3$.[164-167] Imae *et al.*[168] experimentally probed long rod-like micelles with Benoit's theory:[169]

$$(R_g)_\theta^2 = l_p^2\left\{\frac{X}{3}+1+\frac{2}{X}-\frac{2}{X^2}\left[1-e^{-X}\right]\right\} \qquad \text{(at } \theta\text{-condition)} \qquad (3.47)$$

and the model has been applied to many systems. Recently, the configuration of hyaluronan was experimentally probed by Mendichi *et al.*[170] and it was confirmed that hyaluronan has a worm-like chain structure.

Experimentally, large particles or polyelectrolytes are still challenging to probe. Thus far the Zimm equation and various plotting methods are based on the RGD assumption of independent subscatterers. Eqns. 3.27 and 3.31 are expressions of an approximate solution of Maxwell's equations and are only valid when two inequalities are satisfied:[171]

$$|m-1| < 1 \tag{3.48}$$

$$2an_0k|m-1| < 1 \tag{3.49}$$

where m is the relative refractive index (n/n_0) and a is the characteristic dimension of the scattering body, half-length for rod-like structures or radius for spherical structures. Recently, Braun *et al.*[172] invoked Holthoff's time-resolved simultaneous static dynamic light scattering experiments and showed a form factor and polydispersity of relatively large particles. Also, Nomula *et al.*[173] and Nordmeier *et al.*[173] probed polyelectrolytes with a general formula:

$$\frac{Kc}{R(\theta)} = \left(\frac{1}{M_w}\right) + \left(\frac{\langle R_g^2 \rangle z}{3M_w} q^2\right) - \left(\Gamma_1 q^4\right) + \left(2A_2 c\right) - \left(\Gamma_2 q^2 c\right) + \left(3A_3 c^2\right) \tag{3.50}$$

where Γ_1 and Γ_2 are constants that depend upon a specific intermolecular interaction potential characterizing the molecular structure. Results showed that the electrostatic interaction dominated the solution behavior and both single polyelectrolyte and loose aggregates exist in the solution. Witte *et al.*[174] studied the growth and interaction of aggregates with time-resolved static light scattering. *In situ* recording of the change of radius of gyration and conventional analysis methods provided information about polymer configuration like structural models and contour lengths. Aggregation processes are similar to other low molar mass gelators and interactions driving gelation can be probed with dynamic light scattering.

3.1.2 Dynamic Light Scattering (DLS)

3.1.2.1 Theoretical Background

Generally, even a monochromatic light source (e.g., laser), exhibits a narrow spectral distribution of scattered light. This phenomenon is due to the translational motion of the irradiated molecules that are directly related to their Brownian motion. The interaction of light with a moving object gives rise to a Doppler shift that broadens the spectral width of the scattered light. Thus, dynamic light scattering is sometimes called quasi-elastic light scattering (QELS). Dynamic light scattering (DLS) measures the fluctuations in scattering intensity that arise from Brownian motion of the particles.[72] The fact that the intensity fluctuations are not purely random yields correlations on relatively short time scales. This "quasi-random phenomenon" is explained and utilized theoretically and experimentally through the aid of correlation functions to determine how long a given signal is correlated through a correlation time (sampling time or bin width), τ.[175]

The time-autocorrelation function for scattered light intensity is[176]

$$G^{(2)}(t) = < I(0)I(t) > = \lim_{T \to 0} \frac{1}{T} \int_{-T/2}^{T/2} I(t')I(t'+t)dt' \tag{3.51}$$

where t is lag time interval or delay time. This correlation function can be approximated as

$$G^{(2)}(t) = B\left(1 + f\left|g^{(1)}(t)\right|^2\right) \tag{3.52}$$

where $g^{(1)}(t)$ is the electric field autocorrelation function, B is the baseline, and f is an instrumental parameter known as the coherence factor.

Here, when t is very short, one measures the average of the squares because $I(t') \approx I(t'+t)$, which means $G^{(2)}(0) = < I^2 >$. At very long t, one obtains the square of the average: $G^{(2)}(\infty) = < I >^2$. Mathematically, $< I^2 >$ is guaranteed to be larger than or equal to $< I >^2$; thus, we always see correlation functions that decay exponentially. In Eqn. 3.52, the coherence factor is $0< f <1$, and is related to the spatial coherence, detector dark count, and solvent scattering.[177,178]

The electric field autocorrelation function ($g^{(1)}(t)$) is expressed as

$$g^{(1)}(t) = e^{-\Gamma t} \tag{3.53}$$

where Γ is the decay rate (the inverse of the decay time *t*). For simple translational diffusion, the decay rate is

$$\Gamma = t^{-1} = q^2 D_m \tag{3.54}$$

where D_m is the mutual diffusion coefficient and q is the magnitude of the scattering vector. For very dilute solutions, it will turn out that $D_m \approx D_0$ (the diffusion coefficient extrapolated to infinite dilution). Once we know D_0, the hydrodynamic radius is given by the Stokes-Einstein relationship (also seen in Eqn. 2.88) as:

$$R_h = \frac{k_b T}{6\pi \eta_0 D_0} \tag{3.55}$$

where k_b is Boltzmann's constant, and η_0 is the viscosity of the solvent.

Distributions in hydrodynamic radius, R_h, arise from size distributions in solutes and impurities in solvents. For continuous polydisperse systems, the electric field autocorrelation function must be integrated over all possible sizes (i.e. all corresponding Γ values):

$$g^{(1)}(t) \approx \int_0^\infty A(\Gamma) e^{-\Gamma t} d\Gamma \tag{3.56}$$

where $A(\Gamma)$ is the Γ distribution function. Two functions ($g^{(1)}(t)$ and $A(\Gamma)$) are Laplace transform pairs, and the process of estimating $A(\Gamma)$ from $g^{(1)}(t)$ is called an inverse Laplace transformation (ILT).[179] The most common algorithms used to perform the ILT are CONTIN and NNLS.[180,181]

The inverse Laplace transform is a useful algorithm when the distribution is broad. For narrow distributions that exhibit a nearly single exponential decay, we can evaluate the average decay rate over all the distribution functions. Under these conditions Koppel proposed the application of a statistical cumulant generating function called a cumulant expansion to obtain an average decay rate.[182-184]

3.1.2.2 Measurement and Analysis

Diffusion coefficients obtained from dynamic light scattering experiments are *z*-average values, which means they are more strongly affected by large scatterers. Different sizes of scatterers or locally heterogeneous fluctuations of refractive index show different dependencies on scattering angle. Thus, rigorous sampling processes are required to obtain an ergodic system and are critical in dynamic light scattering. Most sample preparation strategies are identical to those mentioned in Section 3.1.1.2. In contrast to static light scattering, dynamic light scattering probes the fluctuation of scattering intensity that arises from Brownian motion of molecules. Molecules moving too fast or slow do not provide a representative correlation function because of instrument specific time and frequency limits. Thus, very high viscosity solvents that essentially freeze molecules are inappropriate for dynamic light scattering studies. Preparing very low sample concentrations is important to probe diffusion. Employing low scattering intensities keeps noise random. Random noise will cancel out during multiple averaging processes used for calculating an autocorrelation function.[185] However, both low concentration and low scattering intensity necessitate long measurement times for statistically meaningful autocorrelation functions. Also, long measurement times increase the chances of detecting dust in the sample. For recently developed commercial dynamic light scattering instruments that employ relatively large pinholes or high power lasers like Argon ion lasers (> 1 W), shortening the measurement time for a given concentration makes it possible to probe rapidly moving sparse particles.

Five or six scattering angles smaller than 90° are appropriate for general dynamic light scattering experiments but angle selection is much less rigorous than in static light scattering. All scattering intensities are stored in specific numbered channels in the instrument and a correlator fits the intensity autocorrelation function shown in Eqn. 3.51. At the same scattering angle, all measured average scattering intensities should be within a 5 % window. During the experiment, an instrumental parameter, f, also known as a coherence factor, can be obtained from the spectral amplitude of the raw data. The baseline, B, is:

$$B = P^2 / N \tag{3.57}$$

where P and N are the total number of photocounts during a measurement and sample times, respectively. Properly working instruments and correctly measured data show good agreement between calculated and empirical values of B.[186]

Time is continuous in ideal dynamic light scattering but a real correlator has a discrete time scale (lag time interval or delay time), t. Thus, an experimentally obtained intensity autocorrelation function has systematic error and does not fully account for strong damping of the temporal fluctuations. Photomultiplier tube dead time and photon counting noise also provide systematic errors but are not a significant technical challenge to overcome. However, the systemic error from a finite time resolution arising from time windowing is not trivial. A multi-tau autocorrelator manipulates several sampling times simultaneously and provides the average intensity autocorrelation function over a window of delay times. The cross product of the number of photons counted by a photomultiplier is recorded in circuitry or software referred to as a channel. Then, channels having different sampling times are corrected to obtain an expected correlation function. The optimal selection of correction scheme is relatively complicated but generally the systematic error is linear in $\Gamma\tau$.[187-190]

Multiple scattering causes another systematic error. Experimentally, 0.1×10^{-4} M is a very low concentration but a sample still contains approximately 10^{19} scatterers in 1 mL of solution. Thus, a laser beam passes through a large number of scatterers and multiple scattering occurs. Pillies[191] discussed the effect of the number of detectors related to multiple scattering and showed that systems having two or more detectors were less affected by multiple scattering than a single detector system. Bantchev *et al.*[192] designed a multi-detector and multi-correlator system and showed it was efficient for anisotropic or polydisperse samples with large dimensions over a wide range of concentration. A concentration window is used to determine diffusion coefficients at infinite dilution because of experimental difficulties to obtain infinitely dilute solutions. Extrapolation to zero concentration in the graph of diffusion coefficients versus sample concentration provides the self-diffusion coefficient, but not all plots show linearity.

The concentration dependence of the diffusion coefficient and its scaling nature has been probed with various dynamic light scattering experiments and model calculations.[193-199] Polymer self-diffusion follows a universal scaling law with a simple exponential equation:

$$D = D_0 \exp\left(-\alpha c^{\nu}\right) \tag{3.58}$$

where D, D_0, α, and ν are the self-diffusion coefficient, diffusion coefficient at zero concentration, prefactor, and exponent ($0.5 \leq \nu \leq 1$), respectively. Later, effects of high concentration or adsorption in multi-component systems were also probed and the scaling theory was extended:

$$D(c) = D_0\left(1 + k_D c\right) \tag{3.59}$$

$$k_D = 2A_2 M_w - \nu_2 - k_f \tag{3.60}$$

where k_D, A_2, M_w, ν_2, and k_f are the virial dynamic, second virial coefficient, weight-average molar mass, specific volume, and friction coefficient, respectively.[200,201]

Ullmann *et al.*[202] and Lin *et al.*[203] reported the failure of the Stokes-Einstein equation for high solution concentrations or adsorption phenomena in multi-component systems. For example, two solutes in a ternary system can be particle/particle, particle/polymer, and polymer/polymer.[204,205] Sometimes, an optical probe whose diffusion is already well-defined is adapted to probe diffusion in the multi-component system. In any case, movement of one solute causes a correlation hole or adsorption.[206,207] Also, the relationship of hydrodynamic interactions and Brownian motion becomes quite intractable with various experimental conditions like concentration, ionic strength, and viscosity.[208] Thus, the failure of the Stokes-Einstein equation has been frequently reported.[209,210] Ullmann *et al.*[211] and Dunstan *et al.*[212] probed viscosity effects on diffusion and reported deviation from the Stokes-Einstein equaton. High solvent or solution viscosity affects diffusion of macromolecules dramatically, so even a small change (microviscosity) can affect macroscopic interpretation of diffusion.[213-216]

Phillies pioneered probe diffusion of particles in solution at various concentrations with the relationship between a correlation function and lag time. An initial slope, $K_{initial}$, in the intensity autocorrelation function versus lag time plot was defined as:

$$K_{initial} \equiv \lim_{t\to 0}\left[\frac{\partial \ln G^2(t)}{\partial t}\right] \tag{3.61}$$

and later, a slope related to the field autocorrelation function. Eqn. 3.53 shows an idealized relationship of the field autocorrelation function and decay rate and is valid experimentally when a plot of $g^{(1)}(t)$ versus lag time window corresponding to diffusion of scatterers is linear.[217-223] Otherwise, the sample is polydisperse and the distribution of decay rate and the average of decay rate need to be probed. Koppel introduced a series expansion of Eqn. 3.56:

$$\ln\left[g^{(1)}(t)\right] = K_0 - K_1 t + \frac{K_2 t^2}{2!} - \frac{K_3 t^3}{3!} + \cdots \tag{3.62}$$

where $K_1 = <\Gamma>$, $K_2 = <(\Gamma - <\Gamma>^2)>$, $K_3 = <(\Gamma - <\Gamma>^3)>$, or $K_n = \left[(-1)^n \frac{d^n}{dt^n} \ln\left(g^{(1)}(t)\right) \right]$.

Hence Eqn. 3.56 can be expressed more directly as:

$$\ln(g^1(t)) = \ln(A) - \overline{\Gamma}t + \frac{\mu_2}{2}t^2 - \frac{\mu_3}{6}t^3 \tag{3.63}$$

and each coefficient corresponds to the hydrodynamic radius and polydispersity through:

$$R_{h,Zavg} = \frac{kT}{6\pi\eta\overline{\Gamma}}q^2 \tag{3.64}$$

Here, a diffusion coefficient obtained from Eqn. 3.63 is the average decay rate. The variance, *V*, in fitting with Eqn. 3.63 can be obtained from the second cumulant, μ_2:

$$V = \frac{100\,\varsigma(\mu_2)\sqrt{|\mu_2|}}{\overline{\Gamma}} \tag{3.65}$$

where $\varsigma(\mu_2)$ is a sign function.[224] *V* of 10 ~ 40 % is acceptable for spherical scatterers like micelles.[224,225] Also, the polydispersity index, *PDI*, is defined as:

$$PDI \equiv \frac{\mu_2}{\overline{\Gamma}^2} = \left(\frac{width}{R_{h,Z-avg}} \right)^2 \tag{3.66}$$

It should be noted that the *PDI* is not the same quantity as the more common expression, the weight average molar mass divided by the number average molar mass.

Provencher derived a regularized data inversion algorithm called CONTIN for an inverse Laplace transform (ILT) to obtain a size distribution of scatterers.[180,226-228] The general regularization technique adapts an objective function, *V*(*α*), composed of the variance and the regularizor and is defined as:

$$V(\alpha) \equiv \left\| \sqrt{M_\varepsilon}\left(y - Ax\right) \right\|^2 + \alpha^2 \left\| r - Rx \right\|^2 \tag{3.67}$$

where M_ε, y, A, x, and α are the covariance matrix of the residuals, experimental data of the field correlation function, matrix involving the kernel of the Fredholm integral equation of the first kind, solution of fitting, and regularization parameter, respectively. r and R in the second term in Eqn. 3.67 are related to each other in the CONTIN algorithm:

$$r = R\bar{x} \tag{3.68}$$

$$R = \frac{1}{\sqrt{M_x}} \tag{3.69}$$

where $\bar{x}$ and M_x are the average and covariance of x. The regularizor imposes the smoothness of the size distribution and the statistical prior knowledge or parsimony. Recently, other regularization techniques like ORT and L-curve using different regularization strategies were published.[229-231] CONTIN is highly sensitive to non-random intensity fluctuations for high scattering intensity and baseline errors. However, CONTIN can be adapted to probe local motion of a polymer chain or even network/gelation.[232] ORT and L-curve provide relatively reproducible results but also provides too strongly regularized solutions. All methods depend on the optimal regularization strength and the normalization with proper baseline to obtain reliable size distributions.[233,234]

3.1.3 Depolarized Dynamic Light Scattering (DDLS)

3.1.3.1 Theoretical Background

Depolarized dynamic light scattering (DDLS) is a light scattering technique based upon the depolarized signal that arises when the incident field is linearly polarized in the vertical direction with anisotropic particles leading to horizontally polarized scattering.[235] The electric field vector of the electromagnetic radiation induces a molecular dipole moment whose magnitude is proportional to the intensity of the electric field:

$$\boldsymbol{\mu}_{\alpha} = \underline{\underline{\alpha}}_{\alpha\beta} \mathbf{E}_{\beta} \tag{3.70}$$

where the "proportionality constant", $\underline{\underline{\alpha}}_{\alpha\beta}$, is the polarizability tensor. $\underline{\underline{\alpha}}_{\alpha\beta}$ generally has off-diagonal elements; in other words, because a molecule is continuously changing orientation, the magnitude and direction of its induced dipole moment fluctuates, which leads to a change in the polarization and the electric field strength of the dipole. The principal axes of the polarizability, the dipole moment and the electric field define an ellipsoid (i.e. the polarizability ellipsoid) containing a principal, major, and minor axis. If the molecule has the same symmetry as the charge distribution or nuclear frame of the rigid molecule, any axis of symmetry of the molecular point group can serve as a principal axis for the polarizability ellipsoid. For the case where all three axes are equal, the polarizability is isotropic; otherwise, two or more different axes are sufficient to make the polarizability anisotropic.[236]

When considering the polarization state of both the incident and scattered light, there are three contributions to the scattering intensity. Figure 3.2 shows a simplified geometry of a scattering system and can be used to deduce the three common conditions for the angle that the polarization of the incident light makes with the z-axis, μ, and the angle that the polarization of the scattered light makes with the z-axis, ψ.

Case 1: Polarized scattering, $\mu = 0$ and $\psi = 0$. The intensity of this component of the scattering is often denoted by the symbol I_{Vv} (for vertically polarized scattered and incident rays).

Case 2: Depolarized scattering. $\mu = 0$ and $\psi = 90°$. The symbol is I_{Hv} for horizontally polarized scattered and vertically polarized incident rays.

Case 3: Horizontal-horizontal scattering. $\mu = \psi = 90°$. The symbol is I_{Hh} is often expressed as a linear combination of I_{Vv} and I_{Hh}.

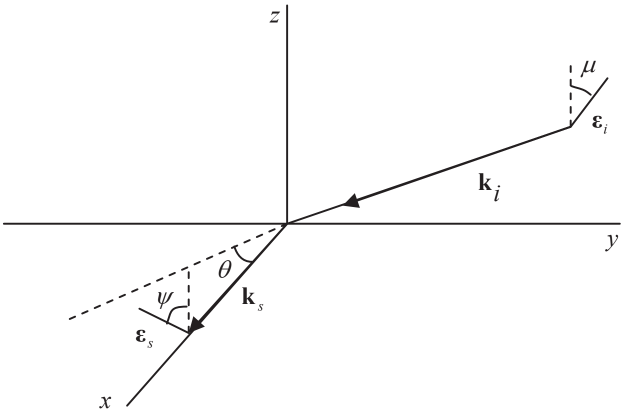

Figure 3.2 Scattering geometry. The x-y plane is the scattering plane, θ is the scattering angle, and $\mathbf{q} = \mathbf{k}_I - \mathbf{k}_S$ does not lie along any labeled axis. $\boldsymbol{\varepsilon}_i$ and $\boldsymbol{\varepsilon}_s$ denote the incident and scattered polarization vectors.

In depolarized dynamic light scattering (DDLS), the scattered electric field in the Vh (horizontally depolarized) configuration, E_y, is approximately proportional to:

$$E_y \propto \sum_j \underline{\underline{\alpha}}^j_{yz}\left[\Omega(t)\right] e^{i\mathbf{q}\bullet rj(t)} \tag{3.71}$$

where $\underline{\underline{\alpha}}^{j}{}_{y}z\left[\Omega(t)\right]$ is the yz component of the polarizability tensor of element j. Here, we can recall that DDLS is based on the same principle as DLS whose resultant normalized electric field autocorrelation function is dependent on the scattered electric field. In DLS, the total electric field that falls upon the detector is

$$E_s(\mathbf{R},t) = -\frac{\omega_0^2 n_0^2 E_0}{c^2 R}\exp(i\mathbf{k}_S \cdot \mathbf{R})\exp(-i\omega_0 t)\alpha(\mathbf{q},t') \tag{3.72}$$

where $\mathbf{R}$ is the location of detector, $R = |\mathbf{R}|$, and ω_0 is the angular frequency which is defined as $\omega_0 \equiv |\mathbf{k}_i| c / n_0$ where n_0, $n_0 = \sqrt{\varepsilon_0}$, is refractive index obtained from average dielectric constant, ε_0.

In Eqn. 3.72, the polarizability of the system can be expressed as the sum of the average polarizability and the contribution arising from local inhomogeneity:

$$\alpha(\mathbf{q}, t') = \langle \alpha \rangle \int_{Vs} \exp(i\mathbf{q}^T \cdot \mathbf{r}) d^3 r + \int_{Vs} \delta\alpha(\mathbf{r}, t') \exp(i\mathbf{q}^T \cdot r) d^3 r \tag{3.73}$$

where the notation V_S represents the scattering volume. In the first term, of Eqn. 3.73, the average component of the polarizability has the property

$$\int_{Vs} \exp(i\mathbf{q}^T \cdot r) d^3 r = \begin{cases} V_S & (\mathbf{q} = 0) \\ 0 & (\mathbf{q} \neq 0) \end{cases} \tag{3.74}$$

Therefore, the average component of Eqn. 3.73 only contributes to the polarizability in the forward scattering direction and the scattering of light at any angle other than the forward direction is a result of fluctuations in the polarizability of the system. Thus, the resultant electric field autocorrelation function in DDLS, which is dependent on E_y, is proportional to the yz component of the polarizability tensor.

In summary, the field scattered by anisotropic particles is the superposition of two terms when the incident light is linearly polarized in the vertical direction. The first of these terms is a vertically polarized component with an amplitude that is proportional to the optical mismatch between the particle and the solvent, while the second term is a depolarized component with an amplitude that is proportional to the particle's optical anisotropy. As a consequence, the second term gives rise to a horizontally polarized scattered field (Case 2).[237,238]

In modern light scattering experiments, the intensity autocorrelation function, $G^{(2)}(t)$, is directly determined from the time dependent signal of a photomultiplier tube (PM or PMT: photomultiplier tube) and an autocorrelator. With Eqns. 3.52 and 3.53, one directly obtains the electric field autocorrelation function, $g^{(1)}(t)$, and the decay rate, Γ. However, for optically anisotropic systems, the resultant decay rates are

$$\Gamma_{Vv} = D_t q^2 \quad \text{(case 1)} \tag{3.75}$$

$$\Gamma_{Hv} = D_t q^2 + 6D_r \quad \text{(case 2)} \tag{3.76}$$

where D_t is the translational diffusion coefficient and D_r is the rotational diffusion coefficient.[239-241]

3.1.3.2 Data Fitting and Analysis

Modern light scattering instruments have a vertically polarized laser source, and deporized dynamic light scattering data can easily be obtained by introducing a horizontal polarizer in front of the detector. The measurement is only possible when the scattering bodies are optically anisotropic (irrelevant to physical shape).[242,243] Experimental methods are similar to those described in Section 3.1.1.2 and 3.2.1.2. However, very weak scattered intensities of depolarized light accentuate the technical difficulties associated with sample preparation and measurement.

For rod-like scattering bodies, Broesma's equations have been studied extensively in many systems:[87,244-246]

$$D_t = \frac{k_b T}{3\pi\eta L}\left[\delta - \frac{1}{2}(\gamma_a + \gamma_b)\right] \tag{3.77}$$

$$D_r = \frac{3k_b T}{\pi\eta L^3}(\delta - \xi) \tag{3.78}$$

where

$$\delta = \ln\left(\frac{2L}{d}\right) \tag{3.79}$$

$$\gamma_a = 0.807 + \frac{0.15}{\delta} + \frac{13.5}{\delta^2} - \frac{37}{\delta^3} + \frac{22}{\delta^4} \tag{3.80}$$

$$\gamma_b = -0.193 + \frac{0.15}{\delta} + \frac{8.1}{\delta^2} - \frac{18}{\delta^3} + \frac{9}{\delta^4} \tag{3.81}$$

$$\xi = 1.15 + \frac{0.2}{\delta} + \frac{16}{\delta^2} - \frac{63}{\delta^3} + \frac{22}{\delta^4} \tag{3.82}$$

Here, L and d are a rod length and diameter, respectively. Broesma's equations work well for rigid rod-like particles. For semi-rigid particles or flexible particles of micelles or lamellae Perrin's formula works better:

$$R_h = \frac{b\left[1-(a/b)^2\right]^{1/2}}{\ln\left[\frac{1+\left(1-(a/b)^2\right)^{1/2}}{a/b}\right]} \tag{3.83}$$

where (a/b) is the ratio of the semi-minor and semi-major axes of the ellipsoid. Hydrodynamic radii of rigid rod-like particles also can be obtained by:[247-249]

$$R_h = \frac{L}{\left[2\delta - 0.19 - \frac{8.24}{\delta} + \frac{12}{\delta^2}\right]} \tag{3.84}$$

Lin *et al.*[250] also probed prolate or oblate micellar structures with depolarized dynamic light scattering and showed:

$$\frac{R_{h,r}}{R_{h,t}} = f_t\left(\frac{a}{b}\right)\left[\frac{3}{2}f_r\left(\frac{a}{b}\right)\right]^{-1/3} \tag{3.85}$$

where two hydrodynamic radii are

$$R_{h,t} = \frac{k_b T}{6\pi\eta D_t} = \frac{b}{f_t(a/b)} \tag{3.86}$$

$$R_{h,r}^3 = \frac{k_b T}{12\pi\eta D_r} = \frac{2b^3}{3f_r(a/b)} \tag{3.87}$$

They[250] also showed that the optical anisotropy, I_{Hv}/I_{Vv}, increased with increasing scattering angle, which meant the micellar system was internally ordered but flexible.

Maeda *et al.*[251] derived the equation for apparent diffusion coefficients from a cumulant expression of a polarized electric field autocorrelation function and showed that the translational and rotational diffusion coefficients of very long rod-like molecules can be obtained without solving an equation having coupled translational and rotational motion. The cumulant analysis in Eqn. 3.63 provided the weighted average diffusion coefficient, $\overline{\Gamma}/q^2$, and Maeda *et al.* showed:[251-253]

$$\left(\frac{\overline{\Gamma}}{q^2}\right)_{Vv} = \left[D_t + \left(\frac{L^2}{12}\right)D_r f_1(k) - (D_3 - D_1)\left\{\frac{1}{3} - f_2(k)\right\}\right] \qquad [k = qL] \tag{3.88}$$

where D_3 and D_1 are lengthwise and sidewise translational diffusion coefficients, respectively, and the subscripts 3 and 1 are conceptually very close to subscripts a and b in Eqns. 3.77 and 3.83. $f_1(k)$ and $\{1/3 - f_2(k)\}$ are weighting factors that only depend on k. $f_1(k)$ accounts for the contribution of rotation to $\overline{\Gamma}/q^2$ and $\{1/3 - f_2(k)\}$ accounts for the contribution of translational anisotropy which arises from the difference between lengthwise (parallel) and sidewise (perpendicular) diffusion. Also, Eqn. 3.88 can have limiting values for very dilute concentrations:

$$\frac{\overline{\Gamma}}{q^2} \to D_t \qquad \text{for } k \gg 1 \tag{3.89}$$

$$\frac{\overline{\Gamma}}{q^2} \to \left[D_t - \frac{1}{3}(D_3 - D_1)\right] + \left(\frac{L^2}{12}\right)D_r \qquad \text{for } k \ll 1 \tag{3.90}$$

Later, Maeda[254] showed a formalism for Hv scattering similar to Eqn. 3.88:

$$\left(\frac{\overline{\Gamma}}{q^2}\right)_{Hv} = \left[D_1 + D_1 f_1(k) - (D_3 - D_1) f_2(k)\right] \tag{3.91}$$

and the first term provides the sidewise translational diffusion coefficient.[255] Rotational diffusion is very sensitive to the chain stiffness and depends on the contour length.[244] Thus, configuration can be probed with polarized and depolarized light scattering. Hagermann *et al.*[256] published the relationship between two rotational diffusion coefficients from depolarized and polarized scattering:

$$\frac{D_{r,Broesma}}{D_{r,Maeda}} = R_a(1 - Y) \tag{3.92}$$

where

$$R_a = 1.0120 - 0.24813X + 0.033703X^2 - 0.0019177X^3 \tag{3.93}$$

$$Y = 0.06469X - 0.01153X^2 + 0.0009893X^3 \tag{3.94}$$

$$X = \frac{L}{l_p} \tag{3.95}$$

Also, Yoshizaki *et al.*[257] used Kuhn segments, N_k:

$$N_k = \frac{L}{2l_p} \tag{3.96}$$

in place of Eqn. 3.95 and showed Eqn. 3.92 can be expressed as:

$$\begin{aligned}\frac{D_{r,Broesma}}{D_{r,Maeda}} = \left[N_k + \frac{1}{2}\left(e^{-2N_k} - 1\right)\right]^{3/2} \times N_k^{\ -3} \times \\ \left[1 + 0.539526\ln(1 + N_k)\right]\end{aligned} \tag{3.97}$$

CHAPTER 4

Materials and Experimental Methods

4.1 Materials

4.1.1 Cellulose Nanocrystals

Cellulose nanocrystals were provided by Dr. Roman’s group. A detailed preparation strategy is described by Beck-Candanedo *et al.*[258,259] Milled black spruce pulp was hydrolyzed with 60 wt % sulfuric acid at a temperature of 50 °C for 105 minutes. An atomic force microscopy (AFM) image is shown in Figure 4.1. Two sample groups of replicates from different batches were obtained and were designated DOE-2-12A and DOE-2-12B, respectively.

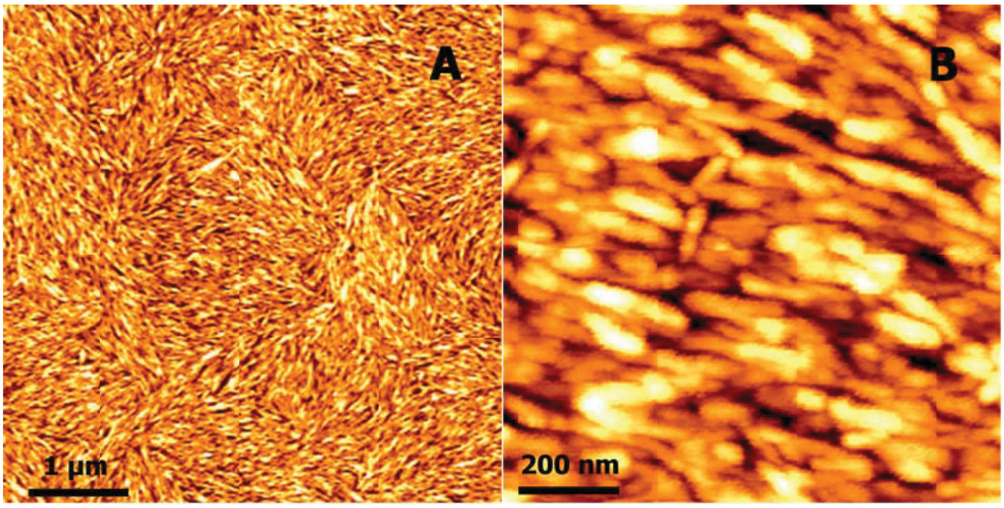

Figure 4.1 (a) 1 × 1 μm and (b) 200 × 200 nm AFM images of cellulose nanocrystals (DOE-2-12B): 0.1 wt % water solution on silicon wafer

4.1.2 Pullulan 4-Chlorocinnamates (P4CCs)

Pullulan 4-chlorocinnamates (P4CCs) were synthesized by Dr. Zelin Liu in Prof. Alan R. Esker's group at Virginia Tech according to the scheme in Figure 4.2. N,N'-carbonyl diimidazole (CDI) was used as a coupling agent for the reaction of pullulan (from *Aurebasidium pullulans*) with 4-chlorocinnamic acid (4CCA). The degree of substitution (DS) of P4CC was defined as the number of functional groups per anhydroglucose unit (AGU). P4CC with a DS of 0.03 was named P4CC03.[260]

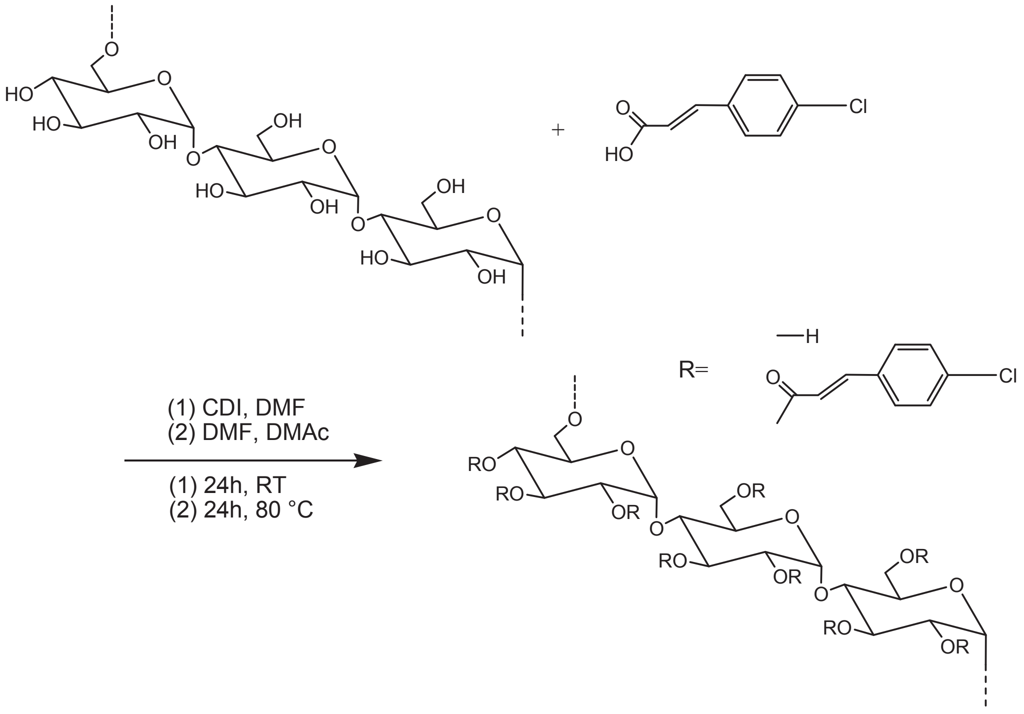

Figure 4.2 Reaction scheme for the synthesis of a P4CC.

4.1.3 2-Hydroxypropyltrimethylammonium Xylans (HPMAXs)

2-Hydroxypropyltrimethylammonium xylans (HPMAXs) were synthesized by Prof. Thomas Heinze's group at the Friedrich-Schiller University in Jena, Germany, according to the scheme of Figure 4.3. Birch xylan (BX) was reacted with 2,3-epoxypropytrimethylammonium chloride (EPTA).[261] DS of HPMAX was defined as the number of 2-hydroxypropyltrimethylammonium groups per anhydroxylose unit (AXU).

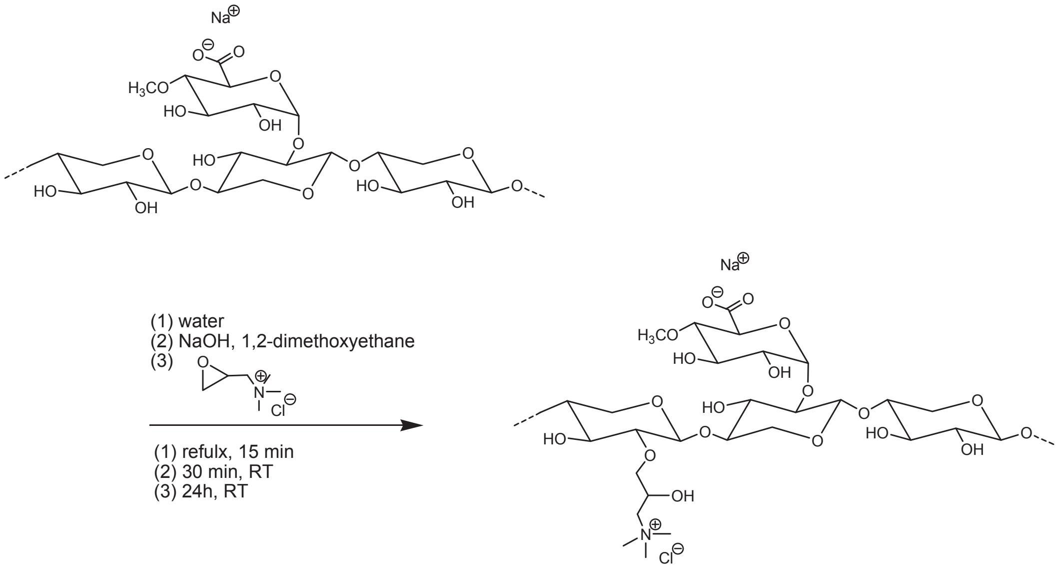

Figure 4.3 Reaction scheme for the synthesis of a HPMAX.

4.2 Sample Preparation for Light Scattering

4.2.1 Sample Cells

10 × 75 mm (OD × length, Fisherbrand®) glass tubes were used as sample cells. First, sample cells were rinsed with ultrapure water (Millipore, Milli-A Gradient A-10, 18.2 MΩ·cm, < 5 ppb organic impurities) that was filtered twice with 0.2 μm pore size cellulose acetate membrane filters (disposable syringe units, ADVANTEC MFS, Inc.). *This ultrapure water was used for all experiments throughout this dissertation and 'water' denotes ultrapure water.* Second, rinsed sample cells were cleaned with a homemade acetone percolator and dried with nitrogen. Finally, dried sample cells were rinsed with water again and capped with clean aluminum foil. Capped sample cells were dried in a vacuum oven overnight. All glassware was cleaned to avoid impurities like dust.

4.2.2 Stock Solutions

4.2.2.1 Cellulose Nanocrystal Stock Solutions

Original cellulose nanocrystals (CNs) were provided as 0.1 wt % aqueous solutions. The original solution was sonicated for 20 minutes and filtered with a 0.8 μm pore size cellulose acetate membrane filter (disposable syringe unit, ADVANTEC MFS, Inc.). Filtered solution was examined with dynamic light scattering at a scattering angle of 90° for 30 seconds. The filtered original solution was diluted and another stock solution of 0.01 wt % was prepared. These stock solutions were used to prepare binary and ternary systems for experiments in Chapters 5, 6, and 7.

4.2.2.2 P4CC03 Stock Solution

0.81 $\mathrm{mg \cdot mL^{-1}}$ P4CC03 stock solution was prepared in a 50 mL volumetric flask cleaned in a manner similar to Section 4.2.2.1. The solution was shaken vigorously and sonicated for 30 minutes. Then, the solution was filtered with a 0.2 μm pore size cellulose acetate membrane filter and was stored in a cleaned 50 mL volumetric flask.

4.2.2.3 HPMAX Stock Solutions

Stock solutions of HPMAX of DS = 0.34 with concentrations of 0.6 and 0.8 $mg{\cdot}mL^{-1}$ were prepared in 20 mL volumetric flasks cleaned in a manner similar to Section 4.2.2.1 for ternary and binary systems, respectively. The stock solutions were shaken vigorously and sonicated for 30 minutes. Then, the solution was filtered with a 0.45 μm pore size cellulose acetate membrane filter (disposable syringe unit, ADVANTEC MFS, Inc.).

4.2.3 P4CC03/Cellulose Nanocrystal/Water Ternary Systems

Two ternary systems, mixed Pre-crosslinking (PreX) and post-crosslinking (Rxn), were prepared with P4CC03 and cellulose nanocrystals. Schematic strategies are illustrated in Figure 4.3 and the properties of samples are summarized in Table 4.1. For PreX samples, four sample cells, containing 2 mL of P4CC03 stock solution were prepared. One of them was selected as the zero UV exposure time sample. Three samples were exposed to UV light for UV crosslinking. Each sample was taken out after specific UV exposure times of 30, 50, and 70 minutes. After UV crosslinking, each sample was diluted with 2 mL of 0.01 wt % cellulose nanocrystal stock solution. Diluted ternary systems were stirred for 20 minutes with a vortex mixer and UV spectroscopy and light scattering experiments were performed immediately. For Rxn samples, 2 mL of P4CC03 stock solution were diluted with 2 mL of 0.01 wt % cellulose nanocrystal solution. Eight diluted samples were prepared in sample cells. One of them was selected as the zero UV exposure time sample. Seven samples were stirred for 20 minutes and exposed to UV light. Each sample was taken out at UV exposure times of 50, 70, 100, 160, 220, 280, and 340 minutes. Samples were labeled with a number denoting the UV exposure time.

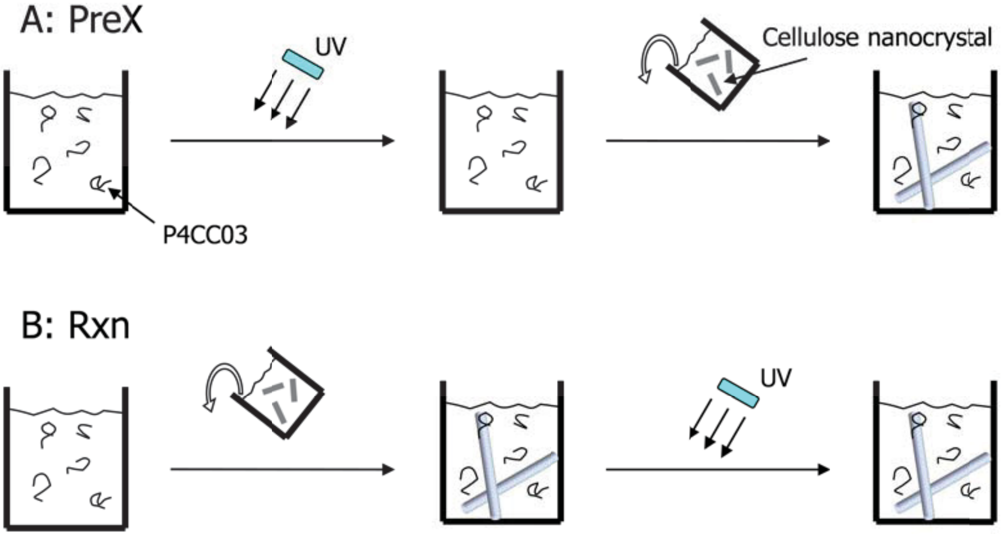

Figure 4.4 Schematic strategies for the preparation of P4CC04/cellulose nanocrystal/water ternary systems: (A) PreX: P4CC03/water solution was exposed to UV light first and diluted with cellulose nanocrystal stock solution; (B) Rxn: P4CC03/cellulose nanocrystal/water ternary system was prepared first and then the sample was exposed to UV light.

Table 4.1 Properties of 4 mL samples of P4CC03 and cellulose nanocrystals

Sample name	P4CC03 conc. $mg \cdot mL^{-1}$	Cellulose nanocrystal conc. wt %
P4CC03 Solution	0.4	-
PreX‡	0.4	0.005
Rxn†	0.4	0.005

‡,† PreX and Rxn samples are labeled with a number denoting the specific UV exposure time.

4.2.4 HPMAX/Cellulose Nanocrystal/Water Ternary Systems

Six HPMAX /water/cellulose nanocrystal ternary systems were prepared with HPMAX and cellulose nanocrystal stock solutions. Each sample was labeled with R, the concentration ratio of HPMAX and cellulose nanocrystal (R = [HPMAX]/[cellulose nanocrystal]). First, 1 mL of HPMAX stock solution was taken into a sample cell and diluted with 1 mL of cellulose nanocrystal stock solution. 0.6 $mg \cdot mL^{-1}$ HPMAX stock solution was diluted with water and mixed with a corresponding cellulose nanocrystal stock solution. Then, ternary systems were stirred for 20 minutes. The characteristics of samples are summarized in Table 4.2.

Table 4.2 Properties of 3 mL samples of ternary systems with HPMAX, cellulose nanocrystals, and water

Sample name	[HPMAX] $mg \cdot mL^{-1}$	[cellulose nanocrystal] $mg \cdot mL^{-1}$
R = 0	0	0.5
R = 0.4	0.2	0.5
R = 0.8	0.4	0.5
R = 4	0.2	0.05
R = 6	0.3	0.05
R = 8	0.4	0.05
R = 12	0.6	0.05

4.3 Experimental Methods

4.3.1 UV-Vis Spectroscopy

UV-Vis spectra were recorded on a Varian Cary® 50 UV-Vis spectrophotometer. 3 mL quartz cuvettes of 1 cm path length were cleaned with a homemade acetone percolator and water. Absorbance was scanned in 1 nm intervals from 200 to 800 nm using dual beam mode. All measurements were done prior to light scattering experiments at room temperature.

4.3.2 Atomic Force Microscopy (AFM)

0.1 and 1 wt % aqueous solutions of DOE-2-12Bs were dried on silicon wafers (1 × 1 cm). Substrates were cleaned by immersion in acetone and then ethanol, followed by rinsing with Mili-Q water. Then, they were sonicated in acetone for 20 minutes. After being cleaned, the substrates were treated for 20 minutes in an UVO-cleaner (Jelight company, Inc., USA) to ensure a hydrophilic surface.

4.3.3 X-ray Photoelectron Spectroscopy (XPS)

Samples for XPS measurements were prepared with similar method to Section 4.3.2. XPS (ESCALAB 200, VG Microtech, Mg-Kα radiation) was performed with a magnesium anode operated at 48 kW with a background pressure of 4×10^{-9} mbar. The spectra were recorded with an analyzer electron pass energy of 20.0 eV, 0.1 eV step and 100 ms dwelling time. The angle between the X-ray beam and surface normal was 15°. Each surface was examined with both a survey scan, that encompassed the region 0 to 1095 eV, and a multiplex of carbon, oxygen, and sulfur.

4.3.4 Zeta-potential Measurements

The zeta-potential of cellulose nanocrystals in cellulose nanocrystal/water, cellulose nanocrystal/HPMAX/water, and cellulose nanocrystal/P4CC03/water systems were measured with a Malvern Nano ZS (Malvern instrument, UK) using Laser Doppler Microelectrophoresis. A 4mW He-Ne laser and Avalanche photodiode were used.

4.3.5 Light Scattering

Dynamic light scattering studies were performed using an ALV/CGS-3 Goniometer System (ALV-GmbH) equipped with a He-Ne laser with a wavelength (λ_0) of 632.8 nm (22 mW output power). Scattering signals were detected with an optical fiber detector and intensity autocorrelation functions were obtained using ALV-5000/EPP digital correlator with 288 maximum channels interfaced to the goniometer system with a computer. Figure 4.5 schematically depicts the light scattering system.

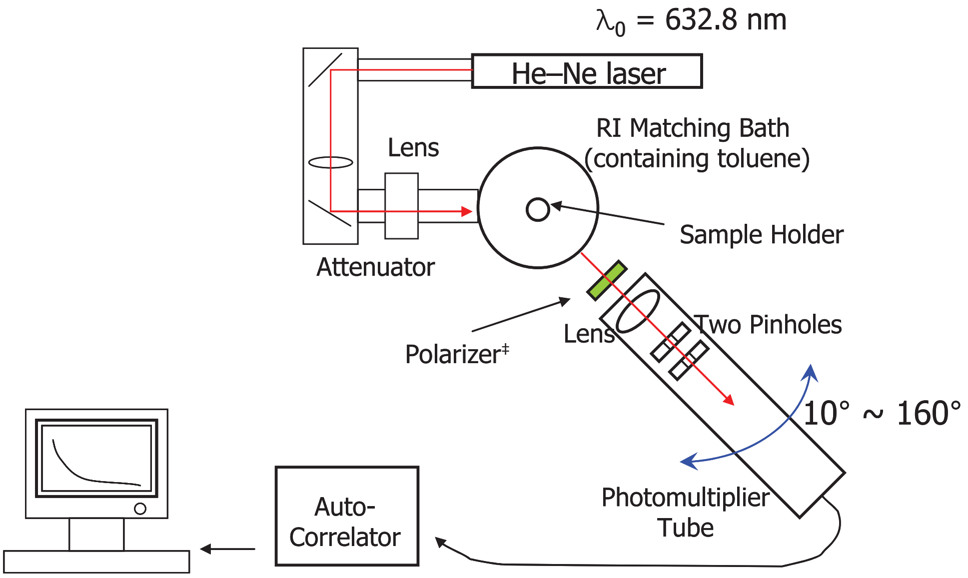

Figure 4.5 Schematic depiction of the ALV/CGS-3 goniometer system. ‡ denotes a Glan-Thomson prism as a polarizer. The PMT moves from 10° to 160°.

The surface of each sample cell was carefully cleaned with pure toluene (CHROMASOLV®, for HPLC, 99.9 %, Sigma-Aldrich) filtered twice with 0.2 μm pore size PTFE membrane filters (disposable syringe units, ADVANTEC MFS, Inc.). Then, the sample was placed in a refractive index (RI) matching bath via the sample holder. Toluene was used as the RI matching solvent and the temperature of the sample was controlled with a water circulator connected to a RI matching bath. All measurements were performed at 298 K. A Glan-Thomson prism was introduced in front of the photomultiplier tube (PMT) for the polarized and depolarized dynamic light scattering. Specific characteristics of the polarization modes are summarized in Table 4.3. Specific data fitting methods were described in Section 3.2.1.2 and 3.2.3.2.

Table 4.3 Polarization modes in light scattering

Incident beam‡	Polarizer in front of PMT	Polarization mode (light scattering name)
Vertical	Horizontal	Hv mode (depolarized DLS)
Vertical	Vertical	Vv mode (polarized DLS)
Vertical	None	DLS

‡ Incident laser beam is originally vertically polarized.

CHAPTER 5

Light Scattering Studies of Rod-like Cellulose Nanocrystals

5.1 Abstract

Cellulose nanocrystals have been studied for their interesting physicochemical properties. Recently, cellulose nanocrystals have been studied as a model probe for characterizing diffusion in complicated polymer solutions. In the present study, two cellulose nanocrystal samples (DOE-2-12A and DOE-2-12B) prepared from black spruce pulp by hydrolysis with sulfuric acid were probed with x-ray photoelectron spectroscopy (XPS) and depolarized and polarized dynamic light scattering. Intensity autocorrelation functions from polarized dynamic light scattering experiments at six scattering angles showed a slight angular dependence for both samples, which is consistent with the relatively large sizes of the cellulose nanocrystals seen in AFM images (Figure 4.1). XPS spectra provided an atomic concentration ratio of carbon and oxygen of 1.27 ± 0.18 and showed sulfate groups on the surface of DOE-2-12B. Also, decay rates from polarized dynamic light scattering experiments showed some angular dependence in both samples. However, the angular dependence was small with DOE-2-12B exhibiting a smaller dependence than DOE-2-12A. Lengths and diameters of cellulose nanocrystals were obtained by Broersma's formula. Lengths and diameters of DOE-2-12A and DOE-2-12B were 229 ± 19 and 19 ± 7 nm and 240 ± 18 and 22 ± 6 nm, respectively. The resultant lengths and diameters of the nanocrystals are comparable to cellulose whiskers obtained from cotton.

5.2 Introduction

It is well known that cellulose molecules are arranged as microfibrils containing crystalline and amorphous regions whose crystallinity depends on their source.[262-265] Physical and chemical properties are significantly affected by microfibril crystallinity and two different crystal structures were reported by Meyer *et al.*[266] and Gardner *et al.*[267] Further studies showed cellulose exists in basically four different polymorphs, I, II, III and IV and conversion between each group was shown in Figure 2.2. All microfibrils show irregular surfaces with disorderd cellulose chains in amorphous regions. Consequently, hydronium ions can penetrate the low density region and promote hydrolytic cleavage of glucosidic bonds. The acid hydrolysis of cellulose fibers provides crystalline, rod-like particles.

Rånby *et al.*[268,269] first reported a stable suspension of cellulose nanocrystals from hydrolyzed wood and cotton by sulfuric acid with an aspect ratio between five to ten. Cellulose nanocrystals also can be prepared from various sources like cotton, tunicate cellulose, hard wood, soft wood, etc.[270-273] The surfaces of cellulose nanocrystals obtained via hydrolytic cleavage with sulfuric acid have sulfate groups as well as hydroxyl groups, which provides electrostatic stabilization of the colloidal particle that prevents precipitation and flocculation in water. Surface charge density depends on the hydrolytic conditions including the acidic species, acid concentration, reaction time, and temperature. For example, cellulose nanocrystals prepared by hydrochloric acid (HCl) mediated hydrolysis formed less stable suspensions because of low surface charge density.[274] The existence of charge on the surfaces of the nanocrystals make them polyelectrolytes. Phase separation with changes in ionic strength and even the formation of gel-like layers were observed.[275] Also, Marchessault *et al.*[276-278] observed strong birefringence in a cellulose nanocrystal suspension and ordered phases that were like typical cholesteric liquid crystals. It is also possible to modify the surfaces of cellulose nanocrystals to alter their chemical and physical properties. Recent studies have grafted polymers like poly(ethylene glycol) onto the cellulose nanocrystal and partial silylation has also been carried out with alkyldimethylchorosilanes.[279,280] Dong *et al.*[259] also showed surface modification of cellulose nanocrystals with fluorescein-5′-isothiocyanate for bioimaging applications. These interesting characteristics of cellulose nanocrystals have been studied extensively for other applications.[281-289]

Various studies have revealed the shape of cellulose nanocrystals from acid hydrolysis in microscopic scale. Its rectangular shape and precise dimensions were probed by Sassi *et al.*[283] and Van Daele *et al.*[284] via transmission electron microscopy (TEM). Also, scattering methods were used to characterize cellulose nanocrystals quantitatively.[285-287] All studies have shown that cellulose nanocrystals that formed stable suspensions are rigid rod-like crystals with aspect ratios greater than five. These characteristics imply that the cellulose nanocrystals are good candidates as an optically anisotropic probe in binary or ternary systems.

Probe diffusion has been developed in polymer physical chemistry to characterize polymer solutions. Dynamics related to the rheology and solvent properties of the system can be probed in complicated systems.[205,206,209,210] Chu *et al.*[204] published an extensive study on probe diffusion for various polymers in a quaternary system and showed translational motion of the probe and cooperative motion between the probe and matrix. Russo and coworkers[213,214] adapted a probe diffusion technique to discuss experimental uncertainty in studying the effect of interactions between polymers on micro- and macroviscosity in a complicated ternary polymer solution. Since the 1990s, various optically or geometrically anisotropic probes of Tobacco Mosaic Virus (TMV), polytetrafluoroethylene, and commercial superparamagnetic paticles have been used to study physicochemical properties of complicated polymer systems in solution.[235,241,288,289]

Geometrically anisotropic probes allow the properties of multi-component polymer solutions to be characterized by depolarized dynamic light scattering (DDLS). However, it is probably fair to say that probes showing appropriate optical and mechanical properties as model systems are limited. Recently, de Souza Lima and coworkers[286,290] reported extensive studies with cellulose nanocrystals and showed the possibility of using cellulose nanocrystals as a model system for probe diffusion with DDLS. In the present study, cellulose nanocrystals from black spruce pulp, obtained via hydrolysis with sulfuric acid, were characterized with x-ray photoelectron spectroscopy (XPS) and depolarized and polarized dynamic light scattering.

5.3 Experimental

5.3.1 X-ray Photoelectron Spectroscopy (XPS)

XPS survey spectra were obtained from the sample used to obtain the AFM images in the previous chapter (Figure 4.1). All measurements were performed for 110 seconds and constant analyzer energy (CAE) mode with pass energy of 50.0 eV was utilized. Specific details are given in Section 4.3.3. The sample was measured several times and reproducibility was examined.

5.3.2 Light Scattering

DOE-2-12A and DOE-2-12B stock solutions were used to prepare binary systems. Procedures for the preparation of the samples were described in Section 4.2.2.1. Hv and Vv modes denote depolarized and polarized dynamic light scattering, respectively (Table 4.3). All light scattering measurements were performed for 300 seconds for each sample at six scattering angles: 30, 45, 60, 75, 90, and 105°. Specific measurement procedures were described in Section 4.3.1. Each sample was measured at least three times.

5.4 Results and Discussion

5.4.1 XPS Study of Cellulose Nanocrystals

Figure 5.1 shows a X-ray photoelectron spectroscopy survey spectrum of cellulose nanocrystals. Specific peaks at 287 and 533 eV are the C 1s and O 1s peaks from cellulose nanocrystals with sulfate groups, respectively.[291] The small peak at 169 eV is the S 2p peak from sulfate groups on the cellulose nanocrystals.[291] The small peak of S 2p is not easily observed. Hence, the inset in Figure 5.1 shows a high resolution S 2p XPS spectrum. Atomic concentrations obtained from the integrated areas under the peaks of the high resolution XPS spectra are summarized in Table 5.1. The C/O ratio is 1.27 ± 0.18 which is comparable to the theoretical value of 1.2. Also, the atomic concentration of sulfur is higher than that of cellulose nanocrystals reported by Jiang *et al*.[291]

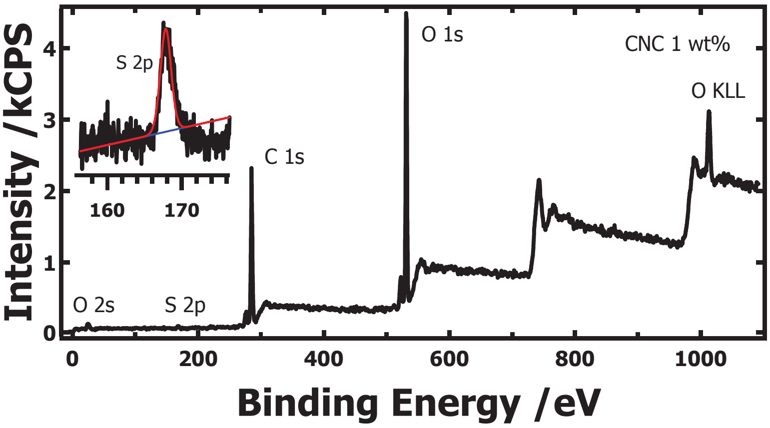

Figure 5.1 An XPS survey spectrum of cellulose nanocrystals. The inset is high resolution S 2p spectrum of cellulose nanocrystals. Cellulose nanocrystals (1 wt % solution) were spin coated onto a silicon wafer cleaned with ozone.

Table 5.1 Atomic concentrations of C, O, and S of cellulose nanocrystals

Atomic concentration /%		
C	O	S
51.4 ± 7.1	40.5 ± 0.5	1.1 ± 0.3

5.4.2 Polarized and Depolarized Dynamic Light Scattering Studies of Cellulose Nanocrystals

Two cellulose nanocrystal solutions from DOE-2-12A and DOE-2-12B were measured with polarized (Vv mode) and depolarized (Hv mode) dynamic light scattering techniques. In both modes, the autocorrelator provided intensity autocorrelation functions:

$$G^{(2)}(t) = B\left(1 + f\left|g^{(1)}(t)\right|^2\right) \tag{5.1}$$

where $g^{(1)}(t)$, B, f, and t are the electric field autocorrelation function, base line, instrumental parameter, and lag time, respectively. Experimentally obtained intensity autocorrelation functions were of the form:

$$g^{(2)}(t) = 1 + f\left|g^{(1)}(t)\right|^2 \tag{5.2}$$

where the base line (B) is already manipulated in regularization. Resultant correlation functions are shown in Figure 5.2 and 5.3. The y-axes and x-axes are $g^{(2)}(t)$ - 1 and lag time (t) from Eqn. 5.1, respectively. All correlation functions shift to faster lag time as scattering angle increases because of a smaller detection volume.

All autocorrelation functions show reasonable single exponential decay patterns, which means all systems have relatively narrow size distributions. In polarized and depolarized dynamic light scattering experiments, optically isotropic probes are not the objective of the discussion. However, the resultant intensity autocorrelation function has a contribution from all scatterers providing translational and rotational diffusion coefficients.[292] For small k:

$$k = qL \tag{5.3}$$

where q and L are a scattering vector and length of scatterer, respectively, translational diffusion dominates the intensity autocorrelation function. Otherwise, as k increases, contributions from rotational diffusion increase.[253] Similar discussions of scattering with respect to k were provided in Chapter 3. Scattering intensities do not show an angular dependence when scatterers are small enough (small k). Figure 5.4 shows intensity autocorrelation functions as a function of q^2t for DOE-2-12A and DOE-2-12B in Vv mode. Autocorrelation functions in Figure 5.4 do not superimpose, but are also narrowly scattered. Figure 4.1 (Chapter 4) shows cellulose nanocrystals have lengths of about 200 nanometers, a size relatively larger than the size needed for the Rayleigh-Gans-Debye (RGD) approximation. Hence, angular dependence cannot be fully ignored and multiple measurements at several different scattering angles should help minimize errors arising from the angular dependence. The systems also have large k and contributions from rotational diffusion should be significant.

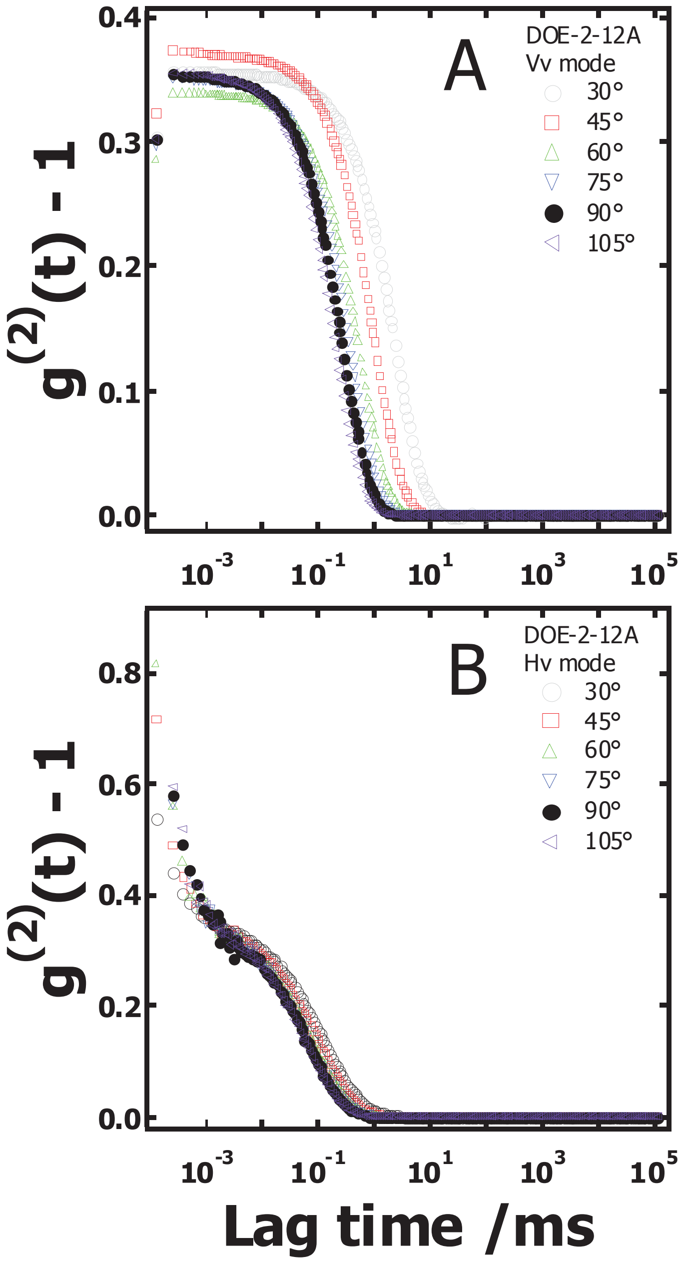

Figure 5.2 Autoorrelation functions of cellulose nanocrystals (DOE-2-12A) measured at six scattering angles and a temperature of 298 K: (A) Vv mode and (B) Hv mode.

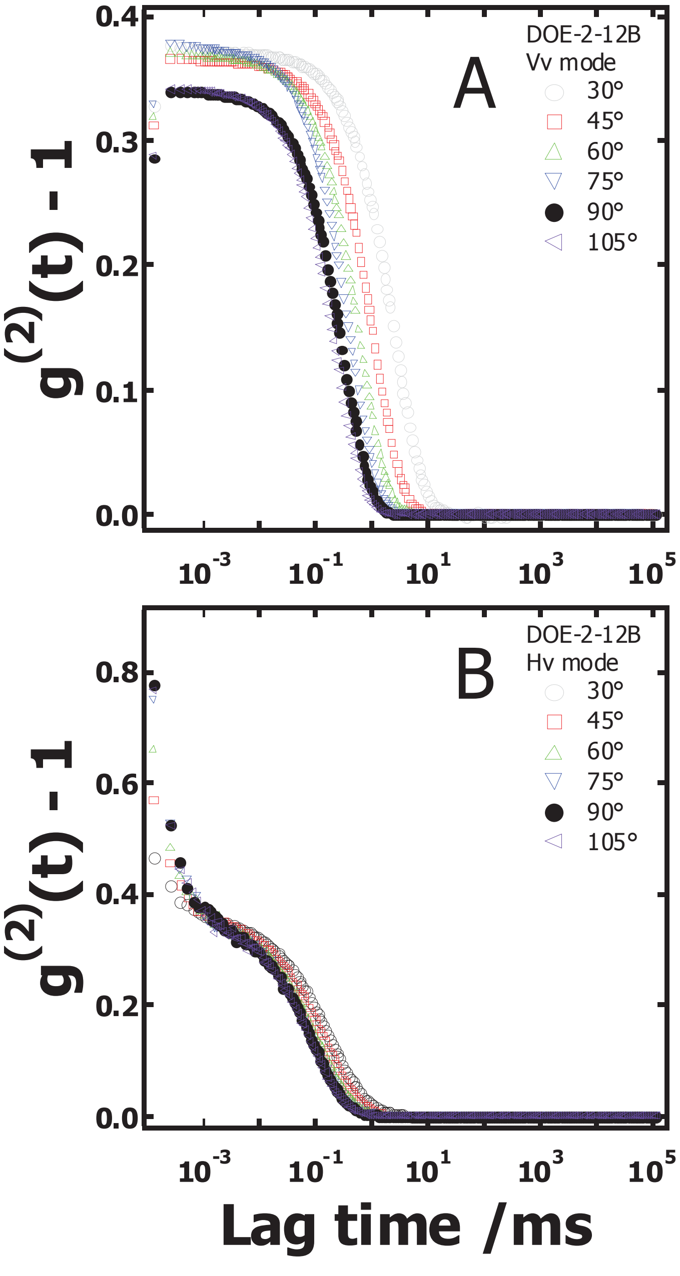

Figure 5.3 Autocorrelation functions of cellulose nanocrystals (DOE-2-12B) measured at six scattering angles and a temperature of 298 K: (A) Vv mode and (B) Hv mode.

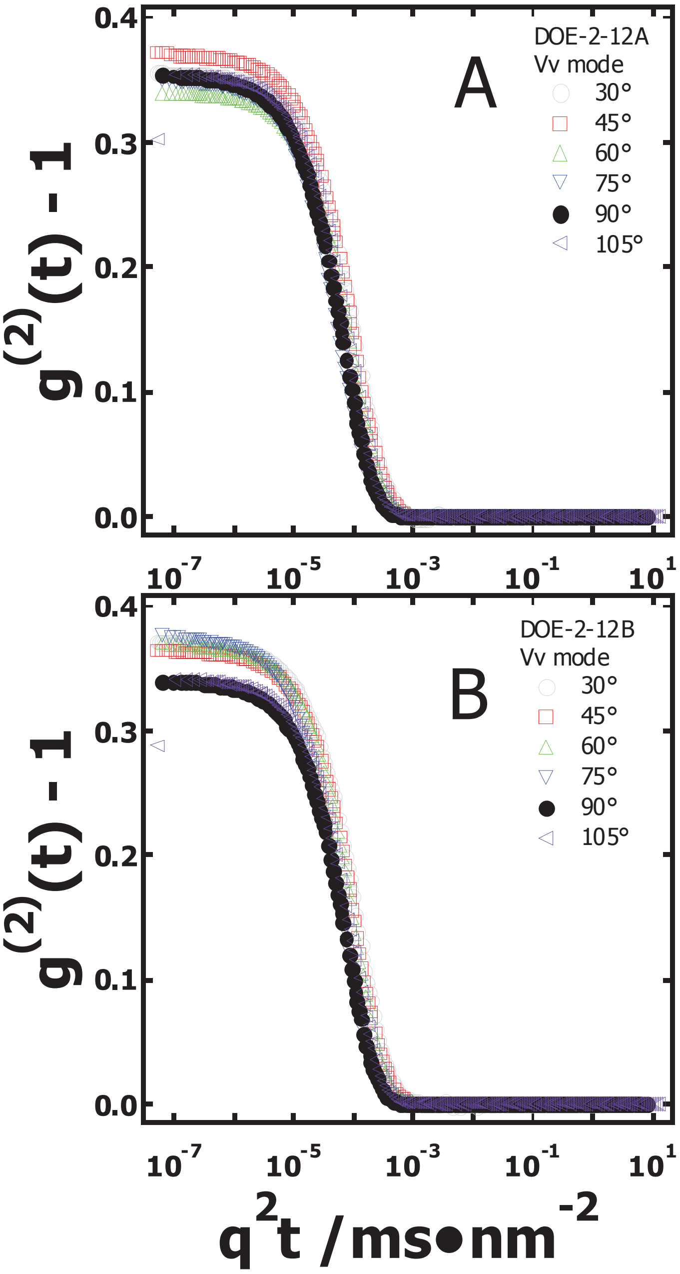

Figure 5.4 Intensity autocorrelation functions versus q^2t for (A) DOE-2-12A and (B) DOE-2-12B measured at six scattering angles and a temperature of 298 K.

For the case of single exponential decay, the relationship between an intensity autocorrelation function, $G^{(2)}(t)$, and an electric field autocorrelation function, $g^{(1)}(t)$, is:[293]

$$G^{(2)}(t) = B\big(1 + f\exp(-2\Gamma t)\big) = B\left(1 + f\left|g^{(1)}(t)\right|^{2}\right) \tag{5.4}$$

where Γ is the decay rate and the electric field autocorrelation function is:

$$g^{(1)}(t) = e^{-\Gamma t} \tag{5.5}$$

Decay rates in Vv and Hv modes relate to translational and rotational diffusion coefficients:

$$\Gamma_{Vv} = D_t q^2 \tag{5.6}$$

$$\Gamma_{Hv} = D_t q^2 + 6D_r \tag{5.7}$$

where subscripts Vv and Hv denote the Vv mode and Hv mode, respectively.

Figure 5.5 shows linear fits of $\ln g^{(1)}(t)$ versus lag time (t) to obtain the decay rates (Γ) for different scattering angles. Linear fits in Figure 5.5 (A) and (C) are consistent with Eqn. 5.5. The relatively larger scatter of the data points in Figure 5.5 (B) and (D) reflect the low scattering intensity. However, linear fitting still afforded reasonable decay rates.

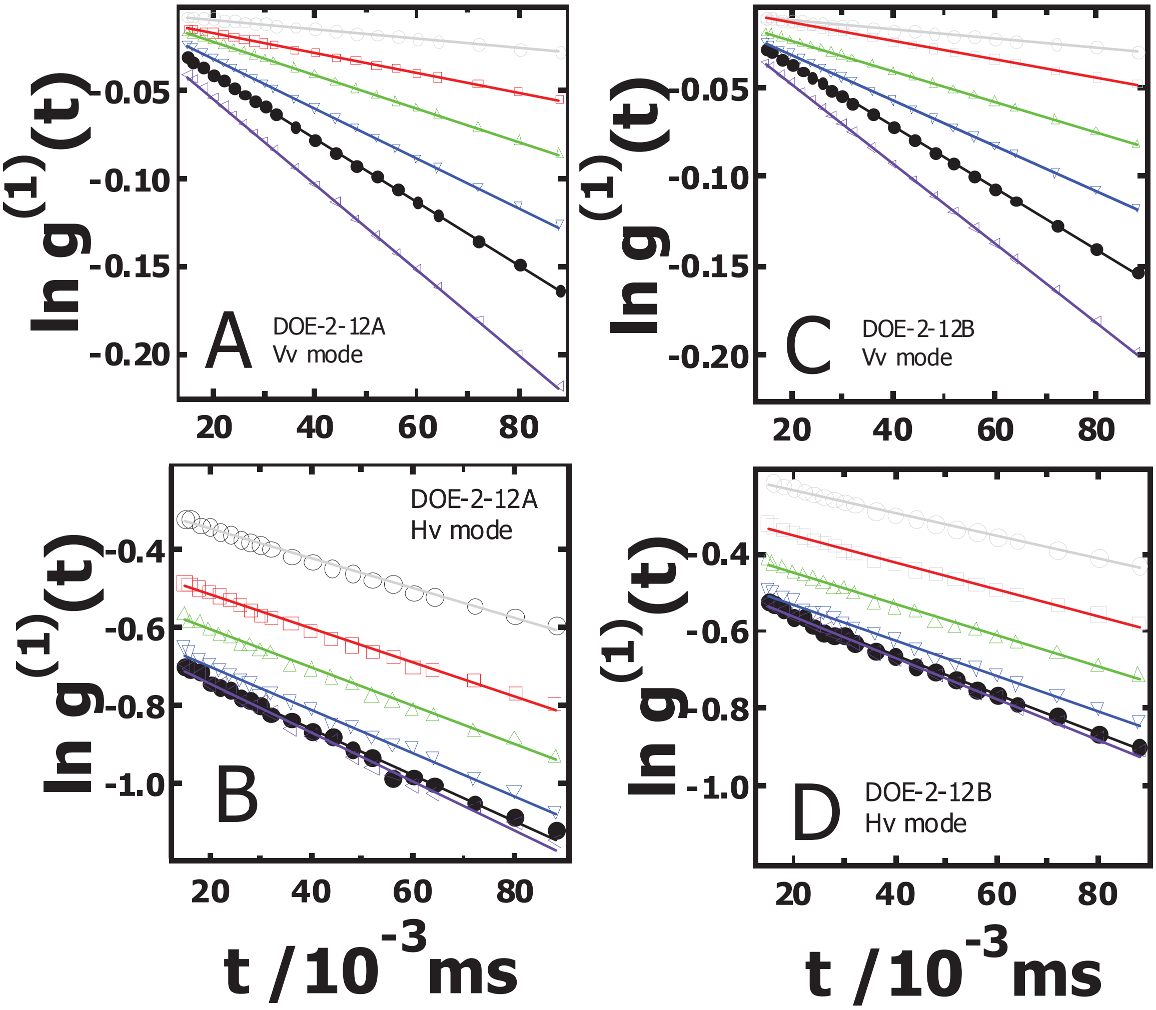

Figure 5.5 ln $g^{(1)}(t)$ versus lag time (t) diagrams for DOE-2-12A and DOE-2-12B samples: (A) DOE-2-12A in Vv mode, (B) DOE-2-12A in Hv mode, (C) DOE-2-12B in Vv mode, and (D) DOE-2-12B in Hv mode. All symbols and colors denoting scattering angles are identical to those in Figure 5.1 and 5.2. Solid lines represent linear fits according to Eqn. 5.5.

Thus multiple measurements were done for each scattering angle and reproducibility was examined. Resultant diffusion coefficients from decay rates along with standard deviations are summarized in Table 5.2. Decay rates in each mode for DOE-2-12A and DOE-2-12B increase with scattering angle.

Table 5.2 Decay rates of DOE-2-12A and DOE-2-12B

Scattering angle	Γ (DOE-2-12A) /s^{-1}		Γ (DOE-2-12B) /s^{-1}	
	Vv mode	Hv mode	Vv mode	Hv mode
30º	260.0 ± 0.1	4271 ± 3	234.7 ± 0.1	3214 ± 2
45º	519.6 ± 0.1	4239 ± 4	468.1 ± 0.1	3372 ± 3
60º	878.3 ± 0.1	4778 ± 4	793.9 ± 0.1	4095 ± 3
75º	1304.0 ± 0.2	5436 ± 5	1175.0 ± 0.1	4462 ± 4
90º	1679.0 ± 0.2	5799 ± 5	1591.0 ± 0.2	4869 ± 3
105º	2255.0 ± 0.3	6178 ± 6	2056.0 ± 0.2	5148 ± 3

Angular dependent decay rates seen in Table 5.2 were further examined through plots of Γ/q^2 versus q^2 in Figure 5.6.[293,294] Linear fits exhibited negative slopes with values close to zero. Decay rates show small but neglectable change. These results indicate the size distribution of the crystals is narrow, which is consistent with observations in Figures 5.4 and 5.5. DOE-2-12A shows a slightly steeper slope than DOE-2-12B, which means DOE-2-12A is relatively more polydisperse in size than DOE-2-12B.

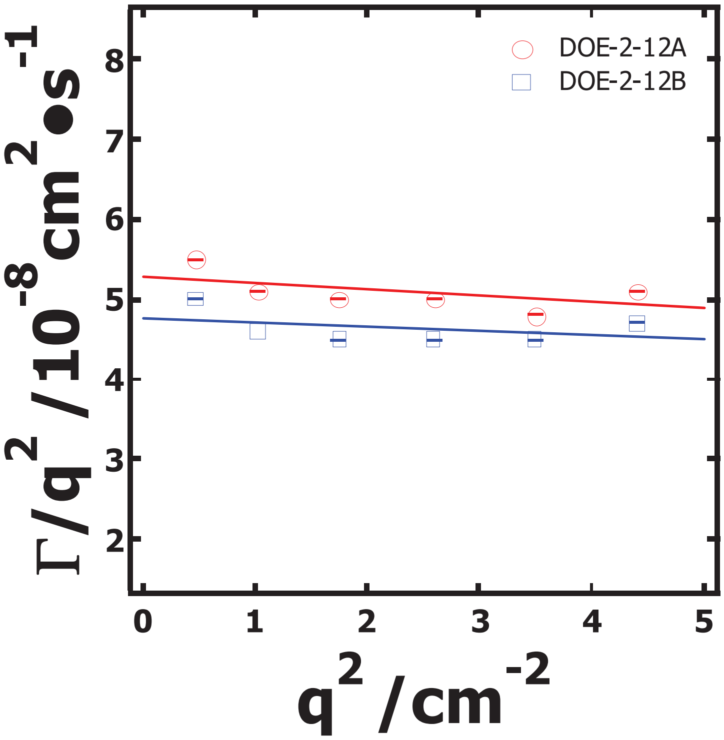

Figure 5.6 Γ/q^2 versus q^2 graph of DOE-2-12A and DOE-2-12B: Open symbols denote decay rates from six scattering angles and solid lines denote linear fits. Error bars on each point are smaller than the size of the symbols.

Figure 5.7 shows plots of Γ versus q^2 used to obtain translational and rotational diffusion coefficients from Eqn. 5.6 or 5.7. Slopes from the linear fits of the Hv and Vv data provide translational diffusion coefficients. Intercepts from linear fitting of the Hv data provide rotational diffusion coefficients. The translational diffusion coefficients obtained from the Hv and Vv mode should have the same values. The DOE-2-12B sample shows better agreement between the translational diffusion coefficients obtained from the Hv and Vv modes and smaller standard deviations.

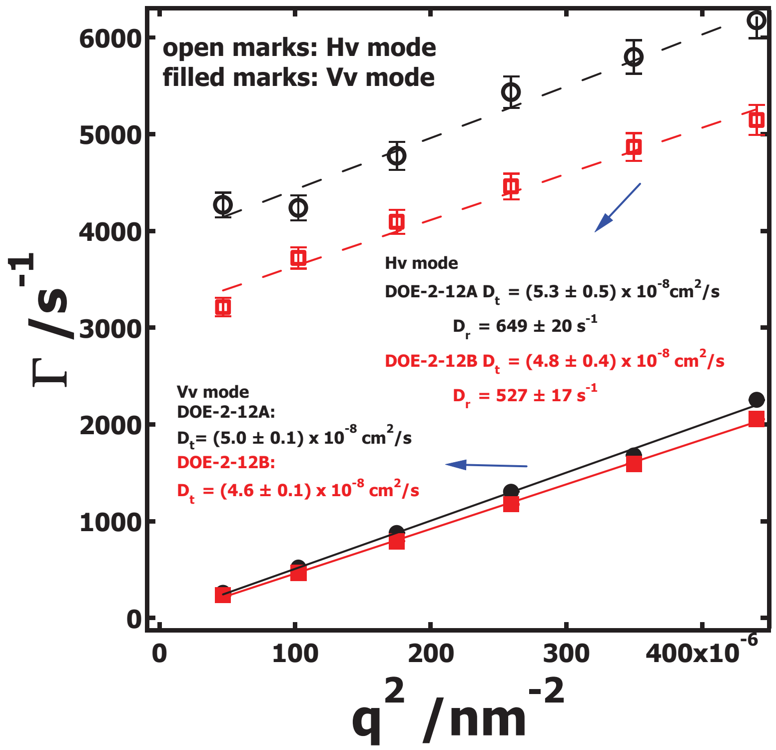

Figure 5.7 Γ versus q^2: Open symbols denote decay rates from depolarized light scattering (Hv mode) and filled marks denote decay rates from polarized light scattering (Vv mode). Dashed and solid lines are linear fits corresponding to data from the Hv and Vv mode, respectively. Each slope provides a translational diffusion coefficient and each intercept of the Hv mode fits provide a rotational diffusion coefficient.

Broersma's equations were used to obtain translational and rotational diffusion coefficients:[87,246-248]

$$D_t = \frac{k_b T}{3\pi\eta L}\left[\delta - \frac{1}{2}\left(\gamma_a + \gamma_b\right)\right] \tag{5.8}$$

$$D_r = \frac{3k_b T}{\pi\eta L^3}\left(\delta - \xi\right) \tag{5.9}$$

where k_b, T, and, η are the Boltzmann's constant, temperature, and viscosity of solvent, respectively. δ, ξ, γ_a, and γ_b are defined:

$$\delta = \ln\left(\frac{2L}{d}\right) \tag{5.10}$$

$$\gamma_a = 0.807 + \frac{0.15}{\delta} + \frac{13.5}{\delta^2} - \frac{37}{\delta^3} + \frac{22}{\delta^4} \tag{5.11}$$

$$\gamma_b = -0.193 + \frac{0.15}{\delta} + \frac{8.1}{\delta^2} - \frac{18}{\delta^3} + \frac{9}{\delta^4} \tag{5.12}$$

$$\xi = 1.14 + \frac{0.2}{\delta} + \frac{16}{\delta^2} - \frac{63}{\delta^3} + \frac{62}{\delta^4} \tag{5.13}$$

where L and d are the rod length and diameter, respectively. Resultant lengths and diameters of cellulose nanocrystals are summarized in Table 5.3.

Table 5.3 Lengths and diameters of cellulose nanocrystals

	Length, L nm	Diameter, d nm
DOE-2-12A	229 ± 19	19 ± 7
DOE-2-12B	240 ± 18	22 ± 6

Table 5.4 shows dimensions of cellulose nanocrystals from various cellulose sources.[258, 286,295] The length and diameter of the cellulose nanocrystals from black spruce pulp are comparable to those of cellulose whiskers from cotton obtained from light scattering studies.[286]

Table 5.4 Lengths and diameters of cellulose nanocrystals from various cellulose sources

Source	Length /nm	Diameter /nm
tunicate[‡,a]	100 ~ several μm	5 ~ 10
bacterial[b]	100 ~ several μm	10 ~ 30
cotton[c]	200 ~ 350	5 ~ 20
wood[d]	100 ~ 300	5 ~ 10

[‡] A marine animal from the Mediterranean sea. [a] Reference 295 (estimated by small angle neutron scattering). [b] Reference 258 (estimated by TEM). [c] Reference 286 (estimated by DDLS). [d] Reference 295 (estimated by AFM).

5.4.3 Discussion

Lengths and diameters of cellulose nanocrystals and their size polydispersity depend on the preparation method as well as the origin of the cellulose fiber. Two cellulose nanocrsytal samples (DOE-2-12A and DOE-2-12B) are replicate preparations from the same source. The translational diffusion coefficient (D_t) and rotational diffusion coefficient (D_r) shown in Figure 5.7 (Hv mode) both influence the length and diameter when solving Eqns. 5.8 ~ 5.13. D_t of DOE-2-12B is 10 % smaller than that of DOE-2-12A and D_r of DOE-2-12B is 23 % smaller than that of DOE-2-12A. The length and diameter of DOE-2-12B are larger than those of DOE-2-12A because DOE-2-12B moves slower than DOE-2-12A. The difference between rotational diffusion coefficients is about 10 % larger than the difference between translational diffusion coefficients. Rotational motion of rodlike particle in a solution is more sensitively influenced than translational motion by particle length changes or by concentration and interaction between particles. Temporary concentration fluctuation and interaction between particles can influence the friction between a particle undergoing Brownian motion and the solution. The friction coefficient is inversely proportional to diffusion coefficient. The rotational diffusion coefficient depends on $1/R^3$ and translational diffusion coefficient depends on 1/R where R is the Stokes radius corresponding to length of the rod.[296] The lengths of DOE-2-12A and DOE-2-12B are different. The stronger dependence of the rotational diffusion coefficient on R leads to deviations between the rotational diffusion coefficients than the translational diffusion coefficients. Furthermore, D_t and D_r are obtained from slopes and intercepts in Figure 5.7. The scattered data in Figure 5.7 means that propogation of errors in the slope and intercepts does not lead to statistically different values of the diameters and radii in Table 5.3. However, as seen in Table 5.3, DOE-2-12A and DOE-2-12B have the same length and diameter within experimental error. The deviation in the mean values is not uniform. There is an 18 % difference for the diameters and a 4 % difference in the means. Nonetheless, these differences are not significant and reflect the relatively poor linear fits of data from depolarization dynamic light scattering shown in Figure 5.5 (B) and (D) and Figure 5.7. Low scattering intensity, interaction among particles, and unexpected scattering from dust are the main contributors to the scattered data shown in Figure 5.5 (B) and (D).

Figures 5.4 and 5.6 show that the angular dependence of the correlation function and decay rate cannot be fully ignored because of the relatively large size of cellulose nanocrystals. The larger slope in the linear fit of Γ/q^2 versus q^2 for DOE-2-12A means that DOD-2-12A is more polydisperse than DOE-2-12B. Also, Figure 5.7 shows good agreement between the two translational diffusion coefficients from Hv and Vv modes for DOE-2-12B, which means that the linear fits are reasonable. Thus, DOE-2-12B is better candidate as probe particle in polymer/probe/solvent ternary system.

AFM images in Figure 4.1 show rod-like shapes of cellulose nanocrystals. However, the dimensions of the cellulose nanocrystals in Figure 4.1 are smaller than those obtained by depolarized dynamic light scattering. Lengths and diameters from depolarized dynamic light scattering are hydrodynamic properties having water layers around the particles in solution and AFM images are obtained from interaction between the tip and the dried surface. Thus, AFM images have smaller dimensions. Cellulose nanocrystals have sulfate groups on their surface from esterification of hydroxyl groups during hydrolysis with sulfuric acid.[297] The XPS survey spectrum in Figure 5.1 shows the peak corresponding to sulfur from sulfate groups and has a surface charge density of 339 mmol·kg^{-1} obtained from conductometric titration. [298] The number of sulfate groups on a cellulose nanocrystal could be estimated from the density of crystalline cellulose (1.6 g·cm^{-3}) and dimensions of cellulose nanocrystals from AFM.[291] Approximately 5000 sulfate groups are introduced per nanocrystal during hydrolysis which means approximately 0.2 sulfate groups exist per AGU on the surface of the cellulose nanocrystals.

5.5 Conclusions

In this study, two cellulose nanocrystal solutions (DOE-2-12A and DOE-2-12B) from black spruce pulp were probed with XPS and polarized and depolarized dynamic light scattering. The two samples come from two identical preparations using sulfuric acid and the same pulp sample. The XPS survey spectrum shows sulfate groups on the surface of DOE-2-12B. All samples show a slight angular dependence of the intensity autocorrelation functions from polarized dynamic light scattering experiments because of the large size of the cellulose nanocrystals. However, Γ/q^2 versus q^2 diagrams showed that the angular dependence was small with DOE-2-12B showing a weaker angular dependence. Decay rates from six scattering angles provide translational and rotational diffusion coefficients. DOE-2-12B showed good agreement between the translational diffusion coefficients obtained from Hv and Vv mode, $(4.8 \pm 0.4) \times 10^{-8}$ and $(4.61 \pm 0.07) \times 10^{-8}$ cm^2/s, respectively. Lengths and diameters of DOE-2-12A and DOE-2-12B deduced from Broersma's formula are 229 ± 19 and 19 ± 7 nm and 240 ± 18 and 22 ± 6 nm, respectively. These results show small differences in scattering did not lead to statistically different sizes deduced from light scattering. The resultant length and diameter of the nanocrystals are comparable to those from cellulose whiskers prepared from cotton reported by De Souza Lima *et al.*[286] and cellulose nanocrystals from other woods.[295,296] XPS survey spectrum and surface charge density show a substantial number of sulfate groups exist that are readily dispersed in stable water suspensions on cellulose nanocrystals. This study demonstrates that DOE-2-12Bs have rigid rod-like structures and dispersive and stable. They can serve as anisotropic optical probes for the characterization of complicated polymer solutions. Also, the hydroxyl and sulfate groups on the surface of DOE-2-12B could be modified to modify the stability and dynamics of the particles in complicated solution systems.

CHAPTER 6

Light Scattering Studies of Interactions Between Pullulan Cinnamates and Rod-like Cellulose Nanocrystals

6.1 Abstract

Interactions between polysaccharides have attracted great interest as a key to improving wood-fiber thermoplastic composites. This study probes interactions between hydrophobically modified pullulan and rod-like cellulose nanoparticles as a potential model system for the modification of wood fibers. Little systematic research has been reported about interactions between polysaccharides and polysaccharide particles in dilute solution. Also, the diffusion of anisotropic probes in dilute polysaccharides is not fully explored. A combination of UV-Vis spectroscopy, zeta-potential measurement, and light scattering techniques reveal the adsorption of pullulan derivatives onto cellulose nanocrystals. In UV-Vis spectroscopy and light scattering, aggregates are readily observed when UV crosslinking reactions occur without cellulose nanocrystals and the system is relatively unaffected by the addition of cellulose nanocrystals after UV crosslinking. Otherwise, aggregates are not observed for long UV exposure time when both pullulan 4-chlorocinnamate (P4CC03) and cellulose nanocrystals (DOE-2-12B) exist in the ternary system. Large aggregates immediately precipitated when they were observed. Zeta-potential measurements also show P4CC03 adsorption onto cellulose nanocrystal. Adsorbed P4CC03 screens the surface hydroxyl and sulfate groups of the cellulose nanocrystals.

6.2 Introduction

Polysaccharides have attracted great interests as renewable and biodegradable materials. Also, polysaccharides are of interest as the biocompatible element in biocomposites.[299,300]

Understanding microscopic interactions between polysaccharides is fundamental to explaining their bulk properties and the design of new biocomposites. Various characterization techniques exist for probing interactions in polymer or polysaccharide systems.[301-303] Poncet *et al.*[304] showed the adsorption of hydrophobically modified polymers onto hydrophobic surfaces via ellipsometry. Kaya *et al.*[305] probed polysaccharide adsorption onto regenerated cellulose surfaces and other surfaces using surface plasmon resonance (SPR). Recently, Liu showed pullulan 4-chlorocinnamate adsorption onto cellulose surfaces using surface plasmon resonance and quartz crystal microbalance with dissipation monitoring (QCM-D).[260] These studies suggested that not only hydrogen bonding but also hydrophobic interactions can be a driving force for adsorption in polysaccharide systems.

However, interactions between polysaccharides and colloidal particles have not yet been fully described and few systematic studies had been published. The interaction between polymers and colloids has been studied by many communities. Colloid science is interested in the stability of the system. The ionic strength of the solution, charge on particles, and additives provide significantly complicated situations.[306,307] Polymers are additives in polymer/colloid systems. Added polymers can prevent aggregation or may make bridges that cause flocculation.[308,309] Either bonded or non-bonded polymers can stabilize or destabilize colloidal suspensions.[310-312] Many important advances of polymer science have been made through comparisons of macromolecular dynamics with theoretical predictions. In polymer/colloid systems, especially semi-dilute solutions or gels, colloidal particles have been extensively used as probes to reveal the structure of complex solutions.[198,313,314] Few studies of interactions between polysaccharides and colloidal particles have been reported.[315-318] Simon *et al.*[317] published the adsorption of amphiphilic polysaccharides onto polystyrene particles and Vieira *et* *al.*[318] showed the adsorption of chitosan onto polystyrene sulfonate (PSS) and poly(methyl methacrylate) (PMMA) particles. Many results showed electrostatic or hydrophobic interactions were the driving force for adsorption. Brown *et al.*[319] probed the interaction between polystyrene latex particles and modified celluloses like hydroxyethyl cellulose (HEC), hydroxypropyl cellulose (HPC), and carboxymethyl cellulose (CMC) and showed there is a significant degree of latex-polymer adsorption even in very dilute solutions. However, understanding polymer/colloidal particle interactions is still theoretically and experimentally complicated.

In this study, the ternary system of a pullulan derivative, cellulose nanoparticles, and water is probed with UV-Vis spectroscopy, zeta-potential measurements, and polarized and depolarized dynamic light scattering in very dilute solutions. Pullulan is hydrophobically modified with 4-chlorocinnamic acid (4CCA) and cellulose nanocrystals (DOE-2-12B) were hydrolyzed from black spruce pulp with sulfuric acid. The advantage of adding 4-chlorocinnamic groups to some of the anhydroglucose units (AGU) is that UV crosslinking is possible even in very dilute solutions. Two series of experiments (PreX and Rxn) of the P4CC03/DOE-2-12B/water ternary system were performed with different sample preparation procedures. The interaction between this partially hydrophobic pullulan derivative and the charged cellulose nanocrystals is discussed.

6.3 Experimental

6.3.1 Zeta-potential Measurements

All samples were prepared in 20 mL vials and sonicated 20 minutes before measurements. 0.4 mg P4CC03 was dissolved in water to prepare P4CC03/water and P4CC03/DOE-2-12B/water systems. The solution was transferred into 1 mL commercial zeta-potential cell for measurements. Measurements were done multiple times. The sample was scanned 100 times and results were averaged for each measurement.

6.3.2 Light Scattering

DOE-2-12B stock solution was used for the preparation of ternary systems. Procedures for the preparation of two ternary systems (PreX and Rxn) were described in Section 4.2.3. The DOE-2-12B/water binary system was prepared by direct dilution of DOE-2-12B stock solution. Cinnamate groups in the two systems undergo [2+2] cycloaddition with a broad range UV radiation source (Dynamics, Light Welder PC-2). Light scattering measurements in Hv and Vv mode were performed for 600 and 300 seconds (each sample), respectively. Each sample was measured at least three times and reproducibility was examined at six scattering angles: 30, 45, 60, 75, 90, and 105°. Specific light scattering measurement procedures and data analysis were described in Sections 4.3.1 and 3.1.

6.4 Results and Discussion

6.4.1 Autocorrelation Functions and Decay Time Distributions of P4CC03/Water, DOE-2-12B/Water, and P4CC03/DOE-2-12B/Water Systems

Figure 6.1 shows representative autocorrelation functions for a P4CC03/water binary system from polarized light scattering experiments (Vv mode). Autocorrelation functions were obtained from six different scattering angles (30, 45, 60, 75, 90, and 105º). Correlation functions show single exponential decay and the intensity autocorrelation function is defined as:

$$G^{(2)}(t) = B\left(1 + f\exp(-2\Gamma t)\right) = B\left(1 + f\left|g^{(1)}(t)\right|^{2}\right) \tag{6.1}$$

where Γ, $g^{(1)}(t)$, B, and f are the decay rate, electric field autocorrelation function, base line, and instrumental parameter, respectively.[293] Decay rates in Vv mode relate to translational diffusion coefficients:

$$\Gamma_{Vv} = D_t q^2 \tag{6.2}$$

where D_t and q^2 are the translational diffusion coefficient and squared scattering vector, respectively. The inset in Figure 6.1 shows a linear fit of the data. According to Eqn. 6.2 the slope gives $D_t = (20.6 \pm 0.4) \times 10^{-8}$ m^2s^{-1}. The intercept, 0.22 ± 0.11 ms^{-1}, is supposed to be zero, however, the experimental data deviates slightly from zero. Non-zero intercept can be an indication of aggregates and will be discussed later in connection with Figure 6.4. The hydrodynamic radius of P4CC03 is obtained from the Stokes-Einstein relationship:

$$R_h = \frac{k_b T}{6\pi\eta_0 D_t} \tag{6.3}$$

where k_b, T, and η_0 are Boltzmann's constant, and the temperature and the viscosity of the solvent, respectively. The obtained hydrodynamic radius was 11.9 ± 0.5 nm. Pullulan and various pullulan derivatives have been studied with light scattering.[124,320] Kato *et al.*[321] probed pullulan having various molar masses. Hydrodynamic radii depended on molar mass and varied from 9.5 to 46 nm. Akiyoshi *et al.*[322] prepared hydrophobically modified pullulan by introducing 1.6 cholesterol groups per 100 glucose units. Obtained hydrodynamic radii of the self-aggregates were ~ 13 nm with an aggregation number of 13. Pullulan is soluble in water, however, the hydrophobically modified pullulan synthesized by Akiyoshi *et al.*[322] was not. P4CC03 is soluble in water but it can aggregate in a P4CC03/water binary system because of hydrophobic interactions between 4-chlorocinamate groups. The molar mass of pullulan used for the preparation of P4CC03 is approximately 75 kDa. A theoretical hydrodynamic radius of ~ 12 nm was obtained from studies the scaling results for pullulan by Kato *et al.*[321] and the ρ parameter (Section 2.2.3) by Burchard *et al.*[114,115] Dynamic light scattering provided the hydrodynamic radius of P4CC03 as 11.9 ± 0.5 nm. The two value agrees well with the calculated value, which means P4CC03 mostly exists as single molecular coils in aqueous solution.

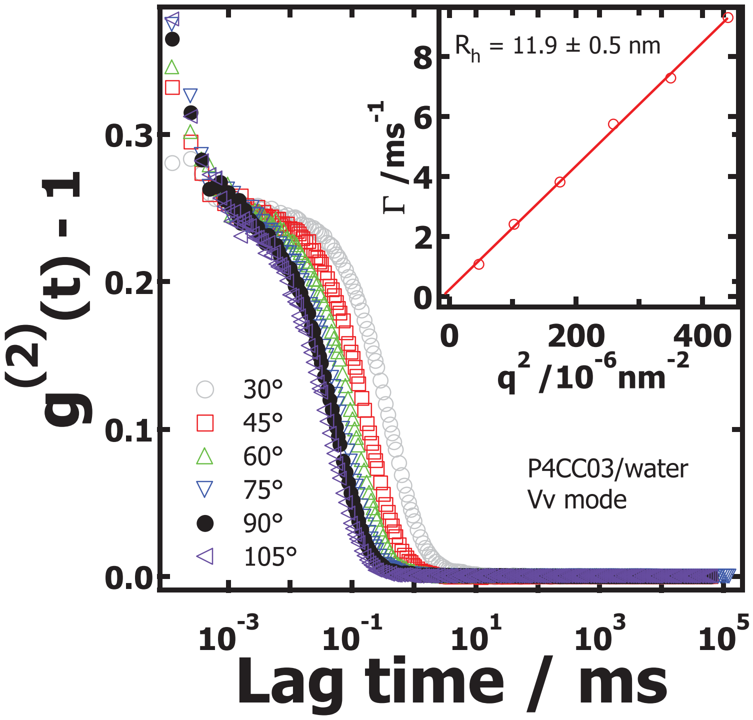

Figure 6.1 Autocorrelation functions of a P4CC03/water binary system from six scattering angles in Vv mode: concentration of P4CC03 in a sample is 0.4 mg·mL^{-1}. The inset shows a linear fit of Γ versus q^2. The slope and intercept are $(20.6 \pm 0.4) \times 10^{-8}$ m^{2}s^{-1} and 0.22 ± 0.11 ms^{-1}, respectively.

Figure 6.2 and 6.3 show autocorrelation functions of a DOE-2-12B/water binary system and P4CC03/DOE-2-12B/water ternary system, respectively. A 0.005 wt % cellulose nanocrystal (DOE-2-12B) solution was prepared and autocorrelation functions were measured in Vv mode. Autocorrelation functions in Figure 6.2 show single exponential decay and Eqn. 6.1 provides electric field autocorrelation functions relative to decay rates. The inset in Figure 6.2 depicts a linear fit of Γ as a function of q^2. The slope and intercept are $(4.61 \pm 0.07) \times 10^{-8}$ m^{2}s^{-1} and $(-0.02 \pm 0.18) \times 10^{-1}$ ms^{-1}, respectively. The Stokes-Einstein relationship provides a hydrodynamic radius of 53 ± 1 nm. Hydrodynamic radii of rod-like particles can be defined with length and diameter ($R_{h,L}$) or a rotational diffusion coefficient ($R_{h,r}$):[247-250]

$$R_{h,L} = \frac{L}{\left[2\delta - 0.19 - \frac{8.24}{\delta} + \frac{12}{\delta^2}\right]} \tag{6.4}$$

where L is the length of the particle and δ is defined as

$$\delta = \ln\left(\frac{2L}{d}\right) \tag{6.5}$$

where d is the diameter of the particle and

$$R_{h,r}^3 = \frac{k_b T}{12\pi\eta D_r} \tag{6.6}$$

where D_r is a rotational diffusion coefficient. Specific diffusion coefficients and size information for DOE-2-12B are provided in Chapter 5. Eqns. 6.4 and 6.6 provide hydrodynamic radii of 52 and 61 nm, respectively. $R_{h,r}/R_h$ is clearly larger than unity which means cellulose nanocrystals have an elongated shape.[250]

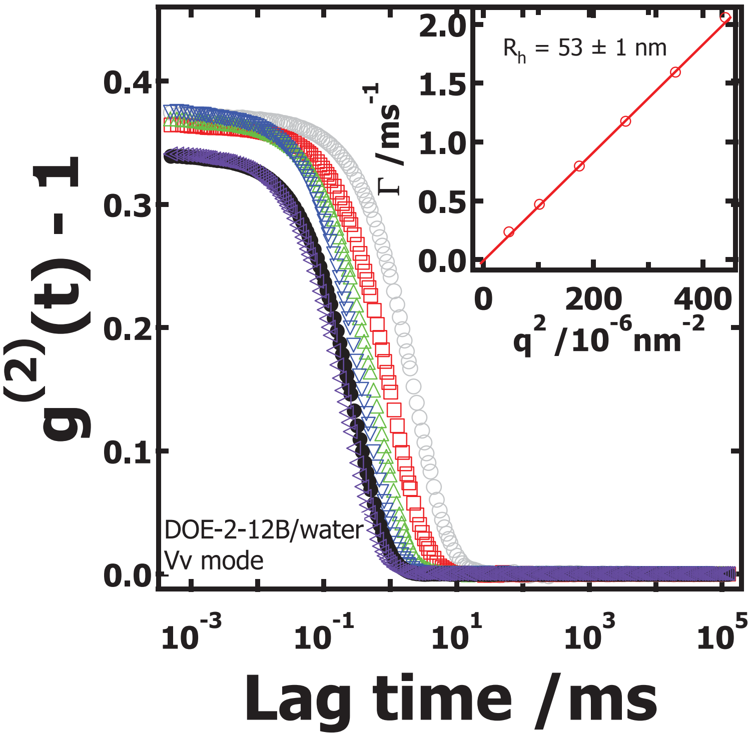

Figure 6.2 Intensity autocorrelation functions of a 0.005 wt % DOE-2-12B/water binary system from six scattering angles in Vv mode. The inset shows a linear fit of Γ versus q^2. The obtained slope and intercept are $(4.61 \pm 0.07) \times 10^{-8}$ m^2s^{-1} and $(-0.02 \pm 0.18) \times 10^{-1}$ ms^{-1}, respectively. All symbols and colors denoting scattering angles are identical to those in Figure 6.1.

Autocorrelation functions of a P4CC03/DOE-2-12B/water system shown in Figure 6.3 still show single exponential decay in Vv mode experiments. The estimated hydrodynamic radius is 57 ± 1 nm. However, the system is complicated because of the interactions between solvent molecules, cellulose nanocrystals, and polymers. Representative decay times (*t*) have a distribution and even show the superposition of diffusive and angle-independent components.[228] Thus, it is intractable to invoke the relationship previously mentioned:

$$g^{(1)}(t) = e^{-\Gamma t} \tag{6.7}$$

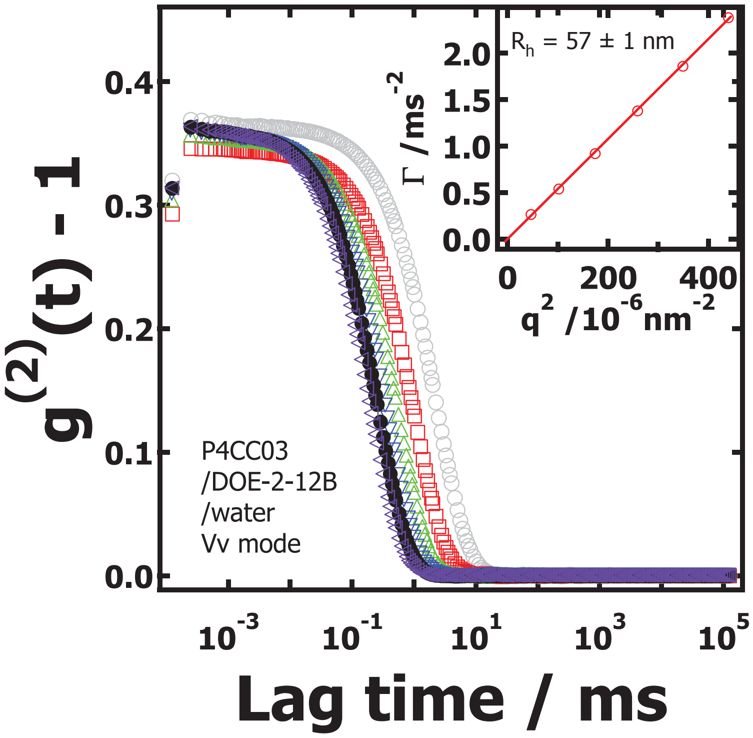

Figure 6.3 Intensity autocorrelation functions of a P4CC03/DOE-2-12B/water binary system from six scattering angles in Vv mode. The inset shows a linear fit of Γ versus q^2. The slope and intercept are $(5.38 \pm 0.06) \times 10^{-8}$ m^2s^{-1} and -0.01 ± 0.02 ms^{-1}, respectively. All symbols and colors denoting scattering angles are identical to those in Figure 6.1.

Modeling of the distribution of decay times from the experimental electric field autocorrelation function can be done with a constrained regularization technique like the CONTIN algorithm.[226-228] Figure 6.4 shows decay time distributions of the three systems in Figure 6.1, 6.2, and 6.3. Dotted red lines show decay time distributions of a DOE-2-12B/water binary system having a peak corresponding to a hydrodynamic radius around 65 nm that is comparable to that from linear fitting and the Stokes-Einstein eqn. Broken blue and solid black lines are decay time distributions of the P4CC03/water and P4CC03/DOE-2-12B/water ternary system, respectively. The fast mode in a P4CC03/water binary system shows good agreement with the size from the linear fit in Figure 6.1. The slow mode corresponds to aggregates of P4CC03. Result shows good agreement with the size of a pullulan chain in good solvent by Kato *et al*.[316] and Burchard *et al*.[114,115] However, aggregation is also inevitable for P4CC03 in water even at very low concentrations because of hydrophobic groups on the AGU. Slower diffusional modes from aggregation can appear in semidilute or dilute solution, even in good solvents.[228] Two modes are observed in the ternary system (solid black line). The slow mode peak is comparable in magnitude to the slow mode peak in the DOE-2-12B/water binary system. It seems that the two modes in the ternary system are shifted to slightly smaller R_h compared to the two modes in a DOE-2-12B/water system. However, the peaks do not show any significant shifts in position.

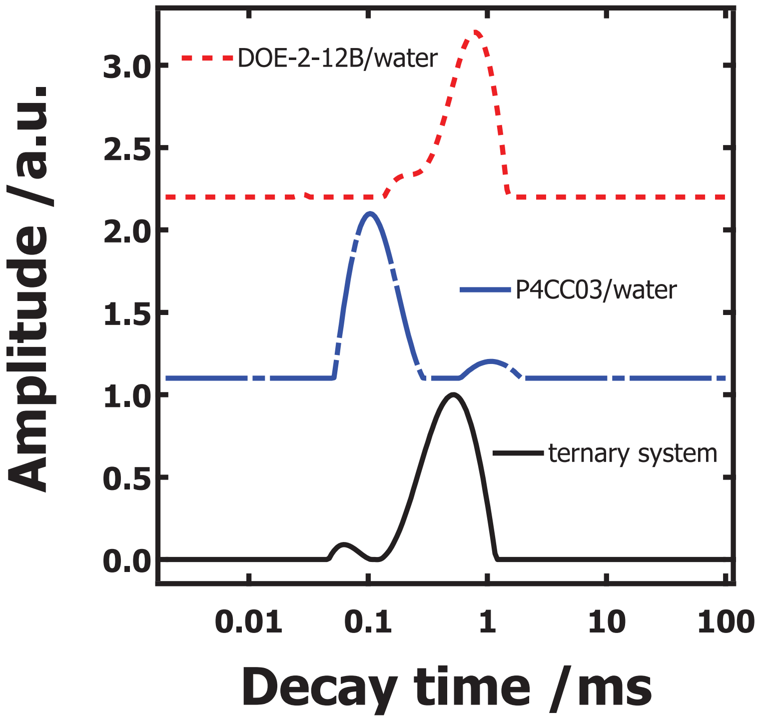

Figure 6.4 Decay time distributions of DOE-2-12B/water, P4CC03/water, and P4CC03/DOE-2-12B/water ternary systems. All distributions correspond to a scattering angle of 90°.

Bimodal or multimodal relaxations in ternary systems have been frequently reported. Shibayama *et al.*[232] observed two modes in a polymer/probe/water ternary system and showed the fast mode and slow mode correspond to a cooperative diffusion of polymer chains and translational diffusion of probes, respectively. Streletzky *et al.*[320] discussed multiple time scales in relaxational modes in ternary systems. In the present study, two modes in both the

P4CC03/water binary and P4CC03/DOE-2-12B/water ternary systems are located in similar positions. Bremmell *et al.*[210] reported that the fast mode reflects internal macromolecular fluctuations and the slow mode represents the translational diffusion of probes when the polymer and probe have similar sizes. These various discussions address systems having viscosity changes or concentrations in excess of the overlap concentration ($C > C^*$). P4CC03/water and P4CC03/DOE-2-12B/water systems have negligible viscosity differences, very low polymer concentrations, and phases with anisotropic structures. These different characteristics compared to ternary systems previously discussed make direct comparisons of simple distributions seen in Figure 6.4 difficult. Also, the low solubility of P4CC03 in water meant P4CC03 adsorption onto DOE-2-12B could not be probed over a wide range of polymer concentrations. For the present system, systematic changes in the particle size distribution (the decay time distributions) could be induced by photocrosslinking as the 4-chlorocinamate groups in the AGU of P4CC03 can be crosslinked by UV light. The influence of *in situ* UV crosslinking on the interactions between P4CC03 and DOE-2-12B was probed with UV-Vis spectroscopy and light scattering techniques and is discussed in the remainder of this chapter.

6.4.2 UV-Vis Spectroscopy Study of P4CC03/Water Binary and Rxn Systems

Figure 6.5 shows UV spectra from a P4CC03/water binary system and P4CC03/DOE-2-12B/water Rxn ternary system. Detailed preparation procedures for the two systems, Rxn and PreX, can be found in Section 4.2.3. Various studies have been reported about UV crosslinking of cinnamic acid for wavelengths from $260 < \lambda_{max} < 280$, where λ_{max} is the peak UV absorbance for the π-π^* transition.[323-326] All spectra in Figure 6.5 show intensive absorbance at a λ_{max} of 287 nm which is characteristic for UV-Vis spectra of materials having cinnamate groups.[327,328] The absorbance significantly decreases as UV exposure time increases in Figure 6.5 (A). Absorbance depends on the number of cinnamate groups in P4CC03. Cinnamate groups make crosslinks by UV-induced [2+2] cycloaddition reaction.[327,329] Pullulan is a very flexible polymer and much more flexible then cellulose.[330] Lee *et al*.[331] showed that the pullulan derivative which is partially substituted with hydrophobic cholesterols retains a flexible backbone. P4CC03 chains also have hydrophobic groups, however, cinnamates are smaller than cholesterol groups. Thus, P4CC03 has a spherical structure in solution. Figures 6.1 and 6.4 also show that P4CC03 mostly exist as single chains. Thus, cinnamate groups are able to make intramolecular crosslinks. Hence, more cinnamate groups make crosslinks with longer UV exposure time and the absorbance of the sample decreases. UV-Vis spectra in Figure 6.5 (B) also show that absorbance decreases as UV exposure time increases. The purple dotted line in Figure 6.5 (A) and the green dotted line in Figure 6.5 (B) show similar absorbance with similar UV exposure time, which means that cinnamate groups in the two systems have similar degrees of crosslinking.

Degree of crosslinking may be affected by P4CC03 adsorption onto DOE-2-12B. Liu discussed that the adsorption of P4CC03 and other pullulan derivatives onto regenerated cellulose surfaces.[260] Cellulose nanocrystals in this study have sulfate groups on their surfaces. However, the hydrophobic effect is the primary driving force for the adsorption and sulfate groups may not significantly influence adsorption of P4CC03 onto cellulose nanocrystals.[260] Light scattering, UV-Vis spectra, and zeta-potential data will be discussed again in the Results and Discussion section.

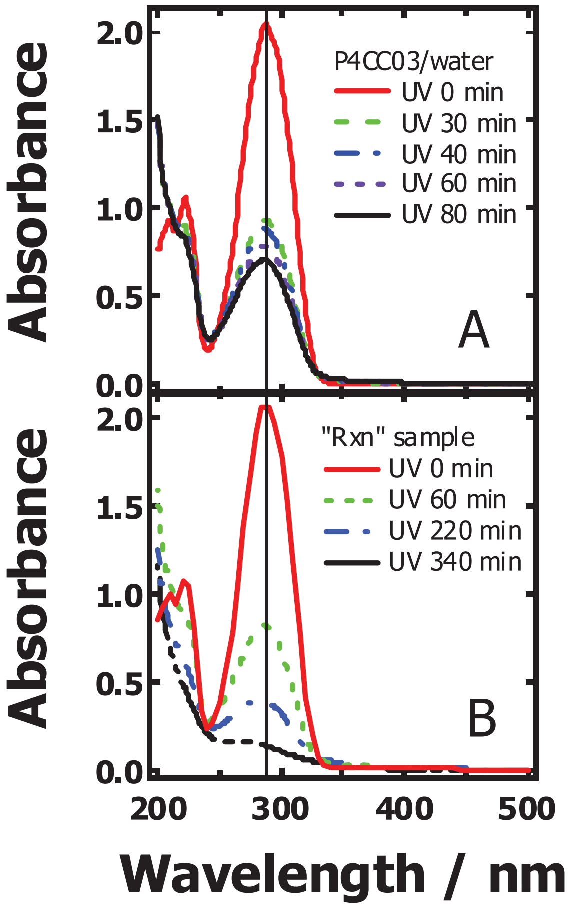

Figure 6.5 UV-Vis spectra of (A) P4CC03/water binary and (B) Rxn binary systems. Spectra of different color correspond to different UV exposure times. All spectra show λ_{max} of 287 nm.

6.4.3 Autocorrelation Functions and Decay Time Distributions of PreX and Rxn Systems

PreX and Rxn samples are probed with polarized and depolarized dynamic light scattering. Figure 6.6 and 6.7 show autocorrelation functions of samples at UV exposure times of 30, 50, and 70 minutes. Figure 6.5 (A) shows that a significant degree of UV crosslinking has occurred by a UV exposure time of 30 minutes, however, autocorrelation functions in Figure 6.6

(A) show few differences from those in Figure 6.3. At UV exposure times of 50 and 70 minutes, autocorrelation functions (Figure 6.6 (C) and (E)) show noisy base lines from aggregation or structural inhomogeneity. Figure 6.7 shows autocorrelation functions of the Rxn sample at UV exposure times of 50 and 70 minutes. The Rxn system does not have noisy base lines for UV exposure times up to 70 minutes. In both samples, little change is observed in the autocorrelation functions from Hv mode experiments. The overall system is still optically anisotropic and cellulose nanocrystals dominate the depolarized scattering whether or not the system has aggregates.

Concentrations of P4CC03 and DOE-2-12B were kept the same in both systems and the only difference was when UV light was applied during the sample preparation procedure. In a PreX system, UV crosslinking occurred before DOE-2-12B was added to the system. Thus, intramolecular and intermolecular reactions were possible for P4CC03. However, in a Rxn system, DOE-2-12B already existed when UV light was applied. While intramolecular and intermolecular reactions were still possible, cellulose nanocrystals could also be incorporated into aggregates. The purple broken line in Figure 6.5 (A) and the green broken line in Figure 6.5 (B) show the UV crosslinking reaction for an UV exposure time of 60 minutes. Similar absorbances imply similar degrees of crosslinking whether or not the sample contained DOE-2-12B. A PreX system showed aggregation or structural inhomogeneity from 50 minutes after UV light was applied. However, a Rxn system did not show any change in autocorrelation functions even up to 70 minutes. One possible explanation is that P4CC03 adsorbs onto DOE-2-12B and limits the size of P4CC03 aggregates that can form in the solution.

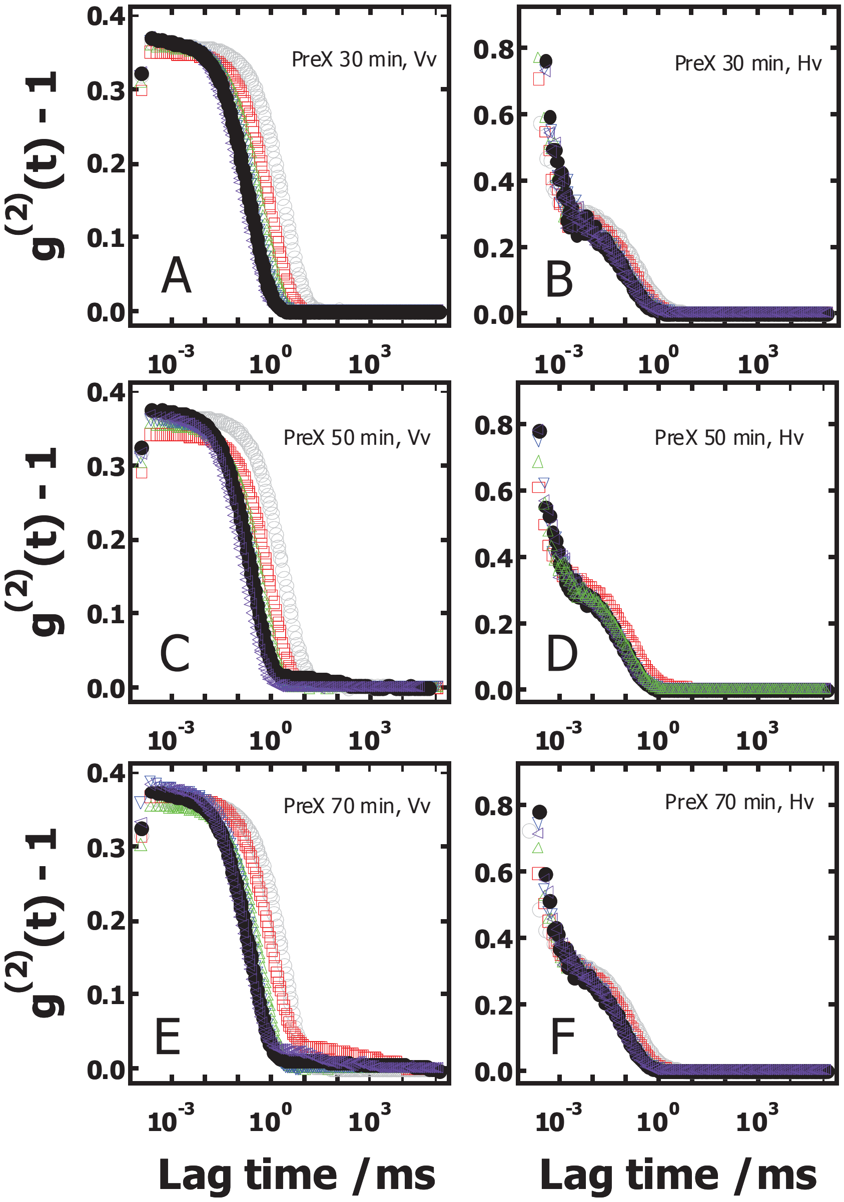

Figure 6.6 Autocorrelation functions of a PreX system after exposure to UV light for times of 30, 50, and 70 minutes at six scattering angles in Vv (A, C, and E) and Hv (B, D, and F) modes. All symbols and colors denoting scattering angles are identical to those in Figure 6.1.

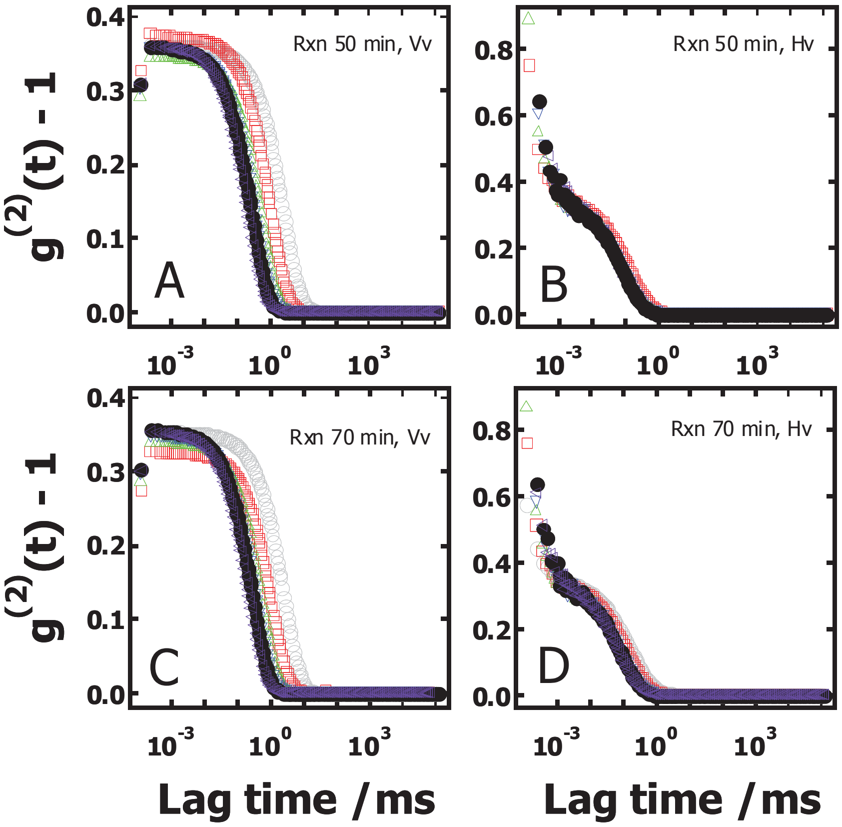

Figure 6.7 Autocorrelation functions of a Rxn system after exposure to UV light for times of 50 and 70 minutes at six scattering angles in Vv (A and C) and Hv (B and D) modes. All symbols and colors denoting scattering angles are identical to those in Figure 6.1.

Figure 6.8 shows decay time distributions for PreX and Rxn systems after UV exposure times of 50 and 70 minutes. Aggregation in PreX samples is clearly observed in Figure 6.8. All peaks are present at similar positions. PreX samples show a third mode of size corresponding to micrometer scale that relates to large aggregates. Peak widths show some differences for each mode. The CONTIN algorithm is sensitive to non-random experimental errors and the width can be dramatically narrowed relative to the L-curve method.[233,234] Figure 6.8 clearly shows that Rxn samples have no large aggregates, while PreX samples have aggregates with micron sizes.

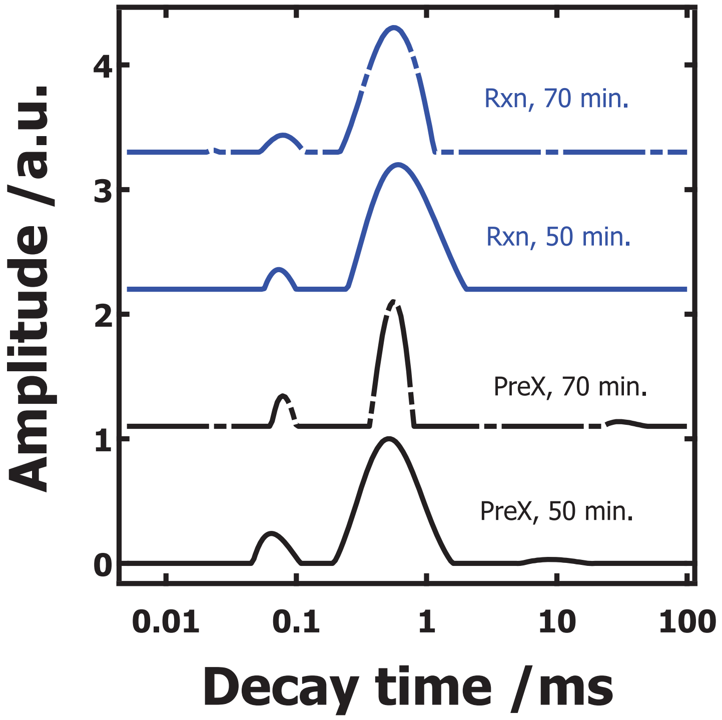

Figure 6.8 Decay time distributions of Rxn and PreX systems after exposure to UV light for times of 50 and 70 minutes. All distributions correspond to a scattering angle of 90°.

Figure 6.9 and 6.10 show autocorrelation functions of Rxn samples for UV exposure times up to 340 minutes in Vv and Hv mode, respectively. At UV exposure times of 220 minutes, autocorrelation functions start to have noisy base lines like those observed in Figure 6.6 for the PreX system. Compared to the time required to observe aggregates for PreX samples, the UV exposure times for the Rxn system are significantly longer. No precipitation was observed for

UV exposure times up to 280 minutes. Autocorrelation functions from Hv mode (Figure 6.10) also show little change, behavior that is similar to autocorrelation functions in Figure 6.6 and 6.7.

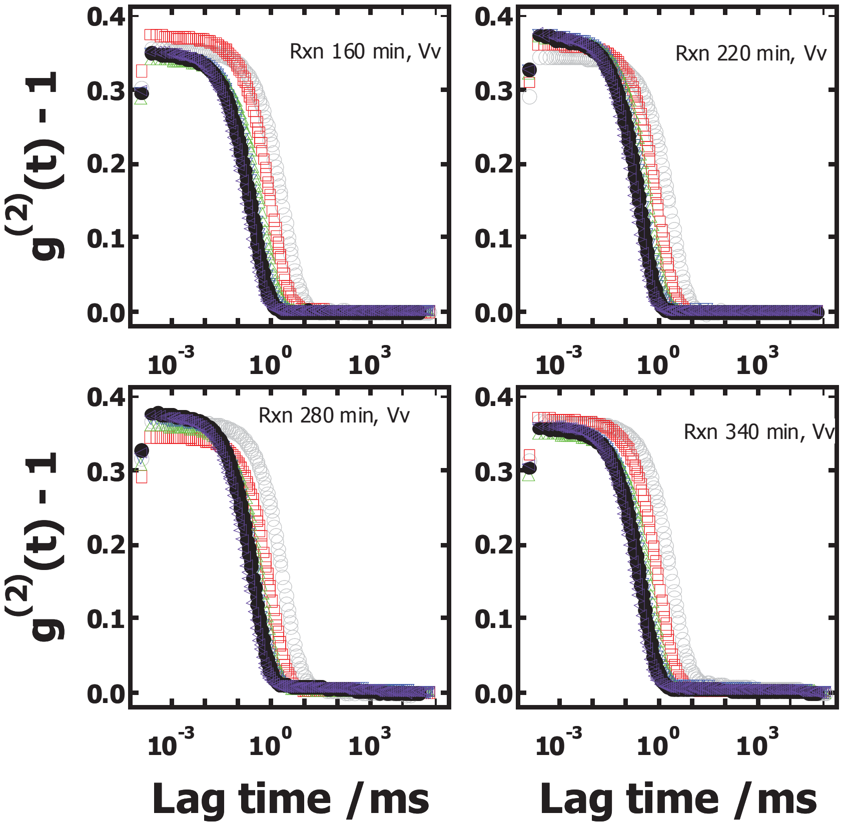

Figure 6.9 Autocorrelation functions of a Rxn system after exposure to UV light for times of 160, 220, 280, and 340 minutes at six scattering angles in Vv mode. All symbols and colors denoting scattering angles are identical to those in Figure 6.1.

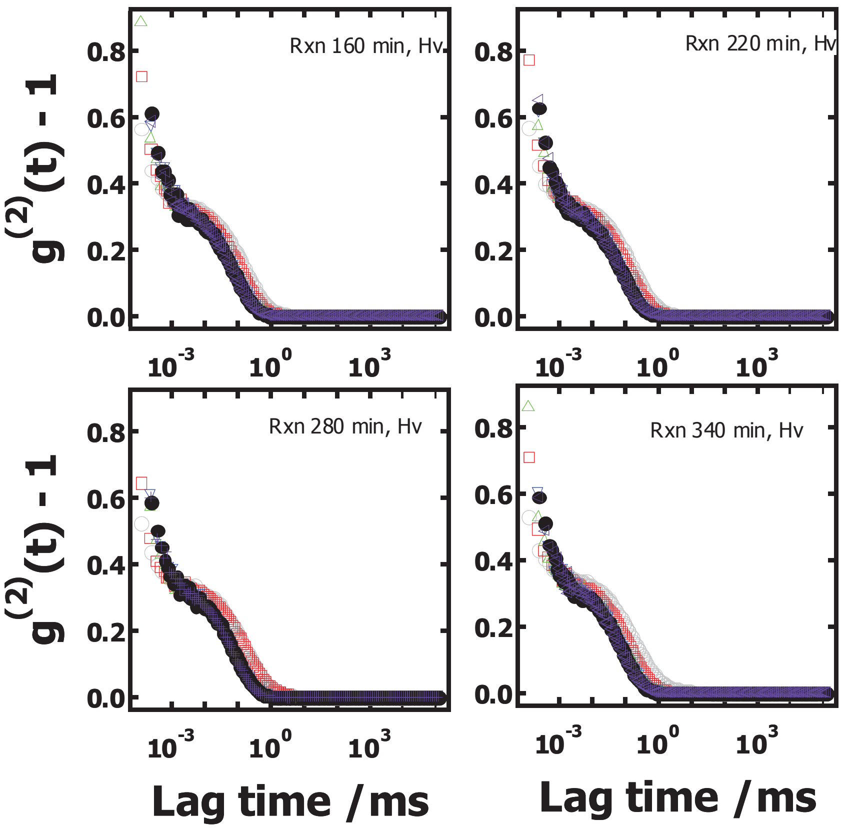

Figure 6.10 Autocorrelation functions of a Rxn system after exposure to UV light for times of 160, 220, 280, and 340 minutes at six scattering angles in Hv mode. All symbols and colors denoting scattering angles are identical to those in Figure 6.1.

Decay time distributions from a CONTIN analysis of autocorrelation functions in Figure 6.9 are shown in Figure 6.11. There is no aggregation up to UV exposure times of 160 minutes. Distributions (solid blue line in Figure 6.11) clearly show the third mode corresponding to aggregates for systems with longer UV exposure times. At UV exposure times of 340 minutes, the third mode disappears because aggregates are so large that they precipitate.

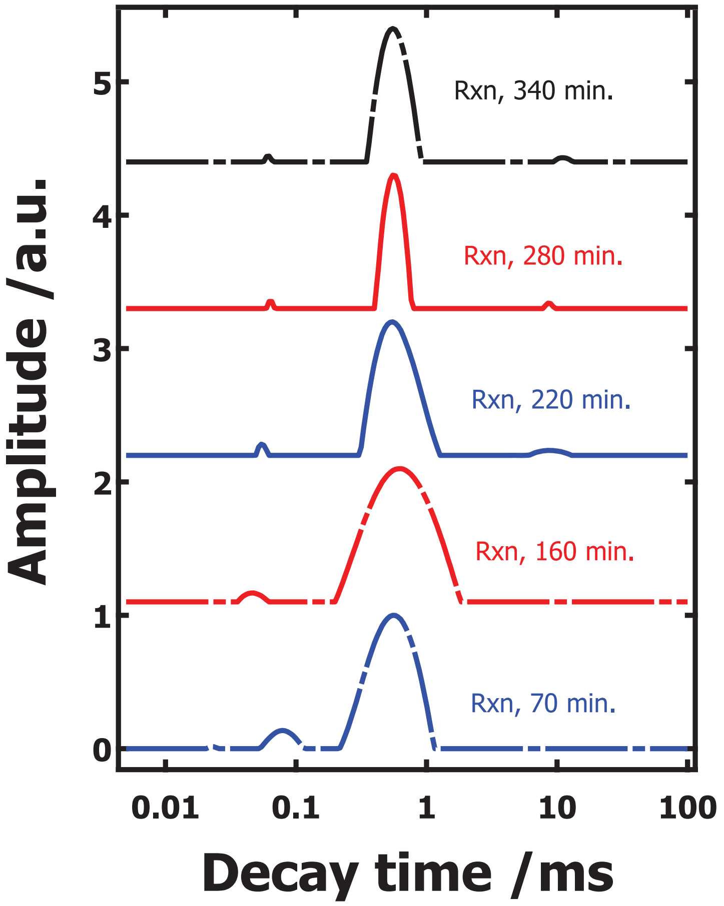

Figure 6.11 Decay time distributions of a Rxn system after exposure to UV light for times of 70, 160, 220, 280, and 340 minutes. All distributions correspond to a scattering angle of 90°.

6.4.4 Zeta-potential Measurements of DOE-2-12B/Water, P4CC03/DOE-2-12B/Water, and P4CC03/Water Systems

In colloidal systems, solid particle surfaces bind one or several layers of liquid molecules or ions. The region containing layers is divided two parts: An inner region where molecules or ions directly adsorb onto the surface (Stern layer) and the outer region where molecules or ions are less strongly associated to the surface (diffuse layer). These layers cause an electrokinetic potential to build between the surface of the colloid and any point in the mass of the suspending liquid. Specifically, electokinetic potentials at the interface between a Stern layer and a diffuse layer (shear plane) is called the zeta-potential which refers to the hydrodynamic interface.[332,333] Zeta-potentials can be related to surface potentials (ψ_0) in 1:1 electrolytes and the surface charge density (σ) can be obtained from the following equation:[334,335]

$$\sigma = \frac{2\varepsilon_r \varepsilon_0 \kappa kT}{e}\left(\frac{e\psi_0}{2kT}\right)\times \left[1+\frac{1}{\kappa a}\frac{2}{\cosh^2(2\psi_0/4kT)}+\frac{1}{(\kappa a)^2}\frac{8\ln[\cosh(e\psi_0/4kT)]}{\sinh^2(e\psi_0/2kT)}\right]^{1/2} \tag{6.8}$$

where ε_r, ε_0, κ, k, and T are the relative permittivity of a medium and a vacuum, the Debye-Huckel parameter, Boltzmann constant, and temperature, respectively. In this experiment, zeta-potential measurements do not provide surface charges. 1:1 electrolyte was not applied to measure zeta-potentials because salt concentration could influence the interaction between P4CC03s and cellulose nanocrystals. Zeta-potentials have been used to discuss not only the mobility and stability of particles in colloids but also adsorptive interactions between particles and polymers.[336-338]

Figure 6.12 shows zeta-potential distributions of DOE-2-12B/water (black), DOE-2-12B/P4CC03/water (red), and P4CC03/water (blue) systems. Average zeta-potentials are summarized in Table 6.1. Hydroxyl groups and sulfate groups in DOE-2-12B provide negative zeta-potentials. The average zeta-potential is -27.8 ± 2.8 and the distribution shows a small shoulder in the lower zeta-potential region because of aggregation. The average value shows good agreement with the value of -31.37 mV for cellulose nanocrystals obtained from recycled pulp reported by Filson *et al.*[339] The black solid line is the zeta-potential distribution of P4CC03. An average zeta-potential of -2.0 ± 1.2 mV is comparable to -0.1 ± 1.2 mV reported by Yim *et* *al*.[340] Several factors such as pH, molar mass, concentration, and the use of different instruments could influence zeta-potential and provide slightly different values.[341]

In the P4CC03/DOE-2-12B/water ternary system, the zeta-potential distribution shows one peak, which means that mobile objects in the ternary system have similar hydrodynamic interfaces. Figure 6.12 and Table 6.1 show that zeta-potential of cellulose nanocrystals slightly decreases when P4CC03s are introduced into the DOE-2-12B/water binary system. P4CC03s adsorb onto DOE-2-12Bs and screen the surface having multiple hydroxyl and sulfate groups. Rezwan *et al*.[336,337] probed bovine serum albumin (BSA) adsorption onto colloidal particles and observed zeta-potential changes. The positive zeta-potential of the particles decreased with increasing amounts of adsorbed BSA. Hossein *et al*.[338] discussed that pullulan derivatives adsorbed onto plasmid DNA through the coordination of Zn^{2+} ions and neutralized the negative charge of the plasmid DNA. In this experiment, P4CC03s adsorbed onto DOE-2-12B and screened the surface whereby the zeta-potential of the system decreased.

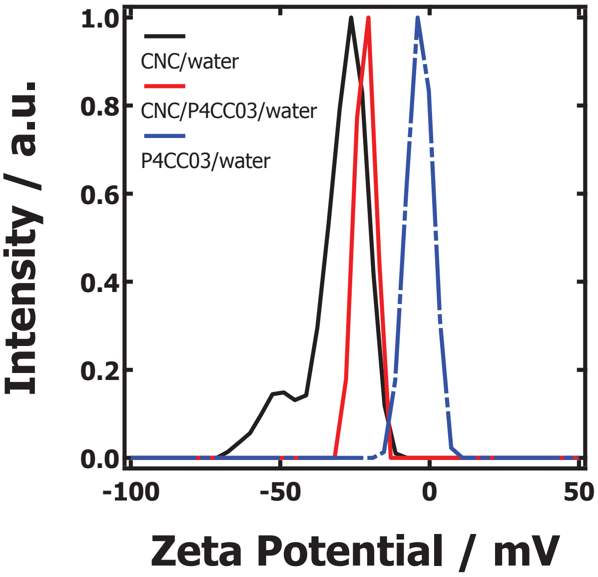

Figure 6.12 Zeta-potential distributions of CNC/water (black), CNC/P4CC03/water (red), and P4CC03/water (blue) systems. CNC denotes cellulose nanocrystals (DOE-2-12B).

Table 6.1 Average zeta-potentials of CNC/water, CNC/P4CC03/water, and P4CC03/water systems: CNC denotes cellulose nanocrystal (DOE-2-12B).

	Zeta-potential mV
CNC/water	-27.8 ± 2.8
CNC/P4CC03/water	-22.5 ± 1.3
P4CC03/water	-2.0 ± 1.2

6.4.5 Discussion

6.4.5.1 P4CC03 Adsorption onto Cellulose Nanocrystals

Zeta-potential distributions and average zeta-potentials in Figure 6.12 and Table 6.1 show that P4CC03s adsorb onto DOE-2-12Bs and screen the hydroxyl and sulfate groups on the DOE-2-12B surface. Figure 6.13 shows P4CC03 adsorption onto cellulose nanocrystals. Liu[260] showed that hydrophobic cinnamate groups enhanced the adsorption of pullulan cinnamate onto regenerated cellulose surface. The P4CC03/DOE-2-12B/water ternary system uses cellulose nanocrystals having sulfate groups. Thus, the interaction between P4CC03 and cellulose nanocrystals would be weaker than between P4CC03 and regenerated cellulose which does not have sulfate groups. Liu[260] reported that the surface concentration (Γ) of P4CC03 on regenerated cellulose is 0.2 ± 0.1 mg·m^{-2} and 0.7 ± 0.1 mg·m^{-2} by surface plasmon resonance (SPR) and quartz crystal microbalance with dissipation monitoring (QCM-D), respectively. Maximum surface concentration (Γ_{max}) of a flat polysaccharide monolayer is ~ 0.45 mg·m^{-2}.[342] DOE-2-12B should have a lower Γ_{max} for P4CC03 than regenerated cellulose because of the sulfate groups. Hence, P4CC03s should adsorb onto cellulose nanocrystals at submonolayer level. Low P4CC03 surface concentrations, in turn, explain the small shift of zeta-potential in the ternary system (Figure 6.12). The molar mass of pullulan before the substitution reaction with 4-cholorocinnamtes is approximately 75 kDa. Thus, approximately 12 4-chlorocinnamate groups exist on P4CC03. Pullulan is a flexible polymer and 4-chlorocinnamte groups can be easily located adjacent to each other on the cellulose nanocrystal surface with hydroxyl and sulfate groups.[330] These 4-chlorocinnamate groups make crosslinks upon exposure to UV light.

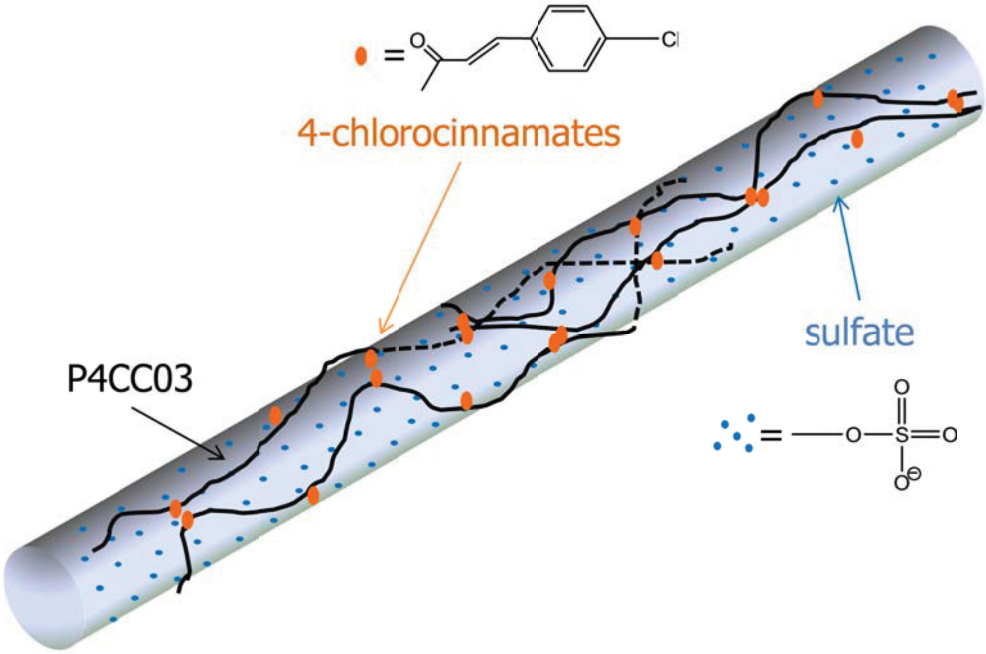

Figure 6.13 P4CC03 adsorption onto a cellulose nanocrystal: There are ~ 12 4-chlorocinnamate groups per P4CC03 chain and ~ 5000 sulfate groups on DOE-2-12B. 4-chlorocinnamate groups are located adjacent to each other because of hydrophobic interaction on the cellulose nanocrystal surface having hydroxyl and sulfate groups. Adjacent 4-chlorocinnamate groups undergo UV dimerization reaction.

Light scattering and UV-Vis spectroscopy data show that the PreX samples form aggregates and the Rxn samples do not for UV crosslinking up to 220 minutes. Longer exposure times lead to aggregation in the Rxn system. Although Figure 6.4 shows the size of P4CC03 aggregates in a P4CC03/water binary system are similar to those of cellulose nanocrystals in a DOE-2-12B/water binary system as well as that of particles corresponding to the slow mode in a P4CC03/DOE-2-12B/water ternary system, it is clear that the cellulose nanocrystals hinder P4CC03 aggregation during UV crosslinking. The UV crosslinking reaction can occur whether P4CC03 chains exist as aggregates in solution or exist on surfaces of cellulose nanocrystals. One possible explanation is that P4CC03 chains adsorbed onto cellulose nanocrystals in the ternary system and zeta-potential measurements show P4CC03 adsorption onto DOE-2-12B in Section 6.4.4. Otherwise, P4CC03 chains exist as both small and large aggregates in solution as they do without cellulose nanocrystals. Figure 6.12 schematically depicts the adsorption of P4CC03 onto cellulose nanocrystals. In a P4CC03/water binary system, UV induced dimerization occurs. Some of these reactions lead to intermolecular crosslinks. Thus, large aggregates are easily observed (A). Similarly, intermolecular and intramolecular UV dimerization reactions are not hindered in PreX sample because cellulose nanocrystals are added in the system after UV exposure ceases (B). In the Rxn samples, UV light is applied after the ternary system is prepared. P4CC03 chains are already adsorbed onto cellulose nanocrystals and most UV crosslinking reactions occur in chains on the surface of cellulose nanocrystals (E). Thus, large aggregates are not readily observed for short UV exposure times. Cellulose nanocrystals have negative charges and electrostatic repulsion that stabilizes the colloidal suspension, thereby making dimerization between P4CC03 on different cellulose nanocrystals more difficult. After long UV exposure times, P4CC03 chains on surface of different cellulose nanocrystals start to bridge via UV crosslinking. Once this occurs, large aggregates that can contain cellulose nanocrystals begin to precipitate.

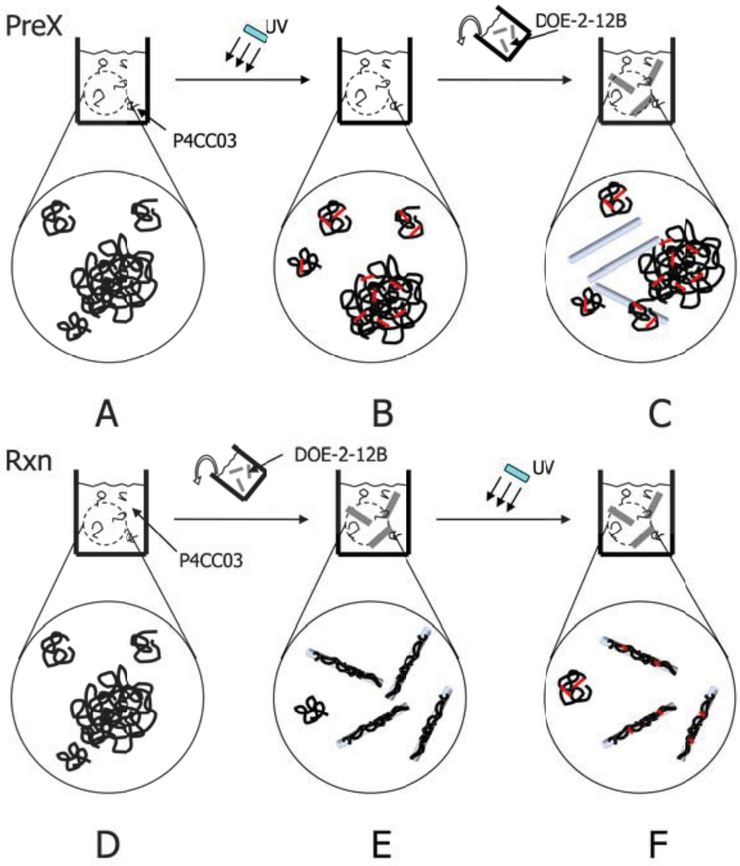

Figure 6.14 Schematic illustration of UV dimerization and subsequent crosslinking in PreX (A, B, and C) and Rxn (D, E, and F) systems. For the PreX system, (A), intermolecular and intramolecular UV dimerization reactions occur (B) and added cellulose nanocrystals have little effect on the system (C). For the Rxn system, (D), P4CC03 adsorbs onto cellulose nanocrystals in a ternary system (E). Most UV dimerization reactions occur within the P4CC03 layer adsorbed on the nanocrystaline cellulose surfaces (F).

6.5 Conclusions

This study probes the ternary system of partially hydrophobically modified pullulan, cellulose nanocrystals, and water. UV-Vis spectra, autocorrelation functions, and decay time distributions of PreX and Rxn samples demonstrate the adsorption of partially hydrophobically modified pullulan onto cellulose nanocrystals in dilute solution. Simple comparisons of autocorrelation functions and decay time distributions of DOE-2-12B/water, P4CC03/water, and P4CC03/DOE-2-12B/water systems from polarized and depolarized light scattering show subtle evidence for P4CC03 adsorption onto cellulose nanocrystals. UV-Vis spectra show that exposure to UV irradiation increases cinnamate dimerization and ultimately crosslinking as exposure time increases. Aggregates are observed for significantly shorter UV exposure times in the PreX system relative to the Rxn system. P4CC03 adsorbs onto cellulose nanocrystal and UV crosslinking occurs at the surface of cellulose nanocrystal. Hence, aggregates in the PreX system observed at short exposure times do not appear in the Rxn system until longer UV exposure times. Zeta-potentials of cellulose nanocrystals in DOE-2-12B/water, P4CC03/DOE-2-12B/water, and P4CC03/water systems also support P4CC03 adsorption onto DOE-2-12B. P4CC03 adsorbs onto cellulose nanocrystals and screens the surface hydroxyl and sulfate groups of the cellulose nanocrystals. Hence, the zeta-potential of the cellulose nanocrystals decreased slightly. These results suggest that probe diffusion with a combination of anisotropic and light scattering technique is effective for studying interactions between polysaccharides. Also, results show that cellulose nanocrystals are a potential anisotropic probe for probe diffusion studies of complicated polymer solutions.

CHAPTER 7

Light Scattering Studies of Interactions Between 2-Hydroxypropyltrimethylammonium Xylans and Rod-like Cellulose Nanocrystals

7.1 Abstract

Adsorption of 2-hydroxypropyltrimethylammonium xylans (HPMAXs) of degree of molar substitution (MS) of 0.34 2-hydroxypropyltrimethylammonium groups per anhydroxylose group onto rod-like cellulose nanocrystals (DOE-2-12B) are investigated by zeta-potential measurements, and polarized and depolarized dynamic light scattering. Zeta-potential measurements show HPMAX adsorption onto cellulose nanocrystals. Decay time distributions of the ternary system and HPMAX/water binary system from CONTIN analysis show that aggregates exist in the binary system and they disappear in the ternary system. Also, any phenomenon related to gelation was not observed in the ternary systems. At low HPMAX concentrations relative to that of DOE-2-12B, HPMAX adsorbed onto some of the DOE-2-12B. Scattering differences from HPMAX adsorbed onto DOE-2-12B and unaltered DOE-2-12B led to partial heterodyning. Hence, the difference decreased as the amount of HPMAX adsorbed onto DOE-2-12B increased with increasing HPMAX concentration. Also, translational and rotational diffusion coefficients of the ternary systems were consistent with the adsorption of HPMAX onto cellulose nanocrystals. Both diffusion coefficients decreased as the concentration ratio of the HPMAX to DOE-2-12B (R) increased and the concentration dependence of the ratio of the rotational diffusion coefficient to the translational diffusion coefficient revealed a strong adsorptive interaction between HPMAX and the cellulose nanocrystals.

7.2 Introduction

Since fiberglass polymer matrix composites were introduced around the time of World War II, plastic composite materials have attracted great interest because of their remarkable thermal and mechanical properties. As such, new high performance composite materials with petroleum-based plastics have continuously evolved.[343-345] However, continuous consumption of petroleum causes environmental problems and finite reserves lead to long-term economic uncertainty. These environmental and economic concerns draw scientific attention to renewable and biodegradable materials. Biocomposites based upon polysaccharides have received attention as promising materials for many industrial applications.[344,346-348] Materials like clay or thermoplastics have been viewed as potential candidates for incorporation into biocomposites. However, relatively poor chemical compatibility between natural polysaccharide fibers and other materials leads to significant challenges.[345,349]

Modification of polysaccharides and characterization of interactions of polysaccharides were extensively studied to understand and overcome the chemical incompatibility. Brumer *et al.* [350] introduced chemoenzymatic modification of crystalline cellulose surfaces with xyloglucan and showed that extensive chemical modification of the cellulose fiber could occur without disrupting fiber structure. Schwikal *et al.*[351] reported modification of birch wood xylan with 2,3-epoxypropyltrimethylammonium chloride. Adsorption of carboxylmethyldextrans onto silicon wafer surfaces was studied by Hartley *et al.*[352] Various surface analysis techniques like X-ray photoelectron spectroscopy (XPS) verified that a carboxyl density in polysaccharides is directly proportional to the thickness of the polymer layer. The result demonstrated that tailoring of the steric and electrosteric properties of polysaccharides significantly affects their interactions with other polysaccharides. Hansen *et al.*[353] reviewed current biomedical as well as industrial applications of hemicelluloses. All discussions have confirmed that the fundamental studies of chemical modification and characterization are a key for potential new applications.

Strong interactions via hydrogen bonding of xylan and cellulose fibrils was reported by Mora *et al*. and Henrikkson *et al*.[354-356] Westbye *et al*.[357] investigated the interaction of xylan and lignin in solution and saw xylan concentration controlled the agglomeration of lignin in aqueous solution. Linder *et al*.[358] examined the adsorption of xylan onto bacterial cellulose gels. Atomic force microscopy (AFM) and dynamic light scattering studies demonstrated that preformed xylan aggregates adsorbed onto cellulose surfaces with increasing adsorption time rather than a progressive build-up of multilayer thick xylan films. In this study, birch xylan was modified with 2,3-epoxypropytrimethylammonium chloride (EPTA) to form a cationic hemicellulose derivative. The resulting 2-hydroxypropyltrimethylammonium xylan (HPMAX) of molar substitution (MS = 0.34) that is defined as the number of 2-hydroxypropyltrimethylammonium (HPMA) groups per anhydroxylose unit (AXU) was selected to obtain the best solution properties. This study had concentrated on the effect on the translational and rotational diffusion of HPMAX adsorption onto anionic cellulose nanocrystals. The ternary system of a xylan derivative (HPMAX)/cellulose nanocrystal (DOE-2-12B)/water was probed with zeta-potential measurements and polarized and depolarized dynamic light scattering.

7.3 Experimental

7.3.1 Zeta-potential Measurements

All samples were prepared in 20 mL vials and sonicated 20 minutes before measurement. 0.4 mg/mL HPMAX/water solutions were prepared. The HPMAX/cellulose nanocrystal/water ternary system was prepared with R = 4 as discussed in Section 4.2.4. R is the concentration ratio of HPMAX to DOE-2-12B. The solution was transferred into 1 mL commercial zeta-potential cells for measurements. Measurements were repeated multiple times. Individual samples were scanned 100 times and results from multiple measurements were averaged.

7.3.2 Light Scattering

DOE-2-12B stock solution was used for the preparation of ternary systems. Procedures for the preparation of ternary systems having different R values were described in Section 4.2.2.3. Dynamic light scattering measurements in Hv and Vv modes were performed for 300 seconds for each sample. Measurements were performed at least three times and reproducibility was examined at six scattering angles: 30, 45, 60, 75, 90, and 105°. Specific light scattering measurement and data analysis procedures were described in Sections 4.3.1 and 3.1.

7.4 Results and Discussion

7.4.1 Zeta-potential Measurements of DOE-2-12B/Water, HPMAX/DOE-2-12B/Water, and HPMAX/Water Systems

Zeta-potential is the electrokinetic potential at the interface between a Stern layer where molecules or ions are directly adsorbed onto the surface and a diffuse layer where molecules or ions are less strongly associated to the surface. Zeta-potential has been introduced to discuss mobility and stability of particles in colloids and adsorptive interactions between particles and polymers.[336-338] In Chapter 6, zeta-potentials of DOE-2-12B/water, DOE-2-12B/P4CC03/water, and P4CC03/water revealed P4CC03 adsorption onto cellulose nanocrystals. Similar experiments were repeated for DOE-2-12B/water, DOE-2-12B/HPMAX/water, and HPMAX/water systems. Zeta-potential distributions and average zeta-potentials are summarized in Figure 7.1 and Table 7.1. The zeta-potential distribution and average value of DOE-2-12B are negative from the hydroxyl and sulfate groups as discussed in Section 6.4.4. The broken blue line in Figure 7.1 shows the zeta-potential distribution of HPMAX. An average zeta-potential is 34.6 ± 1.0 mV is noted in Table 7.1. Cationic HPMA groups in HPMAXs (Figure 4.3) lead to positive zeta-potential. The DOE-2-12B/HPMAX/water ternary system shows a single zeta-potential distribution (solid red line), which means there is one type of mobile object with similar hydrodynamic interfaces. Hence, HPMAX adsorbs onto DOE-2-12Bs in the ternary system and the zeta-potential significantly increases. Table 7.1 and Figure 7.1 show zeta-potentials of DOE-2-12B increase with HPMAX adsorption but are still smaller than values for HPMAX in aqueous solution. Adsorbed HPMAX with positive charges screens the negative hydroxyl and sulfate groups of DOE-2-12B and the Zeta-potential significantly increases. However, positive charges in HPMAX are slightly neutralized by hydroxyl and sulfate groups. Thus, the Zeta-potential in the DOE-2-12B/HPMAX/water ternary system is lower than that in the HPMAX/water binary system.

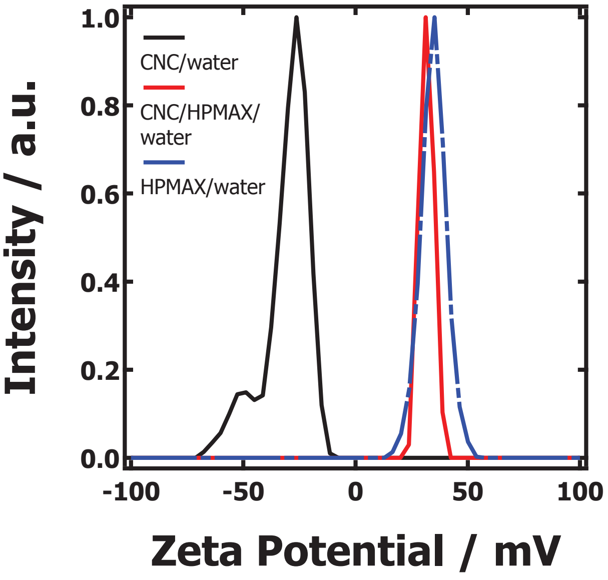

Figure 7.1 Zeta-potential distributions of CNC/water (black), CNC/HPMAX/water (red), and HPMAX/water (blue) systems: CNC denotes cellulose nanocrystal (DOE-2-12B).

Table 7.1 Average zeta-potentials of CNC/water, CNC/HPMAX/water, and HPMAX/water systems: CNC denotes cellulose nanocrystal (DOE-2-12B).

	Zeta-potential mV
CNC/water	-27.8 ± 2.8
CNC/HPMAX/water	31.8 ± 0.1
HPMAX/water	34.6 ± 1.0

7.4.2 Autocorrelation Functions and Decay Time Distributions of HPMAX/DOE-2-12B/Water Ternary Systems and HPMAX/Water Binary Systems

HPMAX/DOE-2-12B/water ternary systems with various R were probed with polarized (Vv) and depolarized (Hv) dynamic light scattering experiments. Figure 7.2 shows experimentally obtained intensity autocorrelation functions of ternary systems in Hv and Vv modes at various R. Intensity autocorrelation functions in Hv mode of a ternary system with R = 0.4 are close to the base line (Figure 7.2 (A)). The intensity autocorrelation functions increase with increasing R. However, intensity autocorrelation functions in Vv mode do not exhibit substantial differences across all R. The intensity autocorrelation function is given by

$$g^{(2)}(t)-1=f\left|g^{(1)}(t)\right|^{2} \tag{7.1}$$

where $g^{(1)}(t)$ and f are the electric field autocorrelation function and optical coherence parameter, respectively.[131] Intensity autocorrelation functions in Hv mode seen in Figure 7.2 (A) have low f values which are caused by partial heterodyning. This optical heterodyning arises from different scattering by "newly frozen" particles and "mobile" particles corresponding to stationary local oscillators and moving scatterers, respectively.[131,222,359-361] Various studies related to increasing polymer concentration and gelation have reported decreasing intensity autocorrelation functions with increasing heterodyning.[131,288] However, Figure 7.2 exhibits decreasing heterodyning with increasing R, which means that optical differences between relatively stationary local scatterers and moving scatterers present at low R disapprear with increasing R. Zeta-potential measurements in Section 7.4.1 suggest HPMAX adsorbs onto DOE-2-12B. Thus, the adsorptive interaction in the ternary system may eliminate heterodyning of the scattering. Strong self-association by hydrogen bonding between linear portions of xylan as well as strong interactions between xylan and cellulose have been reported.[358,362,363] Thus, self-association of HPMAX with various concentrations in the HPMAX/water binary systems needs to be probed.

Figure 7.3 shows representative intensity autocorrelation functions from dynamic light scattering experiments of HPMAX water solutions with various concentrations as a function of the product of the squared scattering wave vector and lag time, q^2t. Light scattering of small hard spheres in an ergodic system exhibit no angle dependence and have to show superimposing intensity autocorrelation functions at different scattering angles.[177] Intensity autocorrelation functions in Figure 7.3 do not superimpose but are also not widely scattered, which implies that the binary system has aggregates. Linder *et al*.[358] saw aggregation of partially hydrophobically modified birch xylan in water via light scattering and atomic force microscopy (AFM). In the HPMAX/water binary system, some 2-hydroxypropyltrimethylammonium groups may provide intermolecular electrostatic repulsive interactions but aggregation is inevitable because of hydrogen bonding. Relatively large aggregates can cause a slight angular dependence of the scattered light. Figure 7.3 shows $g^{(2)}(t) - 1$ for $t = 0$ is relatively unaffected by increasing solution concentration.

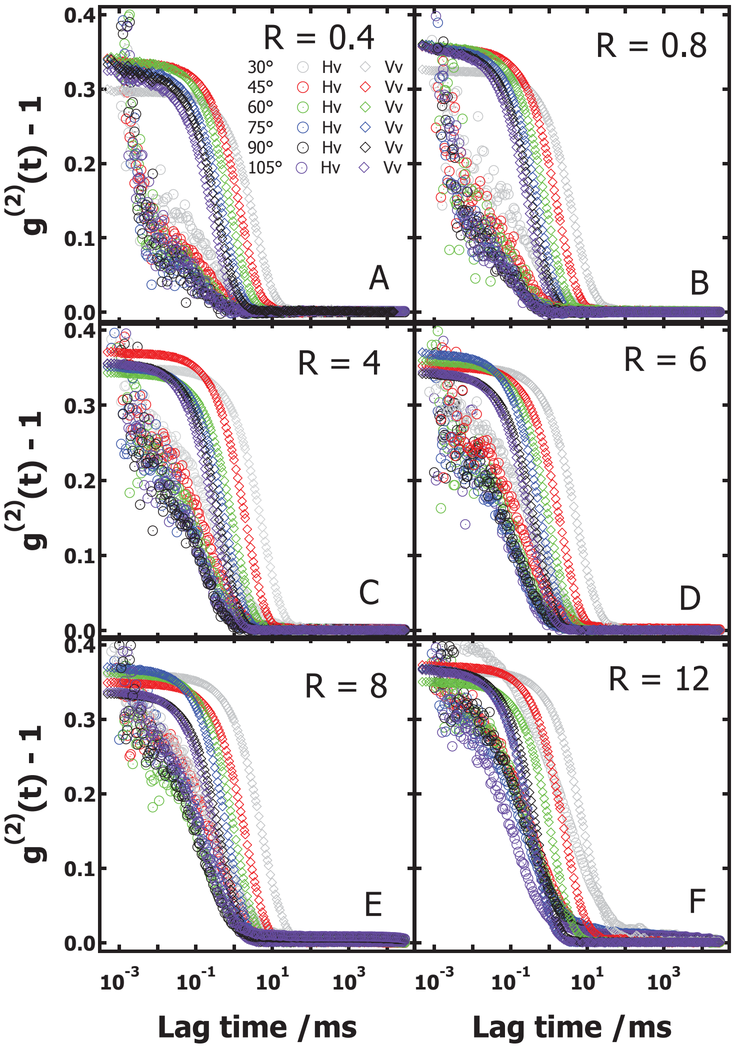

Figure 7.2 Intensity autocorrelation functions of HPMAX/DOE-2-12B/water ternary systems with various concentration ratios (R) of HPMAX to DOE-2-12B. All symbols denoting scattering angles and scattering modes on (A) are identical for (B) through (F). All measurements were made at a temperature of 298 K.

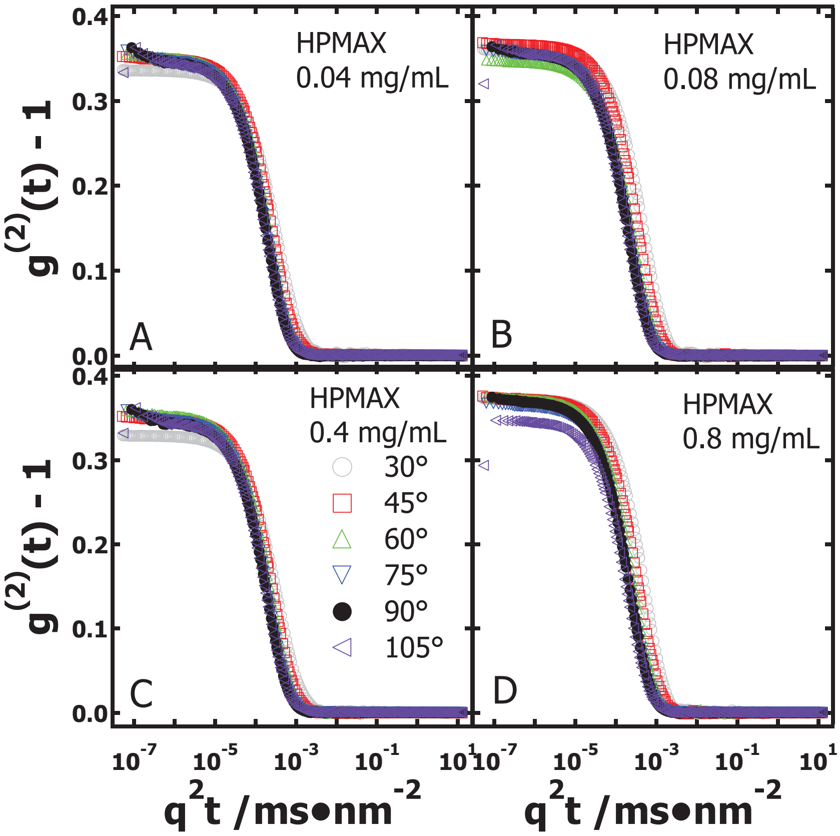

Figure 7.3 Intensity autocorrelation function versus q^2t for aqueous HPMAX solutions with various HPMAX concentrations: (A) 0.04, (B) 0.08, (C) 0.4, and (D) 0.8 mg·mL^{-1}. All symbols denoting scattering angles on (C) are identical for (A), (B) and (D). All measurements were made at a temperature of 298 K.

Figure 7.4 shows decay time distributions of aqueous HPMAX solutions with various concentrations from 0.04 to 0.8 $mg \cdot mL^{-1}$ obtained from a CONTIN analysis with the intensity autocorrelation functions in Figure 7.3. All solutions had bimodal peaks centered at approximately 0.06 and 1.22 ms. Two decay rates correspond to hydrodynamic radii of approximately 4 and 100 nm when we assume the system follows the Stokes-Einstein relationship. The slow mode corresponds to the hydrodynamic radius of aggregates (~ 100 nm) and exhibits negligible changes up to 0.4 $mg \cdot mL^{-1}$ of HPMAX. At 0.8 $mg \cdot mL^{-1}$, the relative amount of scattering from the slow mode increases slightly. Also, a new mode was observed at approximately 0.15 ms corresponds to aggregates of intermediate size from excess HPMAX at the relatively high concentration (0.8 $mg \cdot mL^{-1}$). These observations are consistent with the noisy base lines in Figure 7.2 (F). All HPMAX/DOE-2-12B/water ternary systems are prepared with HPMAX of concentrations from 0.2 to 0.6 $mg \cdot mL^{-1}$ (Table 4.2). Thus, the HPMAX/DOE-2-12B/water ternary system experiments are not influenced by aggregates of the large or intermediate size as seen in Figure 7.4.

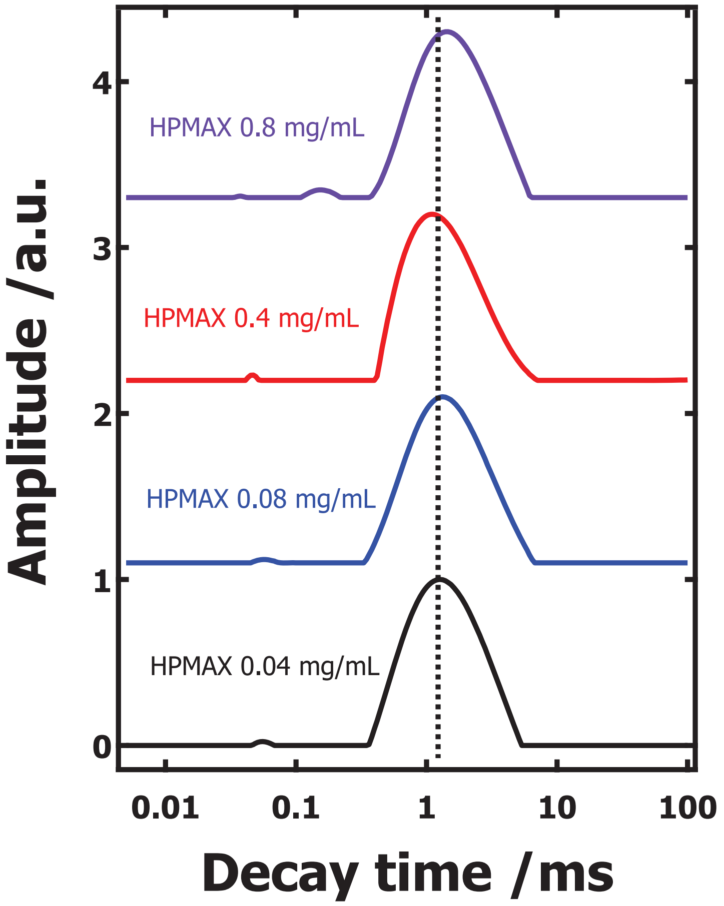

Figure 7.4 Decay time distributions of HPMAX/water binary systems with various HPMAX concentrations from a CONTIN analysis. All distributions correspond to a scattering angle of 90° at a temperature of 298 K.

Decay time distributions corresponding to intensity autocorrelation functions of the Vv mode in Figure 7.2 are shown in Figure 7.5. Compared to the slow mode of HPMAX aggregates at approximately 1.22 ms in Figure 7.4 observed for most HPMAX concentrations, all slow modes show faster decay time distributions for various R values. The ternary system with R = 0.4 exhibits a faster single mode than HPMAX/water binary system. A faster mode means scatterers move faster and have smaller sizes. Then, this decay time distribution peak gradually shifts to slower decay times with increasing R but are still faster than the slow mode of the HPMAX aggregates (Figure 7.4). This behavior is attributed to the adsorption of HPMAX onto DOE-2-12B. A slow mode at R = 8 has a short tail. An intermediate peak at ~ 0.22 ms (~ 60 nm), is observed for R = 12. This tail and intermediate peak are caused by aggregates of excess HPMAX in the ternary systems that are consistent with the noisy base lines observed in Figure 7.2.

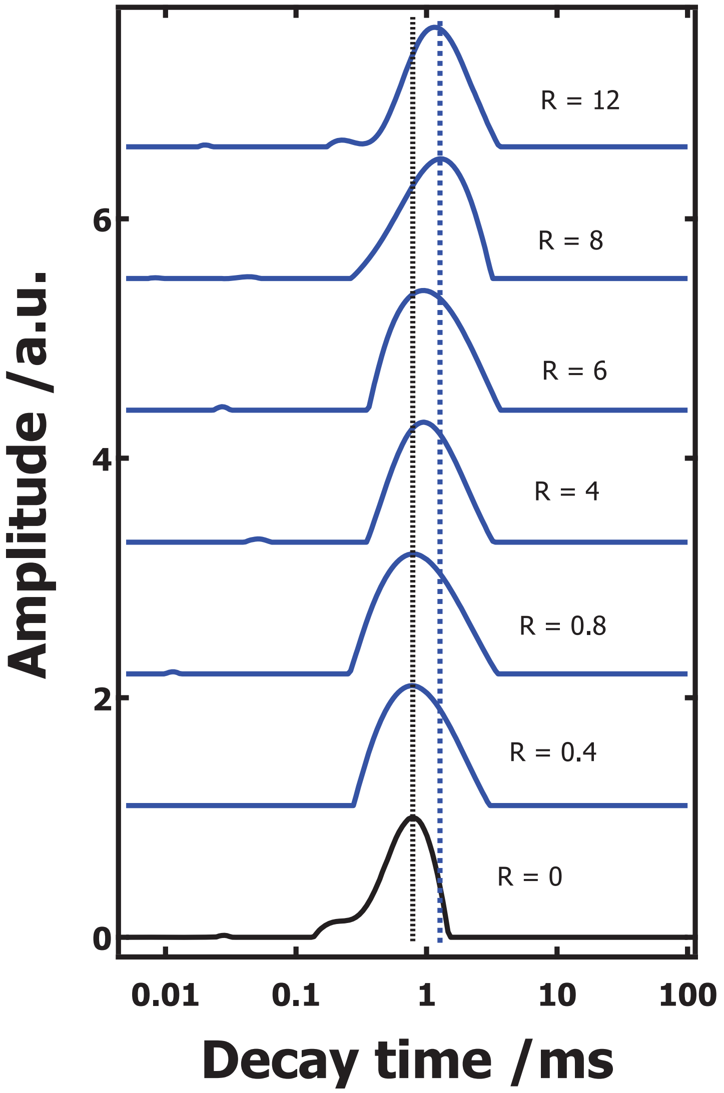

Figure 7.5 Decay time distributions of HPMAX/DOE-2-12B/water ternary systems for various R values from a CONTIN analysis. R is defined as the concentration ratio between HPMAX and DOE-2-12B. R = 0 denotes a DOE-2-12B/water binary system. All distributions correspond to a scattering angle of 90° for the Vv mode at a temperature of 298 K.

7.4.3 Diffusion Coefficients of Cellulose Nanocrystals in HPMAX/DOE-2-12B/Water Ternary Systems

Electric field autocorrelation functions can be represented as

$$G^{(2)}(t) = B\left(1 + f\exp(-2\Gamma t)\right) \tag{7.2}$$

where t, $G^{(2)}(t)$, B, and Γ are the lag time, intensity autocorrelation function, base line, and decay rate, respectively. Decay rates in dynamic light scattering experiments in Vv and Hv modes are characterized by

$$\Gamma_{Vv} = D_t q^2 \tag{7.3}$$

$$\Gamma_{Hv} = D_t q^2 + 6D_r \tag{7.4}$$

where q, D_t, and D_r are the scattering vector magnitude, translational diffusion coefficient, and rotational diffusion coefficient, respectively.

Equation 7.4 assumes no coupling of translational and rotational motion, which means the rod can reorient many times while diffusing a distance comparable to q^{-1}.[348] Otherwise, the scattered time correlation function will be an infinite series of decaying exponential terms with time constants:

$$\begin{aligned} t_{Ms}^{-1} &= q^2 D_t + [s(s+1) + \omega_{Ms}(\gamma) - \gamma/3]D_r \\ (M &= 0,1,2; s = 0,1,2) \end{aligned} \tag{7.5}$$

$$\omega_{Ms}(\gamma) = \sum_{k=1} L_k \gamma^k \tag{7.6}$$

where M and s are orders of angular moments and L_k is a prolate power series coefficient. γ is a coupling parameter defined as

$$\gamma = q^2 \Delta D_t / D_r \cong (qL)^2 / 12 \tag{7.7}$$

where L is the length of the rod.[364-365] Cush *et al.*[366] probed the light scattering from tobacco mosaic virus (TMV) in dextran solution and showed Eqn. 7.4 is satisfied for $1 < \gamma < 3$. The rotational motion is not fully controlled by dextran concentration below the overlap concentration. At higher concentrations, a network of dextran significantly hindered rotational motion of TMV but translational motion was not influenced compared to rotational motion. DOE-2-12B used in this study has $\gamma = 1.65$, so Eqn. 7.4 is clearly satisfied.

Figure 7.6 shows decay rates from polarized and depolarized dynamic light scattering experiments of ternary systems. Solid and broken lines are linear fits according to Eqns. 7.3 and 7.4, respectively. A decrease of the intercept from the broken lines corresponds to decreasing rotational diffusion coefficients with increasing R. Translational diffusion coefficients from slopes of fits for Hv and Vv modes are also decreasing as R increases.

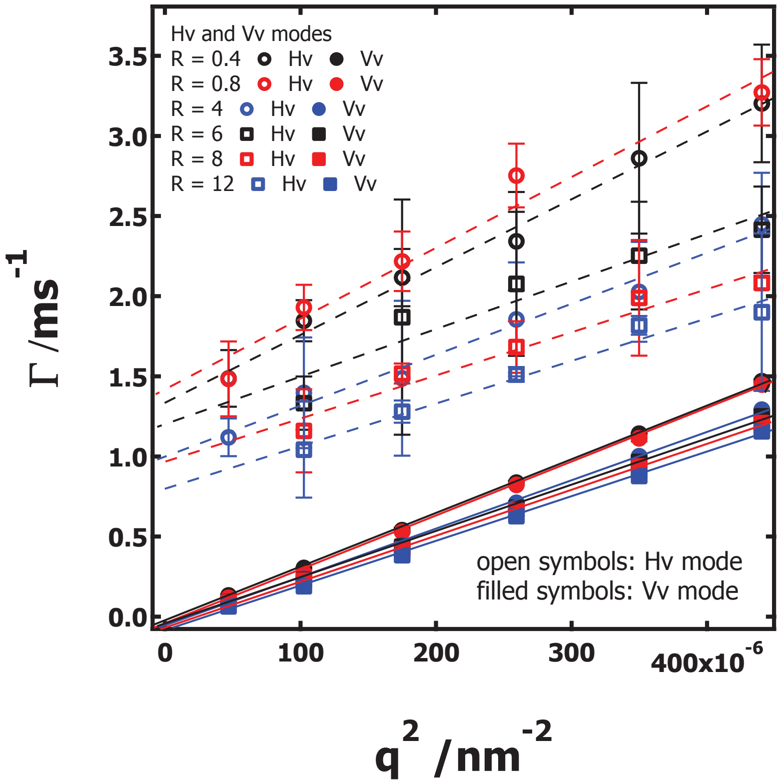

Figure 7.6 Decay rate versus q^2 for HPMAX/DOE-2-12B/water ternary systems: Filled and open symbols are decay rates in Vv mode and Hv mode, respectively. R denotes the ratio between concentrations of HPMAX and DOE-2-12B. Solid and dashed lines are linear fits according to Eqns. 7.3 and 7.4 for Vv and Hv modes, respectively.

Rotational and translational diffusion coefficients obtained from linear fits seen in Figure 7.6 are summarized in Table 7.2. The translational diffusion coefficient deduced from Hv and Vv scattering for R = 0.4 exhibit negligible changes, however, the rotational diffusion coefficient dramatically decreases. This reflects well known observations by other researchers that rotational motion of anisotropic particles is more strongly influenced by the adsorption of polymer onto the particle than translational motion. Hence, all translational diffusion coefficients decrease more gradually with HPMAX adsorption onto DOE-2-12B than the rotational diffusion coefficients.

Table 7.2 Rotational and translational diffusion coefficients of HPMAX/DOE-2-12B/water ternary systems

Sample[‡]	Hv mode		Vv mode
	D_t /10^{-8} cm^2s^{-1}	D_r /s^{-1}	D_t /10^{-8} cm^2s^{-1}
R = 0	4.76 ± 0.45	527 ± 17	4.61 ± 0.04
R = 0.4	4.43 ± 0.32	195 ± 13	3.40 ± 0.04
R = 0.8	4.46 ± 0.49	236 ± 20	3.40 ± 0.05
R = 4	3.19 ± 0.22	165 ± 10	3.07 ± 0.05
R = 6	2.95 ± 0.58	201 ± 28	2.96 ± 0.05
R = 8	2.70 ± 0.34	161 ± 16	2.86 ± 0.05
R = 12	2.64 ± 0.26	135 ± 12	2.79 ± 0.05

[‡]: R = [HPMAX]/[DOE-2-12B]. Each concentration is defined with mg·mL^{-1}. R = 0 sample is DOE-2-12B/water binary system.

7.4.4 Discussion

7.4.4.1 HPMAX Adsorption onto Cellulose Nanocrystals

Zeta-potential distributions shown in Figure 7.1 and Table 7.1 clearly show a significant shift of the distribution peak of cellulose nanocrystals by adding HPMAX. Also, all systems show single distributions. A single Zeta-potential distribution in the ternary system reveals that there is one kind of mobile species and hydrodynamic interface and that HPMAX adsorbs onto DOE-2-12B instead of forming self-aggregates. Kaya[367] showed HPMAX adsorption onto various surfaces including regenerated cellulose and carboxylic acid terminated self-assembled monolayers (SAM-COOH). Maximum surface concentrations (Γ_{max}) of HPMAX adsorbed onto regenerated cellulose surface and SAM-COOH were $\Gamma_{max} \sim 0.15$ and $\Gamma_{max} \sim 1$ mg·m^{-2}, respectively. The significantly higher Γ_{max} on the SAM-COOH surface was attributed to the strong interaction between anionic carboxylic acid groups and cationic HPMA groups. Cellulose nanocrystal surfaces have some sulfate groups as discussed in Chapter 5. Thus, the interaction between cellulose nanocrystals and HPMAX would be comparably strong as between SAM-COOH and HPMAX. When Γ_{max} of SAM-COOH, ~ 1 mg·m^{-2}, is compared to 0. 45 mg·m^{-2} for a flat polysaccharide monolayer, HPMAXs should have greater than monolayer level adsorption onto cellulose nanocrystals. In turn, the relatively strong interaction between HPMAX and cellulose nanocrystals causes strong HPMAX adsorption onto cellulose nanocrystals and explains the significant change of the zeta-potential distribution of the cellulose nanocrystals by adding HPMAX. Figure 7.7 and 7.10 schematically depict HPMAX adsorption onto the cellulose nanocrystals. HPMAX has relatively shorter and semi-flexible chain. It has approximately 28 HPMA groups and 9 4-O-methyl glucuronic acid groups per molecule. van der Waals and electrostatic interactions between excess HPMA groups and the approximately 5000 surface sulfate groups on a cellulose nanocrystal drive HPMAX adsorption onto the cellulose nanocrystal.

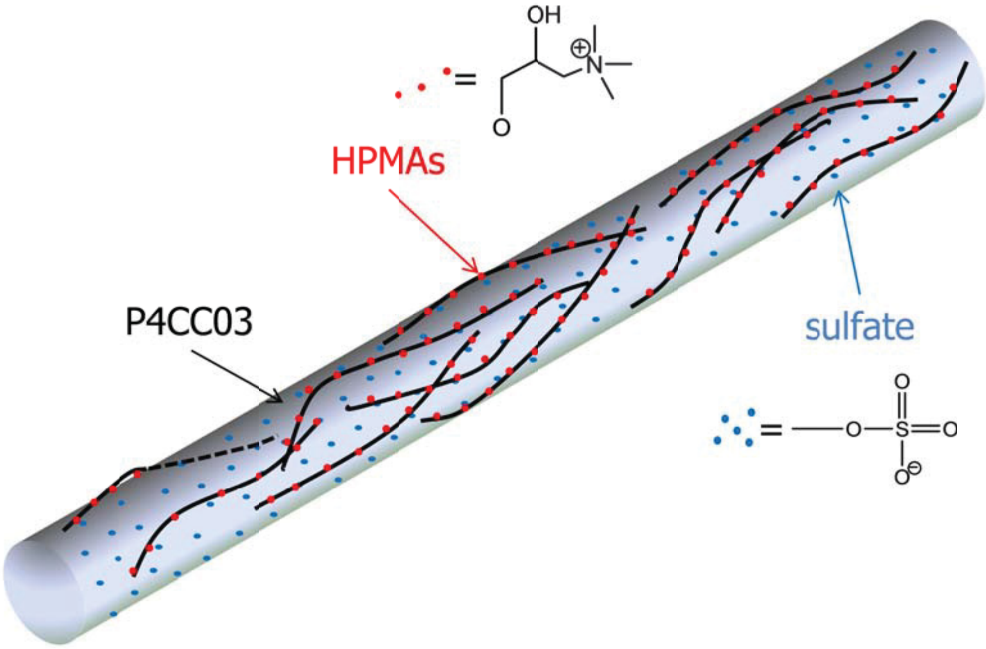

Figure 7.7 HPMAX adsorption onto cellulose nanocrystal surface: There are ~ 28 HPMA groups per HPMAX chain and ~ 5000 surface sulfate groups per DOE-2-12B. HPMAX adsorbs onto the cellulose nanocrystal through van der Waals and electrostatic interactions between the cationic HPMA groups in HPMAX and the anionic sulfate groups on cellulose nanocrystal.

Diffusion coefficients summarized in Table 7.2 show changes as R increases. The relationship between the diffusion coefficient and the polymer concentration is generally expressed as a stretched exponential function: [198,319,368]

$$D_t = D_0 \exp\left(-\alpha c^{\nu}\right) \tag{7.8}$$

where D_0, α, c, and ν are the diffusion coefficient at finite dilution, prefactor, concentration of polymer, and scaling exponent, respectively. Eqn. 7.8 is applicable to both polymer self-diffusion and probe diffusion. For probe diffusion, α and ν depend on the probe size and the interaction between the probe and polymer, respectively. Figure 7.8 shows a stretched exponential fit of D_t versus R as well as the dynamic viscosity (η) of the ternary systems with R. Translational diffusion coefficients can be found in Table 7.2 and the viscosities were measured with an Ubbelohde viscometer for various R values. The inset is $\ln(D_t/D_0)$ versus $R^{1/2}$. In this study, two concentrations of HPMAX were used to prepare a broad range of R. Equation 7.8 shows the universal relationship between diffusion coefficient and concentration (c) of polymer, not the concentration ratio of polymer to probe used in this study. Figure 7.8 shows the viscosity is essentially constant over the entire range of R, which means the two different probe concentrations do not influence the viscosities of the ternary systems in contrast to viscosity changes reported by Cush *et al.*[366] Thus, R could be analogous to polymer concentration for all ternary systems and applicable instead of concentration (c) in Eqn. 7.8. Stretched exponential fits of D_t versus R (solid red line) provides ν of 0.16 ± 0.01. Equation 7.8 normally shows the concentration dependence of diffusion coefficient to have exponents of $0.5 \leq \nu \leq 1$. Deviation in ν reflects adsorptive interactions between probes and polymer or polymer-induced probe aggregation. Figure 7.5 shows no polymer-induced probe aggregates and zeta-potential measurements and previous studies show the adsorption of HPMAXs onto cellulose nanocrystal.[367] The inset in Figure 7.8 highlights the significant deviation of the data from $\ln(D_t/D_0)$ versus $R^{1/2}$ because of the adsorptive interaction.[319] The dashed line indicates the predicted linear dependence of $\ln(D_t/D_0)$ on $R^{1/2}$ where no interaction between HPMAX and DOE-2-12B exist. Brown *et al.*[319] showed $v = 0.5$ for a polystyrene(PS)/carboxylmethyl cellulose (CMC)/water system with no adsorptive interaction and a smaller value of $v = 0.3$ for PS/hydroxylethyl cellulose (HEC)/water and PS/hydroxylpropyl cellulose (HPC)/water system where an adsorptive interaction exists. The electrostatic nature of adsorptive interaction in the HPMAX/DOE-2-12B/water system would be significantly stronger than that in PS/HEC/water or PS/HPC/water systems. As such, stronger deviation from $v = 0.5$ for the HPMAX/DOE-2-12B/water system is reasonable.

Cush *et al.*[366] and Kim *et al.*[369] studied probe/polymer/solvent ternary systems with anisotropic probes and discussed that the ratio of the diffusion coefficients (D_r/D_t) presumably cancels effects due to viscosity and that rotational motion of the probe is more strongly influenced by topological constraints of the polymers than the translational diffusion coefficient. Figure 7.9 shows $\ln(D_r/D_t)$ with various R values and numerical values of the diffusion coefficients are summarized in Table 7.2. Kim *et al.*[369] reported three mechanistic regimes for polymer adsorption onto probe particles defined by the concentration dependence of $\ln(D_r/D_t)$. The regimes were characterized by primary and secondary adsorption of polymer chains, and adsorption of polymeric micelles. The concentration dependence of $\ln(D_r/D_t)$ in Figure 7.9 is not strong compared to that for secondary adsorption and is comparable to primary adsorption. Zeta-potentials related with surface concentration of HPMAX deduced from previous studies also support monolayer-level adsorption of HPMAXs onto cellulose nanocrystals.[367]

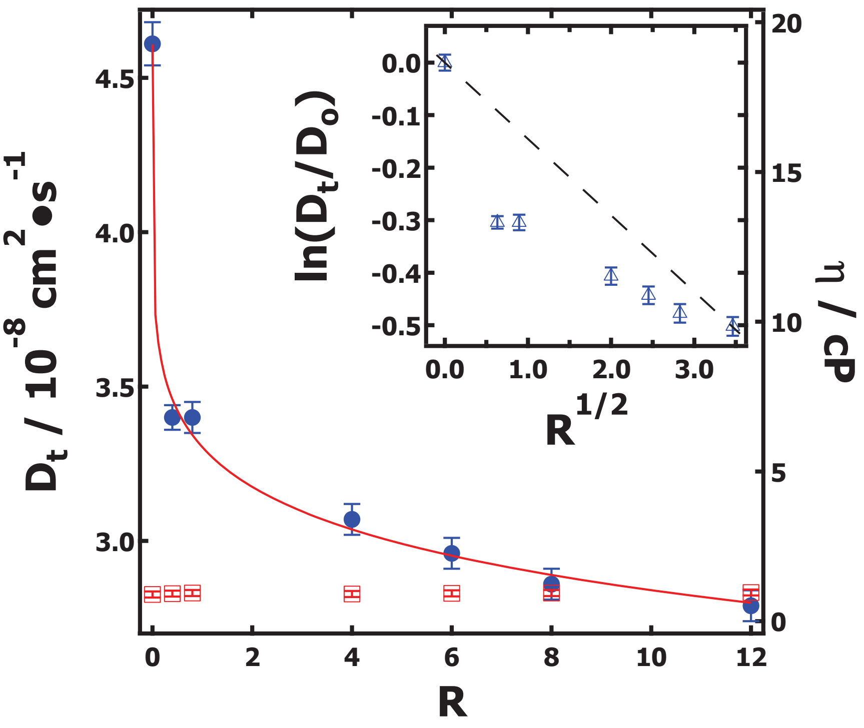

Figure 7.8 Profiles of D_t (●) and viscosity (η; □) versus R. The inset is $\ln(D_t/D_0)$ versus $R^{1/2}$. Curve fitting with a stretched exponential provides $v = 0.16 \pm 0.01$. η is essentially constant over the entire range of R. The inset shows deviation between the linear relationship of $\ln(D_t/D_0)$ and $R^{1/2}$. The dashed line represents the predicted linear relationship between $\ln(D_t/D_0)$ and $R^{1/2}$ where the interaction between HPMAX and DOE-2-12B does not exist.

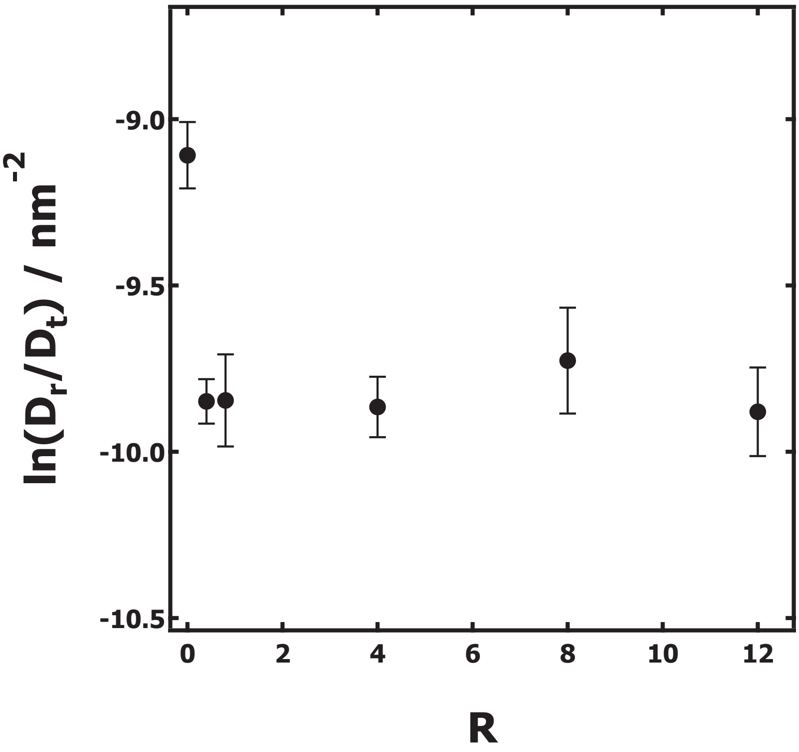

Figure 7.9 Profiles of $\ln(D_r/D_t)$ versus R. An insignificant concentration dependence of $\ln(D_r/D_t)$ is observed over all HPMAX concentrations studied, although solutions with HPMAX deviate significantly from R = 0.

Polarized and depolarized dynamic light scattering experiments in this study reveal HPMAX adsorption onto cellulose nanocrystals as expected from previous research related to xylan interactions with cellulose.[354-356] Figure 7.10 provides a schematic illustration of HPMAX adsorption onto cellulose nanocrystals (DOE-2-12B) in solution with various polymer/particle concentration ratios (R). Autocorrelation functions and decay time distributions from Vv mode mostly exhibit a single mode in HPMAX/DOE-2-12B/water ternary systems and its relaxation time increases as R increases. In Figure 7.4, decay time distributions of HPMAX aggregates seen in the HPMAX/water binary system show no significant differences with HPMAX concentration from 0.04 ~ 0.4 $mg \cdot mL^{-1}$. In Figure 7.5, HPMAX/DOE-2-12B/water ternary systems show that decay time distribution of the scatterers gradually shifts towards the slower mode because of HPMAX adsorption onto the cellulose nanocrystals. However, the slow mode at $R = 12$ still shows the size of scatterers are smaller than the size of HPMAX self-aggregates in HPMAX/water binary system. Comparisons between decay time distributions in Figures 7.4 and 7.5 show that HPMAX self-aggregates in the binary system, but adsorbs onto cellulose nanocrystals, rather than undergoing self-aggregation, in the ternary system. Increasing intensity autocorrelation functions from the Hv mode with increasing R implies that partial heterodyning decreases. Partial heterodyning is weakened as HPMAX concentration increases. Most heterodyning effects have been reported from gelation in complex polymer solutions. Norisuye *et al.*[370] and others discussed experimental phenomena related to gelation in complicated polymer solutions such as a significant changes in scattering intensity or the appearance of a characteristic long tail in the size or decay time distribution function.[131,370-372] These phenomena are not observed in the HPMAX/water binary systems. Also, Figure 7.8 shows that influence of increasing HPMAX concentration on viscosity of the ternary system is negligible. Thus, scattering differences caused by adsorption arise from partial heterodyning at low R and these scattering differences decrease with increasing HPMAX concentration (increasing R). For low R values, HPMAX adsorbs onto DOE-2-12B. However, not all DOE-2-12B particles have HPMAX on their surfaces (Figure 7.10 (B)). Hence, HPMAX adsorbs onto most surfaces of DOE-2-12B when the concentration of HPMAX is large enough (Figure 7.10 (C)). Autocorrelation functions in Figure 7.2 (F) exhibit noisy base lines that are related to aggregation of excess HPMAX (Figure 7.10 (D)).

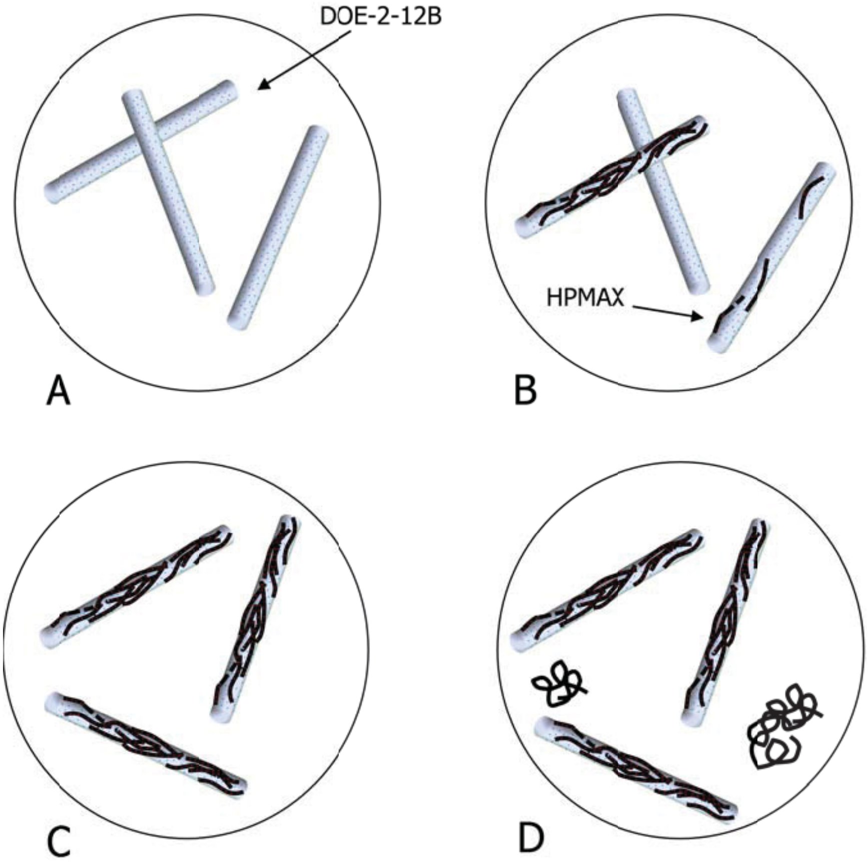

Figure 7.10 Schematic illustration of HPMAX adsorption onto DOE-2-12B at various R values: (A) R = 0, (B) R = 0.4, (C) R = 4, and (D) R = 12. (B) and (C) show cellulose nanocrystals with and without HPMAX adsorbed onto cellulose nanocrystals.

7.5 Conclusions

Zeta-potential measurements, and polarized and depolarized dynamic light scattering showed 2-hydroxypropyl-trimethylammonium xylans (HPMAXs) adsorbed onto rod-like cellulose nanocrystals (DOE-2-12B). Stretched exponential fits of the translational diffusion coefficient versus R and the concentration dependence of $\ln(D_r/D_t)$ demonstrated that adsorptive interactions between HPMAX and DOE-2-12B are strong. When the concentration of HPMAX was low compared to that of DOE-2-12B, HPMAX adsorbed onto some of the DOE-2-12B. Thus, partial heterodyning was observed in the ternary systems with low R values. As the concentration of HPMAX increased, partial heterodyning weakened. Hence, excess HPMAX did not adsorb onto DOE-2-12B in the ternary systems of high HPMAX concentration and as a consequence noisy base lines in the intensity autocorrelation functions were observed in this regime.

CHAPTER 8

Overall Conclusions and Suggestions for Future Work

8.1. Overall Conclusions

This study demonstrated that interactions between water-soluble polysaccharides in dilute solutions were strong enough to measure by light scattering. Also, the potential of cellulose nanocrystals as probes for studying complicated polysaccharide solutions was shown. Cellulose nanocrystals were prepared by hydrolysis of milled black spruce pulp with 60 wt % sulfuric acid at a temperature of 50 °C for 105 minutes. AFM images proved cellulose nanocrystals have an anisotropic structure. XPS survey spectra clarified that DOE-2-12B contains sulfate groups. The atomic concentration ratio of carbon to oxygen ($C/O = 1.27 \pm 0.18$) was comparable to the theoretical value for crystalline cellulose. XPS and conductometric titration showed nonnegligible numbers of sulfate groups on DOE-2-12B surface. Two replicates (DOE-2-12A and DOE-2-12B) were prepared from different batches and probed with depolarized and polarized dynamic light scattering. Intensity autocorrelation functions of the DOE-2-12B sample exhibited a weaker angular dependence than those of DOE-2-12A, which meant DOE-2-12B contained relatively smaller aggregates. Also, translational diffusion coefficients from Hv and Vv modes, $(4.76 \pm 0.38) \times 10^{-8}$ and $(4.61 \pm 0.07) \times 10^{-8}$ cm^2/s, respectively, showed good agreement for DOE-2-12B. The length and diameter of DOE-2-12B from Broersma's formula were 240 ± 18 and 22 ± 6 nm, respectively. The resultant length and diameter of DOE-2-12B were comparable to those of cellulose whiskers prepared from cotton. Hence, DOE-2-12B had a coupling parameter of 1.65 at the scattering angle of 90º. This value implies that DOE-2-12B is suitable as an anisotropic probe for studying polymer/probe/solvent ternary systems.

The ternary system of partially hydrophobically modified pullulan (P4CC03), cellulose nanocrystals, and water was probed with UV-Vis spectroscopy, dynamic light scattering, and zeta-potential measurements. Pullulan from *Aurebasidium pullulans* was modified with 4-chlorocinnamic acid (4CCA). P4CC03 had three 4-chlorocinnamic groups per 100 anhydroglucose units (AGUs). Unlike unmodified pullulan, P4CC03 had restricted solubility in water. Initially, little information about interactions between P4CC03 and DOE-2-12B was obtained by simple comparisons of intensity autocorrelation functions because of an extremely dilute concentration of P4CC03. Hence, two ternary systems (Rxn and PreX) having different sample preparation procedures were prepared. Detailed procedures were described in Section 4.2.3. A combination of UV-Vis spectroscopy and light scattering showed P4CC03 adsorbed onto DOE-2-12B during Rxn experiments. Also, average zeta-potentials and distributions demonstrated P4CC03 adsorption onto DOE-2-12B. Adsorbed P4CC03 screened DOE-2-12B surface hydroxyl and sulfate groups. Hence, the zeta-potential of DOE-2-12B in the DOE-2-12B/water system was slightly higher than that of the P4CC03/DOE-2-12B/water ternary system.

2-Hydroxypropyltrimethylammonium xylans (HPMAXs), synthesized by the reaction of birch xylan (BX) with 2,3-epoxypropytrimethylammonium chloride (EPTA), had a degree of molar substitution (MS) defined as the number of 2-hydroxypropyl-trimethylammonium groups per anhydroxylose unit (AXU). In this study, six HPMAX/water/cellulose nanocrystal ternary systems containing different concentration ratios between HPMAX (molar degree of substitution, MS = 0.34) and DOE-2-12B were investigated with light scattering and zeta-potential measurements. Significant changes of the zeta-potentials by HPMAX adsorption onto DOE-2-12B were observed. Strong attractive interactions between the xylan and cellulose provided qualitative and quantitative evidence of HPMAX adsorption onto DOE-2-12B. Decreasing partial heterodyning with increasing concentration of HPMAX in the ternary system indicated that HPMAX only adsorbed onto some of the DOE-2-12Bs at low HPMAX concentration. Hence, the scattering difference between the two modes from DOE-2-12B in the presence and absence of HPMAX led to partial heterodyning that decreased as HPMAX concentration increased. Also, translational and rotational diffusion coefficient changes were consistent with HPMAX adsorption onto DOE-2-12B. The concentration dependence of the ratio of rotational diffusion coefficient to the translational diffusion coefficient also supported a strong adsorptive interaction between HPMAX and DOE-2-12B.

Collectively, these studies showed the adsorption of hemicellulose and models for lignin-carbohydrate complexes (LCCs) onto cellulose nanocrystals in dilute water solutions could be detected through dynamic light scattering. The adsorption of each polysaccharide was observed even at very dilute concentrations. Also, these studies showed cellulose nanocrystals are promising anisotropic particles for probe diffusion studies of complicated polymer solutions.

8.2 Suggested Future Work

The probe diffusion studies of the ternary system with polysaccharides, cellulose nanoparticles, and water in this dissertation provided a fundamental guide for studying interactions between polysaccharides in very dilute solutions. However, a thorough understanding of the interaction is still challenging. In this section, some suggestions based on experience and preexisting knowledge are provided.

8.2.1 Surface Modification of Cellulose Nanocrystals

Various studies of macromolecular dynamics have shown that polymer/probe/solvent ternary systems are a straightforward model system for understanding interactions between polysaccharides and colloidal particles.[306-318] Spherical probes from polymers, inorganics, or metals like polystyrene and silica have frequently been used.[216,373-375] However, little is known about how the local structure of a polymer solution and interactions between polymers and probe affect anisotropic particle depolarized scattering.[241,289,324] PTFE latex particles and tobacco mosaic virus (TMV) are representative anisotropic probes that have been used previously.

Throughout this dissertation, diffusion studies of anisotropic probes (cellulose nanocrystals) showed that there were significant attractive interactions between cellulose nanoparticles and matrix polymers such as a modified hemicellulose and a pullulan derivative. This attractive interaction between water-soluble natural polymers in very dilute solutions has been discussed by Brown *et al.*[319] Vieira *et al.*[318] discussed the driving force of adsorption of a polymer onto colloidal particles with charge neutralization, electrostatic, and hydrophobic attractions. Surface modification of anisotropic probes would provide a wider window for studying these various interactions with polysaccharides. Compared to cellulose nanocrystals, PTFE latex particles and TMVs exhibit relatively restricted applications because of a relatively small aspect ratio or difficulty in tailoring the surface structure.

Habibi *et al.*[376] and de Souza Lima *et al.*[290] recently reviewed cellulose nanocrystal preparations and applications. They noted the advantages of surface modification of abundant hydroxyl groups by physicochemical functionalization. Esterification, etherification, oxidation, silylation, and polymer grafting provide stable negative or positive charges as well as tunable surface energies with hydrophobic matrices.[377-382] The techniques used in this thesis could be applied to surface modified cellulose nanocrystals.

8.2.2 Probe Diffusion

This study focused on probing the interaction, especially adsorption, between polysaccharides and cellulose nanocrystals. Thus, various experimental conditions were held constant. Otherwise, the movement of particles in ternary systems is influenced by the physicochemical environment including viscosity (concentration of added polymer), temperature, and ionic strength.[206,209,210,213,216,289,317,383] Probe diffusion studies with these variables would reveal local structures as well as dynamics of polysaccharides of complicated polysaccharide solutions.

Phillies *et al.*[206,373] reported the polymer concentration dependence as well as molar mass dependence of diffusion of spherical probes by studying ternary systems of polystyrene latex particles, dextrans, hydroxypropylcelluloses (HPCs), and solvents. These dynamics are well described by stretched exponentials:

$$D_t = D_{t,0} \exp(-\alpha C^{\nu}) \tag{8.1}$$

$$\alpha \propto M^{0.82} \tag{8.2}$$

$$g^{(1)}(t) = A \exp(-\theta \cdot t^{\beta}) \tag{8.3}$$

where D_t, $D_{t,0}$, C, $g^{(1)}(t)$, M, A, and θ are the translational diffusion coefficient, translational diffusion coefficient for an infinitely dilute concentration, concentration of polymer, electric field autocorrelation function, molar mass of polymer, spatial amplitude, and time constant, respectively. α, ν, and β are scaling parameters. Also, the Stokes-Einstein relationship does not fully explain the system at high polymer concentrations which led to the concept of microviscosity, η_{μ}:

$$\eta_{\mu} = \frac{kT}{6\pi D_t R} \tag{8.4}$$

where R is the radius of a probe whose size is already known. The microviscosity and translational diffusion coefficient are correlated in numerous cases.[206,213] Mustafa *et al.*[213] discussed the microviscosity in ternary systems similar to that of Phillies *et al.*[217] The viscosity window was divided into three regimes: underconstrained ($\eta_\mu < \eta$), macroscopic ($\eta_\mu \approx \eta$), and overconstrained ($\eta_\mu > \eta$). Diffusion of a probe is only slightly affected by polymers in an underconstrained regime. In an overconstrained regime, polymer adsorption onto the probe or aggregation of the probes is observed.

Understanding polymer dynamics such as diffusion in systems that have microviscosity effects remains a challenging problem. Anisotropic probes providing rotational diffusion coefficients would be helpful for studying dynamics of complicated ternary systems. Cush *et al.*[366] examined the diffusion of TMV in dextran solution and discussed that D_r/D_t cancels viscosity effects on the diffusion of the probe. Also, they showed D_r is more easily influenced by topological constraints than D_t.[366,384]

HPC is a semirigid polymer and similar model systems can be prepared with hydroxyproyl xylans (HPXs).[385] HPX has a less rigid backbone and hydroxypropyl groups make the resulting polymer amphiphilic. Also, HPX does not adsorb significantly onto model regenerated cellulose surfaces but interacts with methylated surfaces. Figure 8.1 and 8.2 show intensity autocorrelation functions and size distributions of four HPXs having different degrees of substitution. Characteristics of the HPXs are summarized in Table 8.1. All HPXs were kindly provided by Prof. Wolfgang Glasser at Virginia Tech.

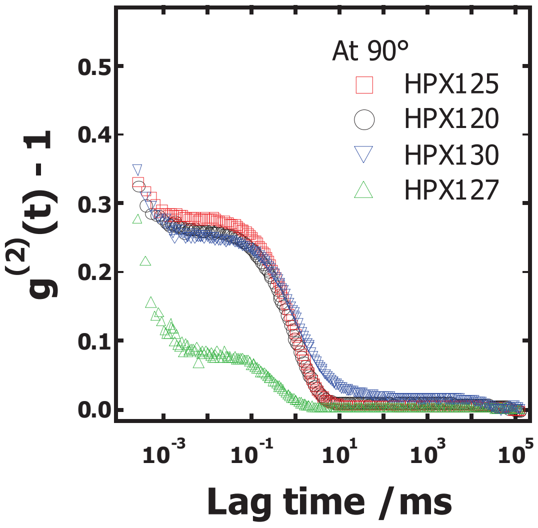

Figure 8.1 Intensity autocorrelation functions of HPXs obtained at a scattering angle of 90º. All measurements were performed at six scattering angles and a temperature of 298 K.

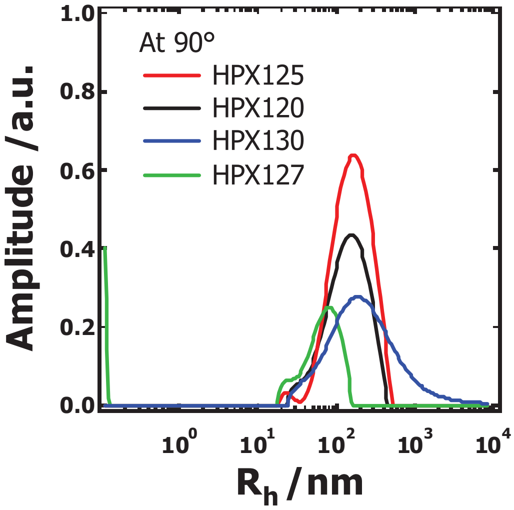

Figure 8.2 Size distributions of HPXs obtained from a CONTIN analysis. The colors of each distribution correspond to the colors used in Figure 8.1.

Table 8.1 Selected characteristics of HPXs

Samples[a]	DS[b]	CAC[‡] mg·L^{-1}
HPX120	0.37	90
HPX125	0.88	9
HPX127	1.69	20
HPX130	1.54	4

[a] Numbers in sample names denote the pH of aqueous solution used for the hydroxylpropylation of xylans (120 = 12.0, etc.).

[b], [‡] Degree of substitution (DS) and critical aggregation concentration (CAC) data were obtained from the dissertation of Dr. Kaya.[367]

Table 8.1 shows DS increases and CAC decreases with increasing pH for the HPX samples. HPX127 shows deviations and these are observed in Figure 8.1 and 8.2. The intensity autocorrelation function of HPX130 in Figure 8.1 reveals the possibility of multiple relaxation modes and the size distribution is significantly broader compared to the other HPX samples.[385] This broadness may come from relatively greater hydrophobicity which leads to greater aggregation and a lower CAC.

Ionic strength also influences the interactions between polymers and colloidal particles. Simon *et al.*[317] reported the adsorption of hydrophobically modified carboxymethylpullulans (HMCMPs) onto polystyrene particles as well as the desorption of HMCMPs induced by the addition of NaCl to the ternary system. This salting-out is due to the hydrolysis of ester bonds along the polysaccharide backbones that results in a competition between electrostatic repulsions and hydrophobically driven adsorption. Bremmell *et al.*[210] showed that probe diffusion studies in polyelectrolyte solutions with various salt concentrations can reveal information about relaxation modes in complicated polymer solutions. However, some discussions are still hypothetical and further studies are needed.

Figure 8.3 shows decay rates (Γ) versus the square of the scattering wave vector (q^2) for HPMAX (DS = 0.34)/water binary systems with various NaCl concentrations. Each solid line denotes linear fits of the form:

$$\Gamma = D_t q^2 \tag{8.5}$$

Increasing translational diffusion coefficients with increasing salt concentration are shown in Figure 8.4. This interesting observation for the effect of salt concentration on the diffusion coefficient of a polysaccharide should be addressed in extended studies.[386-389]

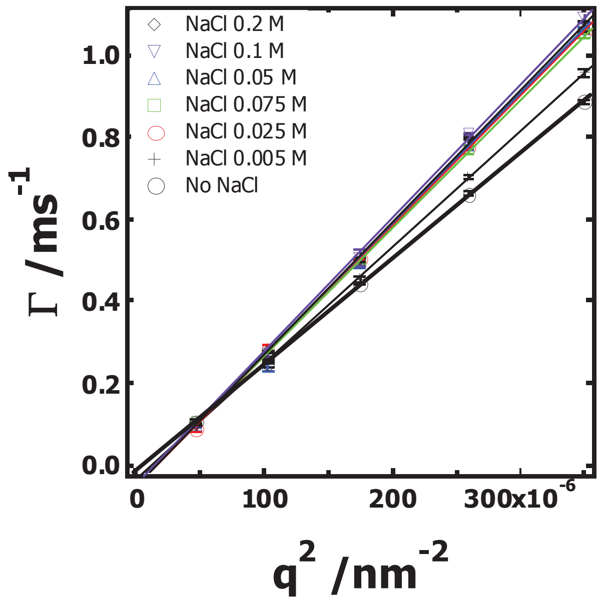

Figure 8.3 Γ versus q^2 profiles obtaibed for HPMAX (MS = 0.34)/water binary solutions with various amounts of NaCl at five scattering angles (30, 45, 60, 75, and 90°). The linear fits have non-zero intercepts.

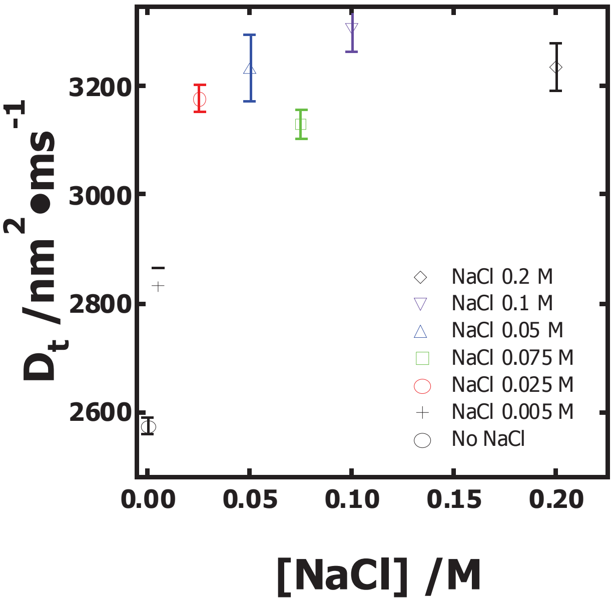

Figure 8.4 Translational diffusion coefficients ploted versus NaCl concentration where D_t increases with increasing salt concentration. All measurements were performed at five scattering angles and a temperature of 298 K.

Also, MS should influence the adsorption of cationic polysaccharides onto negatively charged cellulose nanocrystal probes. Adsorption of HPMAX with different MS onto self-assembled monolayers (SAMs) was probed and a maximum in adsorption was observed for intermediate MS when the SAM contained terminal carboxyl groups.[385] This interesting tendency can be examined in the ternary system of HPMAX/cellulose nanocrystal/water with polarized and depolarized light scattering. Figure 8.5 shows intensity autocorrelation functions versus q^2t profiles. All profiles show a slight angular dependence but no significant differences were observed relative to Figure 7.2 (Chapter 7). On the basis of the study by Kaya, experiments with lower DS may prove more interesting.

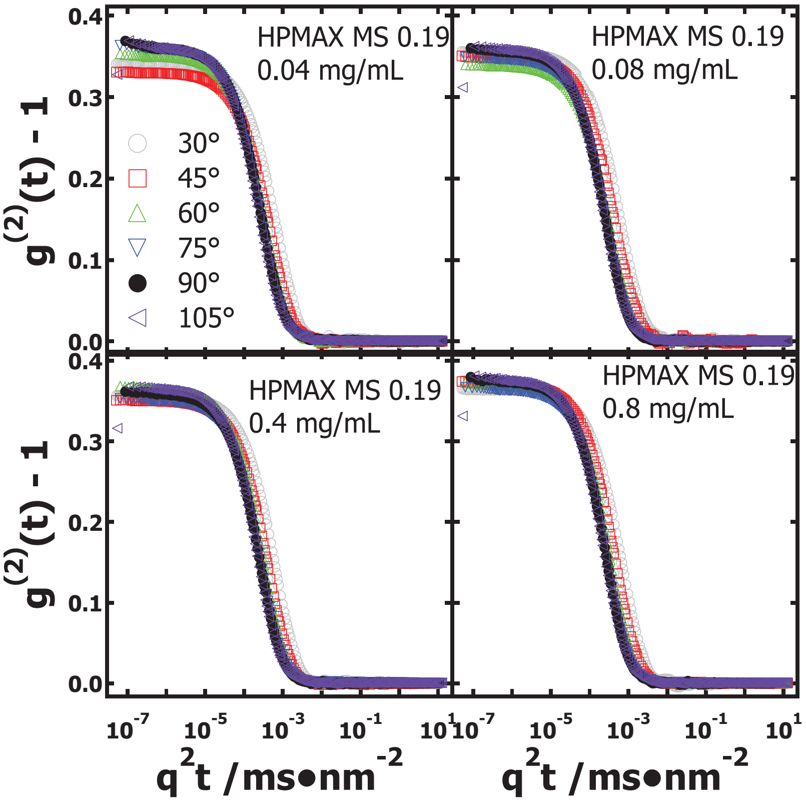

Figure 8.5 Intensity autocorrelation functions versus q^2t profiles obtained from HPMAX (MS = 0.19)/ water binary systems of various HPMAX concentrations. All symbols denoting scattering angles are identical in each graph. All measurements were performed at six scattering angles and a temperature of 298 K.

Bibliography

(1) Thomas, R. J. In *Wood Technology: Chemical Aspects* Goldstein, I. S.; Gould, R.F., Eds.; American Chemical Society: Washington, D. C., 1977.

(2) Perez, J.; Munoz-Dorado, J.; de la Rubia, T.; Martinez, J. *Int. Microbiol*., **2002**, *5*, 53.

(3) Jane, F. W.; Wilson, K.; White, D. J. B. In *The Structure of Wood*; Adam & Charles Black: London, 1970.

(4) Fujita, M.; Harada, H. In *Wood and Cellulosic Chemistry*; 2nd ed.; Hon, D. N.-S. and Shiraishi, N., Eds.; Marcel Dekker, Inc.: New York, NY, 2001.

(5) Reiter, W. D. *Curr. Opin.Plant Biol.* **2002**, *5*, 536.

(6) Dadswell, H. E.; Hillis, W. E. In *Wood Extractives*; Hillis, W. E., Ed.; Academic Press Inc.: New York, NY, 1962.

(7) Revol, J. F.; Goring, D. A. I. *Wood Sci.* **1982**, *14*, 120.

(8) Payen, A. *Compt. Rend.,* **1838**, *7*, 1052.

(9) Nevell, T. P.; Zeronian, S. H. In *Cellulose Chemistry and its Applications* John Wiley & Sons inc.: New York, 1985.

(10) Rees, D. A. In *Polysaccharide shapes* Chapman & Hall: London, 1977. 72

(11) Zechmeister, L.; Toth, G. *Ber. Dtsch. Chem. Ges*. **1931**, *B64*, 854.

(12) Freudenberg, K.; Blomgvist, C. *Ber. Dtsch. Chem. Ges*. **1935**, *B68*, 2070.

(13) Klemm, D.; Heublein, B. *Angewandte Chemie*. **2005**, *44*, 3358.

(14) Marchessault, R. H.; Sarko A. *Advan. Carbohyd. Chem*. **1967**, *22*, 421.

(15) Walton, A. G.; Blackwell, J. In *Biopolymers* Academic Press Inc.: New York, NY, 1973.

(16) Davis, W. E.; Bamy, A. J.; Peterson, F. C.; King, A. J. *J. Amer. Chem. Soc*. **1943**, *65*, 1294.

(17) Marrinan, H.; Mann, J. *J. Poly. Sci*. **1956**, *21*, 301.

(18) Hayashi, J.; Sueoka, A.; Ohkita, J.; Watanabe, S. *J. Polymer Sci. Polymer Lett. Ed*. **1975**, *13*, 23.

(19) Hess, K.; Kissig, H. *Physik. Chem. B*. **1941**, *49*, 235.

(20) Marchessault, R. H.; Sarko, A. In *Advanced Carbohydrate Chemistry*; M. L. Wolfrom, Ed.; Academic Press: New York 1967.

(21) Cardner, K. H.; Blackwell, J. *Biopolymers* **1974**, *13*, 1975.

(22) (a) Kolpak, F. J.; Blackwell, J. *Macromolecules* **1975**, *8*, 563.; (b) Kolpak, F. J.; Blackwell, J. *Macromolecules* **1976**, *9*, 273.; (c) Kolpak, F. J.; Weigh, M.; Blackwell, J. *Polymer* **1978**, *19*, 123.

(23) Sarko, A. *Tappi* **1985**, *61*, 59.

(24) Gardiner, F. S.; Sarko, A. *J. Appl. Poly. Sci., Appl. Poly. Symp*. **1983**, *37*, 307.

(25) Gardiner, F. S.; Sarko, A. *Can. J. Chem*. **1985**, 63, 173.

(26) McCarthy, J.L.; Islam, A. In *Lignin: Historical, Biological, and Materials Perspectives* Glasser, W.G.; Northey, R.A.; Schultz, T.P., Eds.; American Chemical Society: Washington, D.C., 1999.

(27) Adler, E. *Wood Sci. Technol*. **1977**, *11*, 169.

(28) Klyosov, A. A; Klesov, A. A In *Wood-Plastic Composites* John Wiley & Sons inc.: New York, 2007.

(29) Preston, R. D. In *Xylem Cell Development*; Barnett, J. R., Ed.; Castlehouse Publ. Ltd.: London, 1981.

(30) Alen, R. In *Forest Products Chemistry*; Stenius, P. Ed.; Tappi: Jyvaskyla, 2000.

(31) Freudenberg, K.; Neish, A. C. In *Biochemistry and Biophysics, Vol. 2* Springer-Verlag: Berlin-Heidelberg, 1968.
(32) Alder, E.; Ellmer, L. R. *Acta Chem. Scand.* **1948**, *2*, 839.
(33) Marton, J.; Alder, E. *Acta Chem. Scand.* **1961**, *15,* 370.
(34) Gierer, J.; Soderberg, S. *Acta Chem. Scand.* **1959**, *13,* 127.
(35) Sarkanen, K. V.; Schuerch, C. *Anal. Chem*. **1955**, *27*, 1245.
(37) Ludwig, C. H.; Nist, B. J.; McCarthy, J. L. *J. Amer. Chem. Soc*. **1964**, *80*, 1186.
(38) Alder, E.; Lundquist, K. *Acta Chem. Scand.* **1961**, *15,* 223.
(39) Freudenberg, K.; Chen, C.-L.; Harkin, J. M.; Nimz, H.; Renner, H. *Chem. Commun*. (*London*) **1965**, *11*, 224.
(40) Lenz, B. L. *Tappi*, **1968**, *51*, 511.
(41) Robert, D. R.; Brunow, G. *Holzforschung,* **1984**, *38*, 85.
(42) Larsson, S.; Miksche, G. E. *Acta Chem. Scand.* **1971**, *25,* 647.
(43) Nimz, H. *Holzforschung,* **1966**, *20*, 105.
(44) Freudenberg, K.; Chen, C.-L. *Chem. Ber.* **1967**, *100*, 3683.
(45) Freudenberg, K.; Racenak, D.; Pinoresinol, D.-L. *Chem. Ber*. **1953**, *86*, 755.
(46) Preston, R. D. *Annu. Rev. Plant Physiol*., **1979**, *30*, 55.
(47) Sun, R.; Sun, X. F.; Tomkinson, J. In *Hemicellulose: Science and Technology* Goldstein, I. S.; Gatenholm, P.; Tenkanen, M., Eds.; American Chemical Society: Washington, D. C., 2002.
(48) Saha, B.C. *J. Ind. Microbiol Biotechnol*. **2003**, *30*, 279.
(49) Johansson, M. H.; Samuelson, O. *Carbohydr. Res.* **1977**, *54*, 295.
(50) Beelik, A.; Conca, R. J.; Hamilton, J. K.; Parlow, E.V. *Tappi*, **1967**, *50*, 78.
(51) Sun, R.; Sun, X. F.; Tomkinson, J. *ACS Symp. Ser.* **2004**, *864*, 2.
(51) (a) Braconnot, H. *Ann*. **1833**, *7*, 242.; (b) Schönbein, C. F. *Philos. Mag*. **1847**, *31*, 7.
(53) Rubim, M. B. *Bull. Hist. Chem.* **2001**, *26*, 40.
(54) Walden, P. *Zeitschrift Naturwissenschaften* **1947***, 34*, 321.
(55) Baekeland, L. H. *J. Franklin Inst.* **1910, *169*, 55.**
(56) Baekeland, L. H. *Chem.Metall.l Eng.* **1910, *8*, 328.**
(57) Baekeland, L. H. *Angewandte Chemie* **1909**, *22*, 2006.
(58) Baekeland, L. H. *Chemical News and Journal of Industrial Science* **1910**, *100*, 18.
(59) Machta, J. *Phys. Rev. A* **1989**, *40*, 1720.
(60) Mark, J.; Ngai, K.; Graessly, W.; Mandelkern, L.; Samulski, E.; Koenig, J.; Winall, J. In *Physical Properties of Polymers* Cambridge University Press: Cambridge, 2004.
(61) Hiemenz, P. C.; Lodge, T. P. In *Polymer Chemistry* CRC Press: Florida, 2007.
(62) Rubinstein, M.; Colby, R. H. In *Polymer Physics* Oxford University Press: New York, 2008.
(63) Stein, R. S.; Powers, J. In *Topics of Polymer Physics* Imperial College Press: London, 2006.
(64) Bower, D. In *An Introduction to Polymer Physics* Oxford University Press: New York, 2002.
(65) Folry, P. J. In *Principles of Polymer Chemistry* Cornell University Press: Ithaca, 1953.
(66) Flory, P. J. In *Statistical Mechanics of Chain Molecules* Hansher Publisher; Oxford University Press: New York, 1969.
(67) Kuhn, W. *Kolloid Z.* **1934**, *68*, 2.
(68) Kratky, O.; and Porod, G. *Rec. Trav. Chim. Pays-Bas.* **1949**, *68, 1106.*

(69) Doi, M.; Edwards, S. F. In *The Theory of Polymer Dynamics* Oxford University Press: New York, 1986.
(70) Lindner, B. *J. Stat. Phys.* **2008**, *130*, 523.
(71) Rouse, P. E. *J. Chem. Phys.* **1953**, *21*, 1272.
(72) Zimm, B. H. *J. Chem. Phys.* **1956**, *24*, 269.
(73) Öttinger, H. C. *Colloid. Polym. Sci.* **1987**, *265*, 101.
(74) Edwards, S. F. *Proc. Phys. A* **1968**, *1*, 15.
(75) Mergell, B.; Everaers, R. *Macromolecules* **2001**, *34*, 5675.
(76) Lumley, J. *Annu. Rev. Fluid Mech.* **1969**, *1*, 367.
(77) Ferry, J. D. In *Viscoelastic Properties of Polymers*, 3rd Ed. Wiley: New York, 1980.
(78) Doi, M. In *Introduction to Polymer Physics* Clarendon Press: Oxford, 1996.
(79) Magda, J.; Larson, R.; Mackay, M. *J. Chem. Phys*. **1988**, *89*, 2504.
(80) Larson, R. In *Constitutive Equations for Poylmer Melts and Solutions* Buttersworths: New York, 1988.
(81) O'Sullivan, A. C. *Cellulose* **1997**, *4*, 173.
(82) Burchard, W. In *Polysaccharides* Danitriu, S. Ed.; Marcel Dekker, Inc.: New York, 2005
(83) Takahiro, S.; Yashuhiro, M. *Polym. J.* **2009**, *41*, 241.
(84) Steve, W. C.; Qi, W. *Struct. Chem.* **2009**, *20*, 291.
(85) Flory, P. J. *J. Am. Chem. Soc.* **1941**, *63*, 3083.
(86) Flory, P. J. *Chem. Revs.* **1946**, *39*, 137.
(87) Krejci, L. E.; Lucile, S.; John, H. *Arch. Biochem.* **1949**, *22*, 262.
(88) Ueda, S.; Fujita, K.; Komatsu, K.; Nakashima, Z. *Appl. Microbiol.* **1963**, *11*, 211.
(89) Tsunashima, Y.; Moro, K.; Chu, B.; Liu, T. Y. *Biopolymers* **1978**, *17*, 251.
(90) Kishikawa, Y.; Wiegand, S.; Kita, R. *Biomacromolecules* **2010**, *11*, 740.
(91) Ludwig, C. *Sitz. Ber. Akad. Wiss. Wien. Math.-naturw. Kl* **1856**, *20*, 539.
(92) Soret, C. *Arch. Geneve.* **1879**, *3*, 48.
(93) Schmidt, J.; Burchard, W.; Richtering, W. *Cellulose* **2003**, *10*, 13.
(94) Burchard, W. *Cellulose* **2003**, *10*, 213.
(95) Klohr, E.; Zugenmaier, P. *Macromol. Symp.* **1997**, *120*, 219.
(96) Saalwächter, K.; Burchard, W.; Klüfers, P.; Kettenbach, G.; Mayer, P.; Klemm, D.; Dugarmaa, S. *Macromolecules* **2000**, *33*, 4094.
(97) Saalwächter, K.; Burchard, W. *Macromolecules* **2001**, *34*, 5587.
(98) Schulz, L.; Seger, B.; Burchard, W. *Macromol. Chem. Phys.* **2000**, *201*, 2008.
(99) Silver, F. H.; Swann, D. A. *Int. J. Biol. Macromol.* **1982**, *4*, 425.
(100) Shogren, R.; Jamieson, A. M.; Blackwell, J. *J. Biol. Chem.* **1982**, *257*, 8627.
(101) Burchard, W.; Schmidt, M.; Stockmayer, W. H. *Macromolecules* **1980**, *13*, 1265.
(102) de Gennes, P.-G. In *Scaling Concepts in Polymer Physics*; Cornell University Press: New York, 1979.
(103) Geissler, E.; Hecht, A.-M.; Horkay, F. *Phys. Rev. Lett.* **2007**, *99*, 267801.
(104) Förster, S; Schmidt, M. In *polyelectrolytes in solution: Advances in Polymer Science, Vol. 120* Springer: Dordrecht, The Netherlands, 1995.
(105) Coviello, T.; Kajiwara, W.; Dentini, M.; Crescenzi, V. *Macromolecules* **1986**, *19*, 2826.
(106) Esquenet, C.; Buhler, E. *Macromolecules* **2002**, *35*, 3708.
(107) Buhler, E.; Boué, F. *Macromolecules* **2004**, *37*, 1600.
(108) Kojima, K; Berry, G. C. *Polymer* **1988**, *29*, 2249.
(109) Burchard, W. *Biomacromolecules* **2001**, *2*, 342.

(110) Burchard, W. *Makromol. Chem., Macromol. Symp.* **1988**, *18*, 1.
(111) Delay, M.; Tardieu, A. *Nature* **1983**, *30L*, 415.
(112) Delay, M.; Gormiec, A. *Biopolymers* **1983**, *22*, 1203.
(113) Benoit, H.; Benmouna, M. *Polymer* **1984**, *25*, 1059.
(114) Burchard, W.; Schmidt, M.; Stokemayer, W. H. *Macromolecules* **1980**, *13*, 1265.
(115) Stauch, O.; Schubert, R.; Savin, G.; Burchard, W. *Biomacromolecules* **2002**, *3*, 565.
(116) Ioan, C. E.; Aberle, T.; Burchard, W. *Macromolecules* **1999**, *32*, 7444.
(117) Ioan, C. E.; Aberle, T.; Burchard, W. *Macromolecules* **1999**, *32*, 8655.
(118) Ioan, C. E.; Aberle, T.; Burchard, W. *Macromolecules* **2001**, *34*, 326.
(119) Ioan, C. E.; Aberle, T.; Burchard, W. *Macromolecules* **2000**, *33*, 5730.
(120) Ioan, C. E.; Aberle, T.; Burchard, W. *Macromolecules* **2001**, *34*, 3765.
(121) Bauer, J.; Burchard, W. *Macromolecules* **1993**, *26*, 3103.
(122) Galinsky, G.; Burchard, W. *Macromolecules* **1996**, *29*, 1498.
(123) Writtgren, B.; Wahlund, K.-G. *J. Chomatoghr. A*. **1997**, *760*, 205.
(124) Roger, P.; Baud, B.; Colonna, P. *J. Chomatoghr. A*. **2001**, *917*, 179.
(125) Viebke, C.; Williams, P. A. *Anal. Chem.* **2000**, *72*, 3896.
(126) Moon, M. H.; Shin, D. Y.; Lee, N.; Hwang, E.; Cho, I.-H. *J. Chomatoghr. B*. **2008**, *864*, 15.
(127) Viebke, C.; Williams, P. A. *Anal. Chem*, **2000**, *72*, 3896.
(128) Pavel, K. In *Classical Light Scattering from Polymer Solution* Elsevier: New York, 1987.
(129) Johnson, C. S., Jr.; Gabriel, D. A. In *Light Scattering* Dover Publications: New York, 1993.
(130) Dhont, J. K. G. In *An Introduction to the Dynamics of Colloids* Elselvier: New York, 1996.
(131) Brown, W. In *Light Scattering – Principles and development* Oxford University Press, Inc.: New York, 1996. 295
(132) Hecht, E. In *Optics* Addison Wesley: Boston, 1998.
(133) Rayleigh, L. *Proc. Roy. Soc. London Ser. A* **1910**, *84*, 25.
(134) Smoluchowski, M. V. *Ann. d. Physik* **1909**, *25*, 205.
(135) Einstein, A. *Ann. d. Physik* **1910**, *33*, 1275.
(136) Zimm, B. H. *J. Chem. Phys.* **1948**, *16*, 1093.
(137) Debye, P. *Ann. Phys*. **1915**, *4*, 809.
(138) Zimm, B. H. *J. Chem. Phys.* **1948**, *16*, 1099.
(139) Wyatt, P. J. *Anal. Chim. Acta* **1993**, *272*, 1.
(140) Tanford, C. In *Physical Chemistry of Macromolecules* Wiley: New York, 1961.
(141) Zanten, J. H. V. *J. Chem. Phys*. **1995**, *102*, 9121.
(142) Folta-Stogniew, E.; Williams, K. R. *J. Biomol. Tech*. **1999**, *10*, 51.
(143) Berry, G. C. *J. Chem. Phys*. **1966**, *44*, 4550.
(144) Debye, P. *J. Phys. Coll. Chem*. **1947**, *51*, 18.
(145) Andersson, M.; Wittgren, B.; Wahlund, K. –G. *Anal. Chem*. **2003**, *75*, 4279.
(146) Jackson, C.; nilsson, L. M.; Wyatt, P. J. *J. Appl. Polym. Sci.* **1990**, *45*, 191.
(147) Gan, Z.; Fung, T. J.; Jing, X.; Wu, C.; Kuliche, W.-K. *Polymer* **1999**, *40*, 1961.
(148) Dřímalová, E.; Velebný, V.; Sasinková, V.; Hromádková, Z.; Ebringerová, A. *Carbohydr. Polym.* **2005**, *61*, 420.
(149) Fishman, M. L.; Hoagland, P. D. *Carbohydr. Polym*. **1994**, *23*, 175.

(150) Kulicke, W.-M.; Clasen, C.; Lohman, C *Macromol. Symp*. **2005**, *223*, 151.
(151) Zentz, F.; Verchere, J.-F.; Muller, G. *Carbohydr. Polym*. **1992**, *17*, 289.
(152) Picout, D. R.; Ross-Murphy, S. B.; Errington, N.; Harding S. E. *Biomacromolecules* **2003**, *4*, 799.
(153) Lee, S. L.; Lee, H. K.; Kim, S. C. *Polymer* **2004**, *45*, 4491.
(154) Ratcliffe, I; Williams, P. A.; Viebke, C.; Meadows, J. *Biomacromolecules* **2005**, *6*, 1977.
(155) Dentini, M.; Crescenzi, V.; Fidanza, M.; Coviello, T. *Macromolecules* **1989**, *22*, 954.-959
(156) Kratky, O.; Porod, G *J. Colloid. Sci.* **1949**, *4*, 35.
(157) Casassa, E. F. *J. Chem. Phys*. **1955**, *23*, 596.
(158) Burchard, W.; Kajiwara, K. *Proc. Roy. Soc. London Ser. A.* **1970**, *316*, 185.
(159) Wilhelm, E.; Arberle, T.; Burchard, W.; Landers, R. *Biomacromolecules* **2002**, *3*, 17.
(160) Stauch, O.; Schubert, R.; Savin, G.; Burchard, W. *Biomacromolecules* **2002**, *3*, 565.
(161) Ross-Murphy, S. B. In *Physical Techniques for the Study of Food Biopolymers* Chapmann & Hall: London, 1994.
(162) Denkinger, P.; Burchard, W.; Martin, K. *J. Phys. Chem.* **1989**, *93*, 1428.
(163) Borsali, R.; Lecommandoux, S.; Pecora, R.; benoît, H. *Macromolecules* **2001**, *34*, 4229.
(164) Brûlet, A.; Boué, F.; Cotton, J. P. *J. Phys. II* **1996**, *6*, 885.
(165) des Cloiseaux, J. *Macromolecules* **1973**, *6*, 403.
(166) Sharp P.; Bloomfield, V. A. *Biopolymers* **1968**, *6*, 1201.
(167) Yoshizaki T.; Yamakawa, H. *Macromolecules* **1980**, *13*, 1518.
(168) Imae, T.; Ikeda, S. *J. Phys. Chem*. **1986**, *90*, 5216.
(169) Benoit, H.; Doty, P. *J. Phys. Chem*. **1953**, *57*, 958.
(170) Mendichi, R.; Šoltés, L.; Schieroni, A. G. *Biomacromolecules* **2003**, *4*, 1805.
(171) Zimm, B. H.; Dandliker, W. B. *J. Phys. Chem*. **1954**, *58*, 644.
(172) Holthoff, H.; Borkovec, M.; Schurtenberger, P. *Phys. Rev. E* **1997**, *56*, 6945.
(173) (a) Nordmeier, E.; Dauwe, W. *Polym. J.* **1992**, *24*, 229.; (b) Nomula, S.; Cooper, S. L. *J. Phys. Chem. B* **2000**, *104*, 6963.
(174) Witte, T.; Decker, B.; Mattay, J. Huber, K. *J. Am. Chem. Soc.* **2004**, *126*, 9276.
(175) Teraoka, I. In *Polymer solutions – An Introduction to Physical Properties* wiley: New York, 2002.
(176) Schmitz, S. K. In *An Introduction to Dynamic Light Scattering by Macromolecules* Academic Press, Inc.: San Diego, 1990.
(177) Berne, B.; Pecora, R. In *Dynamic Light Scattering* Wiley: New York, 1976.
(178) DeLong, L. Mark; Russo, Paul S. In *Advances in Chemistry Series Vol. 277* Oxford University Press, Inc.: New York, 1990.
(179) Ostrowski, N,; Sornette, D.; Parker, P.; Pike, E.R. *Optica Acta* **1981**, *28*, 1059.
(180) Provencher, S. W. *J. Chem. Phys*. **1976**, *64*, 2773.
(181) Morrison, I. D.; Grabowski, E. F.; Herb, C. A. *Langmuir* **1985**, *1*, 496.
(182) Koppel, D. *J. Phys. Chem*. **1972**, *57*, 4814.
(183) Chu, B. In *Laser Light Scattering – Basic Principles and Practice*, 2nd Ed.: Academic Press, Inc.: San Diego, 1991.
(184) Santos, N. C.; Castanho, M. A. R. B. *Biophys. J.* **1996**, *71*, 1641.
(185) Ruf, H.; Gould, B. J.; Haase, W. *Langmuir* **2000**, *16*, 471.
(186) Phillies, G. D. *J. Anal. Chem*. **1990**, *62*, 1049.

(187) Jakeman, E. In *Photon Correlation and Light Beating Spectroscopy*; Cummins, H. Z. and Pike, E. R., Eds.; Plenum: New York, 1973.
(188) Digiorgio, V. In *Photon Correlation Spectroscopy and Velocimetry*; Cummins, H. Z. and Pike, E. R., Eds.; Plenum: New York, 1977.
(189) Schmidt, M.; Burchard, W.; Ford, N. C. *Macromolecules* 1978, 11, 452.
(190) Phillies, G. D. J. *Rev. Sci. Instrum.* **1996**, *67*, 3423.
(191) Phillies, G. D. J. *J. Chem. Phys*. **1981**, *74*, 260.
(192) Bantchev, G. B.; Russo, P. S.; McCarley, R. L.; Hammer, R. P. *Rev. Sci. Instrum.* **2006**, *77*, 043902.
(193) Phillies, G. D. J. *Macromolecules* **1986**, *19*, 2367.
(194) Phillies, G. D. J. *Macromolecules* **1987**, *20*, 558.
(195) Phillies, G. D. J.; Peczak, P. *Macromolecules*, **1988**, *21*, 214.
(196) Phillies, G. D. J._*Macromolecules* **1988**, *21*, 3101.
(197) Phillies, G. D. J. *J. Colloid Interface Sci.* **1987**, *119*, 518.
(198) Phillies, G. D. J. *J. Phys. Chem.* **1989**, *93*, 5029.
(199) Phillies, G. D. J. *J. Phys. Chem. B* **1997**, *101*, 4226.
(200) Streletzky, K. A.; Phillies, G. D. J. *J. Chem. Phys.* **1998**, *108*, 2975.
(201) Desvergne, S.; Héroguez, V.; Gnanou, Y.; Borsali, R. *Macromolecules* **2005**, *38*, 2400.
(202) Ullmann, G; Phillies, G. D. J. *Macromolecules* **1983**, *16*, 1947.
(203) Lin, T.-H.; Phillies, G. D. J. *Macromolecules* **1984**, *17*, 1686.
(204) Chu, B; Wu, D.-Q. *Macromolecules* **1987**, *20*, 1606.
(205) Kent, M. S.; Tirrell, M.; Lodge, T. P. *Macromolecules* **1992**, *25*, 5383.
(206) Phillies, G. D. J.; LaCroix, M. J. *J. Phys. Chem. B* **1997**, *101*, 39.
(207) Phillies, G. D. J. *J. Chem. Phys.* **2005**, *122*, 224905.
(208) Phillies, G. D. J. *Macromolecules* **2002**, *35*, 7414.
(209) Won, J.; Onyenemezu, C.; Miller, W. G.; Lodge, T. P. *Macromolecules* **1994**, *27*, 7389.
(210) Bremmell, K. E.; Dunstan, D. E. *Macromolecules* **2002**, *35*, 1994.
(211) Ullmann, G.; Phillies, G. D. J. *J. Phys. Chem*. **1986**, *90*, 5473.
(212) Dunstan, D. E.; Stokes, J. *Macromolecules* **2000**, *33*, 193.
(213) Mustafa, M.; Russo, P. S. *J. Colloid Interface Sci.* 1987, 129, 240.
(214) Russo, P. S.; Mustafa, M.; Cao, T.; Stephens, L. K. *J. Colloid Interface Sci.* **1988**, *122*, 120.
(215) Ngai, K. L.; Phillies, G. D. J. *J. Chem. Phys.* **1996**, *105*, 8385.-8397
(216) Bremmell, K. E.; Wissenden, N.; Dunstan, D. E. *Adv. Colloid Interface Sci*. **2001**, *141*, 89.
(217) Phillies, G. D. J. *Macromolecules* **1976**, *9*, 447.
(218) Phillies, G. D. J.; Wills, P. R. *J. Chem. Phys*. **1981**, *75*, 508.
(219) Phillies, G. D. J. *J. Chem. Phys.* **1982**, *77*, 2623.
(220) Phillies, G. D. J. *J. Chem. Phys*. **1983**, *79*, 2325.
(221) Phillies, G. D. J. *J. Chem. Phys*. **1984**, *80*, 6234.
(222) Phillies, G. D. J. *J. Phys. Chem.* **1995**, *99*, 4265.
(223) Phillies,G. D. J.; Hunt, R. H.; Strang, K.; Sushkin, N. *Langmuir* **1995**, *11*, 3408.
(224) Phillies, G. D. J.; Yambert, J. E. *Langmuir* **1996**, *12*, 3431.
(225) Koene, R. S.; Mandel, M. *Macromolecules* **1983**, *16*, 220.
(226) Provencher, S. W. *Comput. Phys. Commun.* **1982**, *27*, 213.
(227) Provencher, S. W. *Comput. Phys. Commun.* **1982**, *27*, 229.

(228) Provencher, S. W.; Štěpánek, P. *Part. Part. Syst. Charact.***1996**, *13*, 291.
(229) Schbablegger, H.; Glatter, O. *Appl. Optics* **1991**, *30*, 4889.
(230) Hansen, C. *SIAM Rev.* **1992**, *34*, 561.
(231) Hansen, C. *SIAM J. Sci. Comput*. **1993**, *14*, 1487.
(232) Shibayama, M.; Isaka, Y.; Shiwa, Y. *Macromolecules* **1999**, *32*, 7086.
(233) Ruf, H. *Prog. Colloid. Polym. Sci*. 2000, 115, 255.
(234) Ruf, H.; Gould, B. J.; Haase, W. *Langmuir*, **2000**, *16*, 471.
(235) Sohn, D.; Russo, P. S.; Davila, A.; Poche, D. S.; McLaughlin, M. L. *J. Colloid Interface Sci.* **1996**, *177*, 31.
(236) Pecora, R. In *Dynamic Light Scattering – Application of Photon Correlation Spectroscopy* Plenum Press: New York, 1985.
(237) Degiorgio, V.; Piazza, R.; Bellini, T.; Visca, M. *Adv. Colloid Interface Sci*. **1994**, *48*, 61.
(238) Piazza, R.; degiorgio, V. *J. Phys.: Condens. Matter* **1996**, *8*, 9497.
(239) Liu, T.; Chu, B. In *Encyclopedia of Surface and Colloid Science* Marcel Dekker Inc.: New York, 2003.
(240) Badaire, S.; Poulin, P.; Maugey, M.; Zakri, C. *Langmuir* **2004**, *20*, 10367.
(241) Cush, R.; Dorman, D.; Russo, P. S. *Macromolecules* **2004**, *37,* 9577.
(242) Degiorgio, V.; Piazza, R.; Johns, R. *Phys. Rev. E* **1995**, *52*, 2707.
(243) Vailati, A.; Asnaghi, D.; Giglio, M.; Piazza, R *Phys. Rev. E* **1993**, *48*, 2358.
(244) Broesma, S. J. *J. Chem. Phys.* **1960**, *32*, 1626.
(245) Broesma, S. J. *J. Chem. Phys*. **1960**, *32*, 1632.
(246) Broesma, S. J. *J. Chem. Phys*. **1981**, *74*, 6989.
(247) Castanho, M. A. R. B.; Brown, W.; Prieto, M. J. *Biophys. J.* **1992**, *63*, 1455.
(248) Young, C. Y.; Missel, P. J.; Mazer, M. A.; Benedek, G. B.; Carey, M. C. *J. Phys. Chem*. **1978**, *82*, 1375.
(249) Mastuoka, H.; Morikawa, H.; Yamaoka, H. *Colloids Surf. A* **1996**, *109*, 137.
(250) Lin, S.; Lin, J.; Nose, T.; Iyoda, T. *J. Polym. Sci. B* **2007**, *45*, 1333.
(251) Maeda, T.; Fujime, S. *Macromolecules* **1984**, *17*, 1157.
(252) Maeda, T. *Macromolecule* **1989**, *22*, 1881.
(253) Claire,K.; Pecora, R. *J. Phys. Chem. B* **1997**, *101*, 746.
(254) Maeda, T *Macromolecules* **1990**, *23*, 1464.
(255) Drögemeier, J.; Eimer, W. *Macromolecules* **1994**, *27*, 96.
(256) Hagerman, P. J.; Zimm, B. H. *Biopolymers* **1981**, *20*, 1481.
(257) Yoshizaki, T.; Yamakawa, H. *J. Chem. Phys.* **1984**, *81*, 982.
(258) (a) Beck-Candanedo, S.; Roman, M.; Gray, D. G. *Biomacromolecules* **2005**, *6*, 1048.; (b) Grunert, M.; Winter, W. T. *J. Polym. Environ.* **2002**, *10*, 27.
(259) Dong, S.; Roman, M. *J. Am. Chem. Soc.* **2007**, *129*, 13810.
(260) Liu, Z. In *Studies of Biomacromolucule Adsorption and Activity at Solid Surfaces by Surface Plasmon Resonance and Quartz Crystal Microbalance with Dissipation Monitoring* Doctoral dissertation: Vriginia Tech: Blacksburg, 2010.
(261) Schwikal, K.; Heinze, T.; Ebringerová, A.; Petzold, K. *Macromol. Symp.* **2006**, **232**, 49.
(262) Sarko, A.; Muggli, R. *Macromolecules* **1974**, *7*, 486.
(263) Sarko,A.; Southwick, J.; Hayashi, J. *Macromolecules* **1976**, *9*, 857.
(264) Woodcock, C.; Sarko, A. *Macromolecules* **1980**, *13*, 1183.
(265) Nishimura, H; Okano, T.; Sarko, A. *Macromolecules* **1991**, *24*, 759.
(266) Meyer, K. H.; Mirsh, L. *Helv. Chim. Acta.* **1937**, *20*, 232.

(267) Gardner, K. H.; Blackwell, J.; *Biopolymers* **1974**, *13*, 1975.

(268) Rånby, B. G. *Acta Chem. Scand.* **1949**, *3*, 649.

(269) Rånby, B. G.; Ribi, E. *Experientia* **1950**, *6*. 12.

(270) Revel, J.-F.; Bradford, H.; Griasson, J.; Marchessault, R. H.; Gray. D. G. *Int. J. Biol. Macromol.* **1992**, *14*, 170.

(271) Dong, X. M.; Revel, J.-F.; Gray. D. G. *Cellulose* **1998**, *5*, 19.

(272) Favier, V.; Chanzy, H.; Cavaille, J. Y. *Macromolecules* **1995**, *28*, 6365.

(273) Araki, J.; Wada, M.; Kuga, S.; Okano, T. *Colloids Surf. A* **1998**, *142*, 75.

(274) Dong, X. M.; Kumura, T.; Revel, J. F.; Gray, D. G. *Langmuir* **1996**, *12*, 2076.

(275) Yoshiharu, N.; Shigenori, K.; Masahisa, W.; Takeshi, O. *Macromolecules* **1997**, *30*, 6395.

(276) Marchessault, R. H.; Morehead F. F.; Walter, N. M. *Nature* **1959**, *184*, 632.

(277) Revol, J.-F.; Godbout, L.; Dong, X.-M.; Gray, D. G. *Liq. Cryst.* **1994**, *16*, 1.

(278) Revol, J.-F.; Godbout, L.; Dong, X.-M.; Gray, D. G. *Liq. Cryst.* **1994**, *16*, 127.

(279) Araki, J.; Wada, M.; Kuga, S. *Langmuir* **2001**, *17*, 21.

(280) Goussé, C.; Chanzy, H.; Excoffier, G.; Soubeyrand, L.; Fleury, E. *Polymer* **2002**, *43*, 2645.

(281) Zhang, L.; Liu, H.; Zheng, L.; Zhang, J.; Du, Y.; Feng, H. *Ind. Eng. Chem. Res.* **1996**, *35*, 4682.

(282) Fleming, K.; Gray, D. G.; Mattews, S *Chem. Eur. J.* **2001**, *7*, 1831.

(283) Sassi, J. F.; Chanzy, H. *Cellulose* **1995**, *2*, 111.

(284) Van Daele, Y.; Gaill, F.; Goffinet, G. *J. Struct. Biol.* **1991**,*106*, 115.

(285) Terech, P.; Chazeau, L.; Cavaille, J. Y. *Macromolecules* **1999**, *32*, 1872.

(286) De Souza Lima, M. M.; Wong, J. T.; Paillet, M.; Borsali, R.; Pecora, R. *Langmuir* **2003**, *19*, 24.

(287) Braun, B.; Dorgan, J. R.; Chandler, J. P. *Biomacromolecules* **2008**, *9*, 1255.

(288) Camins, B.; Russo, P. S. *Langmuir* **1994**, *10*, 4053.

(289) Jamil, T.; Russo, P. S. *Langmuir* **1998**, *14*, 264.

(290) De Souza Lima, M. M.; Borsali, R. *Macromol. Rapid Commun*. **2004**, *25*, 771.787

(291) Jiang, F.; Esker, A. R.; Roman, M. *Langmuir* **2010**, *26*, 17919.

(292) Pecora, R. *J. Chem. Phys.* **1968**, *48*, 4126.

(293) Gohy, J.-F.; Varshney, S. K.; Jérôme, R. *Macromolecules* **2001**, *34*, 3361.

(294) Xu, R.; Winnik, M. A.; Hallett, F. R.; Riess, G.; Croucher, M. D. *Macromolecules* **1991**, *24*, 87.

(295) (a) Araki, J.; Wada, M.; Kuga, S.; Okano, T. *Colloids Surf., A* **1998**, *142*, 75.; (b) Terech, P.; Chazeau, L.; Cavillé, J. Y. *Macromolecules* **1999**, *32*, 1872.

(296) (a) Serdyuk, I. N.; Zaccai, N. R.; Zaccai, J. In *Methods in Molecular Biophysics: Structure, Dynamics, Function* Cambridge University Press: Cambridge, 2007.; (b) Tsay, J. M.; Doose, S.; Weiss, S. *JACS*, **2006**, *128*, 1639.

(297) Roman, M; Winter, W. T. *Biomacromolecules* **2004**, *5*, 1671.

(298) Shuping Dong, Virginia Tech, Private Communication.

(299) Dahlke, B.; Larbig, H.; Scherzer, H. D.; Poltrock, R. *J. Cellular Plast.* **1998**, *34*, 361.

(300) Herrman, A. S.; Nickel, J.; Riedel, U. *Polym. Degrad. Stab.* **1998**, *59*, 251.

(301) Yamanaka, Y.; Esumi, K. *Colloids Surf A*. **1997**, *122*, 121.

(302) Argillier, J. F.; Audibert, A.; Lecourtier, J.; Moan, M.; Eousseau, L. *Colloids Surf. A*. **1996**, *113*, 247.

(303) Volpart, E.; Selb, J.; Candau, F.; Green, N.; Argillier, J. F.; Audibert, A. *Langmuir* **1998**, *14*, 1870.
(304) Poncet, C.; Tiberg, F.; Audebert, R. *Langmuir* **1998**, *14*, 1697.
(305) Kaya, A.; Du, X.; Liu, Z.; Lu, J. W.; Morris, J. R.; Glasser, W. G.; Heinze, T.; Esker, A. R. *Biomacromolecules* **2009**, *10*, 2451.
(306) Russel, W. B.; Saville, D. A.; Schowalter, W. R. In *Colloidal Dispersions*; Canbridge: Cambridge, 1989.
(307) Hunter, R. J. In *Foundations of Colloid Science*; Clarendon: Oxford, 1986.
(308) Kim, S.; Sung, J. H.; Ahn, K. H.; Lee, S. J. *Langmuir* **2009**, *25*, 6155.
(309) Hooper, J. B.; Schweizer, K. S. *Macromolecules* **2005**, *38*, 8858.
(310) Asakura, S.; Oosawa, F. *J. Chem. Phys.* **1954,** *22*, 1255.
(311) Seebergh, J. E.; Berg, J. C. *Langmuir* **1994**, *10*, 454.
(312) Ogden, A.; Lewis, J. A. *Langmuir* **1996**, *12*, 3413.
(313) Brown, W; Rymden, R. *Macromolecules* **1988**, *21*, 840.
(314) Phillies, G. D. J.; Brown, W.; Zhou, P. *Macromolecules* **1992**, *25*, 4948.
(315) Leonard, M.; Fournier, C.; Dellacherie, E. *J. Colloid Interface Sci*. **1999**, *220*, 380.
(316) Fournier, C.; Leonard, M.; Le Cof-Leonard, I.; Dellacherie, E. *Langmuir* **1995**, *11*, 2344.
(317) Simon, S.; Picton, L.; Le Cef, D.; Muller, G. *Polymer* **2005**, *46*, 3700.
(318) Vieira, D. B.; Lincopan, N.; Mamizuka, E. M.; Petri, D. F. S.; Carmona-Ribeiro, A. M. *Langmuir* **2003**, *19*, 924.
(319) Brown, R.; Rymden, R. *Macromolecules* **1986**, *19*, 2942.
(320) Streletzdy, K. A.; Philliles, G. D. J. *J. Polym. Sci. B* **1998**, *36*, 3087.
(321) Kato, T.; Katsuki, T.; Takahashi, A. *Macromolecules* **1984**, *17*, 1726.
(322) Akiyoshi, K.; Deguchi, S.; Moriguchi, N.; Yanaguchi, S.; Sunamoto, J. *Macromolecules* **1993**, *26*, 3062.
(323) Lendlein, A.; Jiang, H.; Junger, O.; Langer, R. *Nature* **2005**, *434*, 879.
(324) Shi, D.; Matsusaki, M.; Akashi, M. *Bioconjugate Chem.* **2009**, *20*, 1917.
(325) Ketner, A. M.; Kumar, R.; Davies, T. S.; Elder, P. W.; Raghavan, R. *J. Am. Chem. Soc.* **2007**, *129*, 1553.
(326) Tangirala, R.; Baer, E.; Hiltner, A.; Weder, C. *Adv. Funct. Mater*. **2004**, *14*, 595.
(327) Sandholzer, M.; Bichler, S.; Stelzer, F.; Christian, S. *J. Polym. Sci., A* **2008**, *46*, 2402.
(328) Ko, J. H.; Yin, H.; An, J.; Chung, D. J. *Macromolecular Research* **2010**, *18*, 137.
(329) Cohen, M. D.; Schmidt, G. M. J.; Sonntag, F. I. *J. Chem. Soc.* **1964**, 2000.
(330) Muroga, Y.; Yamada, Y.; Noda, I.; Nagasawa, M. *Macromolecules* **1987**, *20*, 3003.
(331) Lee, I.; Akiyoshi, K. *Biomaterials* **2004**, *25*, 2911.
(332) Sze, A.; Erickson, D.; Ren, L.; Li, D. *J. Colloid Interf. Sci*. **20**03, *261*, 402.
(333) Butt, H.-J; Graf, K.: Kappl, M. In *Physics and Chemistry of Interfaces* WHILY-VCH Verlag-GmbH & Co.: Weinheim, 2003.
(334) Ohshima, H.; Healy, T. W.; White, L. R. *J. Colloid Interface Sci.* **1982**, *90*, 17.
(335) Ishikawa, Y.; Noboru, A.; Ohshima, H. *Colloids Surf. B* **2005**, *46*, 147.
(336) Rezwan, K.; Meier, L. P.; Rezwan, M.; Vörös, J.; Textor, M.; Gauckler, L. J. *Langmuir* **2004**, 20, 10055.
(337) Rezwan, K.; Meier, L. P.; Gauckler, L. J. *Biomaterials* **2005**, *26*, 4351.
(338) Hosseinkhani, H.; Hosseinkhani, M. *Current Drug Safty* **2009**, *4*, 79.
(339) Filson, P. B.; Dawson-Andoh, B. E.; Schwegler-Berry, D. *Green Chem*. **2009**, *11*, 1808.

(340) Yim, H.; Yang, S.-G.; Jeon, Y. S.; Park, I. S.; Kim, M.; Lee, D. H.; Bae, Y. H.; Na, K. *Biomaterials* **2011**, *32*, 5187.
(341) Kosmulski, M.; Kartikainen, J.; Mączka, E.; Janusz, W.; Rosenholm, J. B. *Anal. Chem.* **2002**, *74*, 253.
(342) Kawaguchi, T.; Nakahara, H.; Fukuda, K. *Thin Solid Films* **1985**, *133*, 29.
(343) Vinson, J. R.; Sierakowski, R. L. In *The behavior of structures composed of composite materials* Springer: Dordrecht, 2008.
(344) Berglund, L. A.; Peijs, T. *MRS Bull.* **2010**, *35*, 201.
(345) Chivrac, F.; Pollet, E.; Avérous, L. *Mat. Sci. Eng. R* **2009**, *67*, 1.
(346) Averous, L.; Boquillon, N. *Carbohydr. Polym.* **2004**, *56*, 111.
(347) Averous, L.; Le Digabel, F. *Carbohydr. Polym.* **2006**, *66*, 480.
(348) Fowler, P. A.; Hughes, J. M.; Elias, R. M. *J. Sci. Food Agric.* **2006**, *86*, 1781.
(349) Samir, M. A.; Alloin, F.; Dufresne, A. *Biomacromolecules* **2005**, *6*, 612.
(350) Brumer III, H.; Zhou, Q.; Baumann, M. J.; Carlsson, K.; Teeri, T. T *J. Am. Chem. Soc.***2004**, *126*, 5715.
(351) Schwikal, K.; Heinze, T.; Ebringerová, A.; Petzold, K. *Macromol. Symp.* **2006**, *232*, 49.
(352) Hartley, P. G.; McArthur, S. L.; McLean, K. M.; Griesser, H. J. *Langmuir* **2002**, *18*, 2483.
(353) Hansen, N. M. L.; Plackett, D. *Biomacromolecules* **2008**, *9*, 1493.
(354) Gröndahl, M.; Eriksson, L.; Gatenholm, P. *Biomacromolecules* **2004**, *5*, 1528.
(355) Mora, F.; Ruel, K.; Comtat, J.; Joseleau, J.-P. *Holzforschung* **1986**, *40*, 85.
(356) Henriksson, Å.; Gatenholm, P. *Holzforschung* **2001**, *55*, 494.
(357) Westbye, P.; Köhnke, Y.; Glasser, W.; Gatenholm, P. *Cellulose* **2007**, *14*, 603.
(358) Linder, Å; Bergman, R.; Bodin, A.; Gatenholm, P. *Langmuir* **2003**, *19*, 5072.
(359) Bica, C. I. D.; Borsali, R.; Geissler, E.; Rochas, C. *Macromolecules* **2001**, *34*, 5275.
(360) Kloster, C.; Bica, C.; Lartigue, C.; Rochas, C.; Samios, D.; Geissler, E. *Macromolecules* **1998**, *31*, 7712.
(361) Kloster, C.; Bica, C.; Rochas, C.; Samios, D.; Geissler, E. *Macromolecules* **2000**, *33*, 6372.
(362) Saake, B.; Kruse, T.; Puls, J. *Bioresour. Technol.* **2001**, *80*, 195.
(363) Hansson, J. A.; Hartler, N. *Sven. papperstidn.* **1969**, *72*, 521.
(364) Sergio, R.; Aragón, S.; Pecora, R. *J. Chem. Phys.* **1985**, *82*, 5346.
(365) Newman, J.; Swinney, H. L.; Day, L. A. *J. Mol. Biol.* **1977**, *116*, 593.
(366) Cush, R.; Russo, P. S.; Kucukyavuz, Z.; Bu, Z.; Neau, D.; Shih, D.; Kucukyavuz, S.; Ricks, H. *Macromolecules* **1997**, *30,* 4920.
(367) Kaya, A. In *Studies of Polysaccharide Adsorption onto Model Cellulose Surfaces and Self-assembled Monolayers by Surface Plasmon Resonance Spectroscopy* Doctoral dissertation: Vriginia Tech: Blacksburg, 2009.
(368) Phillies, G. D. J. *Macromolecules* **1998**, *31*, 2317.
(369) (a) Kim. M.; Sim, J.-H.; Sohn, D. *Macromolecules*, **2003**, *36*, 9986; (b) Zero, K. M.; Pecora, R. *Macromolecules* **1982**, *15*, 87.
(370) Norisuye, T.; Shibayama, M.; Tamaki, R.; Chujo, Y. *Macromolecules* **1999**, *32*, 1528.
(371) Lang, P.; Burchard, W. *Macromolecules* **1991**, *24*, 814.
(372) Ren, S. Z.; Sorensen, C. M. *Phys. Rev. Lett.* **1993**, *70*, 1727.
(373) Phillies, G. D. J.; Gong, J.; Li, L.; Rau, A.; Zhang, K.; Yu, L.-P.; Rollings, J. *J. Phys. Chem.* **1989**, *93*, 6219.

(374) Joosten, J. G. H.; Gelade, E. T. F.; Pusey, P. N. *Phys. Rev. A* **1990**, *42,* 2161.
(375) Gasilova, E. R.; Toropova, A. A.; Bushin, S. V.; Khripunov, A. K.; Grischenko, L. A.; Aleksandrova, G. P. *J. Phys. Chem. B* **2010**, *114*, 4204.
(376) Habibi, Y.; Lucia, L. A.; Rojas, O. J. *Chem. Rev.* **2010**, *110*, 3479.
(377) Kim, J.; Montero, G.; Habibi, Y.; Hinestroza, J. P.; Genzer, J.; Argyropouls, D. S.; Rojas, O. J. *Polym. Eng. Sci.* **2009**, *49*, 2054.
(378) Habibi, Y.; Chanzy, E. D.; Vignon, M. R. *Cellulose* **2006**, *13*, 679.
(379) Hasani, M.; Cranston, E. D.; Westmana, G.; Gray, D. G. *Soft Matter* **2008**, *4*, 2238.
(380) Braun, B.; Dorgan, J. R. *Biomacromolecules* **2009**, *10*, 334.
(381) Yuna, H.; Nishiyama, Y.; Wada, M.; Kuga, S. *Biomacromolecules* **2006**, *7*, 696.
(382) Mangalam, A. P.; Simonsen, J.; Benight, A. S. *Biomacromolecules* **2009**, *10*, 497.
(383) Yang, T.; Jamieson, A. M. *J. Colloid. Interface Sci.* **1988**, *126*, 220.
(384) Doi, M.; Edwards, S. F. *J. Chem. Soc., Faraday Trans 2* **1978**, *74*, 560.
(385) Kaya, A.; Drazenovich, D. A.; Glasser, W. G.; Heinze, T.; Esker, A. R. *ACS Symp. Ser.* **2009**, *1019*, 173.
(386) Koene, R. S.; Nicolai, T.; Mandel, M. *Macromolecules* **1983**, *16*, 227.
(387) Koene, R. S.; Nicolai, T.; Mandel, M. *Macromolecules* **1983**, *16*, 231.
(388) Drifford, M.; Dalbiez, J. P. *J. Physique Lett.* **1985**, *46*, L311.
(389) Froster, S.; Schmidt, M.; Antonietti, M. *Polymer* **1990**, 31, 781.

Appendix A. Basic Configuration

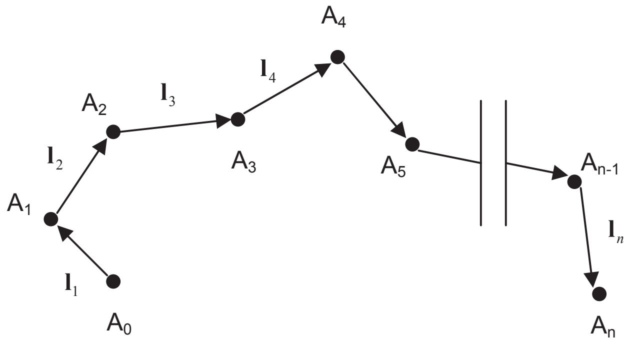

Figure A.1 Schematic picture of skeletal bonds of a chain

The polymer chain configuration is simplified with skeletal bonds as shown in Figure A.1. Each atom in the skeletal bond is numerated serially, e.g. A_0, and $\mathbf{l}_n$ means a bond vector. The vector connects two ends and is named an end-to-end vector, $\mathbf{h}$:

$$\mathbf{h} = \sum_{i=1}^{n} \mathbf{l}_i \tag{A.1}$$

and its scalar magnitude is h^2:

$$h^2 = \mathbf{h} \bullet \mathbf{h} = \sum_{i,j} \mathbf{l}_i \bullet \mathbf{l}_j \ . \tag{A.2}$$

A vector can be expressed as a column matrix and be rewritten:

$$h^2 = \sum_i l_i^2 + 2 \sum_{0<i<j\leq n} \mathbf{l}_i \bullet \mathbf{l}_j \tag{A.3}$$

where the first summation is from the diagonal terms and the second summation is from all *ij* pairs. Then, similarly the scalar length of the vector between the *i*-th and *j*-th atoms can be defined as:

$$h_{ij}^2 = \sum_{i'=i+1}^{j} l_{i'}^2 + 2 \sum_{i<i'<j'\leq j} \mathbf{l}_{i'} \bullet \mathbf{l}_{j'} \tag{A.4}$$

From the definition, $s = R_g$, the radius of gyration is:

$$s^2 = (n+1)^{-1}\sum_0^n s_i^2 \tag{A.5}$$

where s_i is the distance of atom i from the center of gravity or

$$s^2 = x^{-1}\sum_1^x s_k^2 \tag{A.6}$$

where x is the number of repeating units and a vector $\mathbf{s}_i$ is (Figure A.2) is defined as:

$$\mathbf{s}_i = \mathbf{s}_0 + \mathbf{h}_{0i}\,. \tag{A.7}$$

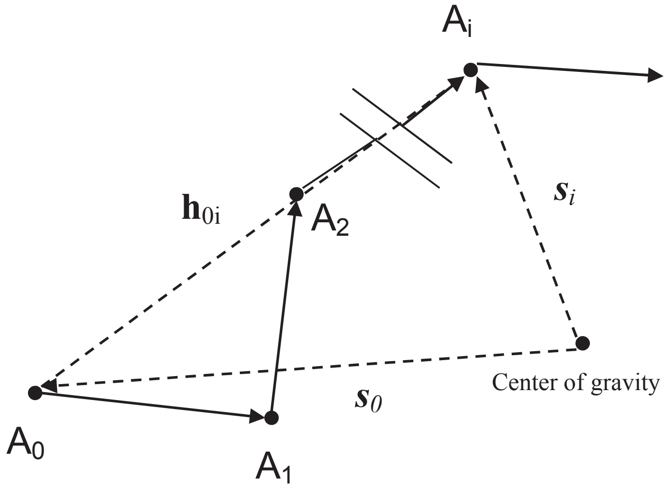

Figure A.2 Schematic picture of the relationship in Eqn. A.6

Eqn. A.5 is rewritten:

$$s^2 = (n+1)^{-1}\sum_0^n s_i^2 = (n+1)^{-1}\sum_0^n \mathbf{s}_i \bullet \mathbf{s}_i \tag{A.8}$$

and Eqns. A.7 and A.8 provide:

$$\begin{aligned} s^2 &= (n+1)^{-1}\sum_0^n (\mathbf{s}_0 + \mathbf{h}_{0i})\bullet(\mathbf{s}_0 + \mathbf{h}_{0i}) \\ &= s_0^2 + 2(n+1)^{-1}\mathbf{s}_0 \bullet \left[\sum_1^n \mathbf{h}_{0i}\right] + (n+1)^{-1}\sum_1^n \mathbf{h}_{0i}^2 \end{aligned} . \tag{A.9}$$

Also, a *random walk* assumption provides:

$$\sum_0^n \mathbf{s}_i = 0 \tag{A.10}$$

and we have from Eqn. A.7:

$$\mathbf{s}_0 = -(n+1)^{-1}\sum_1^n \mathbf{h}_{0i} \tag{A.11}$$

$$\left[\begin{array}{c} \text{Note}: \sum_{i=m}^{n} x = (n-m+1)x \\ \sum_0^n i = \sum_1^n i \end{array}\right]$$

and

$$s_0^2 = (n+1)^{-2}\sum_{i=1}^{n}\sum_{j=1}^{n}\mathbf{h}_{0i} \bullet \mathbf{h}_{0j}\ . \tag{A.12}$$

Then, by substitution of Eqn. A.12 into Eqn. A.9 we have:

$$s_0 = (n+1)^{-1}\sum_1^n h_{0i} - (n+1)^{-2}\sum_{i=1}^{n}\sum_{j=1}^{n}\mathbf{h}_{0i} \bullet \mathbf{h}_{0j} \tag{A.13}$$

and

$$\mathbf{h}_{0i} \bullet \mathbf{h}_{0j} = \frac{\left(h_{0i}^2 + h_{0j}^2 - h_{ij}^2\right)}{2}\ . \tag{A.14}$$

$$\left[\begin{array}{l} \because \mathbf{h}_{0i} \bullet \mathbf{h}_{0j} = |h_{0i}||h_{0j}|\cos\theta \\ h_{ij}^2 = h_{0i}^2 + h_{0j}^2 - 2h_{0i}h_{0j}\cos\theta \end{array}\right]$$

Finally, we find:

$$\begin{aligned} s^2 &= (n+1)^{-2}\left[\sum_{i=1}^{n} h_{0i}^2 + \frac{1}{2}\sum_{i=1}^{n}\sum_{j=1}^{n} h_{ij}^2\right] \\ &= \frac{1}{2}(n+1)^{-2}\sum_{i=0}^{n}\sum_{j=0}^{n} h_{ij}^2 \\ &= (n+1)^{-2}\sum_{0\le i<j\le n} h_{ij}^2 \end{aligned} \tag{A.15}$$

Appendix B. Moments of Distributions and the Unperturbed State

From Eqn. A.3:

$$\left\langle h^2 \right\rangle = \sum_i \left\langle l_i^2 \right\rangle + 2\sum_{i<j} \left\langle \mathbf{l}_i \bullet \mathbf{l}_j \right\rangle , \tag{B.1}$$

The first moment of the distribution represented by Eqn. B.1 shows spatial distributions of bond lengths and the second moment of the end-to-end distance, $\left\langle h^2 \right\rangle$, provides the configuration. We assume that l^2 is the average squared bond length for the given configuration:

$$\sum_i \left\langle l_i^2 \right\rangle = \left\langle \sum_i l_i^2 \right\rangle = n\left\langle l^2 \right\rangle \tag{B.2}$$

where n is the number of skeletal bonds, then, we have:

$$\left\langle h^2 \right\rangle = n\left\langle l^2 \right\rangle + 2\sum_{i<j} \left\langle \mathbf{l}_i \bullet \mathbf{l}_j \right\rangle \tag{B.3}$$

where bond lengths are fixed. Thus Eqn. B.1 becomes:

$$\left\langle h^2 \right\rangle = nl^2 + 2\sum_{i<j} \left\langle \mathbf{l}_i \bullet \mathbf{l}_j \right\rangle . \tag{B.4}$$

For the radius of gyration:

$$\left\langle s^2 \right\rangle = (n+1)^{-2} \sum_{0 \le i < j \le n} \left\langle h_{ij}^2 \right\rangle \tag{B.5}$$

So far, discussions are based upon the *model* state of polymers in solution, regardless of the concentration, and free from (1) external forces, (2) hydrodynamic intermolecular interactions, and (3) thermodynamic interactions. However, two constraints could be considered: steric hindrance from bond direction and rotation. The state that suffices all conditions is referred to as the *unperturbed* state and the subscript zero denotes this state.

Appendix C. The Freely Jointed Chain

The random flight model shows:

$$\left\langle \mathbf{l}_i \bullet \mathbf{l}_j \right\rangle = 0, \quad i \neq j \tag{C.1}$$

Thus, Eqn. B.4 is rewritten as:

$$\left\langle h^2 \right\rangle_0 = nl^2 \tag{C.2}$$

where n (= j-i) is independent of any value of the length. l^2 depends on bond lengths and will change with different lengths of bonds. Thus,

$$C_n = \frac{\left\langle h^2 \right\rangle_0}{nl^2} \tag{C.3}$$

where C_n is the characteristic ratio and for further discussions of higher moments of the distribution of r, C_n is still expressed with the ratio between $\left\langle h^2 \right\rangle_0$ and the product of n and and l^2. From Eqn. B.5, we obtain:

$$\begin{aligned} \left\langle s^2 \right\rangle_0 &= l^2 (n+1)^{-2} \sum_{0 \le i < j \le n} (j-i) \\ &= l^2 (n+1)^{-2} \sum_{j=1}^{n} \sum_{k=1}^{j} k \\ &= l^2 (n+1)^{-2} \sum_{1}^{n} \frac{j(j+1)}{2} \end{aligned} \tag{C.4}$$

We know the summations over j and j^2 and Eqn. C.4 can be rearranged to yield:

$$\frac{\left\langle s^2 \right\rangle_0}{nl^2} = \frac{1}{6} \frac{(n+2)}{(n+1)} \tag{C.5}$$

where the ratio decreases with increasing n. Thus, as $n \to \infty$, Eqn. C.2 and C.5 provide:

$$\left\langle s^2 \right\rangle_0 = \frac{\left\langle h^2 \right\rangle_0}{6} \tag{C.6}$$

$$\left[\text{Note}: \left(\frac{\langle s^2 \rangle_0}{nl^2} \right)_\infty = \frac{1}{6} \quad \text{when } n \to \infty \right]$$

Even when we apply some degree of correlation between two arbitrary bonds, e.g. i and $i+k$, the relationship between the length scale and n can be observed. However, n is much larger than k in most polymer chains and the length scale still depends on n' and l'.

This assumption provides:

$$n'l' = h_{\max} \tag{C.7}$$

where $h_{\max}$ is the fully extended length of the *real* chain and its actual mean square end-to-end length, $\langle h^2 \rangle_0$, is:

$$n'(l')^2 = \langle h^2 \rangle_0 . \tag{C.8}$$

Eqns. C.6 to C.8 show the real chain converges to the hypothetical freely jointed chain when n is infinitely large.

Appendix D. The Freely Rotating Chain

Unlike the freely jointed chain, real chains show correlation among bonds which provide different energies for each configuration because of rotation and bond angles that differ from θ. The projection of bond *i*+1 on *i* is $l\cos\theta$.

Successive projections provide:

$$\langle \mathbf{l}_i \bullet \mathbf{l}_{i+k} \rangle = l^2 \cos^k \theta \tag{D.1}$$

Eqn. B.4 is rewritten as:

$$\begin{aligned} \langle h^2 \rangle_0 &= nl^2 + 2l^2 \sum_{i<j} \cos^{j-i} \theta \\ &= nl^2 + 2l^2 \sum_{i<j} \alpha^{j-i} \end{aligned} \tag{D.2}$$

and the range of the summation is still $0 \le i < j \le n$. From Eqns. C.2 and D.2, we have:

$$\begin{aligned} C_n \equiv \frac{\langle h^2 \rangle_0}{nl^2} &= 1 + \frac{2}{n} \sum_{k=1}^{n-1} (n-k)\alpha^k \\ &= 1 + 2\sum_{k=1}^{n-1} \alpha^k - \frac{2}{n} \sum_{k=1}^{n-1} k\alpha^k \end{aligned} . \tag{D.3}$$

Evaluation of Eqn. D.3 provides:

$$\begin{aligned} C_n &= 1 + 2(\alpha - \alpha^n)(1-\alpha)^{-1} - \frac{2}{n}\left[\alpha(1-\alpha^n)(1-\alpha)^{-2} - n\alpha^n (1-\alpha)^{-1}\right] \\ &= (1+\alpha)(1-\alpha)^{-1} - \frac{2\alpha}{n}(1-\alpha^n)(1-\alpha)^{-2} \end{aligned} . \tag{D.4}$$

$$\left[\begin{aligned} \text{Note}: \sum_{i=m}^{n} x^i &= \frac{x^{n-1} - x^m}{x-1} \\ \sum_{i=1}^{n} ix^i &= \frac{x}{(1-x)^2}\left[x^n (n(x-1)-1)+1\right] \end{aligned} \right]$$

Eqn. D.4 shows that C_n increases when the length of the chain increases and if n is large enough to satisfy $n \to \infty$, Eqn. D.4 becomes:

$$C_\infty = (1+\alpha)(1-\alpha)^{-1} \tag{D.5}$$

Eqns. B.5, C.4, and D.3 provide:

$$\begin{aligned}\left\langle s^2 \right\rangle_0 &= \frac{l^2}{(n+1)^2}\sum_{j=1}^{n}\sum_{k=1}^{j}\left[k\left(\frac{1+\alpha}{1-\alpha}\right)-2\alpha\frac{\left(1-\alpha^k\right)}{(1-\alpha)^2}\right] \\ &= \frac{l^2 n(n+2)(1+\alpha)}{6(n+1)(1-\alpha)}-\frac{2l^2\alpha}{(n+1)^2\left(1-\alpha^2\right)}\sum_{j=1}^{n}\left[j-\left(\frac{\alpha-\alpha^{j+1}}{1-\alpha}\right)\right]\end{aligned} \tag{D.6}$$

where *k*=*j*-*i*. From Eqn. C.15, C.16, C.17, and D.6, we obtain:

$$\left\langle s^2 \right\rangle_0 = \frac{(n+2)(1+\alpha)}{6(n+1)(1-\alpha)}-\frac{\alpha}{(n+1)(1-\alpha)^2}+\frac{2\alpha^2}{(n+1)^2(1-\alpha)^3}-\frac{2\alpha^3\left(1-\alpha^n\right)}{n(n+1)^2(1-\alpha)^4} \tag{D.7}$$

and if *n* is large ($n \to \infty$):

$$\left(\frac{\left\langle s^2 \right\rangle_0}{nl^2}\right)_\infty = \frac{1}{6}\frac{(1+\alpha)}{(1-\alpha)} \tag{D.8}$$

Appendix E. Correlations in Bond Vectors

First, assume that the angle between bonds is fixed and a chain shows free rotation (Figure E.1). Then, the transform between two vectors with reference frames i and i+1 ($\vec{v}$ vector with v_x, v_y, and v_z components for the reference frame i; $\vec{v}'$ for the reference frame i+1) can be expressed with an orthogonal matrix $\mathbf{T_i}$. That is:

$$\vec{v}' = \mathbf{T_i}\vec{v} \tag{E.1}$$

where $\mathbf{T_i}$ is:

$$\mathbf{T_i} = \begin{bmatrix} \cos\theta_i & \sin\theta_i & 0 \\ \sin\theta_i\cos\phi_i & -\cos\theta_i\cos\phi_i & \sin\phi_i \\ \sin\theta_i\sin\phi_i & \cos\theta i\sin\phi_i & -\cos\phi_i \end{bmatrix} \tag{E.2}$$

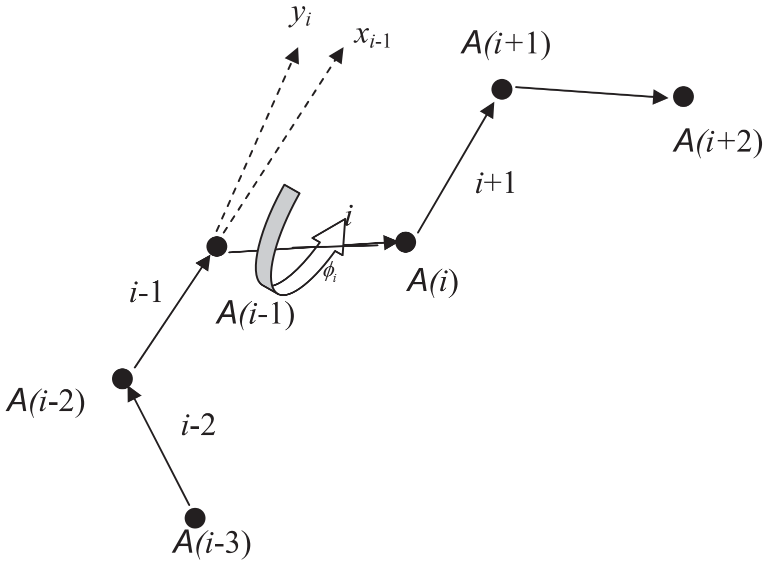

Figure E.1. Cartesian coordinate frame: z_i axis is perpendicular to the plane of this page.

From Eqn. A-3 $\vec{v}$ has components of v_x, v_y, and v_z with reference frame i of a unit vector along axis x_{i+1} of:

$$\begin{bmatrix} \cos\theta_i \\ \sin\theta_i \cos\phi_i \\ \sin\theta_i \sin\phi_i \end{bmatrix}, \tag{E.3}$$

a unit vector along with y_{i+1} of:

$$\begin{bmatrix} \sin\theta_i \\ -\cos\theta_i \cos\phi_i \\ -\cos\theta_i \sin\phi_i \end{bmatrix}, \tag{E.4}$$

and a unit vector along with z_{i+1} of:

$$\begin{bmatrix} 0 \\ \sin\phi_i \\ -\cos\phi_i \end{bmatrix}. \tag{E.5}$$

Thus the relationship between the two coordinate-systems (reference frames, *i* and *i*+1) is:

$$\begin{aligned} v'_x &= v_x \cos\theta_i + v_y \sin\theta_i \\ v'_y &= v_x \sin\theta_i \cos\phi_i - v_y \cos\theta_i \cos\phi_i + v_z \sin\phi_i \\ v'_z &= v_x \sin\theta_i \sin\phi_i - v_y \cos\theta_i \sin\phi_i - v_z \cos\phi_i \end{aligned} \tag{E.6}$$

where $\vec{v}$ and $\vec{v}'$ are column vectors. For example,

$$v = \begin{bmatrix} v_x \\ v_y \\ v_z \end{bmatrix}. \tag{E.7}$$

To obtain the scalar product of two bond vectors $\mathbf{l}_i$ and $\mathbf{l}_j$, we assume $j > i$ and a successive transformation of coordinates from *j* to *i* provides:

$$\mathbf{T_i} \cdots \mathbf{T_{j-2}} \mathbf{T_{j-1}} \mathbf{l}_j \tag{E.8}$$

where $\mathbf{l}_j$ has its one column vector:

$$\mathbf{l}_j = \begin{bmatrix} l_j \\ 0 \\ 0 \end{bmatrix} = l_j \begin{bmatrix} 1 \\ 0 \\ 0 \end{bmatrix} \tag{E.9}$$

where l_j is the scalar magnitude of $\mathbf{l}_j$. Then,

$$\begin{aligned}\mathbf{l}_i \bullet \mathbf{l}_j &= \mathbf{l}_i^T(\mathbf{T_i}\cdots\mathbf{T_{j-2}T_{j-1}})\mathbf{l}_j \\ &= l_\mathbf{i} l_\mathbf{j}[100](\mathbf{T_i}\cdots\mathbf{T_{j-2}T_{j-1}})\begin{bmatrix}1\\0\\0\end{bmatrix} \\ &= l_\mathbf{i} l_\mathbf{j}(\mathbf{T_i}\cdots\mathbf{T_{j-2}T_{j-1}})_{11}\end{aligned} \tag{E.10}$$

where $\mathbf{l}_i^T$ is the transpose of matrix $\mathbf{l_i}$ and subscript 11 denotes the 1,1 element of the matrix product.

$$\left[\begin{array}{l}\text{Note: a vector can be expressed as a column matrix,} \\ \quad \mathbf{v} = [v_x, v_y, v_z] \qquad \text{or} \qquad \mathbf{v} = \begin{bmatrix}v_x\\v_y\\v_z\end{bmatrix} \\ \text{The scalar product of two vectors:} \\ \mathbf{a}\bullet\mathbf{b} = [a_x, a_y, a_z]\bullet[b_x, b_y, b_z] = a_x b_x + a_y b_y + a_z b_z \\ \mathbf{a^T b} = [a_x, a_y, a_z]\cdot\begin{bmatrix}b_x\\b_y\\b_z\end{bmatrix} = [a_x b_x + a_y b_y + a_z b_z] \\ \mathbf{v} = \begin{bmatrix}v_x\\v_y\\v_z\end{bmatrix}, \quad \mathbf{v^T} = [v_x, v_y, v_z], \quad (\mathbf{v}^T)^T = \mathbf{v}\end{array}\right]$$

Similarly, the average bond projection of *i* along the bond to *j* is:

$$\langle \mathbf{l}_i \bullet \mathbf{l}_j \rangle = l_i l_j \langle \mathbf{T_i}\cdots\mathbf{T_{j-1}} \rangle_{11} \tag{E.11}$$

where angle brackets denote the statistical mechanical average. Thus, formally:

$$\langle \mathbf{T_i}\cdots\mathbf{T_{j-1}} \rangle = \frac{\int\cdots\int (T_i\cdots T_{j-1})\exp[-E\{l\}/RT]d\{l\}}{\int\cdots\int \exp[-E\{l\}/RT]d\{l\}} \tag{E.12}$$

and the assumption that each rotation is independent leads to:

$$\left\langle \mathbf{T_i} \cdots \mathbf{T_{j-1}} \right\rangle = \prod_{h=i}^{j-1} \left\langle \mathbf{T}_h \right\rangle \tag{E.13}$$

Then, previous discussions (Eqns. B.4, E.10, and E.11) lead to

$$\begin{aligned} \frac{\left\langle h^2 \right\rangle}{nl^2} &= 1 + \frac{2}{nl^2} \sum_{i<j} \mathbf{l}^{\mathbf{T}} \left\langle \mathbf{T} \right\rangle^{j-i} \mathbf{l} \\ &= 1 + \frac{2}{nl^2} \mathbf{l}^{\mathbf{T}} \left[\sum_{k=1}^{n-1} (n-k) \left\langle \mathbf{T} \right\rangle^{k} \right] \mathbf{l} \end{aligned} \tag{E.14}$$

where $\mathbf{h} = \sum_{i=1}^{n} \mathbf{l}_i$. The summation in Eqn. E.14 can be solved with:

$$\sum_{1}^{n-1} \left\langle \mathbf{T} \right\rangle^{k} = \left(\left\langle \mathbf{T} \right\rangle - \left\langle \mathbf{T} \right\rangle^{n} \right) \left(\mathbf{E} - \left\langle \mathbf{T} \right\rangle \right)^{-1} \tag{E.15}$$

and similar to Eqns. D.4 and D.5:

$$\frac{\left\langle h^2 \right\rangle}{n} = \mathbf{l}^{\mathbf{T}} \left[\left(\mathbf{E} + \left\langle \mathbf{T} \right\rangle \right) \left(\mathbf{E} - \left\langle \mathbf{T} \right\rangle \right)^{-1} - \frac{2 \left\langle \mathbf{T} \right\rangle}{n} \left(\mathbf{E} - \left\langle \mathbf{T} \right\rangle^{n} \right) \left(\mathbf{E} - \left\langle \mathbf{T} \right\rangle \right)^{-2} \right] \mathbf{l} \tag{E.16}$$

Also, a long chain approximation ($n \to \infty$) leads to the simplification:

$$\left(\frac{\left\langle h^2 \right\rangle}{n} \right)_{n \to \infty} = \mathbf{l}^{\mathbf{T}} \left(E - \left\langle T \right\rangle \right) \left(E - \left\langle T \right\rangle \right)^{-1} \mathbf{l} \, . \tag{E.17}$$

$$\left[\because \left\langle \mathbf{l}_i \bullet \mathbf{l}_j \right\rangle = \mathbf{l}_i^{\mathbf{T}} \left\langle \mathbf{T_i} \cdots \mathbf{T_{j-1}} \right\rangle \mathbf{l}_j \right]$$

Then, Eqn. E.9 provides:

$$C_n \equiv \frac{\left\langle h^2 \right\rangle_0}{nl^2} = \left[(\mathbf{E} + \left\langle \mathbf{T} \right\rangle)(\mathbf{E} - \left\langle \mathbf{T} \right\rangle)^{-1} - \frac{\mathbf{2} \left\langle \mathbf{T} \right\rangle}{n} (\mathbf{E} - \left\langle \mathbf{T} \right\rangle^{\mathbf{n}})(\mathbf{E} - \left\langle \mathbf{T} \right\rangle^{-\mathbf{2}}) \right]_{11} \tag{E.18}$$

Also,

$$C_\infty \equiv \lim_{n \to \infty} \left[\frac{\left\langle h^2 \right\rangle_0}{nl^2} \right] = \left[\left(\mathbf{E} + \left\langle \mathbf{T} \right\rangle \right) \left(\mathbf{E} - \left\langle \mathbf{T} \right\rangle^{-1} \right) \right]_{11} \tag{E.19}$$

Similar to the discussions in Appendix D, we can derive:

$$\begin{aligned}\frac{\left\langle s^2\right\rangle_0}{nl^2} &= \frac{(n+2)}{6(n+1)}\left[\left(\mathbf{E}+\langle\mathbf{T}\rangle\right)\left(\mathbf{E}-\langle\mathbf{T}\rangle^{-1}\right)\right]_{11}-\frac{\left[\langle\mathbf{T}\rangle\left(\mathbf{E}-\langle\mathbf{T}\rangle\right)^{-2}\right]_{11}}{n+1} \\ &+\frac{2\left[\langle\mathbf{T}\rangle^{2}\left(\mathbf{E}-\langle\mathbf{T}\rangle\right)^{-3}\right]_{11}}{(n+1)^2}-\frac{2\left[\langle\mathbf{T}\rangle^{3}\left(\mathbf{E}+\langle\mathbf{T}\rangle\right)\left(\mathbf{E}-\langle\mathbf{T}\rangle^{-4}\right)\right]_{11}}{n(n+1)^2}\end{aligned} \quad . \tag{E.20}$$

If we assume that $\langle\mathbf{T}\rangle$ is analogous to a quantity like $\cos\theta$, Eqn. E.20 reduces to Eqn. D.7.

In a symmetric rotation (Figure E.1), the chain makes free rotation with angle ϕ_i and clearly $\langle\sin\phi_i\rangle = 0$. From Eqn. E.2,

$$\langle\mathbf{T_i}\rangle = \begin{bmatrix} \cos\theta i & \sin\theta i & 0 \\ \sin\theta i\langle\cos\phi i\rangle & -\cos\theta i\langle\cos\phi i\rangle & 0 \\ 0 & 0 & -\langle\cos\phi i\rangle \end{bmatrix} \tag{E.21}$$

where $\langle T\rangle^k = (\cos\theta)^k$. Substitution of Eqn. E.21 into Eqn. E.19 provides:

$$C_\infty = \left(\frac{1+\cos\theta}{1-\cos\theta}\right)\left(\frac{1+\langle\cos\phi\rangle}{1-\langle\cos\phi\rangle}\right). \tag{E.22}$$

Appendix F. Geometry of Contour Lengths

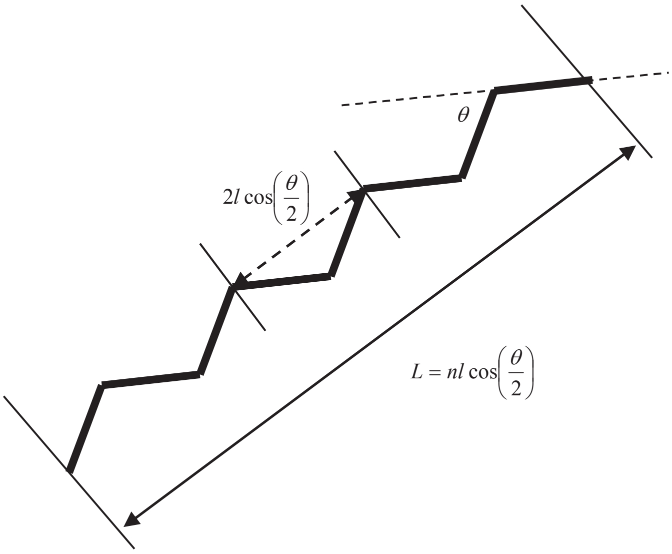

Figure F.1 The contour length of an all-trans conformation of a short polymer chain with 8 backbone chain bonds. We can see: $L = nl\cos\left(\frac{\theta}{2}\right)$.

Appendix G. Kratky and Porod Worm-like Chain Model

Eqn. 2.42 can be expanded for very small angles, $\theta \to 0$:

$$\cos\theta \cong 1 - \frac{\theta^2}{2} \tag{G.1}$$

$$\left[\begin{aligned} &\text{Note: Taylor Series,} \\ &\cos x = 1 - \frac{x^2}{2!} + \frac{x^4}{4!} - \cdots \\ &\quad = \sum_{n=0}^{\infty} \frac{(-1)^n}{(2n)!} x^{2n} \end{aligned}\right]$$

and for small *x*,

$$\ln(1-x) \cong -x \tag{G.2}$$

Leads to:

$$\ln(\cos\theta) \cong -\frac{\theta^2}{2}. \tag{G.3}$$

θ is still much smaller than the unity and Eqn. 2.42 can be rewritten as:

$$\kappa = -\frac{1}{\ln(\cos\theta)} \cong \frac{2}{\theta^2}. \tag{G.4}$$

Oncemore, persistence length, l_p, is defined as:

$$l_p \equiv \kappa \cdot l = l\frac{2}{\theta^2}. \tag{G.5}$$

The characteristic ratio of a worm-like chain is defined as:

$$C_\infty = \frac{1+\alpha}{1-\alpha} \cong \frac{2-(\theta^2/2)}{(\theta^2/2)} \cong \frac{4}{\theta^2} \tag{G.6}$$

and C_∞ is very large as expected. Also, as seen in Eqn. 2.59, the Kuhn length, l_k, is twice l_p:

$$l_k = l\frac{C_\infty}{\cos(\theta/2)} \cong l\frac{4}{\theta^2} = 2l_p. \tag{G.7}$$

$$\begin{bmatrix} \text{Note:} \\ l_k = \dfrac{C_\infty n l^2}{L} = \dfrac{C_\infty n l^2}{nl\cos(\theta/2)} = \dfrac{C_\infty l}{\cos(\theta/2)} \end{bmatrix}$$

From Eqns. 2.30 and 2.41,

$$\begin{aligned} \langle h^2 \rangle &= l^2 \sum_{i=1}^{n} \sum_{j=1}^{n} \langle \cos\theta_{ij} \rangle \\ &= l^2 \sum_{i=1}^{n} \sum_{j=1}^{n} (\cos\theta)^{|j-i|} \\ &= l^2 \sum_{i=1}^{n} \sum_{j=1}^{n} \exp\left(-\frac{|j-i|}{l_p} l \right) \end{aligned} \tag{G.8}$$

where the summation over all bonds can be solved by integration over all contour lengths of the worm-like chain. Thus, we set:

$$l\sum_{i=1}^{n} \to \int_0^L \mathrm{d}u \quad \text{and} \quad l\sum_{j=1}^{n} \to \int_0^L \mathrm{d}v \tag{G.9}$$

and solve the equation:

$$
\begin{aligned}
\left\langle h^2 \right\rangle &= \int_0^L \left[\int_0^L \exp\left(-\frac{|u-v|}{l_p} \right) dv \right] du \\
&= \int_0^L \left[\exp\left(-\frac{u}{l_p} \right) \int_0^u \exp\left(\frac{v}{l_p} \right) dv + \exp\left(-\frac{u}{l_p} \right) \int_u^L \exp\left(-\frac{v}{l_p} \right) dv \right] du \\
&= l_p \int_0^L \left[\exp\left(-\frac{u}{l_p} \right) \left(\exp\left(\frac{u}{l_p} \right) - 1 \right) + \exp\left(-\frac{u}{l_p} \right) \left(-\exp\left(\frac{L}{l_p} \right) + \exp\left(-\frac{u}{l_p} \right) \right) \right] du \\
&= l_p \int_0^L \left[2 - \exp\left(-\frac{u}{l_p} \right) - \exp\left(-\frac{L}{l_p} \right) \exp\left(\frac{u}{l_p} \right) \right] du \\
&= l_p \left[2L + l_p \left(\exp\left(-\frac{L}{l_p} \right) - 1 \right) - l_p \exp\left(\frac{L}{l_p} \right) \left(\exp\left(\frac{L}{l_p} \right) - 1 \right) \right] \\
&= 2Ll_p - 2l_p^2 \left(1 - \exp\left(-\frac{L}{l_p} \right) \right)
\end{aligned}
\tag{G.10}
$$

Appendix H. Radii of Gyration of Worm-like Chains

We have $\langle h^2 \rangle$ from Appendix G and the mean-square radius of gyration of a worm-like chain. First, from Eqns. G.8 and G.9, we obtain:

$$\begin{aligned}\langle R_g^2 \rangle &= \frac{1}{N^2}\sum_{i=1}^{N}\sum_{j=1}^{N}\langle r_{ij}^2 \rangle \\ &= \frac{1}{N^2}\frac{1}{l^2}\int_0^L\int_0^L dvdu\langle r_{uv}^2 \rangle \\ &= \frac{1}{L^2}\int_0^L\left[\int_0^L\langle r_{uv}^2 \rangle dv\right]du\end{aligned} \tag{H.1}$$

and with Eqn. G.10 the following equation is also reasonable:

$$\langle R_g^2 \rangle = \frac{2l_p^2}{L^2}\int_0^L dv\int_0^L du\left[\frac{|u-v|}{l_p} - 1 + \exp\left(-\frac{|u-v|}{l_p}\right)\right]. \tag{H.2}$$

Solving Eqn. H.2 yields:

$$
\begin{aligned}
\left\langle R_g^2 \right\rangle &= \frac{2l_p^2}{L^2}\int_0^L \left[\int_u^L \left[\frac{|u-v|}{l_p} - 1 + \exp\left(-\frac{|u-v|}{l_p} \right) \right] dv \right] du \\
&= \frac{2l_p^2}{L^2}\int_0^L \left[\int_u^L \left(\frac{|u-v|}{l_p} \right) dv - \int_u^L dv + \int_u^L \exp\left(-\frac{|u-v|}{l_p} \right) dv \right] du \\
&= \frac{2l_p^2}{L^2}\int_0^L \left[\int_u^L \frac{u}{lp} dv - \int_u^L \frac{v}{lp} dv - \int_u^L dv + \int_u^L \exp\left(-\frac{|u-v|}{l_p} \right) dv \right] du \\
&= \frac{2l_p^2}{L^2}\int_0^L \left[\left. \frac{v^2}{2l_p} \right|_u^L - \left. \frac{uv}{l_p} \right|_u^L - \left. v \right|_u^L + \int_u^L \exp\left(-\frac{|u-v|}{l_p} \right) dv \right] du \\
&= \frac{2l_p^2}{L^2}\left[\left. \frac{L^2 u}{2l_p} \right|_0^L - \left. \frac{u^3}{6l_p} \right|_0^L - \left. \frac{Lu^2}{2l_p} \right|_0^L + \left. \frac{u^3}{3l_p} \right|_0^L + \int_0^L \left[\int_u^L \exp\left(-\frac{|u-v|}{l_p} \right) dv \right] du \right] \\
&= \frac{Ll_p}{3} - l_p^2 + \frac{2l_p^3}{L} - \frac{2l_p^4}{L^2}\left(1 - \exp\left(-\frac{L}{l_p} \right) \right) \\
&= \frac{l_p}{3L^2}\left[L^3 - 3L^2 l_p + 6Ll_p^2 - 6l_p^3\left(1 - \exp\left(-\frac{L}{l_p} \right) \right) \right] \qquad \text{(H.3)}
\end{aligned}
$$

In Eqn. H.3 the last integral was provided by Eqn. G.10 and integration was done for $u \rightarrow L$, not $0 \rightarrow L$.

Appendix I. Fourier's Law and Fick's Law

It is known that the law of heat conduction can explain the relationship between time, rate of heat conduction, temperature, and area. In general, the differential form, is:

$$\mathbf{q} = -k\nabla T \tag{I.1}$$

where **q,** *k*, and ∇T are the heat flux, thermal conductivity, and local temperature gradient, respectively. For a one-dimensional problem defined in terms of *x*, Eqn. I.1 is:

$$q_x = -k\frac{\mathrm{d}T}{\mathrm{d}x}\,. \tag{I.2}$$

The integral form is then given as:

$$\frac{\partial Q}{\partial t} = -k\oint_s \nabla\mathbf{T}\,\mathrm{d}\mathbf{A}\,. \tag{I.3}$$

Integration of Eqn. I.2 provides:

$$\frac{\Delta Q}{\Delta t} = -kA\frac{\Delta T}{\Delta x}\,. \tag{I.4}$$

The first law can also be expressed in two forms: (1) in terms of fluxes, *J*, and (2) in terms of the element of volumes, *A*d*x*:

$$\begin{aligned} &(1) \quad \frac{\mathrm{d}Q}{\mathrm{d}t} = \left(J_{in} - J_{out}\right)A \\ &(2) \quad \mathrm{d}Q = \mathrm{d}c\left(A\mathrm{d}x\right) \end{aligned} \tag{I.5}$$

and these two equations yield:

$$\begin{aligned} \frac{\mathrm{d}c}{\mathrm{d}t}\left(A\mathrm{d}x\right) &= \left(J(x) - J(x+\mathrm{d}x)\right)A \\ &= -D_m\left[\left(\frac{\mathrm{d}c}{\mathrm{d}x}\right)_x - \left(\frac{\mathrm{d}c}{\mathrm{d}x}\right)_{x+dx}\right]A \end{aligned} \tag{I.6}$$

and ultimately give:

$$\frac{\mathrm{d}c}{\mathrm{d}t} = D_m \frac{\mathrm{d}^2 c}{\mathrm{d}x^2}. \tag{I.7}$$

$$\left[\text{Note}: \left[\left(\frac{\mathrm{d}c}{\mathrm{d}x}\right)_{x+dx} - \left(\frac{\mathrm{d}c}{\mathrm{d}x}\right)_x\right] = \frac{\mathrm{d}^2 c}{\mathrm{d}x^2}\mathrm{d}x\right]$$

Eqn. I.7 is Fick's second law and satisfies the condition:

$$[\text{rate of accumulation}] = -[\text{flux gradient}].$$

In general the definition of chemical potential is written as:

$$\begin{aligned} \mu_2 &= \mu_2^\circ + RT \ln a_2 \\ &= \mu_2^\circ + RT \ln \gamma_2 c \end{aligned} \tag{I.8}$$

where the subscript 2 means the solute, μ_2° is chemical potential of pure solute, R is the gas constant, and a_2 and γ_2 are activity and activity coefficient of the solute, respectively. μ_2 in Eqn. 2.90 is substituted with Eqn. I.8:

$$\begin{aligned} F_{diff} &= -\frac{1}{N_{av}}\left(\frac{\mathrm{d}\mu_2}{\mathrm{d}c}\right)\left(\frac{\mathrm{d}c}{\mathrm{d}x}\right) \\ &= -\frac{RT}{N_{av}}\left(1 + \frac{\mathrm{d}\ln\gamma_2}{\mathrm{d}c}\right)\left(\frac{\mathrm{d}c}{\mathrm{d}x}\right) \end{aligned}. \tag{I.9}$$

If we assume the particle is in the stationary-state flow condition and that the F_{diff} that the particle experiences is the same as the viscous resistance, the stationary velocity, v_0 is:

$$v_0 = -\frac{kT}{\varsigma c}\left(1 + c\frac{\mathrm{d}\ln\gamma_2}{\mathrm{d}c}\right)\left(\frac{\mathrm{d}c}{\mathrm{d}x}\right) \tag{I.10}$$

where ς is the friction coefficient and the product of the concentration and the stationary velocity equals the flux, J:

$$J = -\frac{kT}{\varsigma}\left(1 + c\frac{\mathrm{d}\ln\gamma_2}{\mathrm{d}c}\right)\frac{\mathrm{d}c}{\mathrm{d}x} \tag{I.11}$$

and Eqn. I.11 and Fick's first law provides:

$$\begin{aligned} D_m &= \frac{kT}{\varsigma}\left(1 + c\frac{\mathrm{d}\ln\gamma_2}{\mathrm{d}c}\right) \\ &= D_{t,0}\left(1 + c\frac{\mathrm{d}\ln\gamma_2}{\mathrm{d}c}\right) \end{aligned}. \tag{I.12}$$

Appendix J. The One-dimensional Fick's Law at Semi-infinite Concentration

First of all, let's invoke the van Hove space-time self-correlation function to explain the probability that the particle can be found in a given time and distance. Its one-dimensional form is:

$$P(r,t) = 4\pi r^2 \left(\frac{1}{4\pi D_t t}\right)^{3/2} \exp\left(-\frac{r^2}{4D_t t}\right) \tag{J.1}$$

where r is the distance after time t and Eqn. J.1 is equivalent to the distribution of end-to-end distances with $6D_t t = Nb^2$:

$$\begin{aligned} P(N,h)dh &= 4\pi h^2 P(N,\mathbf{h})dh \\ &= 4\pi h^2 \left(\frac{3}{2\pi Nb^2}\right)^{3/2} \exp\left(\frac{-3|\mathbf{h}|^2}{2Nb^2}\right)dh \end{aligned} . \tag{J.2}$$

The concentration is related to the probability and depends on the distance and time:

$$\frac{\partial c(x,t)}{\partial t} = D_m \frac{\partial^2 c(x,t)}{\partial x^2} \tag{J.3}$$

and the solution is:

$$c(x,t) = c_0 \frac{1}{\sqrt{4\pi D_m t}} \exp\left(-\frac{x^2}{4D_m t}\right). \tag{J.4}$$

One initial condition and two boundary conditions are used to solve Eqn. J.3:

$$\begin{bmatrix} \text{initial condition}: c(x,0) = 0 \\ \text{boundary conditions}: (1)\ c(\infty,t) = c(-\infty,t) = 0 \\ \qquad\qquad\qquad\qquad (2) \int_{-\infty}^{\infty} c\,dx = S \ (\text{hold for all } t) \\ S \approx \text{initial conc.} = c_0 \end{bmatrix} \tag{J.5}$$

and the resultant equation is very similar to the result from thin film diffusion.* Eqn. J.3 can be obtained again by differentiation of Eqn. J.4. First,

---

*Borg, R. J.; Dienes, G. J. In *Introduction to Solid State Diffusion* Academic Press: Boston, 1988.

$$\frac{\partial c}{\partial t} = c_0 \frac{1}{\sqrt{4\pi D_m t}} \exp\left(-\frac{x^2}{4D_m t}\right)\left(-\frac{1}{2}t^{-1} + \frac{x^2}{4D_m}t^{-2}\right) \tag{J.6}$$

where differentiation with respect to x yields:

$$D_m \frac{\partial c}{\partial x} = D_m c_0 \frac{1}{\sqrt{4\pi D_m t}} \exp\left(-\frac{x^2}{4D_m t}\right)\left(-\frac{2x}{4D_m t}\right) \tag{J.7}$$

and the second derivative is:

$$D_m \frac{\partial^2 c}{\partial x^2} = D_m c_0 \frac{1}{\sqrt{4\pi D_m t}} \exp\left(-\frac{x^2}{4D_m t}\right)\left(-\frac{2}{4D_m t} + \frac{2x}{4D_m t}\frac{2x}{4D_m t}\right). \tag{J.8}$$

From Eqns. J.6, J.7, and J.8 we can obtain Eqn. J.3.

Apendix K. Shear Flow

Shear flow, q, is defined as:

$$q \equiv \sigma t = \frac{VQ}{I} \tag{K.1}$$

where τ, t, V, Q, and I are the *shear stress*, thickness, total *shear force*, *first moment of area* (*the first moment of inertia* or *statical moment of inertia*), and *second moment of inertia*, respectively. Also,

$$Q = \int_A y \mathrm{d}A \tag{K.2}$$

where A and y are the given area and the perpendicular distance to the element dA from the x axis, respectively.

$$I = \int\int_A y^2 \mathrm{d}x\mathrm{d}y \tag{K.3}$$

when the force is applied on the x axis.

Appendix L. The Maxwell Element

The Maxwell model was developed to explain a material obeying Hooke’s law (a spring model) as well as Newton’s law (a dashpot model). The basic assumption is that such materials can undergo viscous flow and also respond elastically. The combination of the two laws provides:

$$\varepsilon = \varepsilon_{elast} + \varepsilon_{visc} \tag{L.1}$$

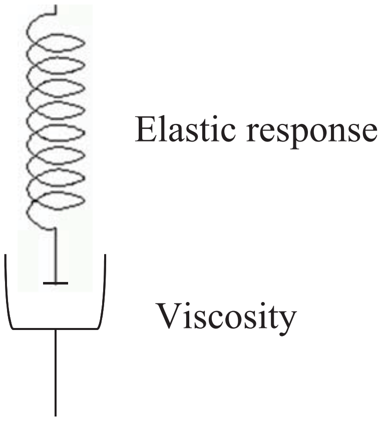

Figure L.1 Schematic Maxwell model

Assuming the stress is a constant:

$$\varepsilon(t) = \frac{\sigma(t)}{G(t)} + \frac{\sigma(t)t}{\eta} \tag{L.2}$$

Appendix M. Concentration, Volume Fraction, Hydrodynamic Volume, and Viscosity

From Eqns. 2.122 and 2.123, the relationship between the specific viscosity and the hydrodynamic volume can be obtained. As a starting point, the volume fraction, ϕ, is defined as:

$$\phi \equiv \frac{\text{solute volume}}{\text{solution volume}} = \frac{c}{M}(\text{molar volume of solute}) \tag{M.1}$$

where c is the concentration of the solute (mass/volume) and M is molar mass. The volume fraction can be written as:

$$\phi = \frac{\text{volume of all coils}}{\text{total volume}} = \frac{(n_B \times N_{av})V_h}{V} \tag{M.2}$$

where n_B, N_{av}, V_h, and V are moles of coils, Avogadro's number, the hydrodynamic volume of a polymer coil, and total volume, repectively. Eqn. 2.122 also reflects:

$$\eta_{sp} = 2.5\phi = 2.5\frac{(n_B \cdot N_{av})V_h}{V}. \tag{M.3}$$

c can be expressed as:

$$c = \frac{n_B \times M}{V} \tag{M.4}$$

where M is the molar mass. Eqns. M.3 and M.4 provide:

$$\begin{aligned} \eta_{sp} &= 2.5\phi = 2.5\frac{(n_B \cdot N_{av})V_h}{V} \\ &= 2.5\left(\frac{n_B M}{V} \cdot \frac{V_h N_{av}}{M}\right). \\ &= \frac{c}{M} N_{av} V_h \end{aligned} \tag{M.5}$$

Eqns. M.5 and 2.121 provide Eqn. 2.124:

$$\eta = \eta_s\left(1 + 2.5\frac{c}{M}N_{av}V_h + \cdots\right)$$

Also, from the definition of intrinsic viscosity, Eqn. M.5 provides:

$$\left[\eta\right] \approx \frac{N_{av}}{M} V_h \approx \frac{kT\, N_{av}}{\eta_s M_0\, N} \tau \,. \tag{M.6}$$